# Full-discharge simulation and optimization with the RAPTOR code, from present tokamaks to ITER and DEMO

## Simon VAN MULDERS

# Abstract

Tokamak devices aim to magnetically confine a hydrogen plasma at sufficiently high pressure to achieve net energy production from nuclear fusion of light isotopes. Predictive modeling and optimization is crucial for reliable operation of tokamak reactors, like ITER and DEMO, due to the smaller margin for experimentation, contrarily to current devices.

Exploitation of a fusion reactor requires a reliable *stationary operating point*, maximizing the reactor performance, whilst maintaining a safe margin from physics instabilities and engineering limits. Active control of plasma profiles aims to improve confinement quality and MHD stability. Of particular interest are rational values of the safety factor $q$, where instabilities can be triggered: periodic sawteeth and neoclassical tearing modes (NTMs). Hybrid and advanced scenarios prolong the pulse duration by shaping the $q$ profile.

Fast and reliable access to the desired operating point needs to be ensured during the plasma current *ramp-up* phase. In addition, an optimized *ramp-down* strategy is critical for safe and fast termination, both in planned and emergency shutdown scenarios. Navigating the plasma state through a stable envelope within the operating space demands proper understanding of the non-linear plasma dynamics, including the impact of actuators like heating, (localized) current drive, gas injection and plasma shaping.

By combining fast numerical schemes with reduced physics models, the RAPTOR transport solver achieves rapid simulation of plasma profile dynamics, including current diffusion and transport of heat and particles. A range of transport models is available, varying from empirical to scaling-law-driven to first-principles-based. A new stationary state solver is developed for rapid plasma scenario optimization. Coupled to a neural network surrogate transport model, the ITER hybrid scenario is optimized at different plasma currents, densities and pedestal heights and for varying heating mix. We show how the electron cyclotron current drive (ECCD) deposition can be optimized to shape the $q$ profile, aiming for a maximum fusion gain $Q$, while maintaining $q > 1$, avoiding sawtooth oscillations. We find the optimum plasma current for maximizing $Q$ and describe the operating ranges enabled by 20 MW and 40 MW of EC power.

ASDEX Upgrade (AUG) allows to study advanced scenarios with centrally elevated $q$ profile in reactor-relevant conditions. Fast formation of an elevated $q$ profile is achieved through heating during the ramp-up, and maintained stationary by off-axis neutral beam injection (NBI) and central, counter-current ECCD. Inter-discharge modeling in RAPTOR is successfully applied to optimize the NBI onset time and ECCD deposition, aiming for an early stationary phase, while avoiding the onset of NTMs. We demonstrate how trajectory optimization allows

## Abstract

to obtain and sustain the desired $q$ profile, with $q_{min}$ between 1 and 1.5, including an early $q_{min} < 1.5$ condition.

Terminating a DEMO plasma is a daunting challenge, due to the variety of constraints and the highly non-linear and self-organized nature of a burning plasma. As the plasma current is reduced, the current density tends to peak, complicating control over the vertical plasma position. Furthermore, strong impurity radiation can trigger a radiative collapse, requiring careful control of the plasma state. We propose the application of non-linear, dynamic optimizations in RAPTOR to achieve a safe pulse termination. Plasma current, shaping, heating and impurity gas injection are optimized to maintain the plasma stable throughout the ramp-down. The importance of heating throughout the ramp-down and optimized plasma current traces are confirmed by dedicated AUG ramp-down experiments, successfully simulated in RAPTOR.

**keywords:** integrated tokamak simulation, profile control, transport modeling, plasma scenarios, RAPTOR, ASDEX Upgrade, ITER, DEMO, numeric optimization, partial differential equations, optimal control.

# Résumé

Les tokamaks visent à confiner magnétiquement un plasma d'hydrogène à une pression suffisamment élevée, pour obtenir une production nette d'énergie à partir de la fusion nucléaire d'isotopes légers. La modélisation et l'optimisation prédictives de la décharge complète sont cruciales pour le fonctionnement fiable des réacteurs tokamak, comme ITER et DEMO. L'exploitation d'un réacteur de fusion nécessite un *point de fonctionnement stationnaire*, maximisant la performance du réacteur, tout en maintenant une marge de sécurité vis-à-vis des instabilités physiques et des limites techniques. Le contrôle actif des profils cinétiques et de densité de courant du plasma vise à améliorer la qualité du confinement et la stabilité Magnétohydrodynamique. Des scénarios hybrides et avancés permettent de prolonger la durée de l'impulsion en façonnant le profil $q$. Cette thèse se concentre sur l'optimization de ces scénarios ainsi que sur la meilleure méthode de les atteindre et de terminer la décharge correctement.

Naviguer le plasma d'un tokamak dans une région stable à l'intérieur de l'espace de fonctionnement exige une bonne compréhension de la dynamique non linéaire du plasma, y compris de l'impact des actionneurs tels que le chauffage, le courant (localisé), l'injection de gaz et la forme du plasma. Un accès rapide et fiable au point de fonctionnement stationnaire doit être assuré pendant la phase de montée du courant du plasma. A la fin de la décharge, une stratégie optimisée pour la diminution du chauffage et du courant du plasma est essentielle pour un arrêt sûr et rapide, tant dans les scénarios d'arrêt planifié que d'urgence.

En combinant des méthodes numériques efficaces avec des modèles physiques réduits, le code de transport RAPTOR permet de simuler rapidement la dynamique des profils radiaux du plasma, y compris la diffusion du courant et le transport de la chaleur et des particules. Une gamme de modèles de transport turbulent est disponible, allant des modèles empiriques aux modèles basés sur des lois d'échelle et un modèle dérivé des premiers principes.

Un nouveau solveur, résolvant directement l'état stationnaire des équations, permet une optimisation rapide des scénarios de plasma. Couplée à un modèle gyrocinétique reproduit grâce à un modèle de réseaux de neurones, la méthode proposée est appliquée pour optimiser le scénario hybride d'ITER, pour différentes valeurs du courant de plasma, de la densité du plasma et de la hauteur de 'piédestal' du profil de la température, ainsi que pour des différentes combinaisons de systèmes de chauffage. La distribution du profil de densité de courant générée par le système de chauffage à résonance cyclotronique des électrons (ECRH/ECCD) est optimisée pour modifier le profil de $q$, en visant un gain de fusion maximal $Q$ (rapport en la puissance de fusion obtenue et la puissance de chauffage auxiliaire injectée),

tout en maintenant $q > 1$, pour éviter les oscillations de dent-de-scie et maintenir un bon confinement.

ASDEX Upgrade (AUG), permet d'étudier des scénarios avancés avec un profil $q$ élevé au centre dans des conditions réalistes par rapport à un réacteur de fusion. La formation rapide d'un profil $q$ élevé est obtenue par chauffage pendant la phase de montée du courant du plasma et maintenue stationnaire par l'injection d'un faisceau neutre hors axe (NBI) et du courant entraîné par le système ECCD au centre du plasma, avec une direction opposée au courant total du plasma. La modélisation et l'optimisation entre deux expériences du plasma ont été réalisées avec le code RAPTOR, en optimisant le temps d'activation du faisceau neutre et le profil de densité de courant entraîné par le système ECCD, en visant une phase stationnaire au début de la décharge, tout en évitant l'apparition des îlots magnétiques NTM (neoclassical tearing mode).

Terminer un plasma DEMO est un défi extraordinaire, à cause de la variété des contraintes et de la nature hautement non linéaire et auto-organisée d'un plasma en combustion. Lorsque le courant du plasma est réduit, la densité de courant tend à atteindre un profil radial plus concentré au centre, ce qui complique le contrôle de la position verticale du plasma. En outre, un fort rayonnement dû aux impuretés dans un plasma DEMO peut déstabiliser la phase de terminaison. En appliquant des optimisations non linéaires et dynamiques avec le code RAPTOR on obtient des scénarios de terminaison plus fiable. Le courant, la géométrie du plasma, le chauffage et l'injection des impuretés sont optimisés pour maintenir le plasma stable. L'imporance du chauffage tout au long de la phase de terminaison et de l'optimisation de trajectoire du courant du plasma sont validés par des expériences de terminaison des décharges dans le tokamak AUG. Les effets observés sont simulés avec succès avec le code RAPTOR.

**Mots clés:** simulation intégrée de tokamak, contrôle des profils, modélisation du transport, scénarios plasma, RAPTOR, ASDEX Upgrade, ITER, DEMO, optimisation numérique, équations différentielles partielles, contrôle optimal.

# Contents

# Contents

# Contents

# 1 Introduction

*Non est ad astra molle e terris iter.*
*There is no easy way from the earth*
*to the stars.*

verse 437 of *Hercules*,
Seneca the Younger (c.4BC-AD65)

## 1.1 Global energy perspective

Throughout human history, harnessing novel primary energy sources for the provision of heat and useful work has propelled technological progress. The discovery of fire, the deployment of animal power and the exploitation of fossil fuels have each allowed humans to construct an exceedingly intricate civilization, raising the overall welfare. However, ever since the end of the 20th century, a rising awareness of the unsustainable nature of our society has become increasingly pervasive: anthropogenic carbon emissions are altering the climate, while the primary resources of our planet are being exhausted. Furthermore, struggles over the control of primary reserves and trade routes continuously cause geopolitical tensions, occasionally triggering armed conflicts. To avert irreversible and catastrophic events caused by climate change, and to alleviate the radically unequal distribution of welfare over an evergrowing world population over the coming decades, a massive pivot towards more sustainable practices is essential.

Today, about 80% of all primary energy required to power industry, transportation and our everyday life is extracted from fossil resources like coal (26.8%), natural gas (23.2%) and oil (30.9%) [IEA 2019]. In the absence of affordable carbon capture and storage technologies and abundant $CO_2$ sinks, a zero carbon future will eventually require the replacement of all fossil fuels. To limit global warming to 1.5°C above pre-industrial levels, net-zero anthropogenic carbon emissions need to be achieved by mid-century [Rogelj et al. 2016].

In the past decades, electric energy became increasingly pervasive in final energy consump-
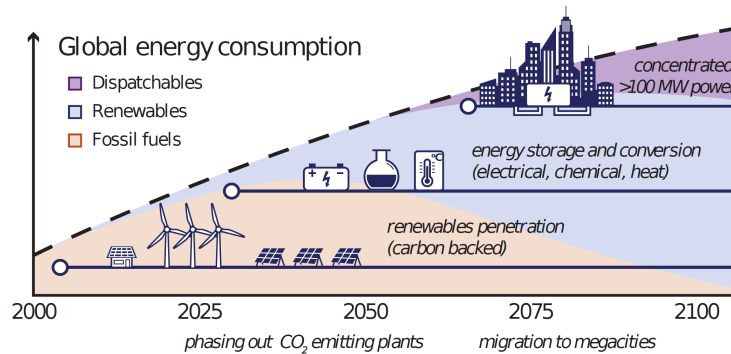
Figure 1.1: Cartoon representation of a primary energy production technology transition towards a phase-out of carbon technologies, while feeding an ever-growing demand. *Source: [The DIFFER Team 2017].*

tion. Electrification is reinforced as robots and 3D printing transform manufacturing, while the future of both transport and heating could well be electric.

Solar and nuclear technologies have a huge potential to generate the bulk of electric energy. Optimism fetched by impressive falls in costs of renewable technologies must be tempered by the vast growth of electric power demand in developing countries, the large system costs to accommodate decentralized electric power generation in the grid and the need for fossil fuel back-up to guarantee security of supply in the absence of large-scale and cheap energy storage. Furthermore, the large land use of renewables has to be contrasted with increasing urbanization, as megacities develop around the world.

Whenever commercially viable next-generation nuclear fission or fusion reactors will be connected to the grid, they could be of key importance to power highly urbanized regions with a low potential for renewables [Nicholas et al. 2021], represented schematically in Figure 1.1.

In the meantime, demand side activation and novel storage technologies can enhance the diffusion of renewables. Energy storage (large-scale batteries, power-to-gas, power-to-hydrogen), activated demand side (smart meters, smart grids) and interconnection with neighbouring grids are all required in order to sustain high penetration of intermittent renewables in the electric power system. Battery technologies are promising, although major cost and capacity issues remain. Electrification of transport, reinforced by urban pollution regulation, would imply a major influx of storage capacity in the electric power system.

The variety of technologies which could sustain a post-fossil fuel era is impressive. The time horizon for these technologies to become competitive with conventional technologies will be decisive for mankind's success in mitigating climate change.

## 1.2 The development of nuclear energy sources

During the 1920s, tremendous progress in the understanding of nuclear physics led to the discovery that the interior of stars is powered by *nuclear fusion*, through the continuous merging of light isotopes into heavier elements [Eddington 1920; Atkinson and Houtermans 1929]. The

incurred mass deficit through the creation of a more stable nucleus is converted into energy, through Einstein's famous relation $E = mc^2$. The binding energy per nucleon starts increasing for elements heavier than iron. Likewise, breaking up larger atoms such as uranium isotopes leads to exothermal reactions.

Scientists and engineers quickly realized that tantalizing quantities of energy could be harvested from nuclear reactions. Compared to the chemical reactions that liberate energy from fossil fuels, synthesized in the Earth's crust over the timespan of geological eras, nuclear reactions generate an energy density over a million times higher.

In the context of the Second World War and the following Cold War, American and Soviet scientists quickly mastered the technology to apply the power of the atom for warfare purposes. However, in 1942, the Chicago pile of Enrico Fermi demonstrated the potential of nuclear fission as a controlled power source. As early as the 1950s, nuclear fission power plants started being deployed on both sides of the Iron Curtain. Today, nuclear fission contributes significant amounts of power to the electricity mix in various countries. Nevertheless, the issue of long-lived radioactive waste and the risks of catastrophic chain reaction events and nuclear proliferation are prone to fervent criticism and unfavorable public opinions throughout the world. Furthermore, large investment costs and limited uranium reserves make the future perspectives of nuclear fission as an energy source unclear.

The controlled application of nuclear fusion for peaceful purposes stands in stark contrast to its nuclear fission counterpart: after more than 70 years of research, a demonstration fusion power plant is still elusive. However, the history of the nuclear fusion research programs throughout the world is a remarkable story of international collaboration and human ingenuity and tenacity in the face of the scientific and engineering challenges posed by the endeavor.

## 1.3 Nuclear fusion and the plasma state

The astronomical size of stars allows them to confine the fusion fuel, i.e. hydrogen isotopes, by the gravitational pull of their own mass. In the star's interior, the temperatures and densities are such that matter exists in the *plasma state*, a collective of charged particles with (fully) ionized atoms and electrons. For nuclear fusion reactions to occur, bringing matter to the plasma state is essential, as individual ions need sufficient kinetic energy to overcome the barrier created by the repulsive Coulomb force amongst equally charged particles.

In the 1950s, John Lawson applied a simple, generic 0D power balance equation to derive a necessary criterion for achieving a net power gain in a fusion reactor containing a plasma constituted by deuterium and tritium ions, the elements featuring the highest fusion reaction cross section at technologically relevant temperatures [Lawson 1957]. Note that this criterion is valid irrespective of the confinement principle and technological implementation of the reactor. Writing a steady state power balance and neglecting bremsstrahlung losses, one

obtains a condition to achieve plasma conditions beyond break-even[1]:

$$n\tau_E \geq \frac{10T}{\langle \sigma v \rangle_{DT} \Delta E_f} \tag{1.1}$$

with $\langle \sigma v \rangle_{DT}$ the average of the DT reaction cross-section multiplied with the relative velocity $v = | \mathbf{v}_D - \mathbf{v}_T |$, averaged over the D and T velocity space distributions[2], $\Delta E_f = 17.6 \, \text{Mev}$, the energy produced by a single DT fusion reaction, $n$ the plasma density, $T$ the plasma temperature and $\tau_E$ the energy confinement time, a metric for thermal insulation, defined as the ratio between the total plasma energy and the heating power required to sustain it. From this expression, estimates of the orders of magnitude of temperature, density and confinement time can be extracted: for low temperatures, the right hand side is a decreasing function with temperature, reaching a minimum in the range $T = [20 \, \text{keV} \, 30 \, \text{keV}]$. In this temperature regime, break-even roughly requires $n\tau_E \geq 0.6 \times 10^{20} \text{m}^{-3}\text{s}$. To achieve terrestrial nuclear fusion, two confinement technologies are under development:

- Inertial confinement relies on powerful lasers to heat a hohlraum that encloses a small target containing the fuel. The hohlraum irradiates the fuel pellet with an X-ray bath, causing ablation of the outer layers of the pellet and, through momentum conservation, a strong inward compression of the fuel in the center of the pellet. Extremely high densities ($n \sim 10^{31} \text{m}^{-3}$) can be confined for a very short time ($\tau_E \sim 10^{-11} \text{s}$), leading recently to the achievement of a burning plasma (predominantly self-heated) at the Lawrence Livermore National Laboratory in Livermore, USA [Zylstra et al. 2022].

- Magnetic confinement of the electrically charged particles that form a plasma is achieved by applying strong magnetic fields with magnetic field coils. Typically, magnetic reactor concepts, like the tokamak and the stellarator, aim for $n \sim 10^{20} \text{m}^{-3}$ and $\tau_E \sim 1 \text{s}$.

While the DT reaction $^2\text{D} + {}^3\text{T} \rightarrow {}^4\text{He} + {}^1\text{n} + 17.6 \, \text{MeV}$, is the most favorable regarding the temperatures, density and thermal insulation to be achieved to realize a net fusion power gain, it gives rise to various difficulties. While deuterium is abundant in seawater, the short-lived tritium has to be synthesized in situ, by irradiating lithium blankets in the reactor wall with the fusion-born neutrons $^6\text{Li} + {}^1\text{n} \rightarrow {}^4\text{He} + {}^3\text{T} + 4.8 \, \text{MeV}$. Furthermore, the radiation of the reactor wall with 14.1 MeV neutrons poses extreme material science challenges.

A plasma is a quasi-neutral ionized gas, in a sense that neutrality can only be violated on spatial scales small compared to the Debye length[3], exhibiting collective, non-linear dynamics.

---

[1]The fusion plasma reaches break-even when the produced fusion power $P_{fus}$ equals the injected auxiliary heating power $P_{aux}$. This corresponds to a fusion gain factor $Q = 1$, with $Q = P_{fus}/P_{aux}$. Note that this condition is necessary but not sufficient for a fusion power plant. An engineering gain factor for the total facility is defined in [Freidberg 2007] as $Q_E = (P_{out}^{elec} - P_{in}^{elec})/P_{in}^{elec}$, including a finite conversion efficiency of fusion power into electricity, and of electricity into plasma heating power.

[2]Formally, $n_D n_T \langle \sigma v \rangle_{DT} = \int \int d\mathbf{v}_D d\mathbf{v}_T f_D(\mathbf{v}_D) f_T(\mathbf{v}_T) \sigma_{DT}(v) v$. Assuming two Maxwellian distributions with $T_D = T_T = T$, $\langle \sigma v \rangle_{DT}$ increases with $T$ until it reaches a maximum for $T \sim 60 \, \text{keV}$.

[3]The Debye length $\lambda_D$ is the spatial distance beyond which the electric field of an individual particle inside the plasma is shielded by surrounding particles [Debye and Hückel 1923].

The ions and electrons that make up the plasma give rise to electromagnetic fields and are at the same time subject to the action of the resulting electromagnetic forces. On spatial scales large compared to the Debye length, and on time scales large compared to the time scale of plasma oscillations caused by local neutrality violations, the plasma can be described as a single fluid, with the magnetohydrodynamics (MHD) theory developed by Hannes Alfvén [Alfvén 1950].

Based on the basic understanding of MHD theory and the guiding center movement of charged particles[4] in the presence of a magnetic field, researchers embarked on the quest to design a viable magnetic confinement device for fusion plasmas. The global MHD stability of a plasma configuration is a fundamental requirement for any confinement device. A variety of projects were started in the USA, the UK and the USSR to develop a scheme to confine a plasma with the temperature and density required for nuclear fusion, among which magnetic confinement devices like linear and toroidal pinches and magnetic mirrors. In 1958, after years of parallel scientific programs under a shroud of secrecy, the declassification of nuclear fusion research was announced at the second Atom for Peace United Nations conference in Geneva.

## 1.4   The tokamak: historical perspective, concept and challenges

> I believe the author has formulated an extremely important and not necessarily hopeless problem.
>
> ――――――――――――――――
> Andrei Sakharov (1921–1989)

This was the reaction of Soviet scientist Sakharov after reading through the notes of Lavrentyev, an autodidact Red Army Sergeant stationed in the remote peninsula of Sakhalin, proposing the use of controlled nuclear fusion reactions for energy production [Clery 2013].

### 1.4.1   Origin of the tokamak

Even though Lavrentyev's concept for electrostatic confinement of a DT plasma was relatively naive, it sparked the creativity of great minds: with the help of his colleague Tamm, Sakharov came up with a clever idea for a plasma confinement device: the tokamak, an acronym for 'toroidal'naya kamera s magnitnymi katushkami' (toroidal chamber with magnetic coils).

At the 1968 IAEA conference in Novosibirsk, Lev Artsimovich, leader of the tokamak endeavor at the Kurchatov Institute in Moscow, reported the achievement of 1 keV on their T-3 tokamak [Artsimovich 1969]. The scepticism of Western scientist was profound. But when a team of

――――――――――――――――

[4]The motion of electrons and ions in a magnetized plasma can be described as the superposition of a fast gyrating motion around the magnetic field lines and a slow drift of the center of the gyro-orbit (guiding center), perpendicular to the magnetic field lines. The charged particles stream unconstrained in the direction parallel to the magnetic field lines.
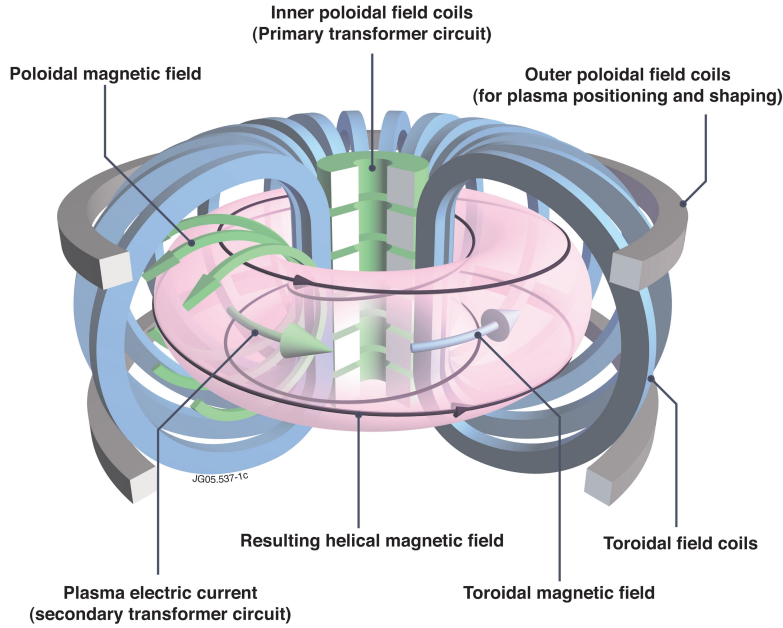
Figure 1.2: Illustration of the tokamak concept. *Source:EUROfusion.*

British scientists were invited behind the Iron Curtain to install their brand new Thomson scattering system temperature diagnostic on T-3, the bold claims of Artsimovich were confirmed [Peacock et al. 1969]. Nuclear fusion as an energy source, boasting the tantalizing promise of capturing a star on Earth, seemed imminent. Worldwide, the tokamak program gained unprecedented momentum: the stellarator in Princeton was quickly refurbished into a tokamak and Euratom initiated the JET project, to construct a flagship European tokamak.

### 1.4.2 Tokamak confinement scheme: global MHD stability

The confinement of individual charged particles in a tokamak plasma can be understood by following the trajectory of their guiding centers. In the presence of a magnetic field $\mathbf{B}$ and an electric field $\mathbf{E}$, particles with charge $q$ and velocity $\mathbf{v}$, experience a Lorenz force $\mathbf{F} = q(\mathbf{E} + \mathbf{v} \times \mathbf{B})$. As a result, they describe tight orbits around magnetic field lines, while streaming freely along the parallel direction. The electric currents driven in the toroidal field coils indicated in Figure 1.2 give rise to a toroidal magnetic field, with closed field lines. However, the inherent non-uniformity of the magnetic field strength and curvature of a tokamak give rise to charge separation in the vertical direction[5] and consequent expulsion of the plasma due to the resulting $\mathbf{E} \times \mathbf{B}$ drift. To stabilize the configuration, a poloidal magnetic field is added, resulting in helical field lines, wrapping around toroidal surfaces. Particles that follow the field lines pass periodically through the upper and lower parts of the tokamak. With respect to the axis of the torus, the vertical drift will alternately cause inward and outward excursions, causing the guiding center to remain in close proximity of a toroidal surface. As a plasma is an

---

[5]The guiding center velocity due to $\nabla B$ and curvature drifts has opposite sign for ions and electrons.

excellent conductor, with a decreasing resistivity for increasing electron temperature [Spitzer 1962], the poloidal magnetic field can be created by driving a toroidal current in the plasma column. Usually this is achieved by ramping the current in a central solenoid, hence inducing an electromotive force in the plasma by changing the enclosed magnetic flux (as described by Faraday's law). Sustaining this flux change with a central solenoid makes tokamak discharges inherently pulsed.

A key quantity to describe the MHD stability of tokamak plasmas is the safety factor profile $q$, defined as $\partial \phi / \partial \psi$, with $\phi$ and $\psi$ representing respectively the toroidal and poloidal magnetic field flux. This parameter provides a metric for the helicity of magnetic field lines: it describes how many toroidal turns a field line must complete to perform a full turn in the poloidal plane[6]. The early tokamak researchers in the Soviet Union found that by limiting the plasma current so that edge $q$ value could be maintained above 2, the most aggressive MHD instabilities, like the m/n=2/1 external kink mode (with $m$ and $n$ respectively the poloidal and toroidal mode numbers), could be eliminated [Artsimovitch et al. 1964] (to avoid higher order external kink modes, preferably $q_{edge} > 3$ [Wesson 2004]). The external kink mode had been predicted theoretically in [Kruskal et al. 1954]. The longitudinal magnetic field needs to be sufficiently strong to withstand a plasma current driven kink motion of the plasma column.

### 1.4.3 Heated plasmas, neoclassical theory and plasma turbulence

As the oil crisis of 1973 convinced policy makers around the world to invest in the development of alternative energy sources, a golden era for tokamak science heightened the hope for a swift deployment of fusion power. On the theoretical front, neoclassical theory was derived, describing Coulomb collisions between single particles performing orbits in a toroidal geometry, where the non-uniform magnetic field and curved geometry give rise to particle trapping and particle drifts across field lines [Galeev and Sagdeev 1968]. The reduction of the Spitzer conductivity due to the presence of trapped electrons was considered by [Hinton and Oberman 1969]. Further derivations in the neoclassical framework gave rise to the fascinating discovery that in the presence of a pressure gradient, 'banana' orbits of trapped electrons give rise to a self-generated current in the plasma, named bootstrap current [Galeev 1970; Bickerton et al. 1971]. Diffusion coefficients from neoclassical theory allowed for estimates on the required size for a fusion reactor, while hopes for a steady state reactor were fueled by the newly discovered bootstrap current, which could potentially provide the poloidal magnetic field required for the tokamak confinement scheme [Kadomtsev and Shafranov 1971].

On the experimental side, increasing temperatures above 1 keV could be achieved by complementing ohmic heating (with decreasing efficiency at higher temperature as the plasma becomes less resistive $\eta \sim T_e^{-3/2}$) with Neutral Beam Injection (NBI) heating[7] [Stix 1972] and

---

[6]The safety factor $q$ is inversely proportional to the enclosed plasma current. For a given equilibrium, the safety factor $q(\rho)$ and the parallel current density $j_{par}(\rho)$ carry the same information, with $\rho$ a generic flux surface label coordinate.

[7]NBI: ions are accelerated to high energy and neutralized so they can penetrate the magnetic chamber and heat the plasma through collisions.

radiofrequency heating[8]. As tangential injection of the NBI and the presence of a tangential wave vector component of the injected electromagnetic waves allows to drive electric current in the plasma [Fisch and Boozer 1980], hopes rose that combining bootstrap and auxiliary current drive could enable steady state tokamak reactors. As researchers realized that the power drain due to ohmic heating in the magnet coils would be unacceptable for the economy of a power plant, the development of tokamaks with superconducting coils was started. By the end of the 70s a superconducting tokamak was constructed at the Kurchatov Institute in Moscow.

A major setback was finding that anomalous transport increased the radial diffusion of heat above the transport levels predicted by neoclassical estimates [Kadomtsev and Pogutse 1971]. Local gradients in temperature and density destabilize drift waves, creating a turbulent state that drives the anomalous diffusion [Mazzucato 1976; Horton 1999]. These turbulence-driven micro-instabilities are responsible for an inverse scaling of the confinement time $\tau_E$ with the heating power $P$: $\tau_E = W_{th}/P \sim P^{-\alpha_P}$, hence $W_{th} \sim P^{1-\alpha_P}$, with $\alpha_P \sim 0.7$ [Doyle et al. 2007] (with $W_{th}$ the thermal energy of the plasma). This behaviour originates from the observed stiffness of radial temperature profiles: as soon as a critical temperature gradient is exceeded, a further increase of heating power leads to a strong enhancement of turbulent transport [Coppi 1980]. The result is that strong resistance is incurred when trying to raise the central temperature and density, as required to boost the core reactivity [Murakami 1983]. Paul-Henri Rebut, director of JET, described this as a lack of significance of auxiliary heating [Fleschner 2022]. A general feeling of malaise shrouded the fusion community: a working power plant concept would need to be either very large, or operate at very high magnetic field (note that for an increased magnetic field, the plasma current can be increased while maintining the plasma stable with respect to external kink modes)[9].

A serendipity would break the status quo and allow for renewed hope: at the Varenna summer school in June 1982, Fritz Wagner would baffle the attendants by reporting on the discovery of a high confinement plasma state (H-mode) on ASDEX near Munich, doubling the confinement time [Wagner et al. 1982; Fleschner 2022]. Increasing the heating of a diverted plasma[10], a bifurcation is triggered. The self-organization of turbulence gives rise to a sheared $\mathbf{E} \times \mathbf{B}$ flow, that grinds down turbulent eddies and hence suppresses radial transport [Biglari et al. 1990; Burrell et al. 1992]. The reduced size of turbulent eddies causes a steepening of pressure gradients near the edge, the so-called pedestal. An important drawback of the new regime was soon discovered: when exceeding a critical edge pressure gradients, set by ideal MHD ballooning and peeling modes [Doyle et al. 2007], Edge Localized Modes (ELMs) are triggered, periodically expelling bursts of energy and particles from the plasma, endangering the integrity of the first wall on a reactor-grade device. Avoiding or mitigating ELMs, towards viable reactor operation,

---

[8]Ion and Electron Cyclotron Heating (ICH/ECH): electromagnetic waves are injected, resonant with the cyclotron motion of either ions or electrons, so they can exchange energy with the plasma.

[9]Note that L-mode plasma confinement has a strong dependence on plasma current and a weak dependence on magnetic field. This has recently been discussed in [Angioni et al. 2023], where transport calculations for L-mode fusion reactors are reported.

[10]A diverted plasma features a so-called X-point (a point where the poloidal magnetic field is null) in the last closed flux surface (LCFS), separating the confined region from an open field line region. When particles cross the LCFS, they stream along the field lines towards the so-called divertor plates that are distant from the core plasma.
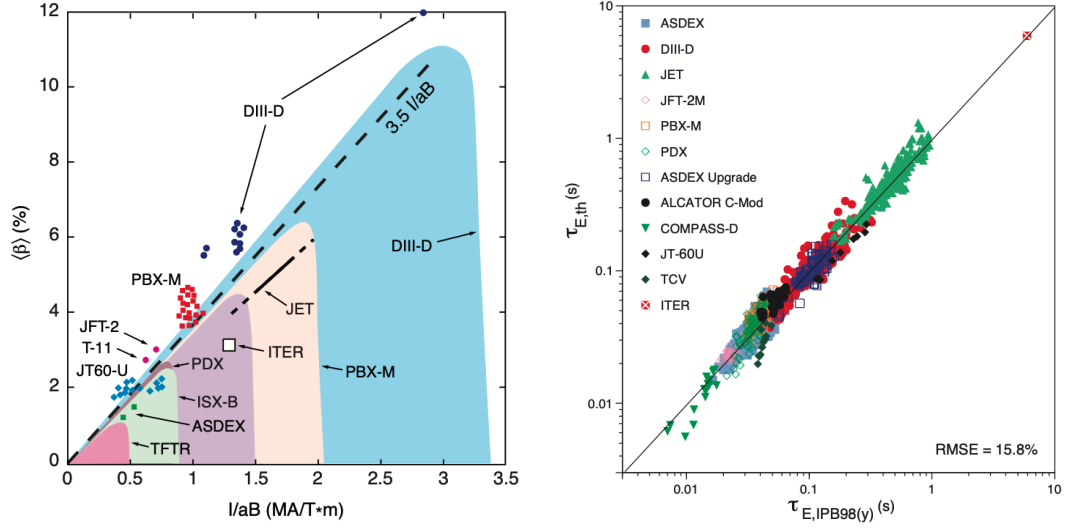
Figure 1.3: Left: The range of $\beta$ achieved in various tokamak experiments. Right: Thermal energy confinement in H-mode plasmas in various tokamak experiments versus the scaling law for ELMy data in the ITER H-mode database version DB3. *Source: [ITER Physics Expert Group on Disruptions, Plasma Control and MHD and ITER Physics Basis Editors 1999; ITER Physics Expert Group on Confinement and Transport and ITER Physics Expert Group on Confinement Modelling and Database and ITER Physics Basis Editors 1999].*

remains an important research topic today [Viezzer 2018; Harrer et al. 2022].

### 1.4.4 Mapping out operating points: scaling laws and operational limits

Combining progressing theoretical understanding with the data extracted from experiments conducted on dozens of machines, scaling laws were developed describing tokamak performance metrics, as well as active stability limits on operating points. Based on experimental and numerical studies of MHD limits, Troyon found a linear dependence between the maximum normalized pressure factor $\beta$ (ratio of thermal pressure to magnetic field pressure $2\mu_0\langle p\rangle/B_0^2$) and the plasma current $I_p$, which can be elegantly summarized as a limit on a normalized pressure factor $\beta_N$ (neglecting the effect of a conducting wall) [Troyon 1984]:

$$\beta_N = \frac{\beta[\%]}{I_p[\text{MA}]/(a[\text{m}]B[\text{T}])} < 3.4 \tag{1.2}$$

For the maximum plasma line-averaged density, a purely empirical scaling, proportional to the plasma current $I_p$, was proposed, by Greenwald [Greenwald et al. 1988]:

$$n_{el}[1 \times 10^{20}\,\text{m}^{-3}] < n_{Gw} = \frac{I_p[\text{MA}]}{\pi a^2[\text{m}^2]} \tag{1.3}$$

Recently, turbulent transport considerations led to the proposition of a first-principles density limit scaling law [Giacomin et al. 2022]. The strong dependence of the revised scaling law on heating power leads to a significantly more favorable predicted density for future fusion

reactors like ITER.

To project performance, confinement time scaling laws had been derived throughout the decades of tokamak research, e.g. the work of Goldston [Goldston 1984]. When the ITER physics basis was reviewed in 1999, the IPB98(y,2) scaling law was introduced, based on a subset of multi-machine databases [ITER Physics Expert Group on Confinement and Transport and ITER Physics Expert Group on Confinement Modelling and Database and ITER Physics Basis Editors 1999]:

$$\tau_{E,th}^{ELMy} = 0.0562 I_p^{0.93} B_0^{0.15} P_L^{-0.69} n_{el}^{0.41} M^{0.19} R_0^{1.97} \epsilon^{0.58} \kappa^{0.78} \tag{1.4}$$

with confinement time $\tau_{E,th}^{ELMy}$ [s], plasma current $I_p$ [MA], toroidal magnetic field $B_0$ (at major radius $R_0$) [T], loss power (corrected for charge exchange and orbit losses) $P_L$ [MW], line-averaged density $n_{el}$ in $10^{19} \text{m}^{-3}$, average isotope mass number in AMU, major radius $R_0$ [m], inverse aspect ratio $\epsilon$ and plasma elongation $\kappa$.

### 1.4.5 The beneficial role of shaping the plasma cross-section

The computational study of MHD stability provided a new avenue to enhance performance. It was found that MHD-quiescent operation could be maintained at higher pressure, by deforming the plasma cross-section, using the shaping capabilities of the poloidal field coils, deviating from the standard circular plasmas of the past decades. Current limits and beta limits could be increased by assuming a plasma with an elongated, triangular plasma shape, e.g. according to the numerical studies in [Troyon et al. 1988; Turnbull et al. 1988, 1989]. Furthermore, strongly shaped plasmas were a natural choice from the engineering point of view, as toroidal field coils with a D shape were found to improve the handling of the electromagnetic forces on the magnets, limiting the need for structural reinforcement [File et al. 1971]. JET adopted a D-shaped vacuum vessel design, contributing to its record-breaking performance achievements. Furthermore, the effect of elongation on turbulence, at the time completely unknown, would turn out to be beneficial [Moret et al. 1997]. In addition, the increased plasma current enabled by a larger volume, would enhance the confinement time. Note that both plasma current $I_p$ and elongation $\kappa$ have correspondingly a strong positive exponent in the IPB98(y,2) scaling law eq. (1.4). Non-linear gyrokinetic simulations confirm that turbulence can be reduced by elongating the plasma [Kinsey et al. 2007]. While the impact of triangularity on turbulence is more complex, it was found that for sufficiently shaped plasmas, a second stability region for the ballooning mode can be accessed, allowing for higher pedestal pressures. This remarkable phenomenon, where the ideal MHD instability is stabilized again when increasing the pressure gradient beyond the value where the mode became unstable, had been derived theoretically before [Mercier 1979; Lortz and Nuehrenberg 1978; Coppi et al. 1980]. It was experimentally observed that increased pedestal pressures could be achieved in a positive triangularity plasma [Neyatani and the JT-60 Team 1996; Saibene et al. 1999; Stober et al. 2000]. In 1992, the TCV tokamak was built in Lausanne, Switzerland, featuring a highly elongated vacuum vessel and 16 individually powered poloidal

field coils, allowing to thoroughly study the effect of plasma shaping on tokamak performance. Ultimately, this led to the discovery that H-mode-like confinement could be achieved in negative triangularity L-mode plasmas [Camenen et al. 2007; Marinoni et al. 2021], opening a promising pathway towards an alternative ELM-free reactor concept [Kikuchi et al. 2019].

### 1.4.6   Integrated science-engineering challenges towards fusion power

Throughout the 90s, record tokamak performance was achieved in JET [Gibson and JET Team 1998] and TFTR (Princeton) [Hawryluk and TFTR Team 1998]. Both tokamaks did a series of DT experiments in this period, hitting a historic milestone that required technological advancement, e.g. regarding remote handling of irradiated materials and making robust diagnostics withstanding 14.1 MeV-neutrons. Both tokamaks reached peak fusion powers above 10 MW, even though the fusion power gain $Q = P_{fus}/P_{aux}$ remained below unity (JET achieved $Q \sim 0.65$).

A meeting between US president Reagan and Soviet leader Gorbachev at the 1985 Geneva Summit led to the initiation of a global collaborative effort to build a grand fusion reactor, which would become known as ITER (Latin for *the way*), aiming to demonstrate the scientific and technological feasibility of fusion energy for peaceful purposes. An agreement was signed in Reykjavik in 1987 between the Soviet Union, the USA, the European Union and Japan, leading to a joint design effort (1992-2001). In 2005, a new ITER Implementing Agreement was signed with an extended number of partners: China, the European Union, India, Japan, Korea, Russia and the USA. The construction of the new reactor started in 2013 in Cadarache, France. ITER is designed to achieve a fusion power of $P_{fus} = 500$ MW and a fusion power gain $Q = 10$ [Shimada et al. 2007]. Achieving this goal would lead to a wealth of technical and scientific results on the operation of burning plasmas (dominantly self-heated) and test the required integrated technologies, materials and physics regimes, paving the way towards a fusion reactor. Outstanding challenges include tritium breeding and heat exhaust. Furthermore, the magnet coils of ITER will be superconducting (500 tonnes of $Nb_3Sn$ and 250 tonnes of NbTi), cooled to 4.2 K with a flow of supercritical helium. To avoid excessive tritium retention, a beryllium (or tungsten) first wall will be installed, with tungsten-armored divertor plates. Recently, JET repeated a series of DT discharges, after the vessel was refurbished to an ITER-like wall in 2010, successfully achieving sustained fusion power and validating the models used for scenario design [Kappatou et al. 2022], giving confidence that ITER will be able to achieve its aims.

After decades of conducting fundamental research and acquiring technical know-how in laboratories around the world, ITER will play a key role in assessing the technical feasibility of the tokamak as an energy source, paving the way for an electricity-producing DEMO reactor, for which various designs are being discussed, among which the European effort described in [Federici et al. 2018]. However, also alternative pathways, like stellarators [Warmer et al. 2016; Klinger et al. 2019; Alonso et al. 2022] and spherical tokamaks [Sykes et al. 2017; Wilson et al. 2020], are increasing their momentum as new prototypes are being built. A growing number of private companies aims to hasten the achievement of a fusion reactor, leveraging new

technologies. Commonwealth Fusion Systems (CFS), a MIT spin-off, is using high temperature superconductors to boost the magnetic field, aiming to achieve ITER-like performance in a much smaller device [Rodriguez-Fernandez et al. 2022a]. This goal should be reached in the SPARC tokamak, currently under construction in Devens, near Boston, USA.

Optimism should however be tempered considering the vast challenges that remain. The presence of 14.1 MeV neutrons, damaging and radioactively activating the reactor structure, will require fusion reactors to be large (high investment cost) and expensive to maintain (requiring remote handling). Furthermore, highly efficient tritium breeding has to be achieved to replenish the burnt fuel as well as the part of the inventory that is retented in the reactor's surfaces and sub-systems. Failure of tritium replenishment would imply a dependence of fusion reactors on expensive tritium produced by fission reactors. A significant fraction of the produced power needs to be recirculated to power auxiliary systems, both external to the reactor (liquid-helium refrigerators, tritium processing, water pumping, vacuum pumping ...) and internal to the reactor (auxiliary plasma heating, magnetic coils) [Kerekes et al. 2023]. Limiting the relative impact of this parasitic power drain tends to favour an increased total power, increasing the size of a fusion power plant. A commercially viable reactor will need to operate reliably and with very little unexpected outages: modeling and control solutions will need to achieve high performance to reduce the number of interruptions to the bare minimum and to achieve control of the highly non-linear, largely self-regulated plasma.

While any of these remaining challenges can easily discourage, let us not forget that our society is in dire need of vast reserves of clean energy. Throughout human history insurmountable setbacks have often been met with ingenious solutions that were previously unimagined. As we have seen in the previous paragraphs, the myriad of technologies and non-linear physics involved in designing and operating a tokamak sometimes gives rise to serendipitous discoveries that overturn the status quo. Perhaps, we can let ourselves be inspired by the words that President Kennedy spoke in 1962, when bolstering public support for the ambitious program to land a man on the Moon by the end of the decade: *"We choose to go to the Moon in this decade and do the other things, not because they are easy, but because they are hard; because that goal will serve to organize and measure the best of our energies and skills, because that challenge is one that we are willing to accept, one we are unwilling to postpone, and one we intend to win, and the others, too."*

## 1.5 Tokamak scenario development: from ramp-up to ramp-down

To achieve a viable tokamak reactor, operation close to stability limits will need to be achieved, pursuing stable, high-performance plasma regimes, maximizing core temperature and density while minimizing external heating and current drive requirements and avoiding disruptive limits. High reliability and minimum occurrence of disruption events[11] are key requirements to make a fusion plant commercially attractive and protect the integrity of its components.

---

[11]Disruption events refer to the sudden collapse of the plasma pressure and current, leading to the loss of the confined plasma, posing significant risks for the design and operation of reactor-grade tokamaks [Hender et al. 2007].

Figure 1.4: A schematic overview of the different discharge phases is presented: ramp-up, flat top and ramp-down. The different phases give rise to various control and scenario development challenges regarding control of bulk quantities, shape control, control of MHD activity, profile control and supervisory control. *Source: [Felici 2011].*

The burning plasma (dominated by self-heating) in a fusion reactor will be highly non-linear and largely self-organized. Reactor vessel surface area will be needed for tritium breeding, leaving limited space for real-time diagnostics. The complexity of scenario development and control is further increased if control over the plasma operating point to modulate the reactor electric power output is foreseen, which would enhance the commercial attractiveness of a fusion reactor [Nicholas et al. 2021]. The actuating power should be minimized to achieve an acceptable fusion power gain. In a burning plasma control will be a daunting challenge, requiring reduced models of the plasma dynamics for discharge preparation, state estimation in the presence of limited diagnostics and advanced real-time control.

### 1.5.1 Actuators, system dynamics and diagnostics

A *tokamak plasma scenario* can be described by a set of bulk quantities ($I_p$, $B_0$, $\beta$ ...) and a set of radially distributed quantities like temperatures, densities and the current density or safety factor profile.

From a control point of view, a useful abstraction is the definition of actuators, system dynamics and sensors. *Actuators* are the control knobs we have available to impact the behavior of the plasma, including:

- auxiliary heating and current drive (including, for EC heating and current drive, control over the deposition radius),

- fueling by means of gas puffing or pellet injection,

- impurity injection,

- plasma shaping and position by means of the poloidal field coils and

- the total plasma current imposed by means of the central solenoid (for scenarios with an inductive current fraction).

Time traces of these actuators can be programmed before the discharge (*feedforward control*), or adjusted during the discharge, based on real-time state estimation and control algorithms running on the plasma control system (*feedback control*). When running a tokamak discharge, various quantities are simultaneously controlled, as summarized in Figure 1.4:

- bulk quantities (like position[12] and plasma current) are routinely feedback controlled (including real-time algorithms to maintain some distance to disruptive limits: proximity control),

- plasma shape,

- the activity of MHD instabilities,

- radial profiles of temperature, density, current density (safety factor) and rotation.

Supervisory control orchestrates the allocation of the available actuators over the various control tasks at hand, deciding on prioritization based on a decision scheme.

The present work mainly treats radial profile control. For our purpose, we define the *plasma state* as the set of relevant radial profiles, i.e. any combination of $q(\rho)$, $T_{i,e}(\rho)$, $n_{i,e}(\rho)$, depending on the scenario objectives ($\rho$ is a generic flux surface label coordinate, normalized so that $\rho = 0$ corresponds to the magnetic axis and $\rho = 1$ corresponds to the LCFS).

The system dynamics of the radially distributed plasma state can be described with a coupled, non-linear, 1-dimensional set of partial differential equations (PDEs). Deriving reduced models of the system dynamics, like the RAPTOR code [Felici 2011; Felici et al. 2011, 2018], allow to rapidly evolve the time evolution of the plasma state, enabling a wealth of applications in the realm of control and optimization.

Measuring quantities within of a tokamak plasma is a challenging scientific endeavor. Extreme $\sim 10\,\mathrm{keV}$ temperatures and strict requirements on maintaining plasma purity often prohibit direct interaction of a measuring instrument with the plasma. Many non-intrusive techniques (e.g. injecting lasers and diagnostic neutral beams that do not perturb the plasma conditions), analysing emitted light from the plasma, have been developed to infer the radial distribution of temperature and density in the plasma (as well as other quantities). Combined with plasma profile system dynamics models, a (real-time) estimate of the plasma state can be obtained, e.g. by applying a Bayesian framework. Note that knowledge of the equilibrium geometry is crucial to allow mapping of spatially resolved measurements into 1-d profiles on a common grid. When post-processing the diagnostic signals acquired during the discharge, the variety of available measurements should be combined into a consensus state observation, including error bar propagation.

---

[12]Feedback control is necessary for vertical position control, to stabilize the vertical instability of elongated plasmas [Lazarus et al. 1990].
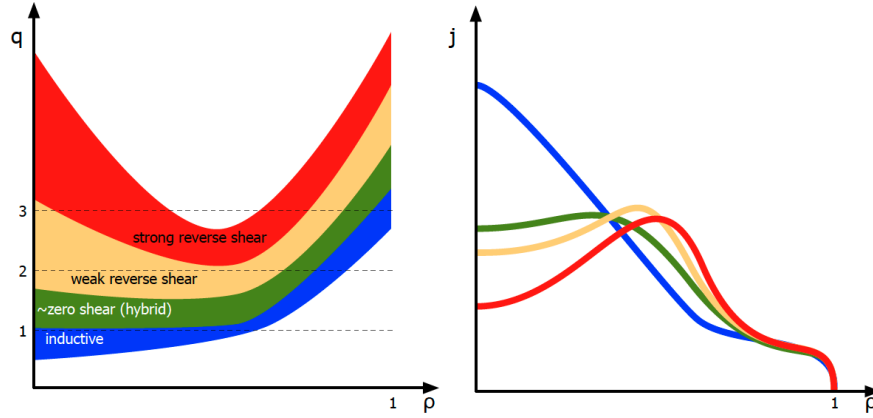
Figure 1.5: Illustration of the definition of various operating scenarios based on the radial distribution of plasma current and the resulting safety factor profile *q*. *Source: [Felici 2011], inspired by [Gormezano et al. 2007].*

### 1.5.2 Neoclassical tearing modes (NTM)

Finite resistivity allows for tearing modes at rational surfaces of the safety factor profile ($q = m/n$, with $m$ and $n$ respectively the poloidal and toroidal mode numbers), breaking and restructuring the magnetic field line geometry, leading to magnetic islands which locally increase outward transport, hence degrading the confinement. Typically, the perturbed bootstrap current fraction due to the pressure profile flattening can sustain the island. Due to the neoclassical nature of the underlying physics, these modes are called *neoclassical tearing modes* (NTMs). Driving localized ECCD can stabilize the NTM by overcoming the incurred bootstrap current deficit. However, the use of auxiliary actuators needs to be minimized to maintain a high fusion gain $Q$ in a fusion reactor [Sauter et al. 2010]. Above a $\beta$ threshold, which can be easily achieved in H-mode plasmas, NTMs are metastable [Sauter et al. 2002b], originating after the onset by a seeding mechanism.

Since the confinement time degradation (~ island width) is proportional to the radius of the resonant surface [Chang and Callen 1990], 2/1 NTMs at the $q = 2$ have a stronger impact compared to higher m/n modes closer to the center. Furthermore, the proximity of the $q = 2$ surface to the plasma edge increases the likelihood of mode locking and disruptions [Hender et al. 2007] (while peripheral ECCD is less efficient). Control and prevention of NTMs in a reactor-grade plasma is an important research topic. On TCV, prevention of NTMs is shown to require less power compared to stabilization [Kong et al. 2019a].

### 1.5.3 Tokamak plasma scenarios: inductive, advanced and hybrid

Different plasma scenarios can be distinguished based on the radial distribution of current during the stationary operating phase of the discharge, corresponding to different shapes of the safety factor profile $q$, as illustrated in Figure 1.5. The safety factor impacts both transport phenomena and the onset of MHD instabilities. Let us define the H factor $H_{98y,2}$, quantifying the plasma confinement enhancement with respect to the IPB98(y,2) scaling law eq. (1.4), i.e.

| Scenario | $I_p$ [MA] | $f_{ni} = \frac{I_{non-inductive}}{I_p}$ | $H_{98y,2}$ | $\ell_i$ | $\beta_N$ | burn duration [s] |
|---|---|---|---|---|---|---|
| Inductive | 15 | 0.15 | 1.0 | 0.8 | 1.8 | $\sim 400$ |
| Hybrid | $\sim 12$ | $\sim 0.50$ | $1-1.2$ | 0.9 | $2-2.5$ | $\geq 1000$ |
| Advanced | $\sim 9$ | 1.00 | $\geq 1.2$ | 0.6 | $\geq 2.6$ | 3000 |

Table 1.1: Operating points for ITER operating scenarios as projected in [Shimada et al. 2007].

$H_{98y,2} = \tau_E / \tau_{E,IPB98(y,2)}$. Some global values expected for ITER scenarios are given in Table 1.1, as reported in [Shimada et al. 2007].

### Inductive scenario

In an *inductive scenario* (with dominant inductively driven current), completed diffusion of the plasma current gives rise to a centrally peaked current density (self-similar to the shape of the conductivity $\sigma \sim T_e^{3/2}$), corresponding to a $q$ profile that increases monotonically from the magnetic axis to the plasma boundary. These conditions often lead to the formation of a $q = 1$ surface and the onset of sawtooth instabilities, caused by an internal kink mode and triggered when the magnetic shear $s$ ($s = (\rho/q)dq/d\rho$) at $q = 1$ exceeds a threshold value. Sawteeth result in a sudden reorganization of plasma profiles, flattening the core pressure profile. The inductive scenario aims to achieve maximized confinement by operating at large plasma current (consistent with scaling law eq. (1.4)). In ITER, a standard inductive H-mode scenario is foreseen to allow for the performance required to reach fusion gain $Q = 10$. The main drawback is that the large current leads to a quick consumption of the flux swing of the central solenoid, rendering this scenario incompatible with steady state operation.

### Advanced scenario

To pursue a steady state reactor, reducing thermal and mechanical fatigue due to cyclic operation, alternative scenarios have been developed, relying on large contributions to the plasma current from non-inductive mechanisms [Kikuchi 1990]. Generally, this is easier to achieve at reduced plasma current, which leads, a priori, to a reduced confinement time. Whilst operating at reduced density and collisionality facilitates efficient auxiliary current drive and large bootstrap fraction, impurity influx mitigation and divertor heat load abatement become more challenging [Bock et al. 2018]. An advanced scenario with fully detached divertor[13] has recently been achieved on DIII-D [Wang et al. 2021].

In an *advanced scenario*, strong off-axis auxiliary current drive, combined with the off-axis driven current by the bootstrap mechanism (including a contribution in the H-mode pedestal), causes the peak in the current density to shift away from the magnetic axis, giving rise to a non-monotonic $q$ profile, with $q > 1$ everywhere [Taylor et al. 1994]. Note that elevating the $q$ profile allows to boost the bootstrap fraction $j_{bs} \sim q\nabla p$. Depending on the deficit of current in the core, weak or strong negative magnetic shear $s$ can be achieved. Tokamaks with

---

[13]While under attached conditions high heat and particle fluxes at the divertor plates can lead to potential damage, detachment aims to dissipate the heat and momentum at a location upstream from the divertor plates.

strong current drive resources can reach full steady state operation [Sauter et al. 2001], with all current driven non-inductively.

A region of negative magnetic shear can stabilize micro-instabilities [Antonsen et al. 1996], leading to a local suppression of turbulent driven transport, much like the pedestal region of an H-mode plasma, and the formation of a so-called internal transport barrier or ITB (also plasma rotation has been reported as an important physics driver to the formation of ITBs [de Vries et al. 2009]). As such, the confinement loss incurred by reducing the plasma current can be compensated by achieving an H factor much larger than unity (e.g. $H_{98y,2} \sim 1.8$ with $\beta_N \sim 5$ for DIII-D [Ferron et al. 2015]). Note that the bootstrap current driven by the steepened pressure profile of the ITB reinforces the off-axis peak in the current density required to sustain its own existence.

Advanced scenarios rely on active control to tailor the $q$ profile. Furthermore, the broad current density profile and corresponding low internal inductance $\ell_i$ leads to a reduction of the ideal $\beta_N$ limit [Manickam et al. 1994]. The Troyon upper limit on the maximum $\beta_N$ introduced in eq. (1.2) does not account for the effect of current density tailoring. In practice, $\beta_{N,\,max}$ is dependent on the current distribution and can be increased by concentrating the current density in the center, $\beta_{N,\,max} = 4\ell_i$ [Strait 1994; Wesson 2004], leading to a reduced ideal limit for advanced scenarios. Inclusion of a conductive wall transforms the ideal external kink into a resistive wall mode (RWM), becoming unstable at low plasma toroidal rotation speeds, as projected for ITER, if $\beta_N$ exceeds the no-wall limit, requiring active RWM stabilization [Sabbagh et al. 2006].

**Hybrid scenario**

In the early 2000s, an intermediate scenario started to be developed on various tokamaks, aiming to find a *hybrid scenario*, providing a compromise between an inductive and an advanced scenario [Gruber et al. 1999; Luce et al. 2001]. Typically, a broad current density profile is achieved in the core, without a pronounced off-axis peak, which leads to a central region of low magnetic shear and high magnetic shear towards the edge.

While $H_{98y,2} = 1 - 1.5$ is commonly observed in the hybrid scenario operating space, the physics mechanisms for this improved confinement are still debated. Various references regarding the impact of $q$ profile shaping and electromagnetic turbulence stabilisation, enhanced by low magnetic shear and fast ions, are discussed in Section 4.2.

The broad current density profile required for $q \sim 1$ and $q > 1$, requires off-axis current drive. However, recent experiments [Petty et al. 2009] and 3D non-linear MHD simulations [Jardin et al. 2015; Krebs et al. 2017] have shown the existence of a dynamo effect mechanism, referred to as flux pumping (occurring when a threshold $\beta_N$ is exceeded), leading to a self-regulating redistribution of the current distribution that maintains the safety factor clamped close to unity, while avoiding sawteeth. Flux pumping could be highly attractive for a reactor: on-axis current drive (higher current drive efficiency) would be redistributed while the dynamo effect maintains $q \sim 1$ [Petty et al. 2015], requiring no active tailoring with auxiliary current drive resources. However, the possibility for extrapolation towards the ITER hybrid scenario should

be carefully examined.

The hybrid scenario is considered a promising candidate for DEMO reactor operation [Zohm et al. 2013].

**The role of NTMs in tokamak plasma scenarios**

The low $q_{edge}$ (hence $q = 2$ close to edge) and the presence of sawtooth triggers make the inductive scenario sensitive to NTM triggering, and prone to mode locking and consequent disruption of the plasma. In [Sauter et al. 2002c], the seed island size is reduced by applying a pacing strategy to reduce the sawtooth period, allowing to further increase $\beta_N$.

The absence of sawteeth-seeded NTMs in advanced and hybrid scenarios allows to operate at higher $\beta_N$. However, resistive $\beta$ limits (below the ideal limit $\beta_N = 4\ell_i$) to avoid the onset of NTMs (soft $\beta$ limit), are commonly observed [Sauter et al. 1997]. Lower-helicity NTMs can be avoided by raising $q_{min}$ above the required $m/n$ value. For hybrid scenarios, low shear in the core could lead to resistive infernal modes, providing a seed for NTMs [Brunetti et al. 2014]. Furthermore, when the classical tearing mode stability parameter $\Delta'$ is positive, a linearly unstable tearing mode starts growing, providing the seed for a so-called triggerless NTM [Reimerdes et al. 2002; Kong et al. 2019b, 2022]. An example are the 2/1 modes observed in the DIII-D ITER baseline scenario, for which the onset could be understood by studying the evolution of the $q$ profile [Turco et al. 2018].

### 1.5.4 Access and safe termination: ramp-up and ramp-down phases

To reach a stationary plasma state with the desired current density distribution, challenges are faced throughout all phases of the tokamak discharge. The various phases are defined based on the waveform of the plasma current (see Figure 1.4):

- Access to the stationary operating point requires optimization of the *ramp-up* phase, as well as the early *flat top* phase. The off-axis current peak of advanced scenarios can be created by *early heating* of the plasma [Soeldner and The JET Team 1997], slowing down the inward diffusion of inductive current by raising the plasma conductivity at an early stage. The resulting elevated $q$ profile can be sustained in the stationary phase if sufficient off-axis current drive sources are present.

  Alternatively, the formation of the reverse $q$ profile can be started by adding auxiliary heating and current drive only after the flat-top is reached [Goodman et al. 2005; Bock et al. 2018]. Controlled modification starting from a well-diagnosed plasma at the early flat top eases the reproducibility of the discharge, as the dynamics during the ramp-up phase are very sensitive to the exact timing of the heating, making scenario development cumbersome in the absence of predictive modeling and control techniques. However, the much slower current diffusion time scale of a reactor plasma is prohibitive for *late heating* scenarios, as the desired reactor operating point should be reached early during the flat top phase.

An alternative method that allows for earlier achievement of a stationary elevated $q$ profile is programming an overshoot in the plasma current waveform, as reported for JET in [Hobirk et al. 2012], and reproduced by automated optimization in RAPTOR in [Felici and Sauter 2012] and in TRANSP in [Wehner et al. 2017].

It is important to understand that the time history of the actuators during ramp-up will not only affect the time required to reach stationarity: due to the non-linearity of the underlying physics, the operating point that is eventually reached is dependent on the time history of the plasma state. In [Stober et al. 2007], different stationary states, featuring different current distributions, are obtained, by adjusting only the ramp-up scenario, while all control parameters during flat top are identical. As both time trajectories access different $q$ profiles during the ramp-up, differences in MHD activity, transport regime and H-mode pedestal are triggered, leading to a bifurcation in the time evolution.

- Safe termination of the discharge requires design and control of an optimal *ramp-down* scenario, presently often neglected. However, due to the large plasma current and stored energy of a reactor plasma, and the reduced thickness of a reactor first wall to enable tritium breeding, disruptions cannot be allowed during most of the plasma current ramp-down phase. Emergency shutdown, for example in case of loss of detached conditions in the divertor, requires fast ramp-down scenarios to avoid divertor damage [Siccinio et al. 2020].

  Vertical stability limits, radiative collapse and density limits constrain the ramp-down operating space, while field coil limits and physics time constants (current diffusion time, density and impurity confinement time) limit the maneuverability of the plasma state. Modeling and optimization techniques allow to find faster ramp down scenarios, while avoiding the violation of any of the limits mentioned before [Teplukhina et al. 2017]. Further disruption prevention can be achieved with real-time control algorithms, maintaining sound safety margins between plasma state and disruptive limits [Barr et al. 2021].

For both phases, the optimal control problem is inherently time dependent: the set of profiles must be steered through a stable envelope within the tokamak operating space, avoiding instabilities and technical constraints on actuators at all times. Adequate scenario development requires a combination of feedforward design of actuator time traces and feedback control to counteract model-reality mismatches in real-time. Today, scenario development oftentimes relies on trial-and-error optimization, based on the experience of the physics operator. In the following Section, and in the remainder of this thesis, we will review the potential of reduced models in guiding scenario optimization and control efforts, and its importance for safe and reliable operation of future reactors.

## 1.6 Profile control and fast tokamak modeling: state of the art

### 1.6.1 Towards fast tokamak plasma transport solvers

**Physical foundation**

The physical foundation for tokamak plasma modeling consists of the MHD force balance equilibrium and the diffusion equations for transport of poloidal magnetic flux, energy and particles (for ion species and electrons). As a consequence of ideal MHD, the plasma pressure is constant on flux surfaces. As other quantities of interest can be flux surface averaged, the diffusion equations are 1-dimensional.

The diffusion of poloidal magnetic flux, caused by finite plasma resistivity, is governed by a PDE originating from a projection of the flux surface averaged Ohm's law along the magnetic field lines. Including the equations for cross-field transport of particles and energy, dominated by turbulence driven by plasma micro-instabilities, a system of PDEs is obtained, which is highly non-linear due to mutual dependencies of quantities in these equations. The first tokamak transport simulations were pioneered in the late sixties in the Soviet Union [Kadomtsev and Pogutse 1963; Dnestrovski and Kostomarov 1969].

A hierarchy of tokamak plasma simulators with different levels of physics fidelity and different degree of integration is justified by the wide variety of applications.

**Integrated modeling**

Integrated plasma modeling refers to the consistent solution of plasma profiles within a framework integrating models for core transport, edge pedestal, MHD equilibrium and stability, heating and current drive (H/CD). These modeling tools can be used to estimate the performance of future devices like ITER or to examine capabilities of present-day devices to achieve stable, high-performance scenarios. As reviewed in [Poli 2018], the predictive capability of integrated tokamak simulations has significantly improved during the last decade. An integrated solution requires an efficient outer workflow orchestrating the different physics modules (suites of codes like e.g. JINTRAC [Romanelli et al. 2014], CRONOS [Artaud et al. 2018], OMFIT [Meneghini et al. 2015] and IMAS [Imbeaux et al. 2015]), while the individual models for evaluating physical quantities are guided by state-of-the-art findings in first-principles-based simulations. As a consequence, the most complete integrated plasma modeling workflows (making use of first-principles models without reduced model intermediary) are restricted to solving the steady state solution [Meneghini et al. 2016; Rodriguez-Fernandez et al. 2022b] or solving the dynamic state evolution during a limited timeframe [Citrin et al. 2017].

For ASDEX Upgrade, a simulator (integrated model based on engineering parameters, IMEP) has been developed that predicts transport from magnetic axis to separatrix, requiring only inputs for the magnetic field, the plasma current, the heating power, the fueling rate, the seeding rate, the plasma boundary and the effective charge as inputs [Luda et al. 2020]. Parallel ASTRA simulations are performed with different pedestal widths, each post-processed with

an MHD stability code to find the maximum stable pedestal pressure. The predicted stored energy is found to be more accurate with respect to measurements compared to the IPB98(y,2) scaling law [Luda et al. 2020, 2021]. Reformulating the applied pedestal transport condition into a dimensionless form, IMEP was recently validated for an extended set of C-Mod and JET (with ITER-like wall) discharges [Luda et al. 2023].

**Fast transport solvers**

Fast core transport solvers (originally developed for control-oriented applications, e.g. early work in [Witrant et al. 2007]) achieve real-time execution speeds for time evolution of the plasma profile dynamics, providing a valuable tool for automated discharge optimization, fast full-discharge simulation and model-based control.

The RAPTOR code, described in detail in Chapter 2, is a state-of-the-art lightweight transport solver. From its original conception, RAPTOR was envisioned both as an on-line, interpretative code [Felici et al. 2011] and a predictive simulator, which can be embedded in a non-linear optimization routine [Felici and Sauter 2012]. A distinctive feature of the RAPTOR code is the analytical evaluation of the Jacobian matrices used within the implicit time integration scheme. This allows for a numerically stable evolution of the ODEs, even for a large time step size (stiff and non-linear system of ODEs, obtained by finite element spatial discretization of the transport PDEs). Furthermore, knowledge of these Jacobian matrices allows evolving the plasma profiles sensitivity to a chosen set of parameters and constructing linearized models of the plasma profile dynamics along the nominal state evolution. These two capabilities are highly valuable for optimization and control applications.

Other fast simulators are being used for predictive scenario simulations. The METIS code [Artaud et al. 2018] applies a mixed 0D-1D approach, relying on confinement time scaling laws. For DIII-D, in particular for advanced scenario development, a model for poloidal flux and electron temperature diffusion, also based on scaling laws, is integrated in a trajectory optimization scheme [Barton et al. 2015]. Solvers directly evaluating the stationary plasma state include the PLASMOD code [Fable et al. 2018; Ellis et al. 2018], which solves self-consistently for the MHD equilibrium with a 3-moment solver and utilizes a simple gyro-bohm model to evaluate transport, and the GOTRESS code [Honda and Narita 2019], which solves solely for heat transport and features various turbulent transport models.

### 1.6.2   Fast turbulent transport models and robust coupling with transport solver

**Empirical models**

Quasi-linear gyrokinetic models allow for the evaluation of turbulent fluxes about six orders of magnitude faster than $\delta f$ local non-linear codes. For QuaLiKiz, a quasi-linear gyrokinetic transport model described in [Bourdelle et al. 2015; Citrin et al. 2017], evaluating 25 multi-scale transport fluxes along the radial profile requires ~10min on a single CPU (depending on the physics fidelity) [van de Plassche et al. 2020]. Due to the large number of transport code calls

required by an explicit PDE solver, the solution of the full-discharge time evolution can take several days. Applications for large-scale model validation, control and optimization benefit from a faster transport model evaluation.

Empirical diffusivity formulae extracting salient trends observed in scaling laws and experiments are readily available (e.g. Bohm-gyroBohm model [Erba et al. 1998]). Furthermore, diffusivities can be derived based on experimentally observed logarithmic profile gradients, which remain close to a critical gradient due to the stiff nature of turbulent transport [Sauter et al. 2014; Kim et al. 2016], both for L- and H-mode, allowing for efficient full-discharge simulations [Teplukhina et al. 2017].

**Neural network surrogate models**

The application of neural networks to the prediction of turbulent heat and particle fluxes in the core of a tokamak plasma allows for fast first-principle-based modeling of plasma profiles [Citrin et al. 2015; Meneghini et al. 2017], providing an avenue towards application in real-time tokamak plasma control and automated scenario optimization [Felici et al. 2018] (e.g. neural network evaluation ~10$\mu$s reported in [van de Plassche et al. 2020]). These neural networks are non-linear multivariate regressions of turbulent fluxes obtained with quasi-linear gyrokinetic transport codes. The major speed-up enabled by the quasi-linear assumption allows for the generation of the required large database of turbulent flux calculations. The RAPTOR code was recently coupled to QLKNN-hyper-10D [van de Plassche et al. 2020], henceforth abbreviated to QLKNN, a surrogate turbulent core transport model. The 10-dimensional neural network was trained on a database of $3 \times 10^8$ heat and particle flux calculations of QuaLiKiz. Since the database was populated by applying a hypercube-based approach, the training set covers a wide operating space, including ITER regimes. On present-day tokamaks, routine first-principle-based discharge modeling applying quasi-linear models like QuaLiKiz and TGLF is in good agreement with experimental data[14], hence giving confidence to use these models to predict and optimize ITER performance [Mantica et al. 2019]. The resulting neural network emulation successfully captures core transport features like the stiffness of the core plasma temperature profiles (the turbulent fluxes are highly sensitive to an increase in gradient once a critical gradient is exceeded).

When increasing the number of inputs to the neural network to enhance the physics fidelity, the number of calculations to populate the training database becomes computationally intractable, due to the so-called curse of dimensionality. Sampling the input space based on experimental data can overcome this problem, at the expense of limiting the general applicability of the surrogate model. A new QuaLiKiz neural network, QLKNN-jetexp-15D, successfully applied this approach, using JET data [Ho et al. 2021a].

---

[14]For QuaLiKiz simulations of temperature, density and toroidal rotation for JET hybrid and baseline scenario discharges, an agreement between experimental and simulated profiles in the range 5%-25% is reported in [Citrin et al. 2017].

**Coupling to transport solver**

Coupling a transport solver to a model featuring the stiff behaviour of plasma turbulence can compromise robust convergence. Various solver schemes have been proposed to enhance numerical stability. Both in [Park et al. 2017] and [Honda and Narita 2019], spatial gradients are considered separate variables in the non-linear set of equations, which are respectively solved by application of non-linear iterative schemes or global optimization algorithms. The finite difference scheme proposed in [Pereverzev and Corrigan 2008] introduces an artificial diffusivity (counteracted by a pinch term) to avoid numerical oscillations around the critical gradient in time-dependent simulations. The TGYRO solver presented in [Candy et al. 2009] features a Newton's method to find the logarithmic temperature gradients driving the amount of transport set by the heat sources, from which the temperature profiles are then inferred by integration. Note that the availability of a neural network surrogate transport model aids convergence, by providing a smooth regression and leveraging analytic Jacobians. The evaluation of the Jacobians in addition to the flux evaluations comes with an additional computational cost[15]. However, the analytical Jacobian information is extremely useful for control and optimization applications, avoiding the expensive Jacobian evaluation through finite differencing.

In [Rodriguez-Fernandez et al. 2022b], machine learning and optimization techniques have been leveraged to find a steady state solution for temperature and density, by constructing and continuously updating surrogate models for non-linear gyrokinetic transport fluxes within a gaussian process regression framework. Applying Bayesian optimization techniques, the number of high-fidelity simulations required to achieve a flux-matching solution is minimized. Both training of the surrogate model and the root-finding non-linear solver benefit from automatic differentiation, avoiding the need of finite difference Jacobian approximations, reducing the computational cost and preventing oscillatory behavior.

### 1.6.3 Optimization of tokamak discharges: from predict-first to real-time control

**Predict-first scenario development**

As fast modeling of tokamak discharges becomes more computationally tractable, routine inter-discharge simulations guiding development of scenarios becomes feasible. Full-discharge modeling prior to experiments is foreseen to become common practice on ITER [Humphreys et al. 2015].

Including relevant reduced physics models, fast tokamak simulators reach the physics fidelity required for predict-first simulations. On WEST, RAPTOR-QLKNN, complemented with an impurity radiation model, has been applied to find stable ramp-up strategies in the presence of Tungsten impurities [Maget et al. 2022]. In [Ostuni et al. 2022], integrated modeling, including

---

[15]In [van de Plassche et al. 2020], a JINTRAC-QLKNN run with predictor-corrector scheme and a maximum time step of $1 \times 10^{-3}$s was found to be only a factor two slower compared to a RAPTOR-QLKNN run with an implicit scheme and a time step of 0.1s, illustrating the expense of evaluating the neural network Jacobians (in addition to the need for additional transport model calls in the Newton solver of the implicit scheme).

RAPTOR-QLKNN, is applied to gain understanding in the chain of events leading to radiative collapse in WEST.

JINTRAC, coupled with the QLKNN-jetexp-15D surrogate model has been used to model the impact of impurities on the hollowing of the $T_e$ profile observed in the ohmic ramp-up phase of a JET D hybrid scenario discharge [Ho et al. 2021b].

**Flight simulators**

A flight simulator provides a tool for pre-discharge simulations, including the plasma control system itself and a reduced plasma model. The simulator requires identical inputs to the pulse schedule of the actual machine, and provides a holistic virtual model of the machine elements relevant to the plasma operation, e.g. the coils [Fable et al. 2022]. The outputs of the code are a set of time traces (e.g. plasma current, stored energy, density, plasma position and shape evolution) and the aim is to provide a first-order estimate whether control and physics aims and constraints are satisfied (e.g. simulating the effect of the expected plasma current density distribution on the required poloidal field coil currents [Fable et al. 2022]). At AUG, the Fenix flight simulator has been developed [Janky et al. 2021]. For ITER, controllers will be tested with increasingly complex simulators, before being commissioned for application on the tokamak [Ravensbergen et al. 2023].

**Automated non-linear optimization routines**

Fast full-discharge simulators can be embedded in automated optimization routines and play a valuable role in guiding the efforts of more extensive integrated modeling tools. Actuator trajectory optimization problems can include constraints on the plasma state to ensure operation within stability limits. This approach was applied for optimization of the ramp-up phase in [Felici and Sauter 2012], [van Dongen et al. 2014], [Wang et al. 2017] and [Wehner et al. 2019] and in [Teplukhina et al. 2017] for optimization of the ramp-down phase.

**Advanced model-based profile control**

Model-reality mismatches, arising from unmodeled disturbances and physical phenomena not captured by the model, inhibit pre-calculated optimal actuator trajectories from steering the plasma to the optimal state.

Iterative learning control (ILC) aims to improve feedforward actuator requests, based on the measured time-trace of the deviation with respect to the imposed reference in a previous discharge, using a time-varying linear model of the profile dynamics to optimize reference tracking for the next discharge. Application of ILC within the scope of tokamak plasma control is promising as (phases of) discharges are highly repetitive and some quantities are hard to measure in real-time (proposed for current density control in [Felici and Oomen 2015] and for density control in [Ravensbergen et al. 2017]).

An alternative approach to tackle model mismatches and disturbances is the development of feedback controllers. Linear model predictive control (MPC) is a promising feedback control method, using linear models for the plasma state response to actuator increments. Important is the distinction between models based on the underlying physics (like RAPTOR) and models acquired from system identification procedures (data-driven black-box approach like in [Moreau et al. 2013]), the latter being unfit for extrapolation to different tokamak operating points. These on-line running MPC algorithms require a real-time estimate of the plasma state, which can be obtained by combining the real-time available measurements in a model-based dynamic state observer as discussed in [Felici et al. 2014]. For TCV, RAPTOR was used as a real-time dynamic state observer, correcting the prediction with measurements, applying an extended Kalman filter (EKF) approach [Carpanese et al. 2020].

As presented in [Kim and Lister 2012], [Maljaars et al. 2015] and [Barton et al. 2015], the feedforward actuator signals can be updated on-line, by repeatedly solving actuator trajectory optimization problems during the discharge. Using linear models[16], on-line solution of the optimal control problem is tractable, producing the actuator trajectory adjustment aiding recovery of the optimal plasma state. Furthermore, an MPC controller can cope with varying actuator constraints (depending on real-time allocation of auxiliary resources by a supervisory controller, e.g. the integrated control architecture presented in [Pajares et al. 2019] or [Vu et al. 2019]) and provide early warnings for future transgressions of operational or physical limits. MPC based on linearized RAPTOR models has been tested in simulations [Maljaars et al. 2015] and successfully applied in profile control experiments on TCV [Maljaars et al. 2017]. Similar experiments on DIII-D realize improved $q$-profile tracking by combining feedforward optimization and on-line linear MPC [Barton et al. 2015; Wehner et al. 2017].

## 1.7 The ASDEX Upgrade Tokamak: machine and data analysis

The experimental results in this thesis are mainly obtained from ASDEX Upgrade (AUG). Table 1.2 compares size, operating parameters and heating power of AUG with the smaller TCV device located in Lausanne, and future reactors ITER and DEMO, for which modeling results will be discussed in this thesis.

ASDEX Upgrade (AUG) is a medium-sized tokamak with Tungsten first wall (see Figure 1.6) at the Max-Planck-Institut für Plasmaphysik in Garching near Munich, operational since 1991. Heating systems include 8 NBI sources (maximum 2.5 MW each), 8 gyrotrons for ECH providing up to $\sim$ 5 MW and 4 ICH antennas providing up to $\sim$ 4 MW. Differences in orientation of the NBI sources lead to different radial deposition profiles of heating and current drive in the plasma, more or less off-axis. The ECH deposition radius can be adjusted with tilting mirrors.

Among the most relevant diagnostics for this work we mention: a Thomson scattering system measuring electron temperature and density profiles; a laser interferometer measuring line-

---

[16]Note that the longer confinement and current diffusion time scales on large devices like ITER relax the computational demand on profile evolution optimizers running on the real-time control system, potentially enabling the on-line solution of non-linear optimization problems.

|                          | TCV  | AUG  | ITER    | DEMO  |
|--------------------------|------|------|---------|-------|
| Major radius $R_0$ [m]   | 0.88 | 1.65 | 6.2     | 9.0   |
| Minor radius $R_0$ [m]   | 0.25 | 0.5  | 2.0     | 2.9   |
| Plasma volume $V$ [m$^3$] | 2    | 12   | 840     | 2300  |
| Plasma current $I_p$ [MA] | 1    | 1.2  | 15      | 17.75 |
| Toroidal field $B_T$ [T] | 1.5  | 3.2  | 5.3     | 5.9   |
| Max NBI power [MW]       | 2.3  | 20   | 33      | 50    |
| Max ECH power [MW]       | 3.5  | 5    | 20 (40) | 50    |
| Max ICH power [MW]       | -    | 4    | 20      | -     |

Table 1.2: This table compares size, operating parameters and heating power of various tokamaks discussed in this thesis.



Figure 1.6: Inside the AUG vacuum vessel, note the tungsten tiles. *Source: www.ipp.mpg.de.*

integrated density along 5 lines of sight; a lithium beam diagnostic providing information on the electron density at the edge of the plasma; an electron cyclotron emission diagnostic measuring the electron temperature based on the photons emitted due to the electron gyro-motion, a charge exchange recombination spectroscopy system allowing to estimate ion temperature profiles, based on analysis of the light emitted from radiative decay of an impurity with an electron in the excited state, captured during a charge exchange process with a neutral atom.

To compare simulations with experiments, this thesis relies heavily on the **Integrated Data Analysis** (IDA) tool developed at IPP [Fischer et al. 2010, 2020], based on Bayesian probability theory, applying a maximum a posteriori technique (MAP). Combining information from Thomson scattering, the interferometer, the lithium beam and the ECE, radial profiles of $T_e$ and $n_e$ are inferred on a normalized poloidal flux coordinate $\rho_{pol}$ with a temporal resolution of 1ms. Mapping on the flux surfaces applies either the standard CLISTE equilibrium reconstruction [Schneider et al. 2000], or the IDE code, aiming to be more accurate by including kinetic profile constraints [Fischer et al. 2016]. Local error bars reflect at which radii data is available and whether inconsistencies arise between the data from different diagnostics[17].

The **Integrated Data Analysis Equilibrium** (IDE) is a post-discharge analysis tool developed at IPP [Fischer et al. 2016] that aims to produce improved equilibrium reconstructions and current profile estimates (equivalently: safety factor $q$ estimates). An inverse Grad-Shafranov equilibrium solver (minimizing a least-squares criterion comparing measured and modeled data) is coupled to a predictive current diffusion solver. Current density source profiles are evaluated with TORBEAM [Poli et al. 2001] for EC driven current and with RABBIT [Weiland et al. 2018] for NBI driven current. Measurements constraining the reconstructed state include: magnetic measurements (poloidal and radial field coils and flux loops) a pressure constraint from profile measurements and the fast ion contribution calculated by RABBIT [Weiland et al. 2018]; plus divertor tile currents, loop voltage and isoflux constraints. If available, the inner current density profile can be constrained by polarimetry (Faraday rotation), Motional Stark Effect (MSE) and Imaging MSE measurements. If available, IMSE data overrules current diffusion or polarimetry data due to a large weight[18].

---

[17]More information: https://www.aug.ipp.mpg.de/foswiki/bin/view/IDA/IDAElectronProfiles
[18]More information: https://www.aug.ipp.mpg.de/foswiki/bin/view/IDA/IDE_Equilibrium

## 1.8   Motivation of this thesis

The main research questions guiding this thesis can be formulated as follows:

1. Can RAPTOR, a fast transport solver with reduced physics models, be successfully validated and applied to optimize full-discharges on present tokamaks, from ramp-up to ramp-down?

2. Can these fast optimizations be leveraged to identify operational constraints on future tokamaks like ITER and DEMO, designing optimal trajectories to be verified in higher fidelity simulators?

While RAPTOR is a fast transport solver, the variety of implemented modules allows for different degrees of physics fidelity. An important aspect of this thesis work is selecting the adequate models for a given application.

We will show how RAPTOR modeling and optimization can benefit all phases of tokamak operation, from ramp-up (Chapter 3), to the flat-top stationary state (Chapter 4) and ramp-down (Chapter 5 and Chapter 6).

This thesis focuses on off-line simulations. These simulations are applied both for present-day machines, for scenario development on ASDEX Upgrade, and for future reactors, to optimize scenarios for ITER and DEMO. We will argue that inter-discharge simulations (*pre- and post-shot*), enhance the physics interpretability of past discharges, improving understanding of the underlying, non-linear dynamics, while allowing optimization of the next discharge. Simulating and optimizing the discharge before execution enhances reproducibility and reduces the required number of shots to design a scenario.

Routine simulation of discharges allows for a continuous cross-fertilization between experiment and modeling: whilst scenario design is accelerated under guidance of modeling and optimization, (reduced) physics models are improved and validated based on the observed dynamics.

Furthermore, routine shot-to-shot optimization and model validation can be considered a stepping stone towards model-based real-time control, running online modeling and optimization algorithms. Making the necessary adjustments in real-time, based on the underlying (linearized) dynamics, could eventually allow to reach the reliable operation required for a fusion reactor.

## 1.9   Outline of this thesis

- **Chapter 2** presents an overview of the RAPTOR code, a lightweight 1-dimensional transport solver, allowing to solve for the time evolution of poloidal flux $\psi$, electron and/or ion temperature $T_{e,i}$ and density $n_{e,i}$ [Felici et al. 2011, 2018]. Applications in real-time control and scenario modeling and optimization over the last decade are briefly reviewed. RAPTOR owes its fast computational speed to the reduced physics models

and an efficient numerical implementation, reviewed in this chapter. The coupling to an impurity radiation model, introduced in [Maget et al. 2022], is discussed. We present the implementation of a new stationary state solver and illustrate its application and performance with some simple examples. Non-linear optimization schemes in RAPTOR benefit from the availability of analytical gradient information. The application to scenario optimization, for both dynamic and stationary optimal control problems, is introduced in Section 2.5.

*The stationary state solver and its application to find optimum stationary working points, has been reported in [Van Mulders et al. 2021b].*

- In **Chapter 3**, we report on the application of inter-discharge RAPTOR simulation and optimization to develop a reliable and reproducible early heating strategy for an elevated safety factor $q$ profile scenario on ASDEX Upgrade (AUG). A framework to perform routine, post-discharge simulations is introduced and benchmarked against experimental reconstructions of the time evolution of $T_e$ and $q$. RAPTOR simulations are applied to understand the onset of 3/2 tearing modes. Delaying the heating, by an optimized time step found in simulations, has been successful in avoiding these modes. Furthermore, we apply a non-linear optimization scheme to assess how ECCD deposition can be optimized to maintain an early, elevated $q_{min}$ stationary, both for $q_{min} < 1.5$ and $q_{min} > 1.5$. We present how this model-based scenario design process has helped to ensure more robust access to advanced scenarios on AUG.

- **Chapter 4** applies the new stationary state optimizing scheme introduced in Chapter 2, coupled to the neural network surrogate model QLKNN-hyper-10D [van de Plassche et al. 2020], to optimize the performance of the ITER hybrid scenario. The scenario performance is explored at different values of total plasma current, plasma density and pedestal pressure and for different power contributions in a heating mix consisting of electron cyclotron and neutral beam heating. We show that by optimizing the radial distribution of electron cyclotron current drive deposition, the $q$ profile can be tailored, maximizing the fusion gain $Q$, while satisfying $q > 1$, avoiding sawtooth oscillations.
*The results in this chapter have been reported in [Van Mulders et al. 2021b].*

- In **Chapter 5**, we discuss the challenge of finding a safe ramp-down scenario for a DEMO reactor and how automated optimization in RAPTOR can help to find optimum actuator strategies. Various plasma current ramp-down rates are compared. We evaluate the margin towards an upper limit on the internal conductance from vertical control calculations and estimate the amounts of auxiliary heating required to avoid a radiative collapse in the presence of tungsten and seeded xenon. Furthermore, we optimize the time traces of plasma current and elongation to limit the increase of the internal inductance below the upper limit imposed to ensure vertical stability.

- **Chapter 6** benefits from the framework for post-discharge AUG simulations introduced in Chapter 3, to simulate the ramp-down phase for a set of discharges operating at dimensionless parameters close to the ITER baseline regime. Varying the time evolution

|  | **Chapter 3** | **Chapter 4** | **Chapter 5 & 6** |
|---|---|---|---|
| **Phase** | ramp-up + early flat-top | stationary flat-top | ramp-down |
| **Tokamak** | AUG | ITER | AUG, DEMO |
| **Scenario** | advanced, elevated q | hybrid | baseline inductive |
| **Transport** | simple formula with empirical tuning | QuaLiKiz neural net surrogate | gradient driven + scaling law |
| **Aim** | fast and reproducible access to stationary elevated q | maximize fusion gain | fast termination |
| **Limits** | [N]TM | sawteeth, LH threshold power | vertical stability, radiative collapse |

Table 1.3: Overview table highlighting distinct characteristics for the simulation and optimization results presented in the Chapters 3 to 6.

of plasma shaping, plasma current and auxiliary heating during the ramp-down, a better understanding is gained in the essential ingredients for a safe termination scenario. Various salient features observed in experiment are successfully modeled in RAPTOR.

- Overall conclusions are formulated in **Chapter 7**, as well as an outlook for further work.

The simulation and optimization results presented in the Chapters 3 to 6, differ from each other in various aspects: several tokamaks are modeled during different discharge phases, characterized by different aims and limits. Various transport models are used depending on the availability of experimental data or the need for a predictive transport estimate. To help the reader navigate through these chapters, some of these differences are highlighted in Table 1.3.

# 2 The RAPTOR modeling and optimization suite: overview and development

In this chapter we present the status of the RAPTOR code (**R**apid **P**lasma **T**ransport simulat**OR**), a lightweight transport code that solves for the time evolution of current diffusion and a set of kinetic profiles (temperature $T_{e,i}$, density $n_{e,i}$), for a selected number of transport channels. RAPTOR has applications in real-time control [Felici et al. 2011] and predictive discharge simulation and optimization [Felici and Sauter 2012]. Recent updates have been presented in [Felici et al. 2018]. We present in more details the extensions developed during the course of this thesis, which have been partly reported in [Van Mulders et al. 2021b]. An overview of capabilities and applications of RAPTOR are given in Section 2.1. The relation with the underlying MHD equilibrium geometry is discussed in Section 2.2. The transport diffusion equations solved by RAPTOR and the available reduced physics modules are introduced in Section 2.3, while the numerical implementation is presented in Section 2.4. Finally, the optimization routines available in RAPTOR are discussed in Section 2.5.

## 2.1 Evolution of the RAPTOR code: capabilities and applications

### 2.1.1 Real-time control

The fast computation time of RAPTOR allows it to run in real-time on the plasma control system (PCS). The software architecture of a generic PCS is presented in 2.1, as reported in [Vu et al. 2021].
Both on TCV and ASDEX Upgrade (AUG), a model-based plasma state reconstruction algorithm (Extended Kalman Filter) has been implemented to combine real-time measurements and RAPTOR modeling into an on-line state estimate of the radial profiles [Felici et al. 2016]. On TCV, the output of this dynamic observer has been coupled [Carpanese et al. 2020] to the real-time equilibrium reconstruction code LIUQE [Moret et al. 2015]. On AUG, coupling of RAPTOR to the real-time equilibrium reconstruction code JANET++ [Giannone et al. 2013], is planned in the near future, aiming for improved $q$ profile control within the advanced scenario program [Kudlacek et al. 2021a], relying on heating and current density deposition profiles from the on-line implementation of TORBEAM (EC) and RABBIT (NBI) [Weiland et al. 2023].
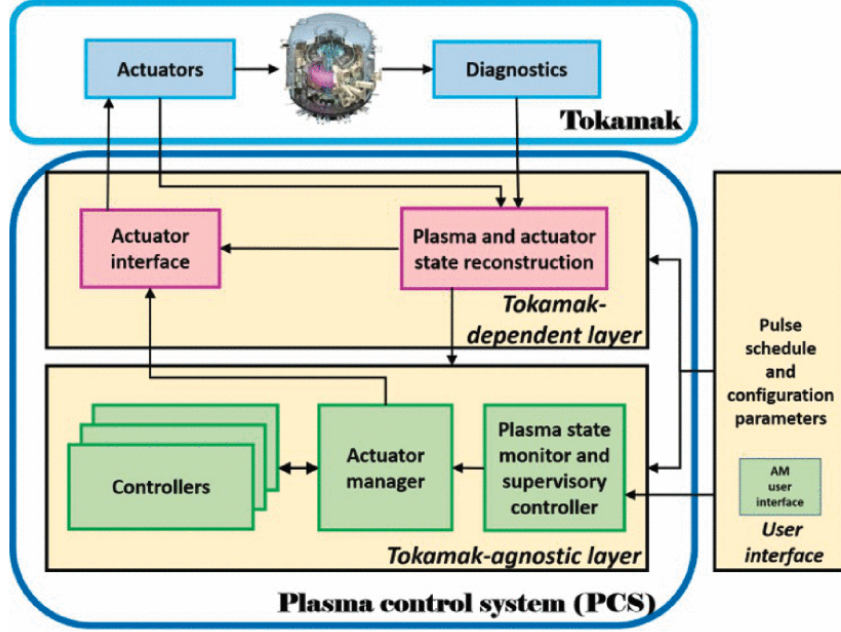
Figure 2.1: Schematic overview of a generic plasma control system. *Source: [Vu et al. 2021].*

A RAPTOR based model predictive controller (MPC) was developed in [Maljaars et al. 2015], calculating actuator adjustments based on solution of a quadratic optimization problem, applying linearized profile dynamics. On TCV, this MPC algorithms has been applied for $q$ profile and plasma $\beta$ control in [Maljaars et al. 2017].

### 2.1.2 Off-line modeling and optimization

**Iterative learning control**

In the absence of real-time measurements, iterative learning control (ILC), a feedforward control technique, provides a promising alternative. As some phases of discharges are highly repetitive, a linearized model along a nominal trajectory can guide shot-to-shot updates to the actuator traces, to bring the plasma state evolution closer to the desired trajectory. To achieve this, a quadratic optimization problem is solved for (much like MPC, but off-line instead of on-line), finding the required actuator adjustments based on the offset between the controlled variable measured signals and the reference.

In [Felici and Oomen 2015], simulations of ILC control for the ITER $q$ profile at the end of ramp-up have been proposed, as well as experimental results on ILC internal inductance control on TCV. On ASDEX Upgrade, ILC has been applied for ion temperature control: adjusting NBI and EC heating traces, the combined time evolution of $T_{e0}$ and $T_{i0}$, as well as $T_{e0}/T_{i0}$ and $W_{mhd}$ have been controlled to a predefined waveform [Felici et al. 2021; Kudlacek et al. 2021b].

**Non-linear optimization**

RAPTOR has been applied extensively for non-linear scenario optimization, benefiting from the cheap evaluation of analytic cost and constraint function gradients, as initially promoted in [Felici and Sauter 2012]. In [van Dongen et al. 2014], ramp-up optimization of the ITER hybrid scenario has been performed. More recently, [Mitchell et al. 2022] has reported on the application of RAPTOR to find a non-inductive ramp-up strategy for the British spherical reactor design STEP. An optimization scheme for the ramp-down phase of tokamak discharges, applied to TCV, AUG and JET has been introduced in [Teplukhina et al. 2017]. Direct optimization of the stationary plasma state, applied to the ITER hybrid scenario, has been reported in [Van Mulders et al. 2021b], as explained in detail in Chapter 4 of this thesis.

**Towards integrated modeling**

The inclusion of new physics modules continuously improve the physics fidelity of RAPTOR simulations. The coupling of RAPTOR to a proof-of-principle neural network surrogate of the QuaLiKiz turbulent transport code [Citrin et al. 2015], allows for real-time-capable, predictive JET simulations of the time evolution of $T_e$, $T_i$, $n_e$ and $q$ [Felici et al. 2018]. A more recent generation of the QuaLiKiz neural networks, known as QLKNN-hyper-10D, is currently available in RAPTOR [van de Plassche et al. 2020], as applied in [Van Mulders et al. 2021b]. Furthermore, a new stationary state solver has been developed in [Van Mulders et al. 2021b], allowing to solve directly for the stationary set of plasma profiles.
With the inclusion of an impurity radiation model, RAPTOR-QLKNN-hyper-10D has been applied recently to study the phenomenology of radiative collapse on WEST [Ostuni et al. 2022], and has been applied to find a stable ramp-up strategy [Maget et al. 2022].
Regarding MHD instabilities, RAPTOR has been upgraded with a Porcelli sawtooth model [Piron et al. 2015] and an equation for the island width evolution of NTMs [Maljaars et al. 2015].

## 2.2   MHD equilibrium

### 2.2.1   Grad-Shafranov equilibrium: equation and solvers

In a tokamak plasma, the outward kinetic force, due to pressure gradient, is compensated by the Lorentz force arising from the interaction between currents and magnetic field: $\mathbf{j} \times \mathbf{B} = \nabla p$. Under the assumption of axisymmetry, the Grad-Shafranov equation [Shafranov 1957; Grad and Rubin 1958] can be derived from the ideal MHD equations, describing the loci of constant magnetic flux in the poloidal plane. The derivation of this equation is briefly summarized below.
Let us introduce a right-handed $(R, \phi, Z)$ cylindrical coordinate system with COCOS=11 ($\sigma_{B_p} = +1$) and with $\sigma_{I_p} = \sigma_{B_0} = +1$ ($B_p$, $I_p$ and $B_0$ are always assumed positive) [Sauter and Medvedev 2013], where $R$ is the distance to the vertical axis of the device, $\phi$ is the angle along the direction
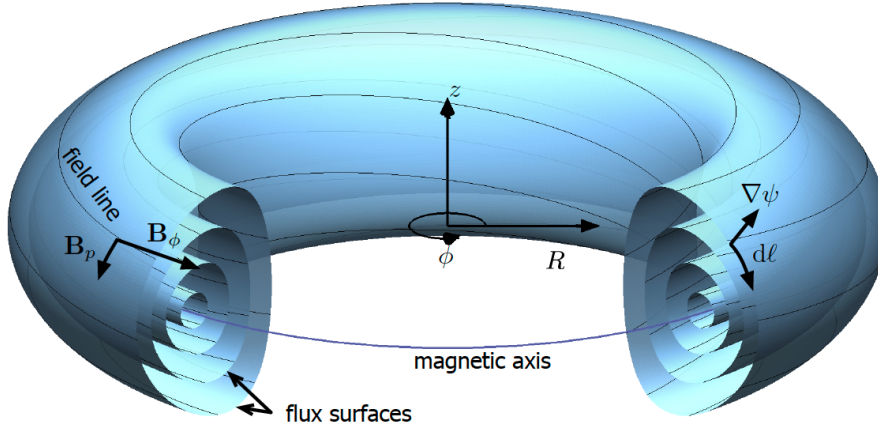
Figure 2.2: Schematic overview of nested magnetic flux surfaces, with right-handed $(R, \phi, Z)$ coordinate system, with various definitions of magnetic field quantities. *Source: [Felici 2011].*

of the toroidal field lines and $z$ is the vertical axis.

As the magnetic field is divergence free ($\nabla \cdot \mathbf{B} = 0$), we can write:

$$\frac{1}{R}\frac{\partial}{\partial R}(RB_R) + \frac{\partial B_Z}{\partial Z} + \frac{1}{R}\frac{\partial B_\phi}{\partial \phi} = 0. \tag{2.1}$$

Under axisymmetry, we can define a function $\psi$, such that:

$$RB_R = \frac{1}{2\pi}\frac{\partial \psi}{\partial Z} \text{ and } RB_Z = \frac{-1}{2\pi}\frac{\partial \psi}{\partial R} \tag{2.2}$$

Defining $F = RB_\phi$, and with the unit vector relations $\nabla\phi = \frac{1}{R}\mathbf{e}_\phi$, $\nabla R = \mathbf{e}_R$ and $\nabla Z = \mathbf{e}_Z$, we can write the magnetic field as:

$$\mathbf{B} = F\nabla\phi + \frac{1}{2\pi}\nabla\phi \times \nabla\psi \tag{2.3}$$

Developing the curl operator within Ampère's law ($\mu_0\mathbf{j} = \nabla \times \mathbf{B}$), invoking axisymmetry and applying the definition of $\psi$ in eq. (2.2), one can derive:

$$\mu_0 j_R = -\frac{\partial B_\phi}{\partial Z}, \mu_0 j_Z = \frac{1}{R}\frac{\partial(RB_\phi)}{\partial R} \text{ and } \mu_0 j_\phi = \frac{1}{2\pi}\left[\frac{\partial}{\partial R}\left(\frac{1}{R}\frac{\partial\psi}{\partial R}\right) + \frac{1}{R}\frac{\partial^2\psi}{\partial Z^2}\right] \tag{2.4}$$

Now, we can apply $\mathbf{j} \times \mathbf{B} = \nabla p$ to show:

$$0 = \mathbf{B}\cdot\nabla p = \frac{1}{2\pi}(\nabla\phi \times \nabla\psi)\cdot\nabla p = \frac{1}{2\pi R}\left(\underbrace{\frac{\partial\psi}{\partial Z}\frac{\partial p}{\partial R} - \frac{\partial\psi}{\partial R}\frac{\partial p}{\partial Z}}_{\text{Jacobian of } \psi \text{ and } p \text{ is null}}\right) \tag{2.5}$$

Projecting the force balance equation in the toroidal direction:

$$0 = (\mathbf{j} \times \mathbf{B})\cdot\mathbf{e}_\phi = \frac{1}{2\pi R^2}\left(\underbrace{\frac{\partial\psi}{\partial R}\frac{\partial F}{\partial Z} - \frac{\partial\psi}{\partial Z}\frac{\partial F}{\partial R}}_{\text{Jacobian of } \psi \text{ and } F \text{ is null}}\right) \tag{2.6}$$

The Jacobian relations in 2.5 and 2.6 imply that both $p$ and $F$ are functions of $\psi$ only. From eq. (2.4) and $F(\psi)$, we can obtain:

$$\mu_0 \mathbf{j} = -\frac{dF}{d\psi}\nabla\phi \times \nabla\psi + \frac{1}{2\pi}(\Delta^*\psi)\nabla\phi \text{ with } \Delta^*\psi = R\frac{\partial}{\partial R}\left(\frac{1}{R}\frac{\partial\psi}{\partial R}\right) + \frac{\partial^2\psi}{\partial Z^2} \tag{2.7}$$

Forming the cross product $\mathbf{j} \times \mathbf{B}$ with eq. (2.7) and eq. (2.3) (with $F = F(\psi)$), applying standard vector identities, one arrives at:

$$\mathbf{j} \times \mathbf{B} = -\frac{1}{\mu_0 R^2}\left(F\frac{dF}{d\psi} + \frac{1}{(2\pi)^2}\Delta^*\psi\right)\nabla\psi \tag{2.8}$$

Substituting eq. (2.8) into the force balance equation $\mathbf{j} \times \mathbf{B} = \nabla p$, while rewriting $\nabla p = \frac{dP}{d\psi}\nabla\psi$ (since $p(\psi)$), the Grad-Shafranov equation is obtained:

$$\Delta^*\psi = -4\pi^2\left(\mu_0 R^2\frac{dp(\psi)}{d\psi} + F(\psi)\frac{dF(\psi)}{d\psi}\right) \tag{2.9}$$

When defining $\psi$ in eq. (2.2), an arbitrary factor can be multiplied. Within the literature, different $\psi$ have been introduced, differing from each other by a factor $2\pi$ and a sign difference. In RAPTOR, the convention of [Pereverzev and Yushmanov 2002] is followed (note that this choice is contained in the COCOS value), resulting in a minimum of $\psi$ on the magnetic axis. Under this convention, $\psi$, henceforth referred to as the poloidal flux $\psi$, can be written as the negative of the surface integral of the magnetic field through a disk perpendicular to $\mathbf{e}_Z$ with radius R:

$$\psi(R,Z) = -\int_0^R \mathbf{B}\cdot\mathbf{e}_Z dS \tag{2.10}$$

Solving the elliptic non-linear PDE eq. (2.9), the geometry of a set of nested magnetic flux surfaces $\psi_i = \psi(R,Z)$ can be calculated. Depending on the known and unknown quantities, different kinds of mathematical problems can be formulated based on the Grad-Shafranov equation, for which a variety of numeric codes are available within the fusion community. We list a short overview and specify the codes from which equilibrium data is extracted for results in this thesis:

- *Fixed boundary equilibrium solver:* Fixing the outer shape of the plasma (defining the last closed flux surface), the equilibrium is uniquely defined by the internal $p(\psi)$ and $F(\psi)$ profiles. The fixed boundary equilibrium code applied in this work is CHEASE [Lütjens et al. 1996], which can also take pressure, current density or $q$ profiles as input function.

- *Free boundary equilibrium solver:* In Chapter 5, equilibria of the CREATE-NL code are used. CREATE-NL is a free boundary equilibrium solver, where also the outer plasma shape is evolved, self-consistently with the currents applied in central and poloidal field coils (set by feedback control laws for current, position and shape control) and the eddy currents in passive structures [Albanese et al. 2015]. Other examples of free boundary

equilibrium solvers are FEEQS [Heumann et al. 2015; Blum et al. 2019], NICE [Faugeras 2020] and FGE [Carpanese 2021].

- *Equilibrium reconstruction code:* The aim of equilibrium reconstruction is to find the set of solutions of $\psi(R,Z)$, $p(\psi)$ and $F(\psi)$ (including outer plasma shape) that optimally reproduces the (magnetic) measurements, while satisfying the Grad-Shafranov equation. Often the problem is ill-defined near the magnetic axis as magnetic measurements provide only information about fields outside the plasma and internal measurements of the current distribution are scarce. This problem can be partly overcome by adding constraints on the internal current density distribution by evolving a current diffusion equation, in an approach called *kinetic equilibrium reconstruction*. The equilibria used in Chapter 3 and 6 originate from the IDE code [Fischer et al. 2020], a kinetic equilibrium reconstruction code used at ASDEX Upgrade.

### 2.2.2 Processing of equilibrium data in RAPTOR

RAPTOR is not equipped with a Grad-Shafranov solver. However, as we will see in the next section, the geometry of the flux surfaces is required as an input to RAPTOR, since geometric terms appear in the radial diffusion equations.

An extension developed in [Teplukhina et al. 2017] allows to provide different plasma geometries at an arbitrary number of time points during the simulation. For intermediate time points, the geometric terms are linearly interpolated. A more dense equilibrium time grid can be applied during ramp-up and ramp-down, when rapid changes in plasma shape and/or plasma profiles occur.

For off-line simulations, the equilibrium geometry information (originating from CHEASE, CREATE-NL, IDE ...) is interfaced to the RAPTOR code through a CHEASE simulation [Lütjens et al. 1996]. Based on the CHEASE output files (e.g. an eqdsk file), the geometric data required for RAPTOR is extracted (according to the definitions used in RAPTOR).

For TCV, the geometry data from real-time LIUQE equilibrium reconstruction [Moret et al. 2015] has been interfaced directly to RAPTOR [Carpanese et al. 2020]. On AUG, real-time coupling to JANET++ [Giannone et al. 2013] has been foreseen, to enable real-time current density control [Kudlacek et al. 2021a].

## 2.3 Diffusion equations in RAPTOR

Ideal MHD applied in an axisymmetric tokamak geometry gives rise to a set of nested magnetic flux surfaces $\psi(R,Z)$. The radial profiles of $p$ and $F$ are governed by the outward diffusion of current, particles and energy. Since these diffusion processes are orders of magnitude slower compared to the Alfvén time $\tau_A = a\sqrt{\mu_0 \rho_m}/B_0 \sim 1 \times 10^{-6}$ s (tokamak size $a$ and mass density $\rho_m$), the diffusion equations can assume a static MHD equilibrium at each time instant. We will review the set of radial diffusion equations implemented in the RAPTOR code.

As we derived in the previous section, under the approximation of ideal MHD, constant values

of $p$ and $F = RB_\psi$ on each flux surface result. Furthermore, one can easily understand that quantities like temperature and density tend to equilibrate on a magnetic flux surface as transport of charged particles along magnetic field lines are unconstrained by the Larmor motion. However, in the presence of toroidal rotation, particles will tend to accumulate on the outboard side, leading to a non-uniform distribution of density and temperature over a given flux surface [Wesson 2004]. Other quantities, like toroidal current density, are inherently non-uniform over flux surfaces. To obtain a set of 1-dimensional diffusion equations, a flux-surface-averaging operation is performed, as indicated with the operator $\langle \cdot \rangle$ and explained in [Felici 2011].

As the radial coordinate, any flux-surface label could be chosen. In RAPTOR, the normalized square root of the enclosed toroidal magnetic flux is used as the independent coordinate, $\rho = \sqrt{\Phi/\Phi_b}$, where $\Phi_b$ is the toroidal flux at the plasma boundary.

We will now review the diffusion equations implemented in RAPTOR. Let us start by defining $V(\psi)$, the enclosed volume within a flux surface, its derivative $V'_\rho = \frac{\partial V}{\partial \rho}$ and $F = RB_\phi$, as well as the geometric terms:

$$g_0 = \langle \nabla V \rangle, g_1 = \left\langle (\nabla V)^2 \right\rangle, g_2 = \left\langle \frac{(\nabla V)^2}{R^2} \right\rangle, g_3 = \left\langle \frac{1}{R^2} \right\rangle. \tag{2.11}$$

These geometric terms reflect the MHD equilibrium and should be extracted from an equilibrium solver, as explained in the previous Section.

Once RAPTOR has calculated a time evolution for the plasma profiles, the equilibrium solution can be updated, rerunning with the consistent set of profiles (after about three iterations, consistent transport and equilibrium solutions are obtained [Van Mulders et al. 2021a]). While $p'$ and $FF'$ are clearly the most natural profile inputs to an equilibrium code, other options are usually implemented to replace $FF'$ by the flux-surface-averaged toroidal or parallel current density, or the safety factor profile $q$.

$$j_\phi = \frac{\langle \mathbf{j} \cdot \nabla \phi \rangle}{\langle |\nabla \phi| \rangle} = \frac{1}{2\pi} \frac{1}{\mu_0 \langle |\nabla \phi| \rangle} (V'_\rho)^{-1} \frac{\partial}{\partial \rho} \left( V'_\rho \frac{1}{F} \left\langle \frac{(\nabla \rho)^2}{R^2} \right\rangle \frac{d\psi}{d\rho} \right), \tag{2.12}$$

$$j_{par} = \frac{\langle \mathbf{j} \cdot \mathbf{B} \rangle}{B_0} = \frac{1}{2\pi} \frac{1}{\mu_0 B_0} (V'_\rho)^{-1} F^2 \frac{\partial}{\partial \rho} \left( V'_\rho \frac{1}{F} \left\langle \frac{(\nabla \rho)^2}{R^2} \right\rangle \frac{d\psi}{d\rho} \right), \tag{2.13}$$

$$j_\phi = -\frac{2\pi}{\mu_0 \langle |\nabla \phi| \rangle} \left[ \mu_0 p' + FF' \left\langle \frac{1}{R^2} \right\rangle \right], \tag{2.14}$$

$$q = \frac{1}{2\pi} \left\langle \frac{1}{R^2} \right\rangle \frac{dV}{d\psi} F. \tag{2.15}$$

The CHEASE code allows to provide $p(\rho)$ and $j_{par}(\rho)$ as profile inputs. Since these quantities are directly predicted by RAPTOR, we do not need to rely on equilibrium metrics from the old equilibrium to obtain derived quantities like $FF'$.

### 2.3.1 Poloidal flux diffusion equation

From resistive MHD theory, one can derive that in a plasma with finite resistivity, the magnetic field diffuses on time scales depending on resistivity $\eta \sim T_e^{-3/2}$ and system size $L$, $\tau_R \sim L^2/\eta$ [Freidberg 2007] (for TCV: $\tau_R \sim 0.15$s, for AUG: $\tau_R \sim 5$s for ITER: $\tau_R \sim 100$s).

In a tokamak, an equation for the diffusion of poloidal flux $\psi$ can be obtained by projecting Ohm's law (without flows: $\mathbf{j} = \sigma\mathbf{E} + \mathbf{j_{ni}}$) along the magnetic field and averaging over the flux surface (as reported in [Felici et al. 2018]):

$$\underbrace{\sigma_\parallel \left( \frac{2\Phi_b \rho}{V'_\rho} \left.\frac{\partial\psi}{\partial t}\right|_\rho - \frac{\rho^2 \dot{\Phi}_b}{V'_\rho} \frac{\partial\psi}{\partial\rho} \right)}_{\langle\mathbf{j_\Omega}\cdot\mathbf{B}\rangle} = \underbrace{\frac{F^2}{8\pi^2\mu_0\Phi_b V'_\rho} \frac{\partial}{\partial\rho}\left[ \frac{g_2 g_3}{\rho} \frac{\partial\psi}{\partial\rho} \right] - \langle\mathbf{j_{ni}}\cdot\mathbf{B}\rangle}_{\langle\mathbf{j}\cdot\mathbf{B}\rangle} \tag{2.16}$$

Where $j_{oh} = \langle\mathbf{j_\Omega}\cdot\mathbf{B}\rangle/B_0$ is the ohmic current density and $j_{ni} = \langle\mathbf{j_{ni}}\cdot\mathbf{B}\rangle/B_0$ is the sum of all non-inductive current sources, including bootstrap current $j_{bs}$ and auxiliary current drive $j_{aux}$. Time evolution of the external magnetic field or movements of the plasma boundary are taken into account through the term including the time derivative of the enclosed toroidal flux $\Phi_b$. Time derivatives are evaluated at constant $\rho$.

Typically this equation is solved in RAPTOR with two Neumann boundary conditions: (1) $\left.\frac{\partial\psi}{\partial\rho}\right|_{\rho=0} = 0$, as $\psi$ reaches a minimum at the magnetic axis; (2) $\left.\frac{\partial\psi}{\partial\rho}\right|_{\rho=1}$, allowing to follow a pre-defined time trace of the total plasma current $I_p(t)$:

$$\frac{g_2 g_3}{\rho} \left.\frac{\partial\psi}{\partial\rho}\right|_{\rho=1} = \left.\frac{16\pi^3\mu_0\Phi_b}{F}\right|_{\rho=1} I_p(t). \tag{2.17}$$

Evolving this equation directly solves for the spatial distribution and temporal evolution of $\psi(\rho, t)$. Note however that $\psi$ is directly linked to the enclosed plasma current at radius $\rho$ and the safety factor profile $q$:

$$I_{pl}(\rho) = \frac{V'_\rho}{4\mu_0\pi^2} \left\langle \frac{(\nabla\rho)^2}{R^2} \right\rangle \frac{\partial\psi}{\partial\rho} \tag{2.18}$$

$$\frac{1}{q} = \frac{1}{2\pi B_0\rho} \frac{\partial\psi}{\partial\rho} \tag{2.19}$$

When solving for $\psi(\rho, t)$, we can equivalently state that we are solving for the current density evolution $j_{par}(\rho, t)$ or the safety factor profile evolution $q(\rho, t)$.

The loop voltage is defined as the spatial distribution of the time derivative of $\psi$:

$$U_{pl} = \frac{\partial\psi}{\partial t} \tag{2.20}$$

For a steady-state plasma, all current is driven non-inductively, and $U_{pl} = 0$. We can also define a stationary state, which is less restrictive: we consider the $\psi$ profile stationary when the current profile $j_{par}$ is constant in time (but not necessarily with $j_{oh} = 0$). Stationarity can be imposed by requiring the time derivative of $I_{pl}(\rho)$ to be zero at all $\rho$, which leads to a

condition on the loop voltage $U_{pl}$ (assuming constant MHD geometry):

$$\frac{\partial I_{pl}(\rho)}{\partial t} = \frac{V'_\rho}{4\mu_0\pi^2}\left\langle\frac{(\nabla\rho)^2}{R^2}\right\rangle\frac{\partial}{\partial t}\frac{\partial\psi}{\partial\rho} = 0 \text{ with } \frac{\partial}{\partial t}\frac{\partial\psi}{\partial\rho} = \frac{\partial}{\partial\rho}\frac{\partial\psi}{\partial t} = \frac{\partial}{\partial\rho}U_{pl} \qquad (2.21)$$

The plasma current distribution remains stationary when a flat loop voltage profile is reached ($dU_{pl}/d\rho = 0$). In other words: the radial derivative of the loop voltage is the driving force for current diffusion. Typically, during the ramp-up (ramp-down) phase, the central solenoid is used to apply a positive (negative) loop voltage at $\rho = 1$, raising (lowering) $U_{pl}|_{\rho=1}$: The non-uniform $U_{pl}(\rho)$ then leads to inward (outward) current diffusion. Note that since the $j_{par}$ evolution is governed by a diffusive equation, the local current density cannot be changed instantaneously. When local positive current drive is applied, the loop voltage will locally drop (a phenomenon called back-emf, originating from Faraday's law of induction), leading to diffusion of current towards this location.

The plasma conductivity is evaluated by multiplying the Spitzer conductivity with a factor accounting for the impact of trapped particles [Sauter et al. 1999]:

$$\sigma_\parallel = 1.9012\times10^4\underbrace{\frac{T_e^{3/2}}{Z_{eff}N(Z_{eff})\log\Lambda_e}}_{\sigma_{Spitzer}}\left(1-\left(1+\frac{0.36}{Z_{eff}}\right)X+\frac{0.59}{Z_{eff}}X^2-\frac{0.23}{Z_{eff}}X^3\right), \qquad (2.22)$$

with the plasma effective charge $Z_{eff}$, the approximation $\log\Lambda_e = 31.3 - \log(\sqrt{n_e}/T_e)$ and the functions $N(Z_{eff}$ and $X(f_t,\nu_{e*})$ defined in [Sauter et al. 1999], with trapped fraction $f_t$ and collisionality $\nu_{e*}$. In RAPTOR, the trapped fraction $f_t$ is calculated with a formula derived in [Sauter 2016], including the effect of triangularity. Note that for an increased impurity content, hence higher $Z_{eff}$, the plasma becomes more resistive, hence leading to a faster diffusion of current.

The bootstrap current density $j_{bs} = \langle\mathbf{j_{bs}}\cdot\mathbf{B}\rangle$ is self-consistently calculated from the density and temperature profiles with the Sauter formula [Sauter et al. 1999], [Sauter et al. 2002a]:

$$j_{bs} = -2\pi\frac{F(\psi)}{R_0B_0}\left(\sum_{j=e,i}\left[p_jL_{31}\frac{\partial\log n_j}{\partial\rho}\right]+p_e(L_{31}+L_{32})\frac{\partial\log T_e}{\partial\rho}+p_i(L_{31}+\alpha L_{34})\frac{\partial\log T_i}{\partial\rho}\right), \quad (2.23)$$

where $L_{ij}$ and $\alpha$ are dependent on the fraction of trapped particles $f_t$ and the plasma collisionality. Note that these formulas have recently been slightly modified [Redl et al. 2021], but this was not yet implemented for the work presented in this thesis.

### 2.3.2 Thermal and particle transport equations

The time evolution of electron/main ion thermal energy density $(3/2)\,n_{e,i}\,T_{e,i}$ and electron particle density $n_{e,i}$ is governed by diffusive equations, accounting for a set of spatially resolved source and sink terms, as well as radial transport across the flux surfaces (as reported in [Felici et al. 2018]):

$$\frac{3}{2}(V'_\rho)^{-5/3}\left(\frac{\partial}{\partial t}\bigg|_\rho - \frac{\dot{\Phi}_b}{2\Phi_b}\frac{\partial}{\partial \rho}\rho\right)[(V'_\rho)^{5/3}n_{e,i}T_{e,i}] + \frac{1}{V'_\rho}\frac{\partial}{\partial \rho}\left(-\frac{g_1}{V'_\rho}n_{e,i}\chi_{e,i}\frac{\partial T_{e,i}}{\partial \rho} + \frac{5}{2}T_{e,i}\Gamma_{e,i}g_0\right) = P_{e,i}$$

(2.24)

$$\frac{1}{V'_\rho}\left(\frac{\partial}{\partial t}\bigg|_\rho - \frac{\dot{\Phi}_b}{2\Phi_b}\frac{\partial}{\partial \rho}\rho\right)[(V'_\rho)n_{e,i}] + \frac{1}{V'_\rho}\frac{\partial}{\partial \rho}\underbrace{\left(-\frac{g_1}{V'_\rho}D_{e,i}\frac{\partial n_{e,i}}{\partial \rho} + g_0 V_{e,i}n_{e,i}\right)}_{=V'_\rho\Gamma_{e,i}} = S_{e,i}$$

(2.25)

Where $\Gamma_{e,i}$ is the electron particle flux, in units of m$^{-2}$s$^{-1}$:

$$\Gamma_{e,i} = -\frac{g_1}{V'^2_\rho}D_{e,i}\frac{\partial n_{e,i}}{\partial \rho} + \frac{g_0}{V'_\rho}V_{e,i}n_{e,i},$$

(2.26)

In the RAPTOR implementation, eq. (2.24) is developed to a state evolution equation for $T_{e,i}(\rho,t)$, with $n_{e,i}$ either solved for with eq. (2.25) or user-specified. Typically, eq. (2.25) is solved for the electron species, while ion and impurity densities are constrained by the equations imposing plasma quasi-neutrality ($n_e = \sum_j Z_j n_j$) and the plasma effective charge ($n_e Z_{eff} = \sum_j Z_j^2 n_j$), with either the main impurity density or the effective charge number pre-defined.

The boundary conditions accompanying these equations are $\frac{\partial T_{e,i}}{\partial \rho}\big|_{\rho=0} = 0$, $\frac{\partial n_{e,i}}{\partial \rho}\big|_{\rho=0} = 0$ (since $\rho = 0$ corresponds to the magnetic axis), $T_{e,i}(\rho = 1, t) = T_{e,i\ b}(t)$, $n_{e,i}(\rho = 1, t) = n_{e,i\ b}(t)$ (the temperature and density boundary conditions can also be imposed at alternative radii, for example at the pedestal top $\rho = \rho_{ped}$ to simulate H-mode plasmas).

### 2.3.3 Heating/current drive sources and sinks

Heating, current drive and fueling sources are either internally calculated within RAPTOR, using ad-hoc models, or prescribed. A variety of models has been implemented for ohmic power, bremsstrahlung, line radiation, electron-ion equipartition heating, alpha heating and various auxiliary heating and current drive sources [Felici 2011]. Details on the alpha heating module, applied for the ITER and DEMO simulations in Chapters 4 and 5, can be found in [van Dongen et al. 2014].
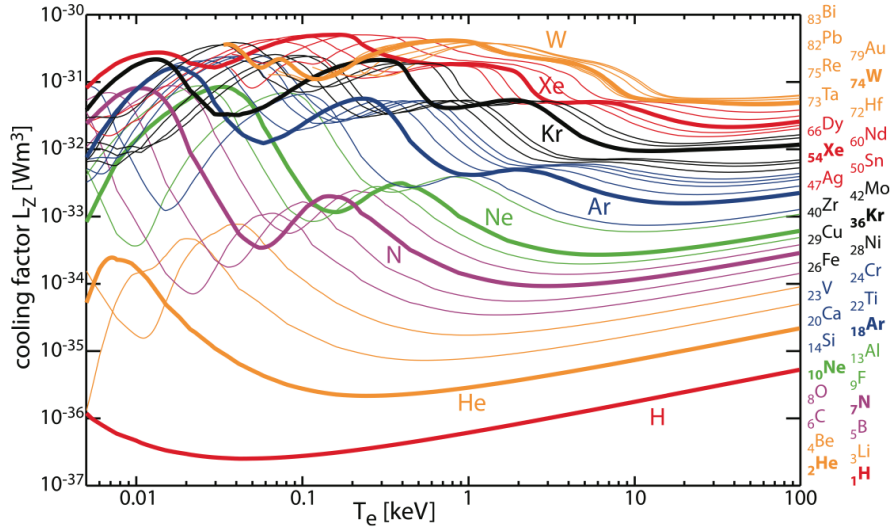
Figure 2.3: Cooling factors for various impurities, as available in the ADAS database. *Source: [Puetterich et al. 2019].*

**Gaussian model for electron cyclotron heating and current drive**

As the gaussian electron cyclotron heating and current drive module of RAPTOR is extensively used within this thesis, we repeat here the basic implementation, as originally reported in [Felici and Sauter 2012]. The power density is modeled as a gaussian profile, with deposition radius $\rho_{dep}$ and width $w_{dep}$. To evaluate the EC driven current, the following formula is used:

$$j_{cd}(\rho, t) = c_{cd} e^{-\rho^2/0.5^2} \frac{T_e}{n_e} e^{4(\rho-\rho_{dep})^2/w_{dep}^2} P_{gyro}(t) \qquad (2.27)$$

This heuristic expression relies on the observation that the current drive efficiency is proportional to $T_e/n_e$ [Lin-Liu et al. 2003] and decreases with increased trapped particle fraction. The current drive efficiency factor $c_{cd}$ is machine (and scenario) dependent and has to be tuned to experimental data or modeling from higher fidelity simulations.

To allow for generic current profile tailoring optimizations, without assuming a shape for the EC power density profile, we also implement the possibility to write the power deposition profile as a sum of spline basis functions. This will be applied later in the $q$ profile optimization presented in Section 2.5.2.

**Radiation models: bremsstrahlung and impurity radiation**

In [Maget et al. 2022], an impurity radiation model has been introduced in RAPTOR to evaluate the radiative losses from nitrogen and tungsten in WEST discharges, applying effective collisional-radiative coefficients from the ADAS database [ADAS].

Up to three impurity densities can be specified, which can be time-dependent (note however that RAPTOR has no impurity transport model implemented). Typically, to match experimental data, one can manually adjust the concentration of a light impurity (e.g. N), to match

the experimentally observed effective plasma charge evolution $Z_{eff}(t)$, and a heavy trace impurity (e.g. W), to match the measured total radiated power $P_{rad\ exp}(t)$. The radiated power calculated in RAPTOR is the sum of bremsstrahlung and the newly implemented impurity radiation contribution:

$$P_{rad} = \underbrace{5.35 \times 10^{-37} Z_{eff} n_e n_i T_e^{\frac{1}{2}}}_{P_{Brems}} + \underbrace{\sum_{j=1,2,3} n_e n_j L_j(T_e)}_{impurity}, \qquad (2.28)$$

where $n_j$ is the impurity density and $L_j$ is the impurity cooling factor, taken from the ADAS database. Note that $L_j$ introduces a non-linear dependency of the radiated power on $T_e$. In Figure 2.3, reproduced from [Puetterich et al. 2019], cooling factors and their $T_e$ dependence are presented. Note that for $T_e > 1\,\text{keV}$, the W cooling factor increases for decreasing $T_e$, leading to a potentially unstable situation. The consequences of this have been explored to characterise radiative collapses in WEST [Ostuni et al. 2022], and to find stable ramp-down scenarios for DEMO in Chapter 5 of this thesis.

In [Ostuni et al. 2022], a tungsten density profile has been estimated by inverting the formula, relying on the observation that W is the dominant radiator for $T_e > 1\,\text{keV}$ (justified by Figure 2.3):

$$n_W(\psi) \sim \frac{P_{rad,W}(\psi)}{n_e(\psi) L_W(T_e(\psi))}, \qquad (2.29)$$

where the spatially resolved radiation profile $P_{rad,W}(\psi)$ is obtained from bolometry inversion.

### 2.3.4 Transport models

In a tokamak, transport of thermal energy and particles (for ions and electrons) is dominated by turbulent fluxes driven by plasma micro-instabilities. In eq. (2.24) and eq. (2.25), analytical formulae[1] are required to evaluate the local thermal diffusivities $\chi_{e,i}(\rho, t)$, particle diffusion coefficients $D_{e,i}(\rho, t)$ and pinch terms $V_{e,i}(\rho, t)$. A range of transport models is presently available in RAPTOR, as briefly reviewed below.

**Analytical transport formula**

A simple ad-hoc formula for the evaluation of $\chi_e$ has been implemented in [Felici and Sauter 2012], taking into account the experimental observations of enhanced energy confinement for higher plasma current and for negative magnetic shear $s$. As this ad-hoc transport model plays a central role in Chapter 3, the analytic formula is repeated here:

$$\chi_e = \chi_{neo} + \underbrace{c_{ano} \rho q F(s) T_{e0}[keV]^{c_{T_e}}}_{\chi_{anomalous}} + \chi_{central} e^{-\rho^2/\delta_0^2} \qquad (2.30)$$

---

[1]As RAPTOR applies an implicit solver scheme that makes use of analytical evaluation of the Jacobians, a differentiable expression is required.

with

$$F(s) = a_{ic}/[1 + e^{w_{ic}(d_{ic}-s)}] + (1 - a_{ic}) \tag{2.31}$$

Formula eq. (2.30) consists of three terms: (1) a small neoclassical contribution; (2) an anomalous contribution; (3) a gaussian diffusion term in the center to reproduce the experimental observation of profile flattening. Within $\chi_{anomalous}$, a shear-dependent factor $F(s)$ is included, to be able to include the effect of improved confinement for negative magnetic shear (eq. (2.31)). This factor can be disabled by setting $a_{ic} = 0$. In [Geelen et al. 2015], an additional factor $T_{e0}[keV]^{c_{Te}}$ was added to the anomalous diffusion term, to capture the degradation of confinement for increased input power. This exponent can be loosely related to the power degradation exponent in confinement scaling laws[2].

### Bohm gyro-Bohm model

The electron and ion heat diffusivities can also be estimated by adding a Bohm-like plus a gyro-Bohm-like contribution [Erba et al. 1998]. The implementation in RAPTOR is:

$$\chi_e = \alpha_B \underbrace{\frac{T_e}{B_0} q^2 2 \frac{1}{n_e T_e} \frac{d(n_e T_e)}{d\rho}}_{\chi_B \sim \frac{T_e}{B_0} q^2 a \frac{\nabla p_e}{p_e}} + \alpha_{gB} \underbrace{\frac{\rho_*}{B_0} \frac{dT_e}{d\rho}}_{\chi_{gB} \sim \frac{T_e}{B_0} \rho_* a \frac{\nabla T_e}{T_e}} \tag{2.32}$$

where $\rho_*$ is the plasma normalized gyro-radius $\rho_* = \sqrt{m_i T_e}/(eaB_0)$. Recent application of this model for real-time state reconstruction for JET has been reported in [Piron et al. 2021].

### QuaLiKiz neural network surrogate model

A proof-of-principle of the coupling of RAPTOR to a surrogate neural network of QuaLiKiz, a quasi-linear gyrokinetic transport model [Bourdelle et al. 2015; Citrin et al. 2017], has been presented in [Citrin et al. 2015] and [Felici et al. 2018]. In QuaLiKiz, the linear gyro-kinetic dispersion relation is solved in $s - \alpha$ geometry, in the electrostatic limit. The quasi-linear approximation is used to calculate the transport fluxes based on the linear response over a range of wavevectors, applying a saturation rule for the electrostatic potential and spectral shape, tuned to non-linear gyrokinetic simulations for ion and electron scale lengths.
A new generation of the QuaLiKiz neural network, QLKNN-hyper-10D, is presented in [van de Plassche et al. 2020], and coupled to RAPTOR. Applications have been presented for JET simulations in [van de Plassche et al. 2020] and for optimizations of the ITER hybrid scenario

---

[2]Assume a stationary plasma where the electron heat flux equals the total input power $P$: $Q_e = n_e \chi_e \frac{\partial T_e}{\partial \rho} = P$. A power degradation exponent $\alpha_P$ for electron thermal energy confinement time $\tau_{th\,e} = W_{th\,e}/P \sim P^{\alpha_P}$ implies $W_{th\,e} \sim P^{1+\alpha_P}$. As $W_{th\,e} = \int \frac{3}{2} n_e T_e dV$ one can loosely relate $T_{e0} \sim P^{1+\alpha_P}$ (assuming constant density). Introducing $\chi_e \sim T_{e0}^{c_{Te}}$ in the power balance yields $P \sim n_e T_{e0}^{c_{Te}} \frac{T_{e0}}{a} \sim (P^{1+\alpha_P})^{c_{Te}+1}$, hence $(1 + \alpha_P)(c_{Te} + 1) = 1$ or $c_{Te} = \frac{1}{1+\alpha_P} - 1$. Note that typical values for the power degradation exponent $\alpha_P = -0.5, -0.6$ and $-0.7$ hence correspond to the respective $T_e$ exponents $c_{Te} = 1.0, 1.5$ and $2.3$, in line with $c_{Te} = 1.2$ applied within Chapter 3 [Geelen et al. 2015].

in [Van Mulders et al. 2021b] (Chapter 4 of this thesis).

The neural network has been trained on a database of $3 \times 10^8$ QuaLiKiz flux calculations. This dataset has been obtained by selecting the QuaLiKiz inputs based on a brute-force hyper-cube scan approach over 9 input dimensions (The dataset is visualized in http://dataslicer. qualikiz.com/QuaLiKiz-dataslicer). A whole range of operating regimes, both on present-day devices and on future machines like ITER and DEMO, are contained within the bounds of the hypercube. The existence of sharp critical gradients for turbulent transport, identical for all transport channels, is incorporated in the training pipeline, enhancing the neural network fitting quality. The inputs to the neural network model are 10 dimensionless, local plasma parameters: logarithmic gradients $R/L_{T_e}$, $R/L_{T_i}$ and $R/L_{n_e}$, ion-electron temperature ratio $T_i/T_e$, safety factor $q$, magnetic shear $s$, inverse aspect ratio $r/R$, collisionality $\nu^*$, effective charge $Z_{eff}$[3]. The outputs are the ion and electron heat fluxes $q_{i,e}$ as well as the particle fluxes $\Gamma_{i,e}$. From the local heat and particle fluxes, the local thermal diffusivities $\chi_{e,i}(\rho, t)$, particle diffusion coefficients $D_{e,i}(\rho, t)$ and pinch terms $V_{e,i}(\rho, t)$ can be evaluated. Furthermore, the Jacobians containing the derivatives of the network outputs with respect to the inputs can be evaluated. These Jacobians allow for the fully analytical evaluation of the derivatives of the transport coefficients to the plasma state through the meticulous application of the chain rule in the RAPTOR-QLKNN interface.

Note that the QLKNN transport model allows for a first-principle-based estimate of turbulent heat and particle transport for the bulk plasma species. However, as the model is not capable to predict the transport suppression in the pedestal region, a boundary condition at the pedestal top location is required in order to simulate H-mode plasmas.

**Gradient-based model**

In [Teplukhina et al. 2017], a gradient-based transport model has been introduced. The assumption underlying this empirical model is the existence of a region in the plasma core where plasma turbulence results in stiff behavior of the corresponding temperature and density profiles. The resilience of the plasma profile gradient scale lengths to increase beyond a critical value is a well-established plasma turbulence characteristic, both experimentally [Ryter et al. 2001] and theoretically [Garbet et al. 2004].

Within the gradient-based transport model, an analytical formula for heat and particle diffusivities is calculated, based on the assumption that in stationary state three radially separated regions are formed: (1) a central region $\rho < \rho_{inv}(= \rho_{q=1})$ with high transport to mimic the profile flattening caused by sawteeth or other transport-enhancing phenomena (in the absence of a $q = 1$ surface, we put $\rho_{inv} = 0.1$, as flattened profiles toward the magnetic axis can occur even in the absence of sawtooth activity, e.g. in the presence of kinetic ballooning modes [Kumar et al. 2020]); (2) an intermediate stiff core region characterized by constant logarithmic gradients $\lambda_{T_e} = -d \ln T_e/d\rho$ and $\lambda_{n_e} = -d \ln n_e/d\rho$; (3) a pedestal region with linear gradients

---

[3]The impact of $\mathbf{E} \times \mathbf{B}$ flow shear can be included in post-processing, based on a 10th input variable $\gamma_{\mathbf{E} \times \mathbf{B}} = -\frac{d v_{\mathbf{E} \times \mathbf{B}}}{dr} R \sqrt{\frac{m_p}{T_{ref}}}$, with $T_{ref} = 1 \, \text{keV}$ as described in [van de Plassche et al. 2020].

$\mu_{T_e} = -dT_e/d\rho$ and $\mu_{n_e} = -dn_e/d\rho$.

Under these assumptions, formulas for heat diffusivity $\chi_e(\rho)$ and particle pinch $V_e(\rho)$ are derived in [Kim et al. 2016], with analytical dependencies on $\rho$, $T_e$, $n_e$, the local heat (or particle) flux and the parameters $\lambda_{T_e,n_e}$ and $\mu_{T_e,n_e}$:

$$
\begin{aligned}
\chi_e &= f\left(\frac{\rho - \rho_{inv}}{\delta\rho_{inv}}\right)\chi_{ST} \\
&+ f\left(\frac{\rho_{inv} - \rho}{\delta\rho_{inv}}\right)\frac{q_e}{V'_\rho\langle(\nabla\rho)^2\rangle n_e T_e}\left[\lambda_{T_e}f\left(\frac{\rho - \rho_{ped}}{\delta\rho_{ped}}\right) + \frac{\mu_{T_e}}{T_e}f\left(\frac{\rho_{ped} - \rho}{\delta\rho_{ped}}\right)\right]^{-1}
\end{aligned}
\tag{2.33}
$$

$$
\frac{V_e}{D_e} = -f\left(\frac{\rho_{inv} - \rho}{\delta\rho_{inv}}\right)\left[\lambda_{n_e}f\left(\frac{\rho - \rho_{ped}}{\delta\rho_{ped}}\right) + \frac{\mu_{n_e}}{n_e}f\left(\frac{\rho_{ped} - \rho}{\delta\rho_{ped}}\right)\right]^{-1} + \frac{\Gamma_e}{n_e V'_\rho\langle(\nabla\rho)^2\rangle}\frac{1}{D_e}
\tag{2.34}
$$

$$
\text{with } D_e = 0.2\chi_e
$$

assuming the particle confinement time is about 5 times longer compared to the energy confinement time [Becker 1988]. Presently, $\Gamma_e = 0$ is assumed, which is justified in the absence of strong particle sources.

As the logarithmic gradients in the core are assumed to be limited to a value slightly above the critical gradient of the dominant turbulent mode for a given scenario and tokamak, empirical values have been derived for H and L-modes on TCV, AUG and JET in [Teplukhina et al. 2017]. The time traces of $\mu_{T_e,n_e}$ are calculated by summing a feedforward and a feedback contribution. The aim of the peripheral temperature gradient $\mu_{T_e}$ is to match a prescribed confinement quality time evolution with respect to the IPB98(y,2) scaling law [ITER Physics Expert Group on Confinement and Transport and ITER Physics Expert Group on Confinement Modelling and Database and ITER Physics Basis Editors 1999], either for the electron confinement time, i.e. $H_e = \tau_{E,e}/\tau_{scl}$, or for the total confinement time $H = \tau_E/\tau_{scl}$. The aim of the peripheral density gradient $\mu_{n_e}$ is to match a prescribed trace of the line-averaged density, which can be set from experimental data or set to a given Greenwald fraction. Details on the application of the model and the setting of feedforward traces and feedback controller gains are given in Section 5.2.4, where the gradient-based model is applied for DEMO ramp-down simulations. A distinct feature of the gradient-based transport model is that the temperature boundary condition can be set at $\rho = 1$, both for L- and H-mode plasmas. The LH transition is modeled through the user-defined time trace of the H factor and the resulting modifications of the transport coefficients eq. (2.33) and eq. (2.34).

## 2.4 RAPTOR numerical implementation

### 2.4.1 State evolution solver

The set of equations eq. (2.16), eq. (2.24), eq. (2.25) features multiple couplings and non-linearities. By requiring analytical gradients for the dependencies of the coefficients on the plasma state, RAPTOR achieves efficient implicit time stepping and enables gradient-based non-linear optimization schemes.

Substituting the radial profiles constituting the plasma state by the sum of a set of finite element basis functions, the infinite-dimensional PDEs are discretized in space. Projecting the resulting equations on the set of basis functions and subsequently applying integration by parts, finite-dimensional ODEs in the finite element coefficients $\hat{\psi}$, $\hat{\mathbf{T}}_{\mathbf{e,i}}$ and $\hat{\mathbf{n}}_{\mathbf{e,i}}$ emerge ([Felici et al. 2018] and references therein):

$$\mathbf{F} = \mathbf{0} = -\mathbf{M}_\psi \dot{\hat{\psi}} - \mathbf{D}_\psi \hat{\psi} + \mathbf{B}_\psi \mathbf{u} + \mathbf{f}_\psi \tag{2.35}$$

$$\mathbf{G} = \mathbf{0} = -\mathbf{M}_{\mathbf{T_{e,i}}} \dot{\hat{\mathbf{T}}}_{\mathbf{e,i}} - \mathbf{D}_{\mathbf{T_{e,i}}} \hat{\mathbf{T}}_{\mathbf{e,i}} + \mathbf{B}_{\mathbf{T_{e,i}}} \mathbf{u} + \mathbf{f}_{\mathbf{T_{e,i}}} \tag{2.36}$$

$$\mathbf{H} = \mathbf{0} = -\mathbf{M}_{\mathbf{n_{e,i}}} \dot{\hat{\mathbf{n}}}_{\mathbf{e,i}} - \mathbf{D}_{\mathbf{n_{e,i}}} \hat{\mathbf{n}}_{\mathbf{e,i}} + \mathbf{B}_{\mathbf{n_{e,i}}} \mathbf{u} + \mathbf{f}_{\mathbf{n_{e,i}}} \tag{2.37}$$

The equations eq. (2.35), eq. (2.36) and eq. (2.37) are derived from the respective equations eq. (2.16), eq. (2.24) and eq. (2.25). The matrices $\mathbf{M}$, $\mathbf{D}$ and $\mathbf{B}$ and the vectors $\mathbf{f}$ follow from the finite element discretization procedure, as explained in more detail in Appendix B of [Teplukhina 2018]. The *Actuator vector* $\mathbf{u}$ contains all external actuator inputs (including the total plasma current $I_p$, e.g. $\mathbf{u} = [I_p, P_{ec}, P_{nb}]^T$). Compacting the notation by introducing the *state vector* $\mathbf{x} = [\hat{\psi}^T, \hat{\mathbf{T}}_{\mathbf{e,i}}^T, \hat{\mathbf{n}}_{\mathbf{e,i}}^T]^T$ and residue function $\mathbf{f} = [\mathbf{F}^T, \mathbf{G}^T, \mathbf{H}^T]^T$, a state evolution equation is obtained:

$$\mathbf{f}(\dot{\mathbf{x}}(t), \mathbf{x}(t), \mathbf{u}(t)) = 0 \tag{2.38}$$

To evolve the plasma state throughout the time window of the simulation, we discretize eq. (2.38) on a time grid $t = [t_0 \dots t_k \dots t_f]$, defining $\mathbf{x}_k = \mathbf{x}(t_k)$, $\dot{\mathbf{x}}_k = (\mathbf{x}_k - \mathbf{x}_{k-1})/(t_k - t_{k-1})$ and $\mathbf{u}_k = \mathbf{u}(t_k)$:

$$\mathbf{f}_k(\mathbf{x}_{k-1}, \mathbf{x}_k, \mathbf{u}_k) = 0 \tag{2.39}$$

In a dynamic RAPTOR simulation, the state is evolved from $\mathbf{x}_{k-1}$ to the next time step $k$ with an implicit method, requiring iterative solution of the non-linear equation eq. (2.39), which is solved for $\mathbf{x}_k$ by Newton's method, with $\mathbf{x}_{k-1}$ and $\mathbf{u}_k$ known (the simulation starts from an initial state $\mathbf{x}_0$). While an implicit method is computationally more expensive than an explicit method, the improved numerical stability allows to select a larger time step $t_k - t_{k-1}$.

The computation speed of optimization problems, as introduced in Section 2.5.1, can be greatly improved when the derivative of the plasma state to a simulation parameter input $p$, i.e. $\partial \mathbf{x}_k/\partial p$, can be cheaply evaluated. Using the forward sensitivity analysis method of [Cacuci 1981], the forward sensitivity equation with respect to parameter input $p$ is obtained:

$$0 = \frac{d\mathbf{f}_k}{dp} = \frac{\partial \mathbf{f}_k}{\partial \mathbf{x}_{k-1}} \frac{\partial \mathbf{x}_{k-1}}{\partial p} + \frac{\partial \mathbf{f}_k}{\partial \mathbf{x}_k} \frac{\partial \mathbf{x}_k}{\partial p} + \frac{\partial \mathbf{f}_k}{\partial \mathbf{u}_k} \frac{\partial \mathbf{u}_k}{\partial p} + \frac{\partial \mathbf{f}_k}{\partial p} \tag{2.40}$$

The Jacobians $\partial \mathbf{f}_k/\partial \mathbf{x}_k$ and $\partial \mathbf{f}_k/\partial \mathbf{u}_k$ are readily available in RAPTOR. Evolving the ODE eq. (2.40) along with the initial set of ODEs eq. (2.39), the state sensitivities $\partial \mathbf{x}_k/\partial p$ are obtained. More details on the forward sensitivity equation and its applications can be found in [Felici 2011]. Note that for the optimization problem described in Section 2.5.1, the forward sensitivity equation is extended to a vector equation, containing a scalar equation for every element of the optimization vector $\mathbf{p}$.
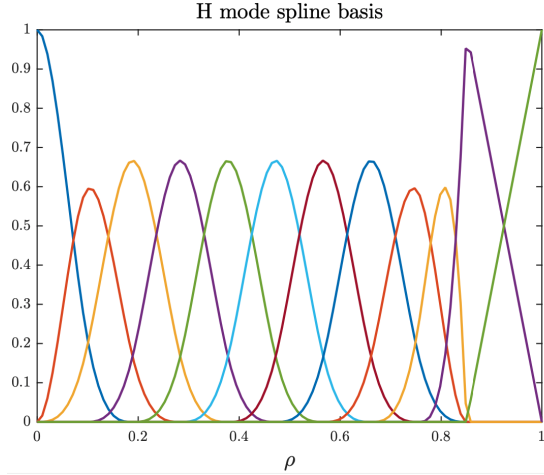
Figure 2.4: Illustration of a set of spline basis functions (different colors correspond to a different spline index) used by the imposed H-mode pedestal model (for temperature or density profiles), allowing for a natural implementation of the boundary condition at $\rho_{ped}$ (in this case $\rho_{ped} = 0.85$). The computational domain for temperature (and density) is reduced to $\rho \in [0, \rho_{ped}]$, while the computational domain for $\psi(\rho, t)$ is left unchanged.

The knowledge of the Jabobian matrices can also be applied to construct a linear time-varying system:

$$\delta\mathbf{x}_k = A_k \delta\mathbf{x}_{k-1} + B_k \delta\mathbf{u}_k \tag{2.41}$$

This set of linearized models at each time step, along a nominal time evolution of the plasma state $\mathbf{x}_{nom}(t)$, is essential for applications in model predictive control [Maljaars et al. 2015] and iterative learning control [Felici and Oomen 2015].

### 2.4.2 Imposed pedestal method

The finite element discretization procedure allows for a flexible choice of basis functions. A generic radial profile $m(\rho, t)$ ($\psi$, $T_{e,i}$ or $n_{e,i}$) is constructed as a sum of the basis functions $\Lambda_\alpha(\rho)$, weighted by the finite element coefficients $\hat{\mathbf{m}}$:

$$m(\rho, t) = \sum_{\alpha=1}^{n_{spl}} \Lambda_\alpha(\rho)\hat{\mathbf{m}}_\alpha(t) \tag{2.42}$$

In RAPTOR, cubic splines (non-periodic B-splines) are typically used as basis functions, with $d\Lambda_\alpha(\rho)/d\rho|_{\rho=0} = 0$, to automatically fulfill the Neumann boundary condition at $\rho = 0$.
As part of this thesis, a new way has been implemented to impose the pedestal region profiles of temperature and density during the H-mode phase of a simulation. Previously, when a boundary condition was applied at $\rho = \rho_{ped}$, the diffusivity in the region $\rho \in [\rho_{ped} \ 1]$ was typically adjusted based on a user-defined gradient $dT/d\rho$ (or $dn/d\rho$) and the steady state heat and particle balance equations. The H-mode module would calculate the diffusivities that would lead in stationary state to a user-defined gradient within $\rho \in [\rho_{ped} \ 1]$. However, often this method would lead to numerical difficulties, giving rise to negative temperatures.

The new *imposed pedestal model* applies a different set of basis functions for temperature and density profiles during the H-mode phase of the simulation, consisting of a set of cubic splines on $\rho \in [0 \; \rho_{ped}]$ and two linear basis functions on $\rho \in [\rho_{ped} \; 1]$, as illustrated in Figure 2.4. Effectively, the computational domain for temperature and density is reduced to $\rho \in [0 \; \rho_{ped}]$, with the cubic spline coefficients as the unknown variables in the state equation eq. (2.38), while on $\rho \in [\rho_{ped} \; 1]$ a linear pedestal is constructed with user-defined values at $\rho = \rho_{ped}$ and $\rho = 1$. The poloidal flux diffusion equation is still solved on the full computational domain $\rho \in [0 \; 1]$, so that the effect of the imposed pedestal on current diffusion is consistently captured. This new model eases RAPTOR H-mode simulations and has been applied in [van de Plassche et al. 2020] and [Van Mulders et al. 2021b].

### 2.4.3 Stationary state solver

In this section we report on the stationary state solver in RAPTOR, implemented as part of this thesis, as reported in [Van Mulders et al. 2021b].

**Implementation of the stationary state solver**

Applying time-constant actuator inputs $\mathbf{u}$ and excluding transient phenomena (e.g. due to MHD activity), the plasma state $\mathbf{x}(t)$ evolves to a stationary solution $\mathbf{x_{SS}}$, characterized by time-independent profiles for the current density and the kinetic quantities. Whenever one is solely interested in the final state reached by the plasma (e.g. when optimizing the flat-top phase of a tokamak plasma discharge), it makes sense to solve directly for the stationary plasma profiles, neglecting the dynamic evolution towards that state which is computationally costly to simulate. The plasma state can be considered stationary if the kinetic profiles $(T_e, n_e)$ are time-constant and the loop voltage is radially flat (from eq. (2.21)):

$$\frac{\partial}{\partial t} T_{e,i} = 0, \; \frac{\partial}{\partial t} n_{e,i} = 0 \text{ and } \frac{\partial}{\partial \rho}\left[\frac{\partial}{\partial t}\psi\right] = \frac{\partial}{\partial \rho} U_{pl} = 0 \tag{2.43}$$

The conditions imposed by equations eq. (2.43) constrain the time derivative of the state vector $\dot{\mathbf{x}}_{\mathbf{SS}}$ to an expression of the following form:

$$\dot{\mathbf{x}}_{\mathbf{SS}} = \left[\dot{\tilde{\psi}}_{\mathbf{SS}}^{\;T}, \dot{\tilde{\mathbf{T}}}_{\mathbf{e,i \, SS}}^{\;T}, \dot{\tilde{\mathbf{n}}}_{\mathbf{e,i \, SS}}^{\;T}\right]^T, \text{ with} \tag{2.44}$$

$\dot{\tilde{\psi}}_{\mathbf{SS}}^{\;T} = U_{pl}[1,1,...,1]^T, \dot{\tilde{\mathbf{T}}}_{\mathbf{e,i \, SS}}^{\;T} = [0,0,...,0]^T, \dot{\tilde{\mathbf{n}}}_{\mathbf{e,i \, SS}}^{\;T} = [0,0,...,0]^T$.
In other words: for a stationary plasma, the state vector time derivative is described by a single scalar, i.e. the value of the constant loop voltage $U_{pl}$.
Finding the stationary solution hence amounts to solving the non-linear set of equations:

$$\mathbf{f}(\dot{\mathbf{x}}_{\mathbf{SS}}(U_{pl}), \mathbf{x_{SS}}, \mathbf{u_{SS}}) = 0 \tag{2.45}$$

Since the number of equations equals the number of finite element coefficients $n_{FE}$, the non-linear system can be solved for $n_{FE}$ unknown variables. The solution profile of the poloidal magnetic flux can be increased with a constant value without changing the physical interpretation. As a consequence of this gauge freedom, $n_{FE} - 1$ independent variables describe the fully unknown stationary state $\mathbf{x_{SS}}$. The final unknown variable in equation eq. (2.45) can be chosen to be either the unknown loop voltage $U_{pl}$ or any actuator command $U_{SS}$ in $\mathbf{u_{SS}}$. This leads to two alternative formulations of the non-linear root-finding problem:

- *option 1*: find the loop voltage resulting in a stationary state for given actuator values $\mathbf{u_{SS}}$

- *option 2*: find the actuator command resulting in a stationary state for given loop voltage $U_{pl}$

As both cases have interesting use-cases, both options are implemented in the stationary state solver.

The system of non-linear equations is solved iteratively with a Newton-Raphson method. A vector $\mathbf{z} \in \mathbb{R}^{n_{FE}}$ is defined, containing all unknown variables, i.e. $\mathbf{z}^T = [\mathbf{x_{SS}}^T, U_{pl}]^T$ (*option 1*) or $\mathbf{z}^T = [\mathbf{x_{SS}}^T, U_{SS}]^T$ (*option 2*). Solving for the stationary state hence amounts to solving the non-linear system of equations $\mathbf{f}$ for the unknown set of variables $\mathbf{z}$. The state function $\mathbf{f}$ is evaluated for an initial guess $\mathbf{z_0}$, along with the Jacobian $\partial\mathbf{f}/\partial\mathbf{z}$. The Jacobian can be evaluated analytically by careful application of the chain rule to obtain $\partial\mathbf{f}/\partial\dot{\mathbf{x}}$, $\partial\mathbf{f}/\partial\mathbf{x}$ and $\partial\mathbf{f}/\partial\mathbf{u}$ and by passing the parametrizations $\partial\dot{\mathbf{x}}/\partial\mathbf{z}$, $\partial\mathbf{x}/\partial\mathbf{z}$ and $\partial\mathbf{u}/\partial\mathbf{z}$ inside the solver. A parameter vector update $\mathbf{z_{i+1}} = \mathbf{z_i} + \Delta\mathbf{z}$ is calculated by solving the locally linearized equation $\mathbf{f} = -\frac{\partial\mathbf{f}}{\partial\mathbf{z}}\Delta\mathbf{z}$ for the increment $\Delta\mathbf{z}$. To make the solution procedure more robust, the step size $|\Delta\mathbf{z}|$ is reduced whenever the update causes the plasma profiles to exhibit unphysical behaviour[4] or the residual error increases (i.e. $|\mathbf{f_{i+1}}| > |\mathbf{f_i}|$). This algorithm is repeated iteratively until the norm of the evaluated equations (representing the residual error) is smaller than a predefined value.

**Dynamic state evolution versus stationary state**

To illustrate the gain in computation time that can be obtained by directly solving for the stationary plasma state (and the plasma loop voltage, applying *option 1* of the solver), the time evolution of radial profiles in a time dependent RAPTOR run is compared to the stationary solution. The state consists of the $T_e$ profile and the $\psi$ profile. A standard MHD equilibrium for the TCV tokamak is selected, with a plasma current $I_p = 200\,\text{kA}$, an imposed electron density profile with $n_{e0} = 10^{19}\,\text{m}^{-3}$ and electron cyclotron heating ($P_{aux} = 1\,\text{MW}$) with a gaussian auxiliary power deposition profile centered around $\rho = 0.4$, providing co-current drive (according to the formula eq. (2.27)). Figure 2.5 presents time traces of the distance of the plasma

---

[4]Updated profiles are considered unphysical if any of the following quantities becomes (locally) negative: $T_{e,i}$, $n_{e,i}$ or $\frac{\partial\psi}{\partial\rho}$.
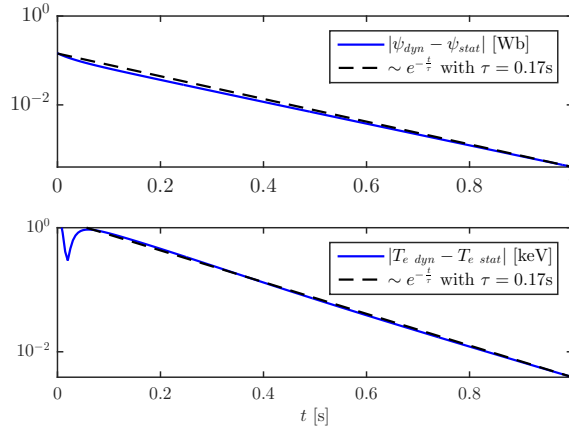
Figure 2.5: **Time evolution to stationary state** (log scale) Time traces of the distance (2-norm of the vector containing the difference on 20 radial grid points) of the $\psi$ and $T_e$ profiles in a time dependent RAPTOR simulation ($_{dyn}$) to their respective stationary solutions ($_{stat}$) for a TCV plasma (1 s simulation with time step 5 ms). The time constant $\tau = 170$ ms of the superimposed exponentials show that both $T_e$ and $\psi$ evolve to a relaxed shape at the slow time scale of current diffusion. *Reproduced from [Van Mulders et al. 2021b].*

profiles ($\psi$ and $T_e$ solved for 1 s) to the stationary solution. The plasma state clearly evolves to the stationary solution at the slow time scale of current diffusion (note the time constant $\tau = 170$ ms of the superimposed exponentials on Figure 2.5). Due to the non-linear coupling of equations eq. (2.24) and eq. (2.16), the temperature profile also evolves on this slow time scale. Assuming a current redistribution time of about $\tau_{crt} = 170$ ms and a typical RAPTOR time step (for TCV plasmas) of 5 ms, more than 100 time steps would be needed to simulate up until $t = 3\tau_{crt}$, where a relaxed state can safely be assumed, each time step requiring the solution of a non-linear system of equations. The stationary state solver on the other hand requires only 5 Newton steps to determine the stationary state of both profiles with a residue $r_i = |\mathbf{f_i}|$ below $10^{-10}$.

### Convergence studies

The Newton-Raphson solver of the RAPTOR stationary state solver converges quadratically to the root of the set of non-linear equations. Figure 2.6 illustrates the quadratic convergence by plotting the residue in the k+1th iteration $r_{k+1}$ versus the residue in the kth iteration $r_k$. Quadratic convergence implies $r_{k+1} \sim r_k^2$. The superimposed trend line $r_k^2$ shows that the series of residues indeed features quadratic convergence. The left panel in Figure 2.6 corresponds to the solution of $\psi$ and $T_e$ with the simple ad-hoc transport formula eq. (2.30), while the right panel in Figure 2.6 corresponds to the solution of $\psi$, $T_e$ and $T_i$ with a neural network emulation of the stiff quasi-linear gyrokinetic transport model QuaLiKiz (QLKNN-hyper-10D).
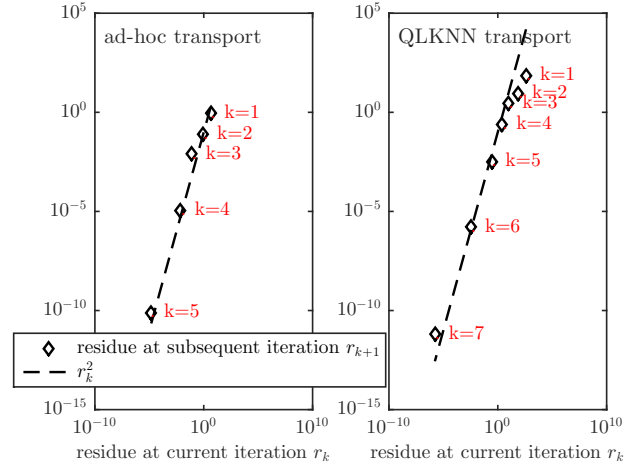
Figure 2.6: **Convergence of the stationary state solver** Quadratic convergence of the RAPTOR stationary state solver is illustrated, both with simple ad-hoc transport model and with neural network surrogate transport model QLKNN-hyper-10D. *Reproduced from [Van Mulders et al. 2021b].*
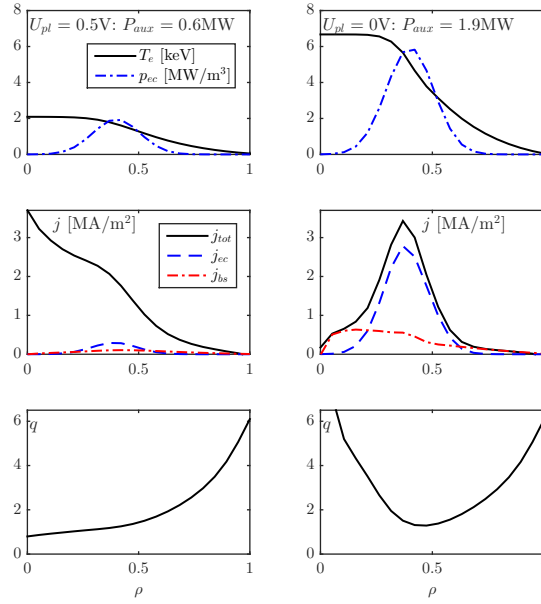


Figure 2.7: **Illustration of a result of the stationary state solver** Illustrative TCV simulation of stationary state profiles for $U_{pl} = 0.5V$ (left) and $U_{pl} = 0V$ (right). As expected, an increased auxiliary power is required ($P_{aux} = 1.9$ MW for $U_{pl} = 0V$ compared to $P_{aux} = 0.6$ MW for $U_{pl} = 0.5$V) to sustain the entire plasma current with the externally driven electron cyclotron current and the internally generated bootstrap current. *Reproduced from [Van Mulders et al. 2021b].*

51
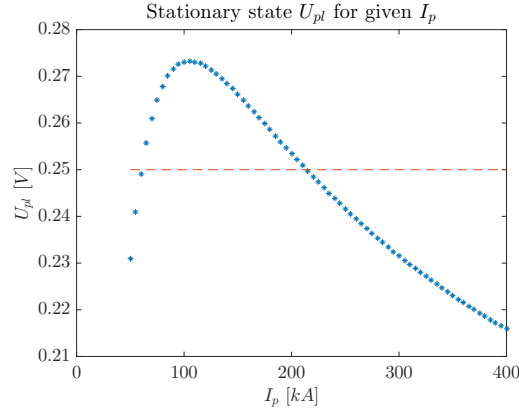
Figure 2.8: Stationary solutions at different levels of plasma current $I_p$. The stationary state solver finds the stationary set of profiles $\psi$ and $T_e$, and the corresponding loop voltage $U_{pl}$ to sustain the state.

**Toy example: TCV steady state scenario**

Let us present a simple example on how the stationary state solver can be applied to obtain the stationary plasma profiles $\psi(\rho)$ and $T_e(\rho)$, as well as the level of electron cyclotron heating and current drive required to sustain a stationary plasma on the TCV tokamak at a user-defined level of the loop voltage. Assumptions regarding MHD equilibrium, total plasma current, electron cyclotron heating and current drive deposition and electron density are identical to the previous example. The magnitude of the electron cyclotron power $P_{aux}$ is now considered an unknown, while the requested loop voltage is directly introduced in the non-linear equation eq. (2.45), which is hence solved to get the plasma state $\mathbf{x_{SS}}$ together with the actuator request $\mathbf{u_{SS}}$ (illustrating *option 2* of the non-linear solver).

Two cases are considered, respectively imposing loop voltages of $U_{pl} = 0.5\,\mathrm{V}$ (left hand side of Figure 2.7) and $U_{pl} = 0\,\mathrm{V}$ (right hand side of Figure 2.7). While the first case allows for a large fraction of ohmic current driven by the tokamak central solenoid, the second case explores steady state operation with no inductive current. Although actual plasma profile predictions depend on the tuning of parameters in the ad-hoc transport model eq. (2.30), this simulation illustrates how the stationary state solver can be used to find the actuator command resulting in a stationary state with an imposed loop voltage $U_{pl}$. An increased auxiliary power is required ($P_{aux} = 1.9\,\mathrm{MW}$ for $U_{pl} = 0\,\mathrm{V}$ compared to $P_{aux} = 0.6\,\mathrm{MW}$ for $U_{pl} = 0.5\,\mathrm{V}$) to sustain the entire plasma current with the externally driven electron cyclotron current and the internally generated bootstrap current. The non-linear problem of retrieving consistent stationary temperature and current density profiles, including the effects of $T_e$-dependent current drive efficiency and $\frac{\partial T_e}{\partial \rho}$-dependent bootstrap current, is successfully solved. Note that steady state TCV tokamak plasmas with plasma currents up to $I_p = 210\,\mathrm{kA}$ have been sustained with the available electron cyclotron heating capacity [Sauter et al. 2000; Coda et al. 2000; Sauter et al. 2001].
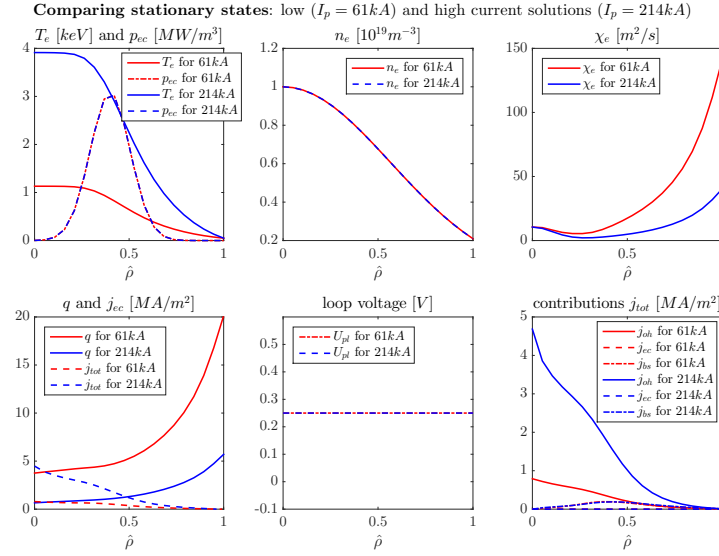
Figure 2.9: Two TCV stationary states that are non-unique solutions for $U_{pl} = 250\,$mV, with $P_{ec} = 1\,$MW. Depending on the initial condition, the solver converges to either of these solutions, as illustrated in Figure 2.10.

**Toy example: bifurcations**

Since the set of equations governing the stationary solution is non-linear, the uniqueness of a solution for a given combination of actuator values cannot be guaranteed. A simple illustration of a non-unique stationary solutions is given here.

Consider a simple TCV set-up, similar to the previous examples, using the simple, ad-hoc transport formula eq. (2.30) and one EC power source of 1 MW, with a gaussian auxiliary power deposition profile centered around $\rho = 0.4$, providing pure heating. In Figure 2.8, we solve for a range of stationary states, for different levels of the plasma current (remember that the plasma current $I_p$ can be considered an actuator). For each value of $I_p$, the $\psi(\rho)$ and $T_e(\rho)$ profiles are sought, and the loop voltage $U_{pl}$, sustaining the required plasma current (*option 1* of the solver).

Considering the curve of stationary states in Figure 2.8, we find a non-monotonic behavior. Initially, to sustain higher plasma currents $I_p$, an increased loop voltage $U_{pl}$ is required. Above some critical value of $I_p$, the reduction of the plasma resistance for increasing $T_e$ becomes however dominant (increasing $I_p$ leads to improved confinement in eq. (2.30)), resulting in reducing $U_{pl}$ for a further increase of $I_p$. Drawing a horizontal line at $U_{pl} = 250\,$mV, we observe that two stationary states can be sustained by this loop voltage: one at low current ($I_p = 61\,$kA) and one at high current ($I_p = 214\,$kA).

Using *option 2* of the stationary state solver, one can attempt whether both stationary states can be retrieved. In this set-up, $U_{pl} = 250\,$mV is given, while $\psi(\rho)$, $T_e(\rho)$ and $I_p$ are unknown. We find that, depending on the initial condition, the solver converges to either of two solutions, illustrated in Figure 2.9.

As a final step, we perform a scan over the space of initial conditions for the solver. For the

53
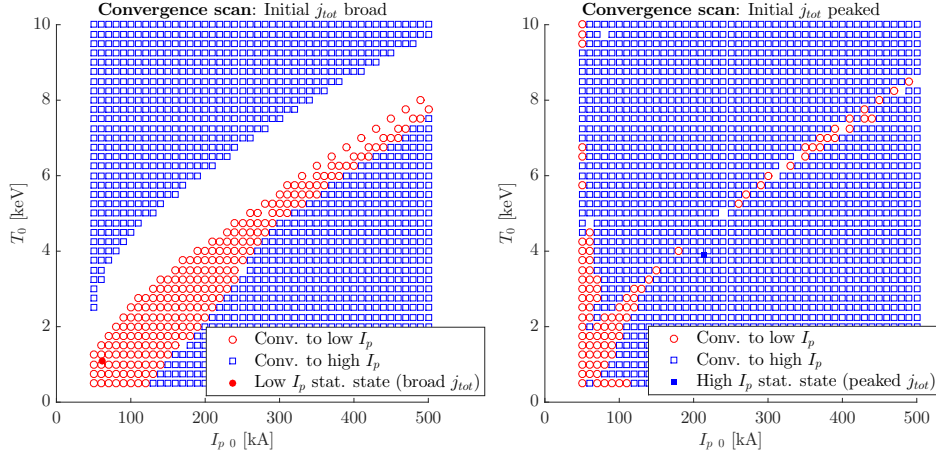
Figure 2.10: Two convergence scans, varying central temperature and plasma current of the initial condition. For the left plot, a more peaked current density profile is provided to calculate the initial condition for $\psi$. The colors indicate whether the corresponding initial condition converges to the high or low plasma current solution in Figure 2.9. In the region that is left blank, the solver does not converge.

initial condition, a set of profiles $\psi$ and $T_e$ is required, as well as an estimate for the plasma current. For the convergence scans in Figure 2.10, initial conditions are constructed with varying central temperature $T_{e0}$ and plasma current $I_{p\,0}$. Furthermore, the simulations in the left panel start from an initial $\psi$ corresponding to a rather broad current density profile with respect to the right hand panel. The regions in the diagram are colored based on the stationary solution to which the corresponding initial state converges: the high-current solution (blue) versus the low-current solution (red). The white band in the left plot indicates initial conditions for which the solver does not converge. The resulting pattern is rather non-trivial. Note in particular how a high-$I_p$ initial condition can still converge to the low-$I_p$ solution and how an initial state with both $I_{p\,0}$ and $T_{e0}$ close to the high-$I_p$ stationary state can still converge to the low-$I_p$ solution if the initial current distribution is broad.

This toy example clearly illustrates the multi-dimensional and non-linear nature of a tokamak operating point.

## 2.5 Optimization routine

### 2.5.1 Dynamic optimization problem

The RAPTOR optimization routine for time dependent simulations has been introduced in [Felici and Sauter 2012] and [Felici 2011], and expanded in [Teplukhina et al. 2017]. The aim is to find a set of actuator time traces (parametrized by a set of optimization variables **p**, i.e. $\mathbf{u}(t) = P(t)\mathbf{p}$, that minimizes a cost function. While the cost function $J$ can be any analytical expression based on the plasma state $\mathbf{x}(t)$, the plasma state time derivative $\dot{\mathbf{x}}(t)$ and the actuator vector $\mathbf{u}(t)$, the problem is often simplified: in [Felici and Sauter 2012] and [van Dongen et al. 2014], the cost function is only dependent on $\dot{\mathbf{x}}(t)$ and $\mathbf{x}(t)$ at the final time
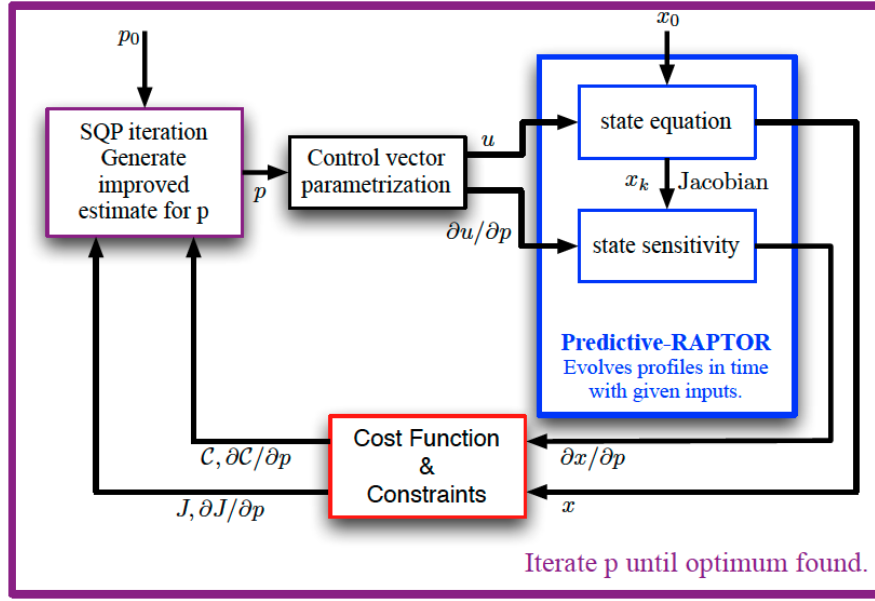
Figure 2.11: Schematic overview of the algorithm to solve a dynamic optimization problem in RAPTOR. *Reproduced from [Felici 2011].*

step of the simulation (end of ramp-up); in [Teplukhina et al. 2017], the cost function is only dependent on time integrals of the actuator variables $I_p(t)$, $P_{tot}(t)$ (total input power) and $\kappa(t)$ (plasma boundary elongation). The complete formulation of the optimal control problem is:

$$\min_{\mathbf{p}} \quad J(\dot{\mathbf{x}}(t), \mathbf{x}(t), \mathbf{u}(t)) \;\; \forall\, t \in [t_0, t_f] \text{ (cost)} \tag{2.46a}$$

$$\text{subject to } f(\dot{\mathbf{x}}(t), \mathbf{x}(t), \mathbf{u}(t)) = 0 \;\; \forall\, t \in [t_0, t_f] \text{ (state)} \tag{2.46b}$$

$$\mathbf{u}(t) = P(t)\mathbf{p} \text{ (actuator parametrization)} \tag{2.46c}$$

$$A_{ineq}\mathbf{p} \leq b_{ineq} \text{ (actuator limits)} \tag{2.46d}$$

$$\mathscr{C}(\mathbf{x}(t)) \leq 0 \text{ (state constraints)} \tag{2.46e}$$

Constraints on the values and the time derivatives of the actuator time traces $\mathbf{u}(t)$ can be imposed as linear constraints on the optimization vector $\mathbf{p}$, with eq. (2.46d). With 2.46e, non-linear constraints can be imposed on the plasma state, e.g. to maintain the safety factor above a minimum value. As explained in [Felici and Sauter 2012] and [Felici 2011], the problem is maintained tractable by formulating integral constraints (instead of a separate constraint for each $t_k$):

$$\mathscr{C}_i = \left( \int_{t_0}^{t_f} (\max\{0, c_i(t, \mathbf{x}(t))\})^2 dt - \epsilon \right) \leq 0 \tag{2.47}$$

Figure 2.11 gives a schematic overview of the optimization routine applied to solve the optimal control problem. RAPTOR evolves both the state equation eq. (2.39) and the forward sensitivity equation eq. (2.40). Based on $\mathbf{x}$ and $\partial \mathbf{x}/\partial \mathbf{p}$, the cost and constraint functions can be evaluated, as well as their gradients $\partial J/\partial \mathbf{p}$ and $\partial \mathscr{C}/\partial \mathbf{p}$ (as explained in detail in [Felici 2011]).

In [Teplukhina et al. 2017], the plasma elongation is included as an optimization variable, requiring numerical evaluation of $\partial J/\partial \mathbf{p}$ and $\partial \mathscr{C}/\partial \mathbf{p}$ with a computationally expensive finite differencing scheme (due to the difficulty of evaluating gradients of the plasma state with respect to geometric terms). Cost and constraint function evaluations and the respective gradient information are provided to a non-linear programming algorithm implemented in the `fmincon` function of Matlab. For all results presented in this thesis, the sequential quadratic programming (SQP) algorithm [Nocedal and Wright 2006] is used. The SQP algorithm constructs a sequence of quadratic sub-problems, locally approximating the non-linear problem eq. (2.46a)-eq. (2.46e) with a quadratic cost function and linear constraints. By providing gradient information of cost and constraints and applying a quasi-Newton method to approximate the Hessian, these sub-problems are cheaply constructed. The optima of the sub-problems approach the optimum of the original non-linear problem by passing through a set of iterations. After each iteration, a RAPTOR run is performed based on the actuator time evolution corresponding to the updated optimization vector $\mathbf{p}$. Convergence to the optimum is achieved when the necessary conditions for optimality, i.e. the Karush-Kuhn-Tucker (KKT) equations [Nocedal and Wright 2006], are fulfilled.

### 2.5.2   Stationary state optimization problem

In this section we show how the stationary state solver is implemented in a non-linear optimization routine, implemented as part of this thesis, as reported in [Van Mulders et al. 2021b]. The aim is to find the combination of actuator values (parametrized by a vector with optimization variables $\mathbf{p}$) maximizing a measure of performance of the plasma state, while conforming to imposed bounds on the plasma state and technical constraints of the tokamak. The performance of the plasma is captured in a cost function $J$. Examples of optimization goals include minimum auxiliary power $P_{aux}$ and maximum stored thermal energy $W_{th}$, nuclear fusion power $P_{fus}$ or bootstrap current $I_{bs}$. A weighted sum allows for the construction of a composite cost function. Non-linear constraints on the plasma state can for example inhibit the formation of a $q = 1$ surface, or avoid known disruptive limits. Simple linear constraints for the optimization variables can be used to impose limits on actuator values, e.g. limiting the available auxiliary power. The vector of optimization variables can contain lumped variables (e.g. total plasma current, total auxiliary power), as well as a number of coefficients defining a radially distributed profile through a set of basis functions (e.g. the radial distribution of auxiliary heating on a set of basis functions).
Let us first formulate a generic parameter optimization problem for the stationary plasma state, and introduce the solution procedure based on non-linear programming.

**Implementation of the stationary state optimization problem**

Consider a parameter optimization problem with a cost function $J$, which can contain terms depending on the plasma stationary state vector $\mathbf{x_{SS}}$, its time derivative $\dot{\mathbf{x}}_{\mathbf{SS}}$ and the actuator vector $\mathbf{u_{SS}}$ eq. (2.48a). The vector $\mathbf{p}$ contains the optimization variables, parametrizing the ac-

tuator values, while the vector $\mathbf{z}$ contains the unknowns parametrizing the stationary solution (as defined in Section 2.4.3). By defining a matrix $\mathbf{A_{ineq}}$ and a vector $\mathbf{b_{ineq}}$, a set of linear limits on the optimization variables can be imposed eq. (2.48b), for example constraining the total available auxiliary heating power. Furthermore, one can impose a set of non-linear bounds with dependencies on the plasma state, the plasma state derivative and the actuator vector eq. (2.48c). The plasma state dependent constraint functions are formulated as integrals, similar to 2.47. Finally, accordance of the optimal state to the stationary state equation eq. (2.45) is imposed in eq. (2.48d):

$$\min_{\mathbf{p}} \quad J(\dot{\mathbf{x}}_{SS}(\mathbf{z}), \mathbf{x}_{SS}(\mathbf{z}), \mathbf{u}_{SS}(\mathbf{z}, \mathbf{p})) \tag{2.48a}$$

$$\text{subject to} \quad \mathbf{A_{ineq}}\mathbf{p} \leq \mathbf{b_{ineq}} \tag{2.48b}$$

$$\mathscr{C}(\dot{\mathbf{x}}_{SS}(\mathbf{z}), \mathbf{x}_{SS}(\mathbf{z}), \mathbf{u}_{SS}(\mathbf{z}, \mathbf{p})) \leq 0 \tag{2.48c}$$

$$\mathbf{f}(\dot{\mathbf{x}}_{SS}(\mathbf{z}), \mathbf{x}_{SS}(\mathbf{z}), \mathbf{u}_{SS}(\mathbf{z}, \mathbf{p})) = 0 \tag{2.48d}$$

A solution to a constrained, non-linear optimization problem like eq. (2.48a)-eq. (2.48d) can be pursued iteratively, applying a non-linear programming solver, starting from an initial guess for the optimization variable $\mathbf{p_0}$. The following steps are repeated until the KKT conditions for optimality are fulfilled.

- For a given optimization vector $\mathbf{p_i}$, apply the Newton-Raphson solver presented in the previous section to find the stationary solution $\mathbf{z_i}$ of the state equation eq. (2.48d).

- Evaluate $J(\dot{\mathbf{x}}(\mathbf{z_i}), \mathbf{x}(\mathbf{z_i}), \mathbf{u}(\mathbf{z_i}, \mathbf{p_i}))$ and

$$\frac{\partial J}{\partial \mathbf{p}} = \left[ \frac{\partial J}{\partial \dot{\mathbf{x}}}\frac{\partial \dot{\mathbf{x}}}{\partial \mathbf{z}} + \frac{\partial J}{\partial \mathbf{x}}\frac{\partial \mathbf{x}}{\partial \mathbf{z}} + \frac{\partial J}{\partial \mathbf{u}}\frac{\partial \mathbf{u}}{\partial \mathbf{z}} \right]\frac{\partial \mathbf{z}}{\partial \mathbf{p}} + \frac{\partial J}{\partial \mathbf{u}}\frac{\partial \mathbf{u}}{\partial \mathbf{p}} \tag{2.49}$$

and similarly for the non-linear constraints: evaluate $\mathscr{C}(\dot{\mathbf{x}}(\mathbf{z_i}), \mathbf{x}(\mathbf{z_i}), \mathbf{u}(\mathbf{z_i}, \mathbf{p_i}))$ and $\frac{\partial \mathscr{C}}{\partial \mathbf{p}}$. Note that $\partial \mathbf{z}/\partial \mathbf{p}$ can be obtained by extracting the Jacobian $\partial \mathbf{f}/\partial \mathbf{z}$ at the solution point from the Newton-Raphson solver and by evaluating:

$$\frac{\partial \mathbf{z}}{\partial \mathbf{p}} = -\left[ \frac{\partial \mathbf{f}}{\partial \mathbf{z}} \right]^{-1}\frac{\partial \mathbf{f}}{\partial \mathbf{u}}\frac{\partial \mathbf{u}}{\partial \mathbf{p}} \tag{2.50}$$

Equation eq. (2.50) effectively imposes the stationarity constraint, restricting the optimization space gradients to the direction maintaining the evaluation of state equation eq. (2.48d) linearly constant, by imposing $\frac{\partial \mathbf{f}}{\partial \mathbf{p}} = 0$.

- $J$, $\mathscr{C}$, $\frac{\partial J}{\partial \mathbf{p}}$ and $\frac{\partial \mathscr{C}}{\partial \mathbf{p}}$ are provided to the SQP algorithm in `fmincon` function of Matlab.

Since we are solving a non-linear optimization problem, there is no general guarantee of finding a global minimum. Therefore, initiating the optimization routine from different, randomly assigned, initial optimization vectors $\mathbf{p_0}$, confidence can be augmented that the obtained stationary solution is globally optimal. The optimization space gradients required by

the non-linear programming solver are evaluated analytically. This avoids the need for a finite difference approach, which would increase the computational cost by requiring additional stationary state evaluations for each dimension of **p**.

**Toy example: tailoring $q$ to maximize $W_{th}$**

The described routine can be applied to optimize stationary plasma profiles, by tailoring the radial distribution of auxiliary heating $p_{aux}(\rho)$ and externally driven current density $j_{aux}(\rho)$, with the goal of maximizing the thermal energy while keeping $q > 1$. For the present illustrative example, the stationary state solver in the inner iteration loop assumes a standard TCV equilibrium with a plasma current $I_p = 200\,\text{kA}$, and solves for the loop voltage in addition to the $T_e$ and $\psi$ profiles (*option 1* of the solver). The total electron cyclotron power is constrained to $P_{aux} = 3\,\text{MW}$, which is assumed to sustain an H-mode. A linear temperature pedestal is imposed in the region $\rho = [\rho_{ped} = 0.9\ 1]$, with the temperature pedestal as a boundary condition for the core $T_e$ profile solved by RAPTOR. The imposed $n_e$ profile is consistent with H-mode operation, with (a small) $n_{e0} = 10^{19}\,\text{m}^{-3}$.

The goal of the parameter optimization problem presented here is to maximize the thermal energy stored by the electrons, which can be formulated as the minimization of:

$$J = -W_{th} = -\frac{3}{2}\int_V n_e T_e dV \tag{2.51}$$

The radial auxiliary power profile is written as a linear combination of the basis functions $g_i(\rho)$ with $i \in [1, 2, ..., n_g]$, drawn in Figure 2.12 for $n_g = 8$[5]. The power deposited at different radial locations is parametrized by the values in the optimization vector **p** (the basis functions are normalized such that $p_i = 1$ corresponds to an integrated auxiliary heating contribution of $1\,\text{MW}$). For each basis function $g_i(\rho)$, both a contribution with positive and negative current drive efficiency are allowed, respectively encoded in $p_i$ and $p_{n_g+i}$ (pure heating can be obtained by assigning $p_i = p_{n_g+i}$). To summarize, the radial distribution profile of auxiliary heating and current drive is obtained by multiplying the basis functions with the corresponding power amplitudes in **p** (including a current drive efficiency $\eta$ for $j_{aux}$):

$$p_{aux}(\rho) = \sum_{i=1}^{n_g} g_i(\rho)\left[p_i + p_{n_g+i}\right] \tag{2.52}$$

$$j_{aux}(\rho) = \sum_{i=1}^{n_g} g_i(\rho)\eta\left[p_i - p_{n_g+i}\right] \tag{2.53}$$

---

[5]The choice of the number of basis functions results from a trade-off: although more basis functions allows the optimizer to find more optimal solutions (since the solutions accessible on a coarser basis are still achievable, in addition to radial distributions with more refined features), the risk for finding local minima increases. Furthermore, overfitted optima can be obtained, which generalize poorly when applied for slightly perturbed model parameters.
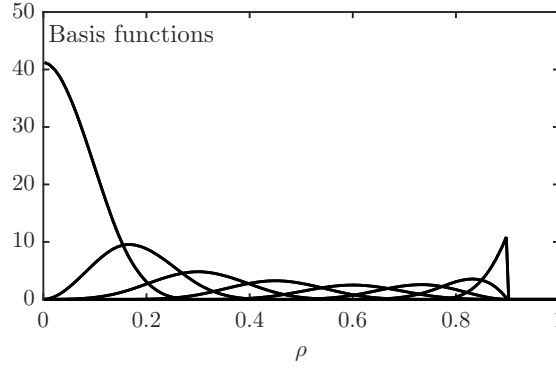
Figure 2.12: **Spline basis functions** This is the set of basis functions (cubic splines on $\rho = [0, \rho_{ped}]$ with $\rho_{ped} = 0.9$) for the construction of the radial distribution of auxiliary heating and current drive density. The basis functions are normalized to ensure for each basis function the correspondence of $p_i = 1$ to an integrated auxiliary heating contribution of 1 MW. *Reproduced from [Van Mulders et al. 2021b].*
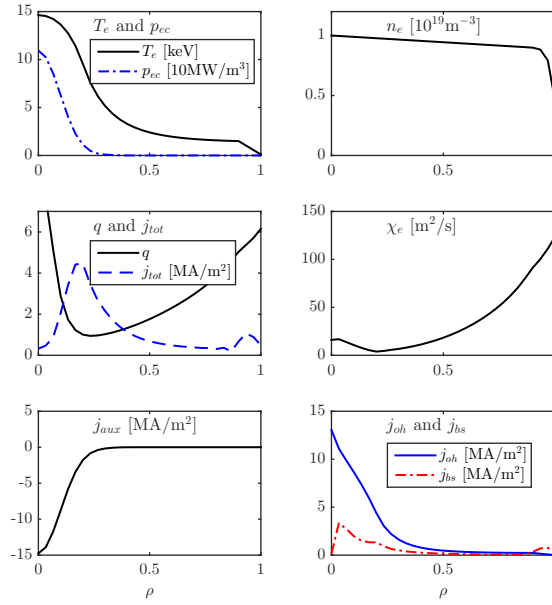


Figure 2.13: **Illustration stationary state optimizer** Radial distribution of electron cyclotron heating and current drive that maximize the stored electron thermal energy for a TCV plasma with fixed total auxiliary power $P_{aux} = 3\,\text{MW}$. The optimizer finds that central counter-ECCD is the optimal choice to maximize $T_e$, yielding a total current density profile with an off-axis peak, creating an internal transport barrier in the $T_e$ profile. *Reproduced from [Van Mulders et al. 2021b].*

The total available power imposes a linear inequality constraint of type eq. (2.48b) on the optimization variables:

$$\sum_{i=1}^{2n_g} p_i \leq P_{aux} \tag{2.54}$$

A non-linear inequality constraint of type eq. (2.48c) on the state allows the algorithm to avoid solutions for which the $q$ profile drops below $q = 1$ (avoiding sawteeth which can seed deleterious NTMs [Gude et al. 1999]). The constraint is formulated as follows:

$$\mathscr{C}_{q>1} = \left[ \int_0^{\rho_e} \max\left(0, \frac{1}{q(\rho)} - 1\right) d\rho \right]^2 - \epsilon \leq 0 \tag{2.55}$$

The obtained optimal plasma state is presented in Figure 2.13. The result is interesting as it demonstrates the ability of the proposed optimization method to exploit non-trivial features of the transport model: driving negative current on-axis, the magnetic shear reaches a large negative value (due to the off-axis peak of the current density), which, through the ad-hoc transport model used [Felici and Sauter 2012], triggers a local drop in the electron heat diffusivity $\chi_e(\rho)$. The total plasma current $I_p = 200\,\text{kA}$ is obtained by driving positive ohmic current (the stationary state solver finds the loop voltage $U_{pl}$ necessary to drive the required ohmic current). The local drop in electron heat diffusivity $\chi_e$ results in a steep gradient for the $T_e$ profile, known as an electron internal transport barrier [Goodman et al. 2005; Zucca et al. 2008]. Note how the bootstrap current driven by both internal and edge transport barriers contributes to the off-axis current density.

## 2.6   Conclusion

In this chapter we have given an overview of the RAPTOR code, complementing and updating the descriptions in [Felici 2011] and [Teplukhina 2018]. Featuring a hierarchy of reduced physics models, ranging from surrogate first-principles-based models to empirical models inspired by scaling laws and experimental observations, the RAPTOR modeling and optimization suite provides an extremely powerful lightweight simulator, with applications in real-time control (state observer [Felici et al. 2011, 2016], kinetic equilibrium reconstruction [Carpanese et al. 2020], model predictive control [Maljaars et al. 2017], iterative learning control [Felici and Oomen 2015; Kudlacek et al. 2021b], non-linear scenario optimization [Felici and Sauter 2012; van Dongen et al. 2014; Teplukhina et al. 2017; Van Mulders et al. 2021b; Mitchell et al. 2022] and full-discharge modeling [Teplukhina et al. 2017; Felici et al. 2018; Maget et al. 2022; Ostuni et al. 2022].

Metrics of the MHD geometry have to be extracted from an equilibrium code, and can vary throughout the simulation time window. The diffusion equations of poloidal flux $\psi(\rho, t)$, temperature $T_{e,i(\rho,t)}$ and/or density $n_{e,i}(\rho, t)$ are evolved in time, capturing various non-linear interactions in the profile dynamics. The flexible finite element discretization scheme and the implicit time stepping scheme allows for a flexible choice of spatial and temporal grids.

A central challenge in the prediction of tokamak profile dynamics is predicting the turbulent

fluxes of temperature and density, or equivalently the evaluation of the diffusivities in the transport equations of heat and particles. In RAPTOR various models are presently available:

- Empirical formulas capturing commonly observed dependencies of plasma confinement on quantities like safety factor $q$ and electron temperature $T_e$, relying on the tuning of a set of model parameters to experimental data.

- QLKNN-hyper-10D, a neural network surrogate [van de Plassche et al. 2020] of the QuaLiKiz code, a quasi-linear gyrokinetic transport model [Bourdelle et al. 2015; Citrin et al. 2017]. The neural network was trained on a dataset of $3 \times 10^8$ QuaLiKiz flux calculations, created by sampling in a hypercube approach over 9 input dimensions, representing local plasma quantities. The model provides first-principles-based turbulent transport estimations over a wide variety of tokamak regimes, since the hypercube spans operating points on both present-day and future devices.

- A gradient-based model, differentiating between a core region with stiff profiles with a logarithmic gradient close to the critical gradient, and a peripheral region where the gradient is set to track a reference trace for the overall confinement and line average density. The confinement reference is set as a scaling facttor with respect to the confinement time predicted by the IPB98(y,2) scaling law [ITER Physics Expert Group on Confinement and Transport and ITER Physics Expert Group on Confinement Modelling and Database and ITER Physics Basis Editors 1999]. Unlike the previous two models, no pedestal top boundary condition is required to simulate L- or H-mode plasmas, allowing for a transport-driven transition between these regimes.

The choice of the modeled transport channels and the adequate transport model for a given application is important, and depends on the availability of experimental data in the same tokamak and scenario to tune and validate model parameters. Furthermore, in the interest of minimizing the computational burden and maximizing the interpretability of the simulation, it is generally desired to keep the simulations as simple as possible, but as complex as required, depending on the relevant dynamics at play. Various applications will be shown in the following chapters.

Various new features in the RAPTOR code have been developed and validated as part of this thesis, including:

- A new solution method allowing to directly obtain the stationary solution of the set of coupled, non-linear diffusion equations, for a selected number of the transport channels $\psi(\rho, t)$, $T_{e,i}(\rho, t)$ and $n_{e,i}(\rho, t)$.

- A framework for fast, automated optimization of the stationary phase of tokamak plasma discharges. Both scalar variables (e.g. heating powers) and radially distributed quantities (e.g. electron cyclotron deposition profile) can be optimized. The stationary state solver and the non-linear programming optimization algorithm profit from the availability

of analytic Jacobians within RAPTOR, yielding swift convergence, even in conjunction with a stiff transport model.

- A new method has been implemented to impose the pedestal region $\rho > \rho_{ped}$, with the boundary condition set at $\rho = \rho_{ped}$. By adjusting the set of finite element basis functions during H-mode, the computational domain for temperature (and density) is effectively limited to $\rho = [0\ \rho_{ped}]$, while poloidal flux diffusion is still solved on the full domain $\rho = [0\ 1]$. A linear gradient is directly imposed on $\rho = [\rho_{ped}\ 1]$, making the simulation more numerically robust. The shape of the pedestal could easily be adjusted to arbitrary shapes, e.g. in order to match experimental edge profile measurements and calculate the consistent amount of pedestal driven bootstrap current.

Furthermore, an impurity radiation model, based on ADAS cooling factor data, which was coupled to RAPTOR to perform WEST ramp-up studies [Maget et al. 2022], has been described. Finally, a pipeline has been set in place to perform inter-discharge full-shot optimizations for ASDEX Upgrade (that can be easily updated to include other tokamaks). This feature will be discussed in Chapters 3 and 6.

# 3 Optimization for fast, reliable access to ASDEX Upgrade advanced scenario

The ramp-up phase of a tokamak brings the low-temperature plasma created after breakdown to the high-$I_p$, high-$\beta$ conditions relevant for fusion reactor studies. Rapid changes in plasma current, stored energy and confinement state, equilibrium geometry and impurity content govern the complex time evolution of the radial profiles of temperature, density and current density (or equivalently, $q$ profile). By simulating key features of the relevant non-linear dynamics, fast transport solvers provide a valuable tool to assess the impact of actuator time traces on the coupled time evolution of these plasma profiles. While the reduced physics models lack the fidelity required to make exact predictions (e.g. due to uncertainty on the pedestal height), the high computational speed make these solvers extremely practical for inter-discharge optimization of actuator trajectories. Obviously, one should only rely on the optimization outcome after carefully assessing whether the reduced models capture the salient physics phenomena and non-linear interactions of the quantities relevant to the optimization problem.

The application of RAPTOR for ramp-up optimization was first proposed in [Felici and Sauter 2012], and applied to optimize access to the hybrid ITER scenario in [van Dongen et al. 2014]. In [Maget et al. 2022], RAPTOR, coupled to the QLKNN-hyper-10D transport model [van de Plassche et al. 2020] and ADAS cooling factor data to evaluate impurity line radiation [ADAS], is used to optimize the ramp-up phase for WEST. By successfully modeling how increased Nitrogen injection can peak the current density and enhance the core temperature, a ramp-up with improved MHD stability and increased margin to tungsten contamination could be proposed. This example illustrates the strength of a modular transport code, where one can select the models required to describe the physics at play.

## 3.1 Early versus late heating

Advanced scenarios aim for an elevated $q$ profile, maximizing the bootstrap current fraction ($f_{bs} = I_{bs}/I_p$, note: $j_{bs} \sim q\nabla p$), to explore the potential of a steady state fusion reactor. Furthermore, these scenarios often achieve improved confinement relative to the IPB98(y,2) scaling law eq. (1.4), further enhancing the bootstrap current fraction. On ASDEX Upgrade (AUG),

an advanced scenario has been developed that applies counter-ECCD near the magnetic axis (where a high current drive efficiency can be achieved), to form an off-axis peak in the total current density. This strategy allows to study an advanced scenario with plasma parameters approaching reactor-relevant conditions [Stober et al. 2020].

During the plasma current ramp-up, the inductive current in the plasma is increased by using the central solenoid to apply a positive loop voltage at the edge of the plasma. The radial variation of the loop voltage profile $U_{pl}(\rho)$ throughout the plasma then provides a driving force for penetration of the ohmic current density. Heating the plasma during the plasma current ramp-up phase allows to reduce the resistivity of the plasma at an early stage, hence slowing down the current diffusion towards the center of the plasma. This *early heating strategy* slows down the tendency of an ohmic plasma to evolve towards a peaked current density profile (in stationary state, a flat loop voltage profile would correspond to a current density profile with a radial dependence self-similar to $T_e^{3/2}$), *freezing* a broad current density profile that corresponds to a more elevated $q$ profile. This approach is of particular interest for advanced scenarios that aim to achieve a stationary, elevated $q$ profile. Once the plasma current reaches the flat-top value, the elevated $q$ profile can be maintained in a stationary state, if the relaxed ohmic current density profile is complemented with off-axis auxiliary current drive sources and a broad bootstrap current density profile. In H-mode plasmas, the bootstrap current driven in the pedestal region provides an important contribution.

On present-day tokamaks, accessing a stationary, elevated $q$ profile early in the discharge allows for a longer time window to study the physics of the advanced scenario, lasting over multiple current diffusion time scales. Studying the stationary phase is important as stationarity is required for a reactor-relevant operating point. Early heating scenarios are of even greater importance for advanced scenarios on future machines like ITER and DEMO, where the current diffusion time scale is much larger due to the bigger size and the higher temperatures of the plasma. A *late heating strategy*, allowing the plasma to evolve to an inductive $q$ profile before auxiliary current drive sources are applied to elevate the $q$ profile, would result in a very long waiting time before the plasma reaches the stationary state conditions envisioned for the burning plasma state, hence compromising the commercial prospects of a fusion reactor based on an advanced scenario.

Disadvantage of the *early heating strategy* are a reduced robustness with respect to the onset of tearing modes, the impact of poorly known initial conditions and the strong sensitivity to the onset timing of heating and fueling actuators. As a consequence, finding the correct timing of the various actuators during ramp-up and the early flat-top phase gives rise to a delicate balancing act. For the JET hybrid scenario, the dependence of discharge stability on small scenario modifications has been reported in [Joffrin et al. 2005] and [Hobirk et al. 2012]. Stationary states with different stationary current density profiles and differing confinement quality can be accessed depending on the ramp-up scenario (even for identical actuator inputs during the stationary state) [Stober et al. 2007]. The different confinement quality is thought to be caused by the presence of NTMs and related differences in the $q$ profile. From the reconstructed $q$ profiles in [Stober et al. 2007], the tearing modes seem to set in as the $q$ profile drops through the corresponding rational surface, with the low local value of the

magnetic shear facilitating the NTM onset. In [Bock et al. 2017], a scenario was developed which includes an ohmic L-mode phase before the high-performance phase, to let the current profile relax and to get rid of the impact of initial conditions. Afterwards, the $q$ profile is modified in a more controllable way, as the dynamics are less sensitive to actuator onset timings when starting from a stationary rather than a transient state. Note that the importance of optimized actuator timings is not limited to scenarios with heating during the ramp-up phase. On DIII-D, the mostly inductive ITER baseline scenario is heated only after the flat-top phase is reached. The onset of a disrupting 2/1 tearing mode has been correlated to a specific feature of the current density profile, namely the formation of a steep well in the $j_{par}$ profile around the $q = 2$ surface [Turco et al. 2018]. The stability of the disruptive 2/1 modes was found to be strongly dependent on the early current diffusion evolution. By manipulating plasma current, heating and density traces, a recipe avoiding the modes could be developed [Luce and Turco 2017].

While the plasma dynamics are highly sensitive to actuator time traces during transient phases, profile simulators allow to evaluate the deterministic impact of actuator modifications. The aim of the model-based scenario development and optimization in the present chapter is to make the counter-ECCD AUG early heating scenario more robust with respect to tearing modes, while reaching the desired, elevated $q$ profile as early as possible in the discharge. Reaching a reactor-relevant operating point in a time-efficient way, this work contributes to the investigation of the feasibility of the advanced scenario tokamak concept. Furthermore, the capability of RAPTOR to predict relatively complex features of the profile dynamics is validated to experimental data, allowing to gain confidence regarding its application for simulation of ITER and DEMO. As will be shown, the use of trajectory optimization helps to achieve the desired $q$ profile evolution, reaching $q_{min} < 1.5$ early in the discharge, while maintaining it above one throughout and with a relatively high magnetic shear near rational surfaces like 3/2 and 2/1.

## 3.2   Workflow for inter-discharge simulations for AUG

The present section discusses the RAPTOR set-up used for pre- and post-shot simulations of AUG discharges, as applied for an extensive set of discharges performed within the advanced scenario program and the ITER baseline program (for the latter, see Chapter 6). For all the AUG simulations presented in this chapter, RAPTOR solves for both electron heat and current density transport, while $T_i$, $n_e$ and $Z_{eff}$ are imposed from experimental measurements. The fact that the ion temperature has a less strong impact on the $q$ profile dynamics compared to the electron temperature justifies the omission of $T_i$ predictions. While $n_e$ and $Z_{eff}$ do have an important impact on the current diffusion evolution, through current drive efficiency, bootstrap current and neoclassical conductivity, shot-to-shot variations are limited, so that predictive evaluation could be avoided for our purposes. A relatively coarse time step of 50ms was found to be sufficient to simulate the salient features of the time evolution of $T_e$ and $q$, allowing to simulate a full AUG shot ($\sim$ 10s) within 2 minutes on a single CPU.

### 3.2.1 Post-discharge simulations

**Equilibrium geometry**

For all discharges discussed in this chapter, the kinetic equilibrium reconstruction code IDE [Fischer et al. 2016] is run. The time-varying equilibrium geometry obtained by IDE is interfaced to the format required by RAPTOR, by running the CHEASE fixed-boundary equilibrium solver [Lütjens et al. 1996], based on EQDSK files of the IDE equilibrium at various times along the ramp-up, flat-top and ramp-down phases of the discharges. The geometric data required by RAPTOR is extracted from the CHEASE output files, as described in [Teplukhina 2018]. The time step between equilibria in RAPTOR is increased from 100ms to 200ms to 1s from the early ramp-up (where the geometry changes rapidly) to the flat-top (where the geometry stays mostly unchanged). As the equilibrium data processing is performed in an automated way, the user can easily increase or decrease the number of IDE equilibria to be loaded and processed. Typically the ramp-up simulation starts at t=0.2s where $I_p$ has a value around 350kA. Starting the simulation early in a relatively cold plasma (with fast current diffusion) reduces the impact of the initial conditions on the plasma state in the simulation.

**Heating and current drive sources**

To evaluate auxiliary current drive, as required for the current diffusion equation evolved within the IDE, the TORBEAM [Poli et al. 2001] and RABBIT [Weiland et al. 2018] codes are run. The time dependent heating and current density deposition profiles for respectively electron cyclotron and neutral beam injection are used as inputs to the RAPTOR simulations:

- The NBI profiles $p_{nb,e}$ and $j_{nb}$ are directly provided as sources for the RAPTOR electron heat and poloidal flux equations.

- A post-shot processing algorithm is run based on the TORBEAM heat deposition profiles for the individual gyrotrons. The workflow is illustrated in Figure 3.1: at each time step and for each gyrotron, a gaussian is fit through the heating deposition profile (black dashed curves on Figure 3.1). From these gaussians one can extract the time traces for deposition radius $\rho_{dep}$ and width $w_{dep}$ that are shown in Figure 3.1. A smoothed $\rho_{dep}(t)$ trace and a time averaged $w_{dep}$ are provided as inputs to the RAPTOR gaussian electron cyclotron module (described in Section 2.3.3), resulting in gaussian heating deposition profiles for the individual gyrotrons. Each gaussian deposits the full gyrotron power $P_{gyro}(t)$ injected in the plasma, assuming full absorption of the microwaves. The current drive deposition profiles are calculated based on formula 2.27 introduced in Section 2.3.3. For all gyrotrons that drive counter-ECCD, the tuning parameter $c_{cd}$ is set to -11. Figure 3.2 shows how this value of $c_{cd}$ allows for a reasonable match of the total driven $I_{ec}$ and the TORBEAM prediction, indicating that the formula successfully captures the main trends of current drive efficiency degradation when depositing further
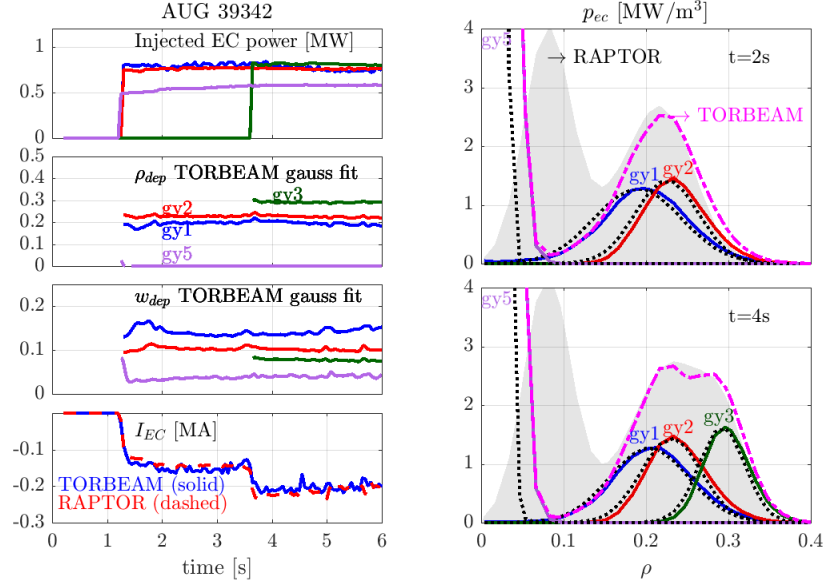
Figure 3.1:  The EC heating deposition profile applied in the RAPTOR simulations is based on the TORBEAM results, as calculated within the IDE framework for the various active gyrotrons. The black dashed curves represent a set of gaussians that are fit through the heating profiles of the individual gyrotrons, at each time step. For each active gyrotron, a time-smoothed $\rho_{dep}$ trace and a time-averaged $w_{dep}$ trace are provided as inputs to the gaussian EC module in RAPTOR. The current drive efficiency is calculated internally in RAPTOR, with a constant normalized current drive efficiency coefficient, with negative value for counter-ECCD experiments. A minimum $\rho_{dep\,min} = 0.08$ is imposed to avoid the formation of a current hole for $\rho \sim 0$.
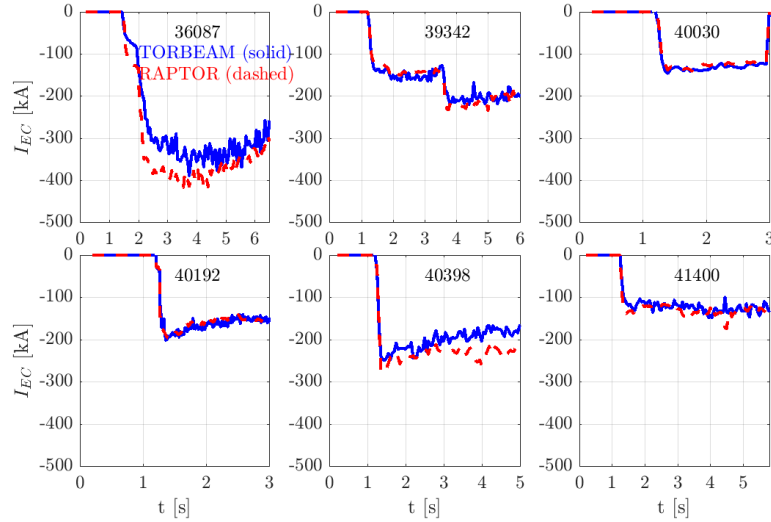


Figure 3.2: For a range of different AUG advanced scenario shots, the total EC driven current calculated by TORBEAM is compared with the current evaluated with the current drive efficiency formula inside the RAPTOR code, with a fixed current drive efficiency parameter $c_{cd} = -11$ (fixed in time and same for all shots).

| $\chi_e$ model | |
|:---:|:---:|
| $c_{ano}$ | 0.15 |
| $c_{neo}$ | 0.50 |
| $c_{T_e}$ | 1.2 |
| $\chi_c$ | 0 |
| $T_{e\,ped}$ model | |
| $\rho_{BC}$ | 0.8 |
| ECCD model | |
| $c_{cd}$ | $-11$ |

Table 3.1: Setting of tuning parameters in the RAPTOR transport and gaussian EC model. Note that these model parameters are kept constant for all simulations performed in this chapter.

off axis.

The strong counter-ECCD near the magnetic axis can lead to the formation of a current hole, reducing the total current density in the center to small or negative values. A zero or negative integrated value $I_p(\rho) = \int j_{par} dA$ causes divergence of $q(\rho)$, which prevents the RAPTOR implicit solver from converging and ends the simulation. This can be avoided by imposing a lower limit on the deposition radius of the innermost EC sources. For the simulation corresponding to Figure 3.1, a lower limit $\rho_{dep} > 0.08$ was imposed on the EC deposition radii. This obviously impacts the inner $q$ profile within the range $\rho = [0\ 0.15]$. However, the impact on the simulated $q$ profile further outward is expected to be small (since $q$ depends mainly on the local $j_{par}(\rho)$ and the integrated value $I_{pl}(\rho)$).

**Electron heat diffusivity**

Experimental observation and theoretical understanding allow to construct simple formulas that contain key dependencies of the electron heat diffusivity on plasma parameters. For example, [Kim et al. 2016] found the ratio of $\chi_e$ to $q^2$ to be constant in the core region for a sequence of TCV L-mode plasmas. For the RAPTOR code, a simple ad-hoc electron heat diffusivity model was proposed in [Felici and Sauter 2012] and extended in [Geelen et al. 2015], as presented in eq. (2.30) in Section 2.3.4.

Table 3.1 summarizes the values of the model parameters applied for the simulations presented in this chapter. Note that no additional transport was added in the core, indicating the experimental $T_e$ profiles are relatively peaked in the center (most simulated and reconstructed $q$ profiles remain above unity, so no sawtooth instabilities are expected). Furthermore, we did not activate the shear-dependence in the anomalous transport term.

**$T_e$ boundary condition**

The boundary condition for the $T_e$ equation is imposed at $\rho = 0.8$. In the region $\rho = [0.8\ 1]$, a linear temperature pedestal is imposed (as described in Section 2.4.2). Note however that the
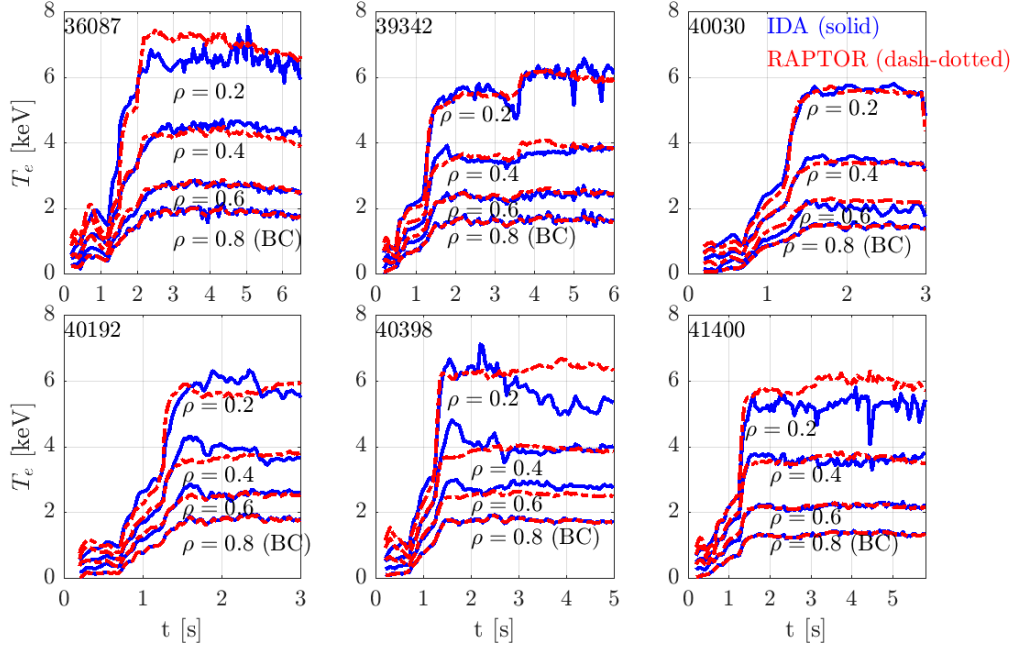
Figure 3.3: RAPTOR predictions of $T_e(\rho, t)$, applying transport formula eq. (2.30) with fixed model parameters (Table 3.1), are compared to the temperature measurements inferred by the IDA for a range of AUG advanced scenario shots. $T_{e\,IDA}(\rho = 0.8, t)$ is used as a boundary condition in the RAPTOR simulations.

current diffusion equation is solved on the full radial domain $\rho = [0\ 1]$, so that the bootstrap current driven by the pedestal is properly taken into account. The time trace for $T_e(\rho = 0.8, t)$ is taken from the IDA inference of $T_e$ measurements [Fischer et al. 2010]. Within the simulation, the H-mode pedestal builds up as a direct consequence of the increase in $T_e$ boundary condition at $\rho = 0.8$; the LH transition timing is not provided explicitly.

Figure 3.3 illustrates the quality of the performance of the RAPTOR $T_e(\rho, t)$ predictions. The simple transport formula provides a robust prediction of core electron temperatures, when $T_e(\rho = 0.8, t)$ is provided as an input.

**Routine full-discharge simulations for model validation**

By routinely performing post-discharge simulations and comparing the modeled $T_e(\rho, t)$ and $q(\rho, t)$ data with the experimentally inferred profile dynamics by IDA and IDE, the applied set of reduced physics models is validated. A full-discharge simulation is presented in Figure 3.4: the main dynamics of $T_e$ and $q$ are successfully captured, from ramp-up to ramp-down. The under-prediction of the outer $q$ profile with respect to the IDE reconstruction, during the flat-top phase requires further investigation.

In Appendix B, a more extensive set of comparisons between RAPTOR post-shot simulations and IDE reconstructions is shown, over a range of discharges from the AUG advanced scenario campaign with counter-ECCD (simulations are shown for most of the discharges mentioned

Figure 3.4:  RAPTOR post-discharge simulation vs IDA/IDE reconstruction for advanced scenario on AUG with counter-ECCD. The $T_e$ evolution is accurately captured, until a 3/2 mode degrades confinement after 3s. Note that RAPTOR under-predicts the outer $q$ profile with respect to the IDE reconstruction, during the flat-top phase.

in this chapter).
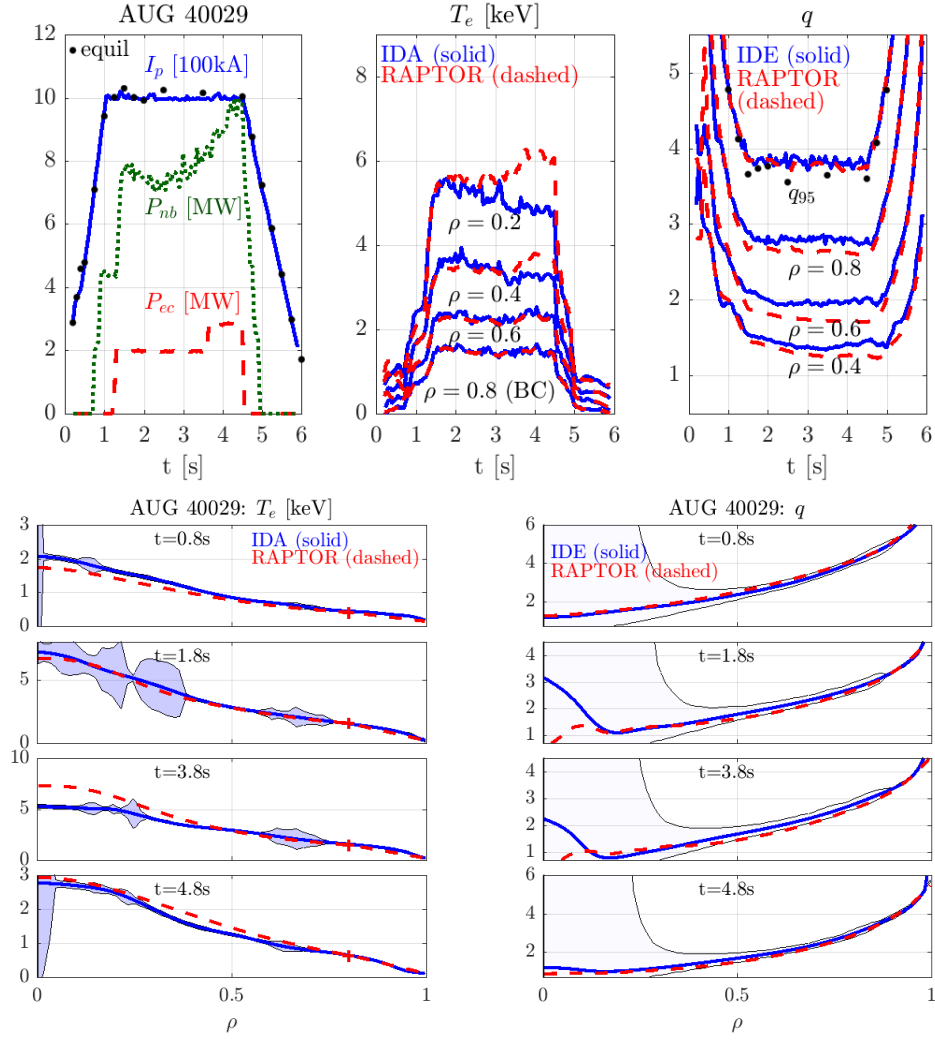
Note that for most IDE $q$ profile estimates presented here, no internal current measurements were available, leading to large error bars. For the $q$ profiles that have an outer and an inner error bar, the outer error bar is calculated without considering the current diffusion constraint (only the magnetics and the pressure constraints determine this error bar).

The successful model validation gives confidence that the proposed set-up can be applied to interpret discharges, guiding further scenario development. In Section 3.2.2, we discuss how predictive, pre-shot simulations can be performed, enabling us to simulate the impact of adjustments to pre-programmed actuator traces and to find optimal actuator traces by solving a dynamic optimization problem.

### 3.2.2 Pre-discharge (predictive) simulations, enabled by data-driven scaling law for pedestal

$T_e$ **boundary condition**

Pre-shot simulations require an estimate of the time evolution of the temperature boundary condition $T_e(\rho = 0.8, t)$, based on variables for which a reasonable estimate is available before the discharge. In the present section, we propose a simple scaling law for the electron pressure at $\rho = 0.8$ ($p_{e\ scaling} \sim n_e T_e(\rho = 0.8)$), derived based on pre-existing data from discharges operating in a similar scenario, with the following inputs:

- plasma current $I_p$,

- total heating power $P_{aux} + P_{oh}$,

- line average density $n_{el}$.

Since the density evolution is manually imposed for the simulations in this chapter, the $T_e(\rho = 0.8, t)$ boundary condition corresponding to the electron pressure predicted by the scaling law can be easily obtained:

$$T_e(\rho = 0.8) = \frac{C}{n_e(\rho = 0.8)} p_{e\ scaling}\left(n_{el}, (P_{oh} + P_{aux}), I_p\right) \tag{3.1}$$

Since the total heating power is one of the input variables to the proposed scaling law, a pre-shot estimate of the ohmic heating power is required. In Appendix A, we present an ad-hoc formula that can be used to evaluate the expected ohmic power, based on the pre-programmed plasma current and auxiliary power. A more consistent approach, using the ohmic power evaluated inside RAPTOR could be implemented. However, the present implementation was found to perform well for the discharges studied in this chapter. Note that even though the ohmic heating power is usually negligible with respect to the total auxiliary heating power, the ohmic contribution can be important in a relatively cold plasma with little auxiliary heating.

Furthermore, early in the ramp-up simulation, before the onset of the auxiliary heating sources, ohmic heating is the only heat source.

To derive a simple scaling law for $n_e T_e(\rho = 0.8)$, we test the assumption of a power law expression with input variables $I_p$, $P_{aux} + P_{oh}$ and $n_{el}$, i.e.

$$n_e T_e(\rho = 0.8) = \alpha_0 n_{el}^{\alpha_n} (P_{aux} + P_{oh})^{\alpha_P} I_p^{\alpha_I} \tag{3.2}$$

eq. (3.2) can be rewritten, taking the natural logarithm on both sides

$$y = \log(n_e T_e(\rho = 0.8)) = \log \alpha_0 + \alpha_n \log n_{el} + \alpha_P \log(P_{aux} + P_{oh}) + \alpha_I \log I_p \tag{3.3}$$

with $y$ the response variable of the scaling law. Linear regression allows to obtain the power law coefficients $\alpha_0$, $\alpha_n$, $\alpha_P$ and $\alpha_I$, based on the available data set $\{n_e T_e(\rho = 0.8); I_p; P_{aux} + P_{oh}; n_{el}\}$. The available data consists of all IDA time points of the shots performed earlier to develop the scenario. No discrimination is made between data points during ramp-up, flat-top and ramp-down phases, nor between H- and L-mode phases (the early heating shots presented in this chapter typically only have a short L-mode time window). Since the RAPTOR simulations and optimizations reported here have been performed in parallel to experimental developments, only shots executed before a given simulation was performed could be used, hence the scaling law evolved with time. After a shot is performed, the power law coefficients are updated, making use of the additional data from the latest shot. The implementation allows the user to select any set of discharges to derive the scaling law. An example is shown in Figure 3.5, where based on a set of 8 AUG advanced scenario discharges, the following scaling law is derived:

$$n_e T_e(\rho = 0.8) = 0.51 n_{el\ 10^{19} m^{-3}}^{0.82} (P_{oh}(I_{p\ MA}, P_{aux\ MW}) + P_{aux\ MW})^{0.53} I_{p\ MA}^{1.71} \tag{3.4}$$

Figures 3.5 and 3.6 illustrate the quality of the scaling law fit. The linear fit of the logarithmic quantities has a $R^2 = 1 - \Sigma(y - y_{scaling})^2 / \Sigma(y - \bar{y})^2 = 0.96$ (with $\bar{y}$ the mean of $y$).

In the left upper plot of Figure 3.5, the IDA data points used to derive the scaling law are shown: the x-axis indicates the IDA measurements of $n_e T_e(\rho = 0.8)$ for all IDA time points; the y-axis indicates the corresponding scaling law prediction. Clustering of the data points along the black solid line gives an indication of the quality of the fit. In the right upper plot of Figure 3.5, the data points of shots from a different scenario (the ITER baseline scenario, with higher/lower pedestal density/temperature) are shown. For high $n_e T_e(\rho = 0.8)$, the bulk of the data points clearly clusters outside of the $\pm 20\%$ bands, indicating that the derived scaling law should only be applied for shots running within a similar parameter regime compared to the scenario for which the scaling law has been derived.

To further illustrate the performance of the fit, the $n_e T_e(\rho = 0.8, t)$ predictions for six of the advanced scenario shots are compared to the IDA time traces in Figure 3.6. Note that even without discriminating H- and L-mode data points, the full time evolution during the ramp-up phase is well captured, encouraging further application of the scaling law approach.
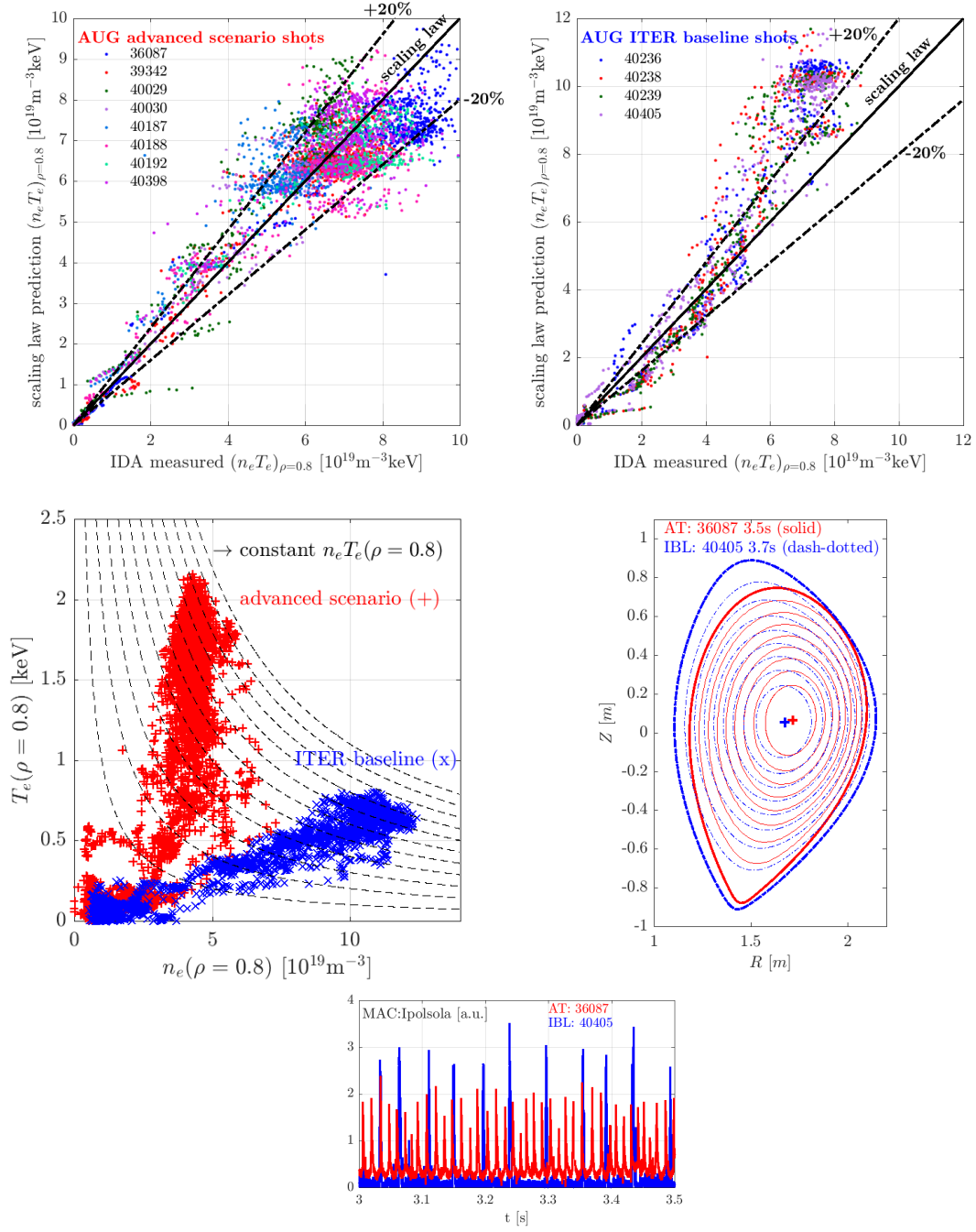
Figure 3.5: A scaling law for $n_e T_e (\rho = 0.8)$ is presented, with input variables $I_p$, $P_{aux} + P_{oh}$ and $n_{el}$, based on IDA data available for 8 AUG advanced scenario shots. The upper left figure shows the data of the advanced scenario shots based on which the scaling law was derived: for the different data points, the scaling law prediction is shown on the y-axis, versus the IDA measurement on the x-axis. The power law exponents are scenario-dependent: when the scaling law is applied for a different regime, namely a set of AUG ITER baseline shots with higher/lower pedestal density/temperature, the IDA points no longer cluster within the scaling law ±20% bands.
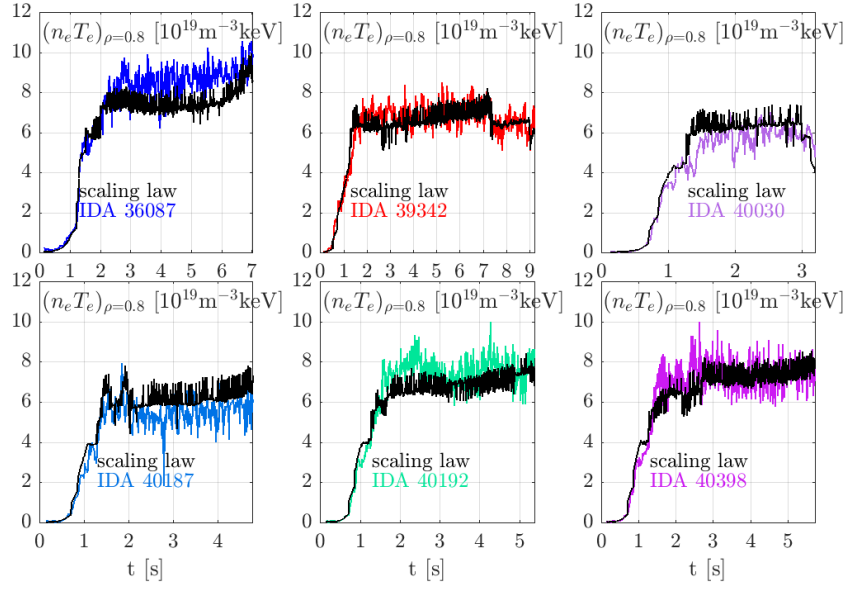
Figure 3.6: The scaling law presented in Figure 3.5 is applied to a set of 6 AUG advanced scenario discharges: based on the input variables $I_p$, $P_{aux} + P_{oh}$ and $n_{el}$, a prediction of the $n_e T_e (\rho = 0.8)$ trace is provided. To illustrate the performance we compare the scaling law prediction (black) to the IDA data (color).

**Comparison pre- and post-discharge simulation**

Predictive pre-shot simulation and optimization rely on the fact that distinct features can be reliably predicted. For the purposes of this chapter, the time evolution of the $q$ profile will be the main focus of our interest. In Figure 3.7, pre- and post-shot simulations are compared, for an advanced scenario shot (40398) executed on AUG with counter-ECCD. For both the evolution of $T_e(\rho, t)$ and $q(\rho, t)$, pre- and post-discharge simulations are in close agreement. For the predictive simulation, the $T_e$ boundary condition is imposed based on the scaling law approach introduced earlier in this section, deriving scaling law exponents based on data available from previous discharges. For the density evolution, the IDA data available from an earlier discharge (39342) is imposed, accounting for a later NBI and fueling onset timing by delaying the rising edge of the $n_e(\rho, t)$ time evolution. Note however that there is some discrepancy between the $q$ profile predicted by RAPTOR and the $q$ profile of the IDE reconstruction (blue). The impact of a different initial state vanishes around 1s, but later on the RAPTOR outer $q$ profile is slightly lower compared to the IDE reconstruction. This discrepancy is similar to the $q$ profile mismatch shown in Figure 3.4 and requires further investigation. Note however that it does not modify significantly the dependence of the core $q$ profile on actuators, which is the focus of the following sections.
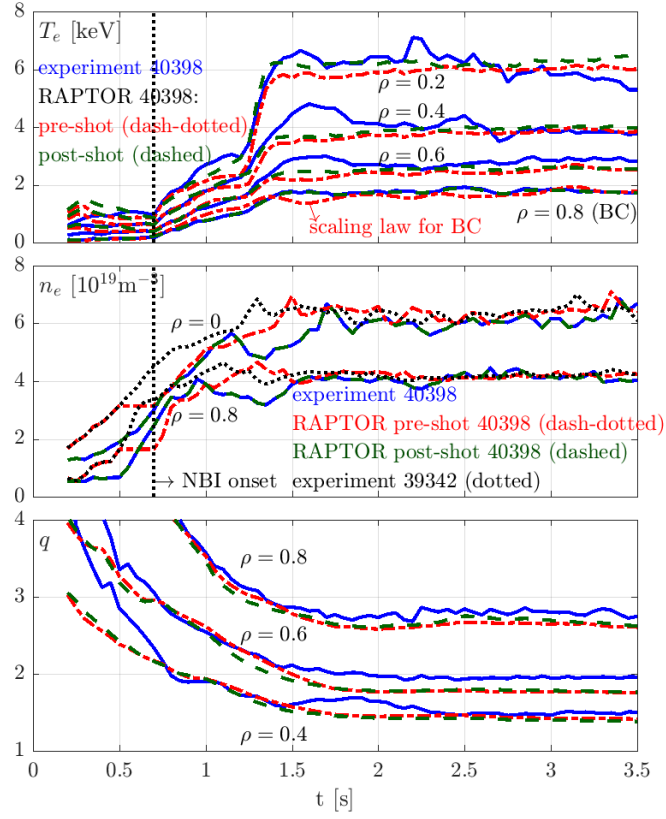
Figure 3.7: Pre- and post-shot RAPTOR simulations of discharge 40398 are compared. The blue traces show the experimental reconstruction from IDA/IDE. In red, the pre-shot simulation is presented: the $T_e(\rho = 0.8)$ boundary condition is set with a scaling law derived based on earlier shots; the density is adapted from the IDA reconstruction of an earlier shot, 39342, taking into account a delay due to the later onset of NBI. The post-shot simulation, utilizing the IDA data of 40398 for $T_e(\rho = 0.8, t)$ and $n_e(\rho, t)$, is shown in green.

## 3.3 Model-based scenario development for fast and reliable access to advanced scenario

In the present section we describe how RAPTOR simulations and optimizations have been leveraged to improve our understanding of the dynamics and performance of the AUG 1 MA counter-ECCD advanced scenario [Stober et al. 2020]. In Section 3.3.1 we discuss the characteristics of the desired stationary operating point. We then show how inter-discharge simulations and optimizations in RAPTOR have allowed *to develop a reliable and reproducible early heating scenario, reaching a stationary state early in the flat-top phase*. As discussed in Section 3.1, early heating scenarios are very sensitive to the timing of actuators during the ramp-up phase. Section 3.3.2 presents how post-discharge simulations led to a hypothesis on the origin of a 3/2 tearing mode observed in the previous early heating attempt. Based on this hypothesis, characteristics are defined, constraining the time evolution of a stable approach strategy towards the desired stationary operating point. Predictive, pre-shot simulations have been used to design a ramp-up strategy avoiding the onset of the deleterious 3/2 mode, as discussed in Section 3.3.3. We show how this strategy has been successfully tested in experiment.

### 3.3.1 Stationary operating point: 1 MA counter-ECCD advanced scenario

Leveraging the large current drive efficiency near the plasma center, near-axis counter-ECCD allows to obtain an elevated $q$ profile in a regime approaching dimensionless parameters close to what is envisioned for DEMO (36087, $I_p = 1$ MA: $\beta_N \sim 2.6$, $H_{98y,2} \sim 1.15$, $q_{95} \sim 3.9$). Pursuing reactor-relevant operating regimes allows to quantitatively validate the available theoretical models, increasing confidence for their application on future machines, while experimentally determining the operational limits, e.g. $\beta_N$ limits for the onset of (resistive) MHD modes. To match the total imposed plasma current $I_p$, in the presence of a large, negative EC current drive contribution, the ohmic current density is raised over the entire plasma radius. As the EC current density is centered at radii $\rho < \sim 0.3$, an off-axis peak in the total parallel current density results, consistent with the desired elevated $q$ profile [Stober et al. 2020]. While a counter-ECCD scenario is interesting to pursue a reactor-relevant advanced scenario operating regime on present-day machines, the large negative auxiliary current is at odds with the aim of approaching non-inductive conditions. As a consequence, the elevated $q$ profile needs to be sustained in a different way in a fusion reactor. We discuss in Chapter 4 how ITER can achieve a scenario with $q > 1$ by applying off-axis co-ECCD.

Let us list some of the properties that make this scenario attractive for a fusion reactor, and formulate some open physics questions that the AUG advanced scenario program aims to answer:

- Maintaining $q > 1$, sawtooth instabilities can be avoided. The absence of sawtooth seed islands allows to raise $\beta_N$ into the regime where NTMs are metastable [Sauter et al. 2002c,b]. In [Bock et al. 2017, 2018], an upper limit has been found $\beta_N \sim 2.7$, above which ideal 2/1 modes are triggered. Note that low magnetic shear at rational surfaces

can destabilize ideal MHD infernal modes, as investigated for TCV in [Martynov 2005]. Furthermore, low magnetic shear at rational surfaces can increase the classical tearing mode stability parameter $\Delta'$, thus making the current density profile more prone to the onset of NTMs, as described in [La Haye et al. 2000] for DIII-D $q_0 > 1$ scenarios. Similarly, [Stober et al. 2007] observed the onset of NTMs when $q_{min}$ drops through the corresponding rational surface, for AUG early heating scenarios. Even in the absence of sawteeth, so-called triggerless NTMs can originate [Reimerdes et al. 2002], while ELM crashes can provide an alternative seed mechanism [La Haye et al. 1997], especially for 2/1 NTMs, as the $q = 2$ is in close proximity to the plasma edge during operation at high plasma current. The proximity to the edge furthermore increases the likelihood for mode locking and subsequent disruption [Hender et al. 2007].

- An elevated $q$ profile allows to increase $\beta_{pol}$, maximizing the bootstrap fraction ($f_{bs} = \frac{I_{bs}}{I_p} \sim \beta_{pol} \sim \beta_N q/\epsilon$, with inverse aspect ratio $\epsilon$).

- A high pedestal pressure can be obtained (a comparison for the electron pedestal pressure to the AUG ITER baseline scenario is shown in Figure 3.5), as advanced scenarios operate at high $\beta_{pol}$, increasing the critical threshold of peeling-ballooning modes through an increased Shafranov shift [Garcia et al. 2015].

- In [Silvagni et al. 2023], the impact of the divertor neutral density $n_{0,div}$ on global confinement quality has been identified, highlighting the importance of edge and scrape-off layer physics. Data analysis and pedestal stability modeling indicate that an increased $n_{0,div}$ causes an outward shift of the location of the maximum pressure gradient in the pedestal, where the maximum pressure coincides with a larger value of the safety factor $q$. This eventually leads to a larger destablizing drive for ballooning modes and a reduced pedestal top value (while increased $n_{0,div}$ is correlated with a measured increase of $n_{e,ped}$, a stronger reduction of $T_{e,ped}$ and $T_{i,ped}$ is incurred [Silvagni et al. 2023]). To obtain good and reproducible performance for AUG advanced scenario discharges, the neutral flux density (measured by ionization gauge [Scarabosio et al. 2009]) is feedback controlled, using deuterium fueling as actuator [Bock et al. 2021].

- A central physics aim of the AUG advanced scenario program is the identification of drivers for enhanced ion transport, studying the respective impact of $q$ profile, $\mathbf{E} \times \mathbf{B}$-shear, ion heating and $\beta_{pol}$ [Stober et al. 2020; Reisner et al. 2020]. It is well known that counter-ECCD at low density can lead to the formation of an ITB in the electron heat channel (e-ITB) [Bottino et al. 2006]. By operating at a high plasma current of $I_p = 1\,\text{MA}$, the present scenario reaches a higher density and a stronger coupling between ion and electron temperatures compared to advanced scenarios at lower $I_p$ [Stober et al. 2020], avoiding the formation of e-ITBs and the central accumulation of heavy ions. Note that the simple transport formula eq. (2.30) is successfully applied over a wide range of discharges, as shown in Figure 3.3, while no shear dependence of confinement is

needed to match the experimental $T_e$ profiles (a shear-dependence would be expected in the presence of e-ITBs).

The need for further optimization of this rather challenging scenario has been discussed in [Stober et al. 2020]. The 1 MA discharge discussed in this paper (shot 36087) applies external heating only after the ohmic current density reaches a relaxed state at full current. Now we will discuss a first attempt to reach this scenario with an early heating strategy.

### 3.3.2 Understanding NTM-triggering in attempt for early heating scenario

While the plasma dynamics are highly sensitive to actuator time traces during transient phases, profile simulators allow to evaluate the deterministic impact of actuator modifications. The top panel of Figure 3.8 presents RAPTOR post-shot simulations of the AUG discharges 36087 (late heating) and 39342 (early heating attempt), providing insight in the trade-off between late and early heating. The bottom panel of Figure 3.8 shows the experimental time traces for $\beta_{pol}$ and $H_{98y,2}$. Note that during the flat-top phase, these discharges control the value of $\beta_{pol}$ to a pre-programmed time trace, by modulation of neutral beam power injection.

- For the *late heating* discharge 36087, the $q$ profile descends towards $q_{min} \sim 1$, before slowly rising towards the desired elevated state. According to the RAPTOR simulation $q_{min} \sim 1$ around 2s, and the elevated $q_{min}$ is achieved around 3.5s.

- By applying the neutral beam heating earlier, during the plasma current ramp-up, the *early heating* discharge manages to achieve a $q$ profile decreasing monotonically in time towards the final state, reaching the desired, elevated $q$ profile earlier in time. The early heating approach is however more prone to the onset of tearing modes. As visible in the magnetic spectrum for shot 39342 in Figure 3.8, a 3/2 mode is triggered around 1.7s. After the onset time of the tearing mode, confinement degrades: the central electron temperature, measured by the ECE diagnostic, drops from $T_e \sim 8.0$ keV to $T_e \sim 5.5$ keV and the experimental $H_{98y,2}$ factor reduces from $\sim 1.1$ to $\sim 1.0$ (see Figure 3.8). As the onset of tearing modes during the early flat-top phase had been anticipated, the plasma is maintained at $\beta_{pol} \sim 1.2$ for several seconds, allowing the tearing mode to disappear before raising $\beta_{pol}$ (and $\beta_N$) further at around 3.5s. The $\beta_{pol}$ ramp leads to a confinement increase in the final phase of the discharge, with $H_{98y,2} \sim 1.15$.
  The simulation hints that a 3/2 NTM is triggered due to the formation of an off-axis $q_{min} \sim 1.5$ at large radius ($\rho \sim 0.4$), roughly 1s after the flat-top plasma current has been reached. As auxiliary heating and current drive start shaping the $q$ profile before the profile has decreased and equilibrated, an off-axis minimum is created with $q_{min} > 1.5$. The monotonic decrease of the $q$ profile continues during the flat-top phase (while the plasma has already a relatively high $\beta_N \sim 2.1$) and brings $q_{min}$ towards the rational value $q = 3/2$. Low magnetic shear around the rational surface could explain the formation of a 3/2 NTM, similar to the observations in [La Haye et al. 2000] and [Stober et al. 2007].
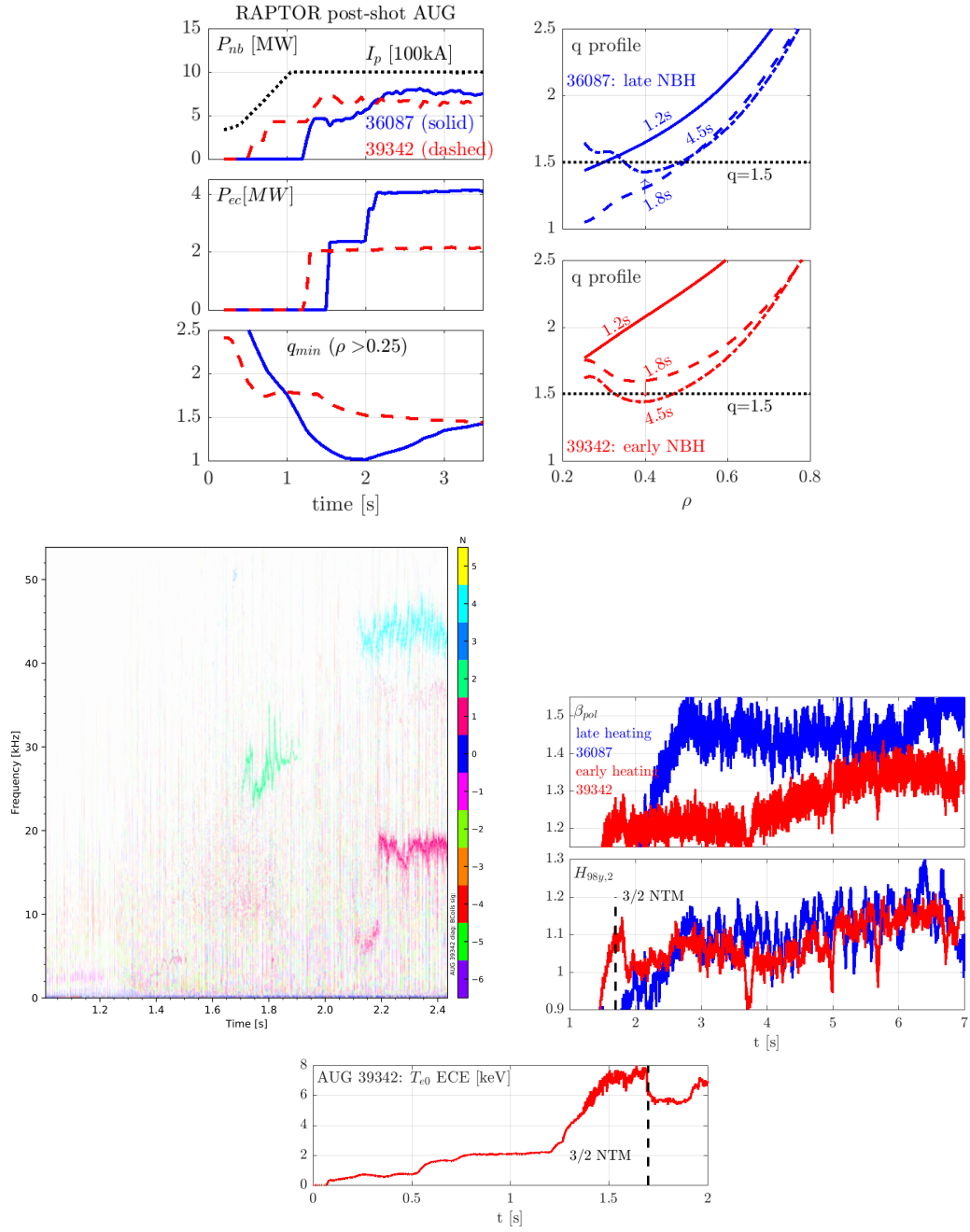
Figure 3.8: Comparison of late heating discharge 36087 (blue) and early heating discharge 39342 (red). (a) RAPTOR post-shot simulation; (b) magnetic spectrogram, showing 3/2 NTM triggered at 1.7s; (c) experimental time traces for $\beta_{pol}$ and $H_{98y,2}$; (d) $T_{e0}$ trace ECE.

### 3.3.3   Predict NBI onset timing to avoid deleterious 3/2 mode

**Aim**

Based on the discussion in the previous section, we formulate a hypothesis for the cause of
the onset of the tearing mode in the early heating attempt (39342):
*having a minimum in the q profile drop through the rational surface q = 3/2 at relatively
large radius ($\rho > 0.2$), with $\beta_N > 2$ is undesirable, as it might cause the onset of a confinement-
degrading NTM.*
Predictive modeling allows to assess the impact of different actuators on the resulting $q$ profile
evolution. In this case, we study the impact of delaying the onset timing of the NBI sources on
the $q$ profile evolution. The rationale for this choice is as follows:
*delaying the NBI injection extends the period during which the plasma is maintained at rela-
tively low temperature, in L-mode, allowing the q profile to decrease more rapidly in time.*
The right delay in NBI heating could hence allow for the formation of the off-axis $q_{min}$ at a
timing when locally the $q$ profile is already below $q = 1.5$. When aiming for a final, stationary
$q_{min}$ below $q = 1.5$, this then avoids an off-axis minimum of the $q$ profile dropping through
the $q = 3/2$ surface. As the $q$ profile dynamics are extremely sensitive to the timing of heating
during the ramp-up phase, predictive simulations are helpful to make a quantitative estimate
of the change in the $q$ profile dynamics.

**Simulation**

Predictive RAPTOR simulations are run, delaying the onset timing of the NBI sources that
are activated during the ramp-up.  After attempting simulations with various time delays,
$\Delta t = 200$ms is selected.  Note that the outage of one of the two current drive NBI sources,
applied during the flat-top phase of the existing scenario, required the replacement of this
source by an alternative NBI source. Predictive simulations in ASTRA [Fable et al. 2013, 2022]
and RAPTOR, performed to assess the feasibility of the replacement of the current drive source,
have been presented in [Schramm et al. 2022] and are shown in Appendix C.
Let us now analyse the predictive RAPTOR simulation implementing the $\Delta t = 200$ms delay
of the NBI heating during the ramp-up phase, shown in red on Figure 3.9.  The time traces
for $T_i(\rho, t)$, $n_e(\rho, t)$ and boundary condition $T_e(\rho = 0.8, t)$, are constructed based on measure-
ments from the previous attempt to establish an early heating scenario (39342). Starting from
discharge 39342, the traces are kept constant between 0.5s and 0.7s, reflecting the delayed
impact of the NBI onset. After 1.27s, when $\beta_{pol}$ control is initiated, the original traces are used
again, without shift in time.
At 1.2s, the $q$ profile has decreased further compared to the previous early heating attempt, as
anticipated due to the longer L-mode phase. The $q$ profile drops through $q = 1.5$ before $\beta_{pol}$
is raised and before auxiliary heating and current drive leads to the formation of an off-axis
$q_{min}$. Furthermore, $q_{min} = 1.5$ occurs at smaller radius. If an NTM is triggered at this earlier
time and lower $\beta_{pol}$ value, the impact on confinement should hence be smaller [Chang and
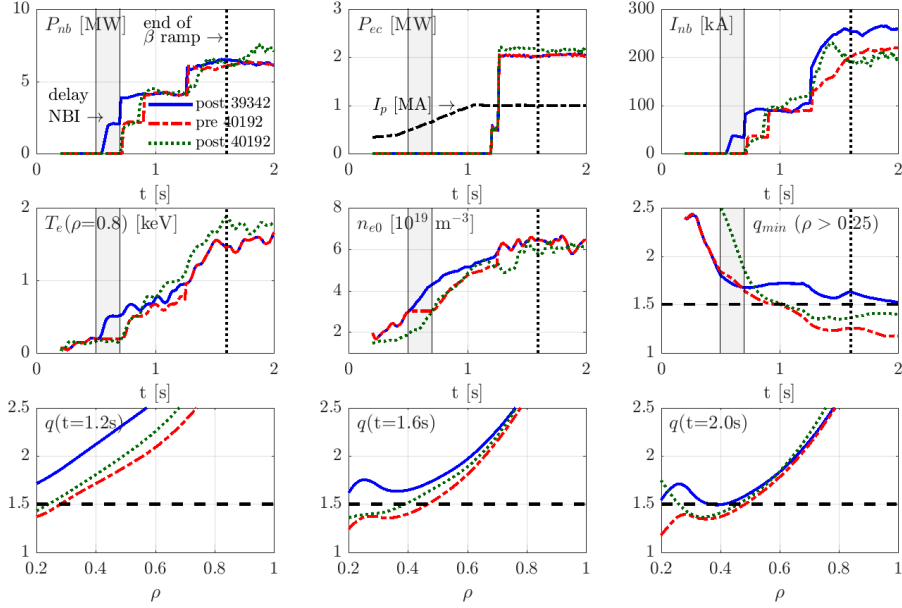
Figure 3.9: These time traces and profiles summarize salient features of three RAPTOR simulations: (1) a post-shot simulation of the early heating attempt 39342, with $t_{nb} = 0.5$s; (2) a predictive simulation assessing the impact of an NBI onset delay of 200ms; (3) a post-shot simulation of a discharge implementing the NBI delay proposed by RAPTOR (40192).

Callen 1990]. At later times, non-zero magnetic shear is maintained at $q = 1.5$.

**Experiment**

The proposed NBI delay has been experimentally tested. In the magnetic spectra of discharges 40029 and 40030, shown in Figure B.5 and B.6 of Appendix B, no n=2 signature is visible during the early flat-top phase. For later shots, a n=2 mode reappears in the spectrogram, usually appearing around 0.8-1.1s (40187: n=2 around 0.8s in Figure B.7; 40188: n=2 around 1.0s in Figure B.8; 40192: n=2 around 1.1s in Figure B.9; 40398: n=2 around 1.1s in Figure B.10; 40825: n=2 around 1.1s in Figure B.11). However, as the mode is formed at a smaller radius and at an earlier time, the impact of the mode is reduced. No clear impact of these early 3/2 modes on the central electron temperature is visible in these experiments. While a non-zero shear is maintained at $q = 1.5$ during the early flat-top phase, the n=2 activity disappears, usually around 1.8s. Excellent confinement can be achieved, even while the early 3/2 mode is present. In discharge 40188, $H_{98y,2} \sim 1.15$ as $\beta_{pol}$ control overshoots with $\beta_{pol} \sim 1.35$ around 1.6s (reducing to $\beta_{pol} \sim 1.25$ afterwards, with confinement degrading as the steep $\nabla T_i$ around $\rho \sim 0.55$ relaxes; confinement recovers during the late $\beta_{pol}$ ramp after 3s[1]). For further details on the achieved parameters in the discharges discussed here we refer the reader to Table B.1, Figure B.2 (time traces $H_{98y,2}$, $\beta_{pol}$ and $\beta_N$) and Figure B.1 (time traces $T_i$ at various radii).

---

[1]Note: $T_i > T_e$ over a wide radial extent, for most of the flat-top phase.

In the absence of the deleterious NTM, the $\beta_{pol}$ reference is raised during the early flat-top phase, to $\beta_{pol} \sim 1.35 - 1.40$ for discharges 40192 and 40398. Discharge 40192 features excellent confinement ($H_{98y,2} \sim 1.10$) and high ion temperatures ($T_{i0} \sim 8\,\text{keV}$), until a 3/2 NTMs abruptly reduces core electron and ion temperatures around 3.1s (likely triggered by a growing n=3 mode, see spectrogram Figure B.9). The mode disappears at 4s and reappears at 4.8s. The continued sporadic occurrence of (short) time windows with 3/2 modes during the later flat-top phase indicates that the scenario continues to be metastable regarding NTMs. Discharge 40398 reaches similar core $T_i$ and $T_e$ values, with a 3/2 mode appearing around 3.8s.

Finally, it is encouraging to note that the post-shot simulation of discharge 40192 (green in Figure 3.9) can recover quite closely the pre-shot predicted $q$ profile evolution (in red). Note that the aim formulated at the beginning of this section is rather precise, requiring subsequently: (1) $q_{min}$ drops through $q = 1.5$ at $\rho < 0.2$ during the low $\beta_{pol}$ phase; (2) off-axis $q_{min}$ is formed by auxiliary heating and current drive, while $q_{min} < 1.5$ remains satisfied, maintaining non-zero shear at the rational 3/2 surface. As a result, we gain confidence that RAPTOR properly captures temporal and spatial evolution of the $q$ profile, before the discharge is launched.

## 3.4  Model-based optimization of stationary, elevated $q_{min}$ scenarios

**Aim**

After improving the robustness of early flat-top phase against the onset of tearing modes, the RAPTOR code is used to optimize the ECCD deposition profile, proposing the number of gyrotrons and the deposition radii to be applied in the experiment. A distinctive feature of the RAPTOR code is the availability of automated optimization routines, as introduced in [Felici and Sauter 2012] and discussed in Section 2.5.1. A fast run time and analytical gradients make a full time dependent non-linear optimization problem between shots computationally tractable. For further development of the 1MA counter-ECCD scenario, the optimizer is used to assess the following questions:

1. For a given amount of total EC power, what is the maximum $q_{min}$ that can be maintained stable?

2. What is the optimal EC deposition profile, allowing to reach the final elevated $q$ profile as early as possible in the discharge?

The remainder of this chapter is organized as follows. The optimization problem is formulated mathematically in Section 3.4.1. In Section 3.4.2 and Section 3.4.3, optimization of the EC deposition radii is discussed, aiming for relaxation of the $q$ profile immediately after the flat-top phase has been reached, respectively with $1.35 < q_{min} < 1.5$ (applying the strategy developed in Section 3.3.3 to avoid the 3/2 mode) and $q_{min} > 1.5$ (attempting to avoid the creation of a $q = 1.5$ surface).

### 3.4.1 Formulation of the optimization problem

For the optimization problems presented below, the cost function is a measure for the stationarity of the plasma:

$$J_{U_{pl}} = \int_{t_1}^{t_2} \int_0^{\rho_e} \left( \frac{\partial U_{pl}}{\partial \rho} \right)^2 d\rho\, dt \tag{3.5}$$

Minimizing the radially integrated squared loop voltage gradient, integrated over a time window, we minimize the driving force for current diffusion, as explained in Section 2.3.1, maximizing the stationarity of the plasma state.

Two state contraints have been used, imposing mimimum values of the safety factor $q_{min}$ and the magnetic shear $s_{min}$ for the final state in the simulation $t_f$. The mathematical formulation of these constraints as integrals has been introduced in [Felici and Sauter 2012].

$$\mathcal{C}_{q>q_{min}} = \left[ \int_0^{\rho_e} W_{q_{min}} max\left(0, \frac{1}{q(\rho, t = t_f)} - \frac{1}{q_{min}} \right) d\rho \right]^2 - \epsilon \le 0 \tag{3.6}$$

$$\mathcal{C}_{s>s_{min}} = \left[ \int_0^{\rho_e} W_{s_{min}} max\left(0, s_{min} - s(\rho, t = t_f) \right) d\rho \right]^2 - \epsilon \le 0 \tag{3.7}$$

With these cost and constraint functions, the optimal control problem can be defined, as explained in more detail in [Felici and Sauter 2012].

$$\min_{\mathbf{p}} \quad J_{U_{pl}}(\dot{x}(t)) \quad \forall\, t \in [t_1, t_2] \text{ (cost)} \tag{3.8a}$$

$$\text{subject to } f(\dot{x}(t), x(t), u(t)) = 0 \quad \forall\, t \in [t_0, t_f] \text{ (state)} \tag{3.8b}$$

$$u(t) = P(t)\mathbf{p} \text{ (actuator parametrization)} \tag{3.8c}$$

$$A_{ineq}\mathbf{p} \le b_{ineq} \text{ (actuator limits)} \tag{3.8d}$$

$$\mathcal{C}_{q>q_{min}} \le 0 \text{ and } \mathcal{C}_{s>s_{min}} \le 0 \text{ (state constraints)} \tag{3.8e}$$

This optimal control problem can be solved by application of the sequential quadratic programming (SQP) algorithm, as discussed in Section 2.5.1.

### 3.4.2 Optimization for early stationary $q$ profile with $q_{min} < 1.5$

**Simulation**

Pre-shot discharge optimization can only use data available before the discharge. In the case presented here, the following simulation set-up is used.

- Density $n_e(\rho, t)$, ion temperature $T_i(\rho, t)$ and neutral beam deposition profiles $p_{nbe}(\rho, t)$, $p_{nbi}(\rho, t)$, $j_{nb}(\rho, t)$ are taken from the post-shot simulation of the earlier discharge 39342, including a 200ms delay to account for the impact of the delayed NBI (as discussed in Section 3.3.3).

- The pedestal temperature $T_e(\rho = 0.8)$ is calculated with a scaling law, as discussed in

Section 3.2.2. The scaling law is based on the data from the set of discharges performed before the discharge that is being optimized.

- A fixed number of EC heating and current drive sources are used, each providing counter-ECCD, delivering a total power $P_{ec}$. The total EC power trace $P_{ec}(t)$ is not updated during the optimization iterations. The optimizer adjusts the EC deposition profile for a given total EC power. Various optimizations are run, with different numbers of gyrotrons activated (corresponding to different amounts of total power $P_{ec}$). The EC sources start delivering power simultaneously in the early flat-top, around 1.2s, right before $\beta_{pol}$ control by NBI modulation is activated. It is found that the constraints in the present section can be satisfied by four active EC sources, depositing a total power around $P_{ec} = 2.8\,\text{MW}$.

  The radii of two EC sources are kept fixed at $\rho_{dep} = 0.08$, to force some EC heating close to the magnetic axis, avoiding tungsten accumulation [Neu et al. 2002]. Deposition inside $\rho_{dep} < 0.08$ can lead to a current hole (explained in Section 3.2), with negative net on-axis current, which can not be properly treated by the RAPTOR transport solver. The radii of the two other EC sources are used as optimization variables $\mathbf{p} = [\rho_{dep\,1}\,\rho_{dep\,2}]^T$: varying the off-axis distribution of EC current density, the optimizer can tailor the $q$ profile. Both $\rho_{dep\,1}$ and $\rho_{dep\,2}$ are constant in time.

The present optimization attempts to predict whether an early stationary state with an elevated $q$ profile with $1.35 < q_{min} < 1.5$ can be maintained. By imposing $q_{min} = 1.35$ for constraint eq. (3.6) and $s_{min} = 0$ for constraint eq. (3.7), we aim for a $q$ profile at 3.5s that is elevated, but has non-zero shear through the $q = 3/2$ surface. The weight functions $W_{q_{min}}$ and $W_{s_{min}}$ are used to activate the constraint over $\rho = [0.1\ 1]$ and $\rho = [0.25\ 1]$ respectively. The second constraint enforces the desired $q$ profile to increase monotonically from the minimum outward, avoiding an oscillatory behaviour where a local extremum can potentially cause zero magnetic shear at the rational surface $q = 3/2$. Note that $q < 1.5$ is not explicitly enforced. However, for the amount of EC power applied in this section, no stationary solution with $q_{min} > 1.5$ has been found.

The cost function eq. (3.5) integrates a measure of stationarity over the time window 1.5s to 3.5s. By running an optimization that captures the $q$ profile dynamics over the full ramp-up and early flat-top phase, while imposing a time integrated cost function for stationarity, we aim to achieve the final $q$ profile as early as possible. Before 1.5s, the delayed NBI recipe developed in Section 3.3.3 allows for a reliable access into the high $\beta_{pol}$ phase. The present optimization makes sure that the final state is consistent with the stability constraints to avoid tearing modes (non-zero shear through $q = 1.5$) and the goal of an elevated $q$ profile ($q_{min} > 1.35$), while reaching this state as early as possible once the current ramp is completed and the reference high $\beta_{pol}$ value is reached (around 1.5s).

Figure 3.10 presents the initial condition provided to the optimizer in blue ($\mathbf{p} = [0.4\ 0.4]^T$), while the obtained optimum is shown in red ($\mathbf{p} = [0.22\ 0.30]^T$). The $q$ profile at 3.5s indeed satisfies the constraints, while the $q_{min}$ value is maintained within $q = [1.35\ 1.45]$ after 1.5s. The simulation also indicates that a $q$ profile close to the final state is achieved immediately
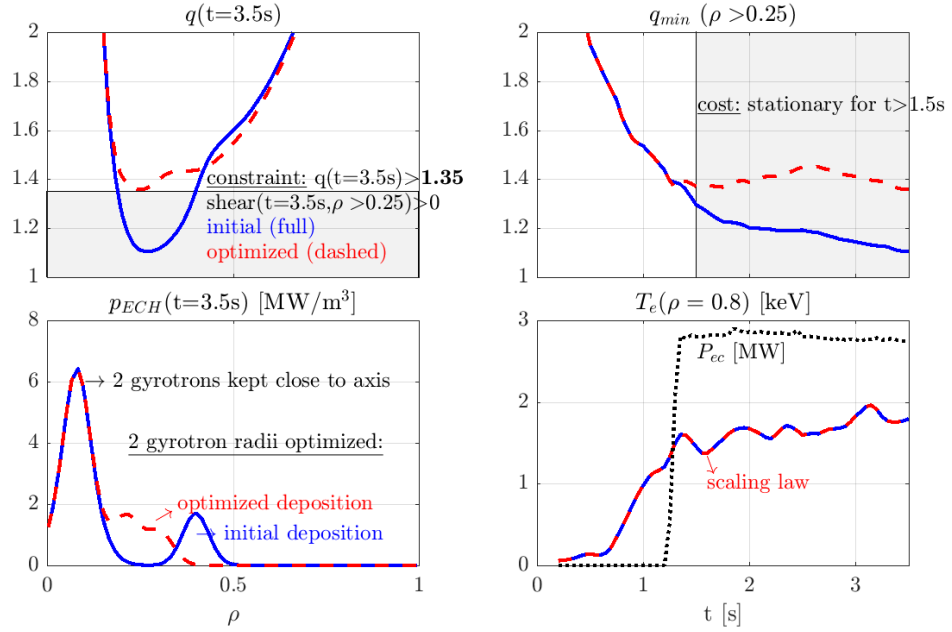
Figure 3.10: Results of forcing fast access to stationary $q_{min} > 1.35$, by automatically optimizing EC deposition location. For the initial and optimized state evolution: (a) $q$ profile at t=3.5s; (b) time evolution of $q_{min}$; (c) EC deposition profile; (d) EC power and $T_e(\rho = 0.8)$ boundary condition (from scaling law).

from the onset of the EC power onward. The scenario hence combines the stable pathway avoiding or minimizing the impact of tearing modes with an elevated $q_{min}$, right from the start of the high $\beta_{pol}$ phase.

Since the present work analyses relatively detailed features of the safety factor profile, simulated with a relatively low fidelity transport solver, the results should be interpreted cautiously. However, even though exact values of the $q$ profile and the derived magnetic shear can be hard to predict due to shot-to-shot variations, the RAPTOR code can provide a quantitative estimate of the impact of an actuator change on the non-linear state evolution of the plasma, providing a valuable tool to guide scenario development. Furthermore, due to the fast run time of the RAPTOR code, various sensitivity studies can be run at low computational expense. An example is shown in Figure 3.11: the optimized simulation is re-run with a $T_e(\rho = 0.8)$ 20% higher and lower compared to the trace predicted by the scaling law (note that the actual achieved temperature $T_e(\rho = 0.8)$ from the IDA is relatively close to the scaling law prediction). The corresponding $q$ profile at 3.5s and $q_{min}$ time trace is strongly affected: an increase in temperature pedestal leads to a larger amount of bootstrap current driven in the pedestal, leading to a more elevated $q$ profile with $q_{min}$ above 1.5. Reversely, the degraded pedestal would lead to a $q_{min}$ around 1.2. The complex interaction between the current in the pedestal and the core will be discussed in more detail later in this chapter.
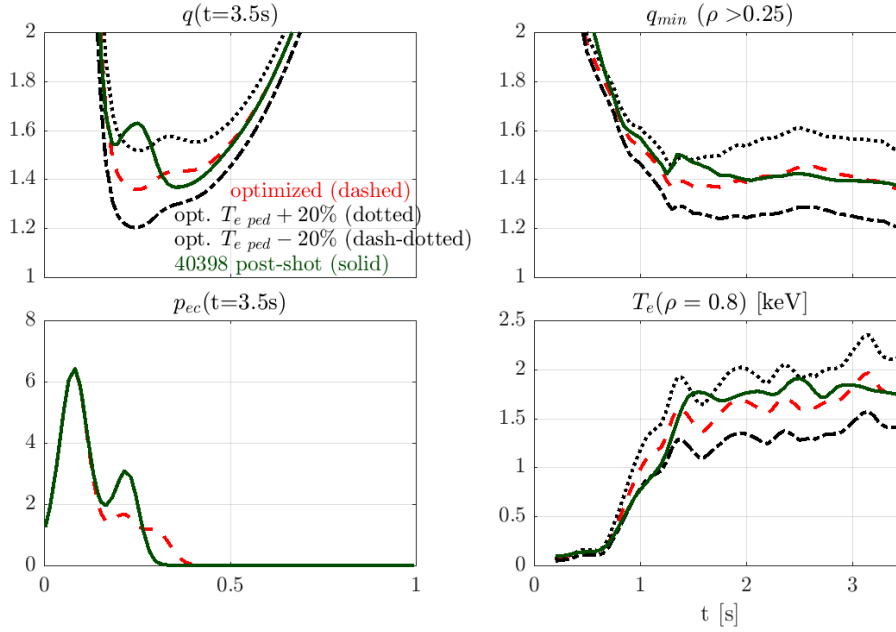
Figure 3.11: Sensitivity $T_e(\rho = 0.8) \pm 20\%$ for the optimized state evolution forcing $q_{min} > 1.35$ and comparison to the post-shot simulation of the discharge implementing the actuator traces proposed by the optimizer (40398): (a) $q$ profile; (b) $q_{min}$ trace; (c) EC deposited power; (d) $T_e(\rho = 0.8)$.

**Experiment**

Let us now analyse discharge 40398, implementing the optimized strategy described above. The EC deposition radii planned for the shot were aimed to be close to the optimum obtained above. Figure 3.11 compares the post-shot simulation to the pre-shot predicted optimum state evolution. Even though the outer EC sources deposited further inward than anticipated, the time evolution of the post-shot reconstruction recovers well the general features desired from the optimum: the post-shot simulation shows a $q$ profile with $q_{min}$ between $q = 1.35$ and $q = 1.5$ and with little time dependence after 1.5s.

In Figure 3.12, the post-shot RAPTOR simulations are compared for: (1) the late heating discharge 36087; (2) the early attempt for an early heating scenario, triggering a confinement-degrading NTM around 1.7s; (3) the optimized early heating discharge 40398. Note that discharge 40398 successfully combines the features of the access scenario described in Section 3.3.3 with the early achievement of an elevated stationary state. Compared to discharge 39342, $q_{min}$ decreases below $q = 1.5$ early during the flat-top phase, aiming for improved stability margin with respect to a potential 3/2 tearing mode. As has been mentioned in Section 3.3.3, a 3/2 is triggered around 1.1s. The mode disappears around 1.8s and has no clear impact on confinement (see Figure 3.13), consistent with the hypothesis that the impact of a mode triggered at lower radius and lower $\beta_{pol}$ is more benign.

The access to an early stationary state is confirmed when comparing the RAPTOR post-shot simulation with a post-shot simulation in ASTRA [Schramm et al. 2022] and with the kinetic equilibrium reconstruction of IDE, as shown in Figure 3.14: after 1.5s, all $q$ profiles show
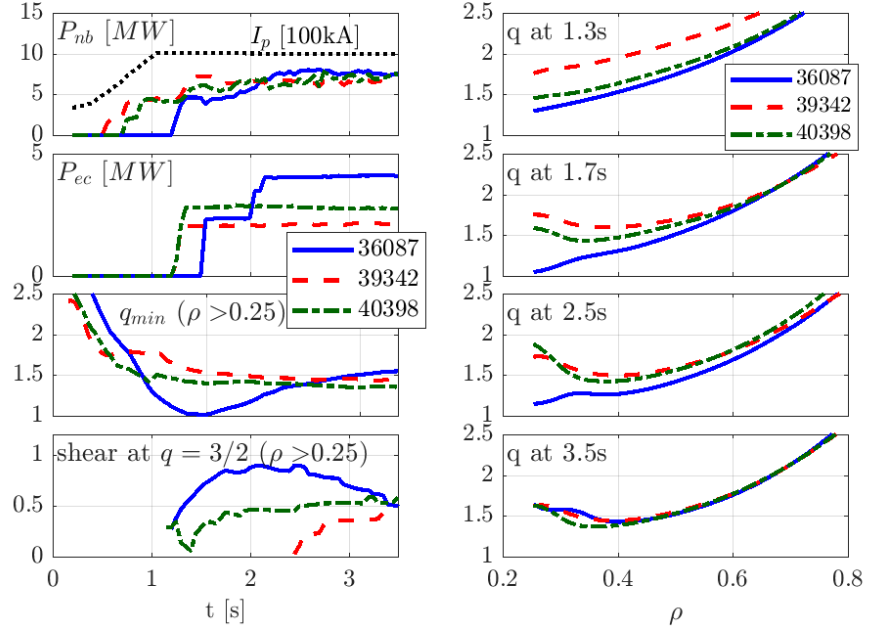
Figure 3.12: Comparison post-shot RAPTOR simulations of the late heating discharge 36087, the early heating discharge 39342 and the optimized early heating discharge 40398.
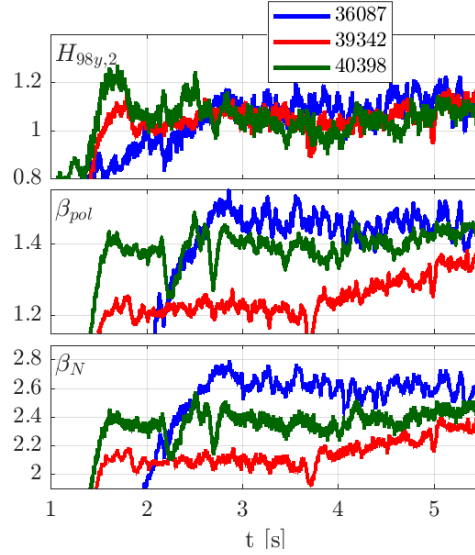


Figure 3.13: Traces of $H_{98y,2}$, $\beta_{pol}$ and $\beta_N$ of the late heating discharge 36087, the early heating discharge 39342 and the optimized early heating discharge 40398.
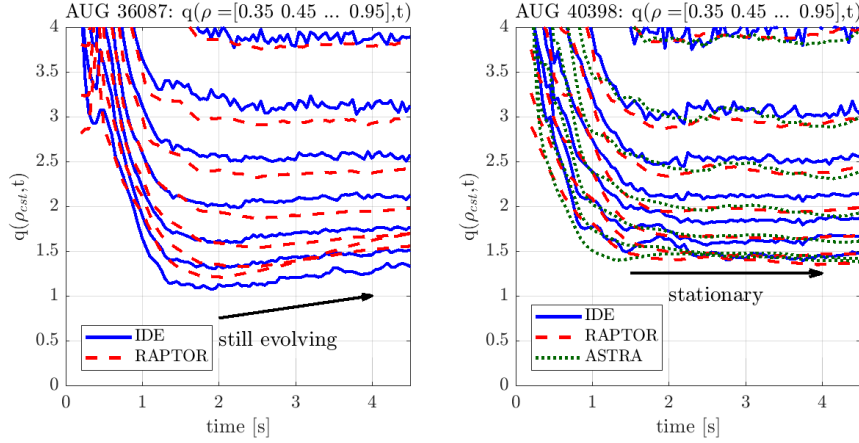
Figure 3.14: The time traces of the safety facor at various $\rho$, for the IDE reconstruction and RAPTOR and ASTRA post-shot simulations: (a) late heating (36087); (b) optimized early heating (40398).

relatively constant time evolution, indicating the successful achievement of an early elevated $q_{min}$. In Figure 3.14 we also show the slow time evolution of the safety factor traces for the late heating discharge 36087, in RAPTOR and IDE. By finding the optimal allocation (timing, power and radial distribution) of the available actuators, we were able to achieve the high performance phase of the advanced scenario (with elevated $q_{min}$ and elevated $\beta_{pol}$) early during the flat-top phase, while avoiding the onset of tearing modes, as confirmed by Figure 3.13.

### 3.4.3 Towards $q_{min} > 1.5$

**Aim**

To avoid or minimize the impact of tearing modes, the previous sections explored a ramp-up strategy where at high $\beta_{pol}$ and for $\rho > 0.25$, a non-zero magnetic shear is maintained through $q = 3/2$. While the proposed strategy was successfully tested in experiment, allowing for fast and reliable access to a stationary elevated $q$ profile, the stationary flat-top operating point is metastable with respect the onset of 3/2 NTMs (e.g. 40192, with short-lived 3/2 NTMs leading to abrubt reductions of the core $T_e$ and $T_i$). Evidently, the onset of 3/2 modes could be avoided by increasing the $q$ profile entirely above $q = 1.5$. In the present section, we solve an optimization problem to assess the feasibility of this approach with the available heating and current drive resources.

**Simulation**

We use a forward simulation set-up identical to the previous section. One more EC heating and current drive source is added, to allow to maintain a stationary safety factor with $q_{min} > 1.5$. This leads to an increase of the EC power to $P_{ec} = 3.6\,$MW (which impacts the pedestal temperature predicted by the scaling law). Within the present optimization problem,

Figure 3.15: Results of forcing fast access to stationary $q_{min} > 1.55$, by automatically optimizing EC deposition location. For the initial and optimized state evolution: (a) $q$ profile at t=3.5s; (b) time evolution of $q_{min}$; (c) EC deposition profile; (d) EC power and $T_e(\rho = 0.8)$ boundary condition (from scaling law).
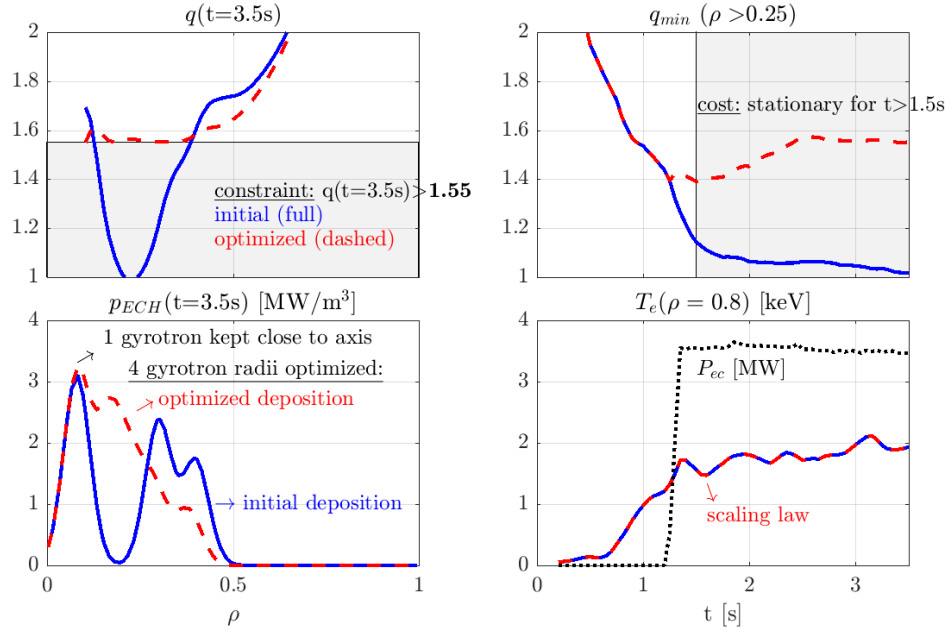
only one EC source is kept fixed at $\rho_{dep} = 0.08$. The radii of the four other EC sources are used as optimization variables $\mathbf{p} = [\rho_{dep\ 1}\ \rho_{dep\ 2}\ \rho_{dep\ 3}\ \rho_{dep\ 4}]^T$. The radii $\rho_{dep\ i}$ are constant in time.

The constraint eq. (3.6) is used to impose $q_{min} = 1.55$ (with weight functions $W_{q_{min}}$ activated over $\rho = [0.1; 1]$). We choose $q_{min} = 1.55$ to maintain a sufficient margin between $q_{min}$ and $q = 1.5$ (without low-shear conditions close to the 3/2 rational surface; an increased margin $\Delta q = q_{min} - 1.5 > 0.05$ might be desirable). The cost function 3.5 is identical to the one applied in the previous section, integrating a measure of stationarity over the time window 1.5s to 3.5s. The optimizer effectively looks for the deposition radii that result in a final $q$ profile fulfilling the constraint on $q_{min}$, while maintaining the $q$ profile as stationary as possible from 1.5s onwards.

Figure 3.15 presents the initial condition provided to the optimizer in blue ($\mathbf{p} = [0.3\ 0.3\ 0.4\ 0.4]^T$), while the obtained optimum is shown in red ($\mathbf{p} = [0.16\ 0.23\ 0.29\ 0.38]^T$). By optimizing the deposition of the counter-ECCD, the optimizer manages to maintain the $q$ profile above $q = 1.55$. Note that a broad ECCD deposition profile is proposed, resulting in a large region with $q \sim 1.55$ and low magnetic shear, extending up to $\rho \sim 0.4$. Between 1 and 2s the $q_{min}$ trace drops below $q = 1.5$, which means that 3/2 modes could still be triggered there. However, they will disappear once the $q$ profile is increased and the $q = 3/2$ surface ceases to exist.

In Figure 3.16, the optimized simulation is shown in the red dashed lines, while the black dash-dotted and dotted lines provide a sensitivity study, presenting the simulation resulting for respectively a 20% decrease or increase of $T_e(\rho = 0.8, t)$. The pedestal temperature clearly
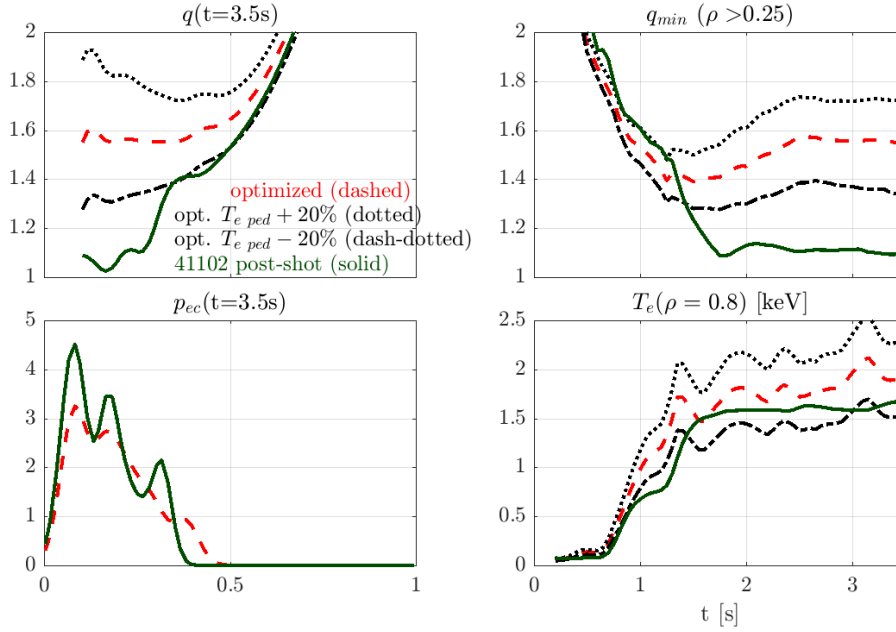
Figure 3.16: Sensitivity $T_e(\rho = 0.8) \pm 20\%$ for the optimized state evolution forcing $q_{min} > 1.55$ and comparison to the post-shot simulation of the discharge implementing the actuator traces proposed by the optimizer (41102): (a) $q$ profile; (b) $q_{min}$ trace; (c) EC deposited power; (d) $T_e(\rho = 0.8)$.

has a strong impact on the $q$ profile, with $q_{min}$ around 1.3 for the degraded pedestal and $q_{min}$ above 1.7 for the enhanced pedestal.

**Experiment**

The green lines in Figure 3.16 present the post-shot simulation of discharge 41102, implementing the optimized strategy described above. Even though the ECCD profile provides a broad profile as proposed by the optimizer, the $q$ profile at 3.5s decreases far below the elevated $q$ profile predicted by the optimizer. Utilizing the flexibility of the RAPTOR code, further simulations have been performed to understand this discrepancy.

Various changes are introduced to the inputs of the post-discharge simulations, swapping them with corresponding input in the optimized simulation, set before the discharge. Imposing the $T_e(\rho = 0.8, t)$ trace, the $n_e(\rho, t)$ evolution and the neutral beam deposition profile evolution of the pre-shot simulation, we gain understanding in the reason why the elevated $q$ profile predicted by the optimizer is not obtained. By inspecting the impact of these individual changes on the $q$ profile, we can understand the observed differences, as illustrated in Figure 3.17.

- The measured $T_e(\rho = 0.8, t)$ is below the temperature pedestal height predicted by the scaling law, leading to a lower current in the pedestal region.

- A stronger peaking of the $n_e(\rho, t)$ profile in the center leads to a local peak in the boot-
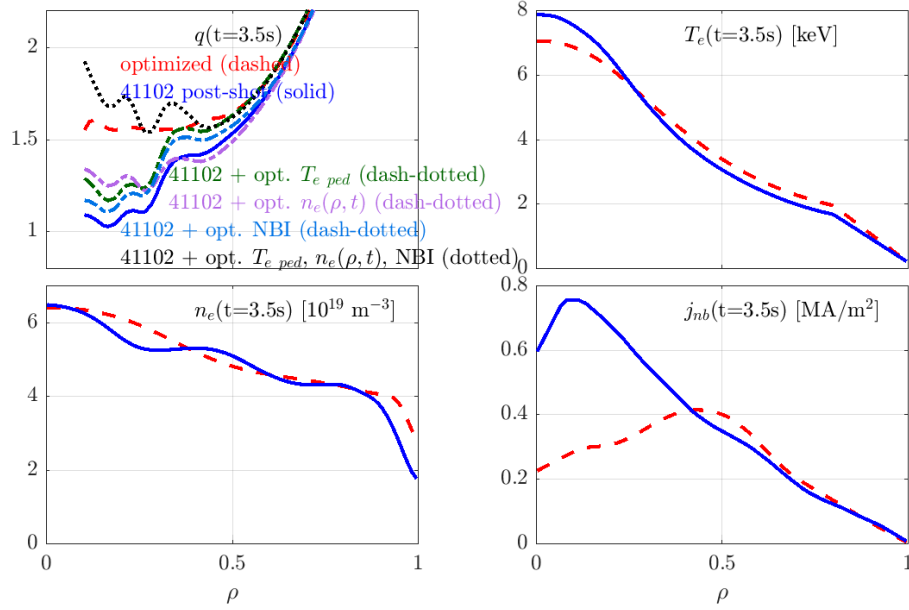
Figure 3.17: Profiles for optimized state forcing $q_{min} > 1.55$ and the post-shot simulation of the discharge implementing the actuator traces proposed by the optimizer (41102). Various changes are introduced to the inputs of the post-discharge simulations, swapping them with corresponding input in the optimized case, as set before the discharge.

 strap current, driving additional current for $\rho < 0.25$.

- The neutral beam current density profile is more peaked compared to the pre-shot assumption (taken from the earlier experiment 39342).

While each of these three factors individually result in a relatively modest impact on the value of $q_{min}$ that can be achieved, the combined impact is very significant, as can be seen in Figure 3.17. This study highlights some of the sensitivity of post-shot simulation to the IDA reconstruction ($T_e(\rho = 0.8, t)$ and $n_e(\rho, t)$) and the RABBIT neutral beam profile calculations, including local features of the profiles.

**Experiments at reduced plasma current**

Several shots have attempted to apply the increased amount of EC power, to achieve $q_{min} > 1.5$. Various of these attempts ended prematurely due to the occurrence of a disruptive 2/1 NTM. A salient example is discharge 40825. Looking at the spectrogram, shown in Figure B.11 of Appendix B, understanding can be gained into the dynamics at play. A sequence of ELM-triggered 2/1 modes is visible, before the mode finally locks and leads to a disruption around 2.1s. While this behavior can be expected due to the metastable nature of the $q$ profile in this scenario, it is unclear whether the evolution of the current density profile decreases the stability. Alternatively, the scenario adjustments could be responsible for changing the ELM

size and thus the seed. The RAPTOR post-discharge simulation indicates that the outer $q$ profile of discharge 40825 is further radially outward compared to earlier discharges like 40398. Closer radial proximity to the plasma edge could lead to stronger coupling to the ELMs, even if the $q$ profile is not more unstable. Note that the verification of this hypothesis requires further analysis, similar to the work on sawtooth-triggered NTMs in [Canal et al. 2013].

Based on this hypothesis, a reduction of the plasma current to $I_p = 900\,\text{kA}$ is proposed. Predictive RAPTOR modeling indicates that the increase of $q_{95}$ should lead to a decrease of the $q = 2$ radius, reducing the potential impact of ELM seeds, while increasing the local magnetic shear can decrease the classical tearing mode stability parameter $\Delta'$ [La Haye et al. 2000], increasing the required seed island size. Maintaining the heating and current drive actuator time traces unchanged, while stopping the plasma current at $I_p = 900\,\text{kA}$, a set of experiments have been performed where 2/1 modes could be successfully avoided. For discharge 41400, a stable flat-top phase without any confinement-degrading modes (spectrum in Figure B.13), with $\beta_{pol} \sim 1.45$, $\beta_N \sim 2.3$, could be maintained, with an $H_{98y,2}$ factor around unity. Note however that the post-discharge RAPTOR simulation of the $q$ profile differs significantly from the IDE reconstruction (Figure B.13 in Appendix B). The discrepancy between RAPTOR and IDE regarding the $q$ profile demands further investigation. Both IDE and RAPTOR however indicate that $q_{min} > 1.5$ was not maintained, while the pre-shot RAPTOR run indicated $q_{min} > 1.5$ can be maintained. Similar to our the illustration for discharge 41102 in Figure 3.17, the low $q_{min}$ in the RAPTOR simulation compared to the pre-shot run is due to a reduced pedestal temperature and a strong peaking of the central density. While unpredicted shot-to-shot variations like these highlight some limitations of model-based shot-to-shot optimizations, we will show in the following section how sensitivity studies on various input variables can be easily run, increasing insight in the robustness and the characteristics of the operating point of a given scenario.

## 3.5   Sensitivity study on the $q_{min} > 1.5$ scenario

In the present section we illustrate how a set of RAPTOR simulations allows to gain insight in the sensitivity of the optimum. The nominal simulation is the optimum obtained in Section 3.4.3, aiming for $q > 1.55$ (Figure 3.15).

### 3.5.1   Sensitivity to initial $q$ profile

The standard initial conditions used for all simulations in this chapter are taken from the IDA $T_e$ profile and IDE $q$ profile for discharge 39342 at 0.2s. We choose to keep the same initial condition at $t = 0.2$s for all shots, to allow comparison of the different shots without differences induced by a different initial state (which is poorly diagnosed). For the sensitivity study in Figure 3.18, an alternative initial $q$ profile is constructed (more elevated, with $q_{min} \sim 4$, indicating a broader current density distribution in the core). Since we start simulating early in the ramp-up, when the plasma is still relatively cold, the difference in $q$ profile has almost
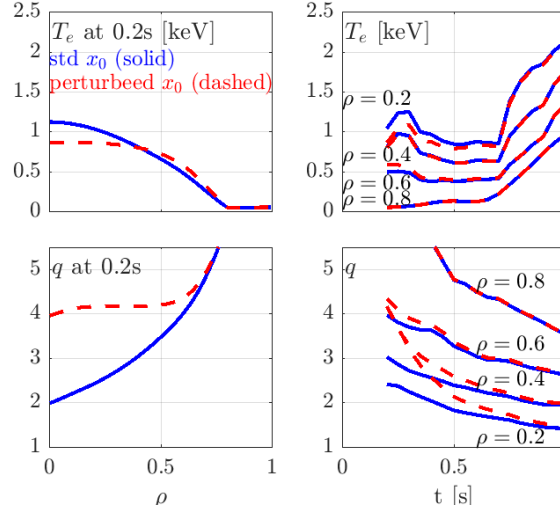
Figure 3.18: Comparison of RAPTOR ramp-up simulations with two different initial $q$ profiles.

entirely disappeared when the NBI is started around 0.7s and the plasma enters into H-mode. We conclude that the initial state has only a minor impact on the $q$ profile evolution after 0.7s.

### 3.5.2 Sensitivity to EC deposition radii

The sensitivity of the optimized $q$ profile to variations in the EC deposition profile is analysed. For each of a series of 50 simulations, the optimization vector $\mathbf{p} = [0.16\ 0.23\ 0.29\ 0.38]^T$ is perturbed, adding a random number to each of the optimization variables, encoding the EC deposition radii (pseudorandom values drawn from the standard normal distribution, with standard deviation 0.02). Figure 3.19 shows the optimum $q$ profile at 3.5s in magenta, as well as the corresponding EC deposition profile. The profiles corresponding to the 50 perturbed simulations are plotted in light grey, together with a mean, an upper and a lower standard deviation. We observe relatively strong variations of the $q$ profile at 3.5s: minor variations in the EC deposition radii can cause significant differences in the $q$ profile: the profiles of the upper and lower standard deviation enclose a band between $q = 1.4$ and 1.7 around $\rho \sim 0.2$. The $q$ profile is quite sensitive to changes in the EC deposition profile since the total current density is quite small with respect to the large (negative) values of the EC current density.

### 3.5.3 Sensitivity to pedestal temperature: coupling pedestal - central $q$ profile

The impact of the pedestal temperature height on the core $q$ profile of the optimized scenario at 3.5s (introduced in Figure 3.16) is analysed in some more detail in this section. The 1MA counter-ECCD scenario features a combination of a high pedestal with low net current in the core. Figure 3.20 shows time traces of the integrated plasma current density in the central region ($\rho < 0.4$, i.e. the region where ECCD is deposited) and in the pedestal region ($\rho > 0.8$). It is interesting to note that the current (ohmic and bootstrap) driven in the pedestal ($\sim$ 190kA) is
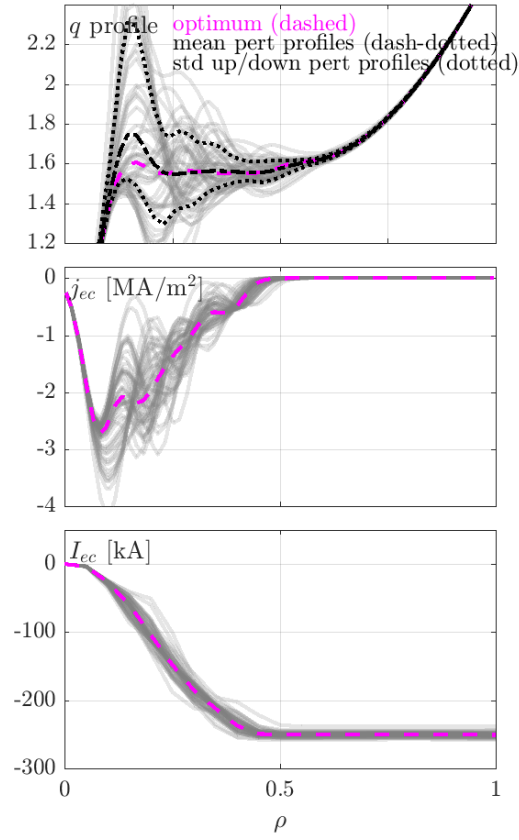
Figure 3.19: For the RAPTOR optimum obtained in Section 3.4.3, the sensitivity of the $q$ profile with respect to variations in the EC deposition radii is studied. The profiles corresponding to 50 perturbed simulations (adding a random number to each of the optimization variables) are plotted in light grey, together with a mean, an upper and a lower standard deviation for the resulting $q$ profile.
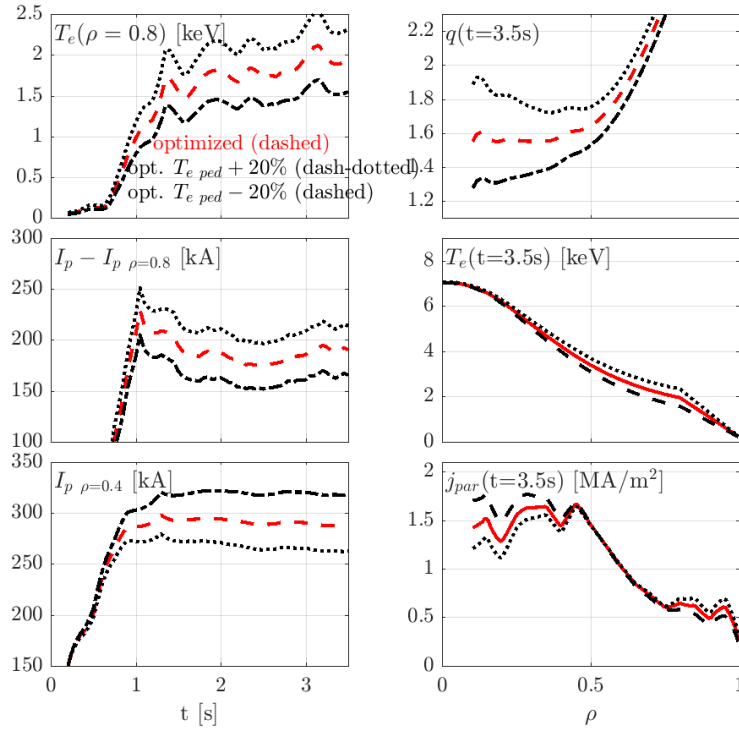
Figure 3.20: Sensitivity study $T_e(\rho = 0.8) \pm 20\%$ for the optimized state evolution forcing $q_{min} > 1.55$, illustrating the coupling between the current in the pedestal and the central $q$ profile. As the total plasma current inside $\rho \sim 0.4$ is relatively small, the $q$ profile is strongly affected.
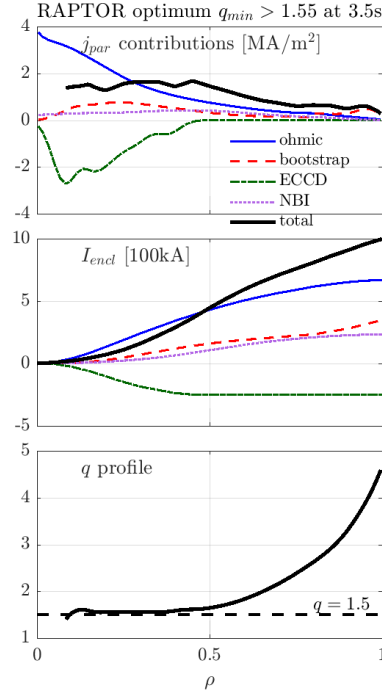
Figure 3.21: Inductive and non-inductive contributions to the current density and the enclosed plasma current at $t = 3.5$s, resulting in the optimized, elevated $q$ profile.

about two thirds of the net current in the central region ($\sim 290$kA). This is a particular feature of the counter-ECCD scenario: a broad current density profile is created by adding a large negative ECCD in the core to the large inductively driven current (for $\rho < 0.4$: NBI, bootstrap and ohmic current drive about $\sim 530$kA, of which about 350kA is ohmic current, while the ECCD amounts to about $\sim -240$kA). Note that the ohmic current within $\rho < 0.4$ is hence larger than the total enclosed current. The individual current density contributions (and enclosed plasma currents) of the various inductive and non-inductive current sources are illustrated in Figure 3.21.

As shown in Figure 3.20, changing the pedestal temperature boundary condition $T_e(\rho = 0.8)$, adding or subtracting 20%, the electron pressure gradient in the pedestal changes, hence changing the amount of bootstrap current. The increase/reduction of $T_e(\rho = 0.8)$ and $I_{bs\ ped}$ is compensated with a reduction/increase of the plasma loop voltage and $I_{oh}$ in the core. The transport model applied predicts a similar $T_{e0}$ (transport is enhanced for increasing $T_e$ and increasing $q$, yielding a similar $T_{e0}$ despite a higher $T_e(\rho = 0.8)$). We can see how the increase/reduction of pedestal bootstrap current is counteracted by a respective reduction/increase of plasma current in the center, through a reduction/increase of the ohmic current (similar $T_{e0}$: similar $\sigma_{neo}$, similar EC current drive efficiency, similar $j_{bs}$). In the outer core region ($\rho > 0.4$ and $\rho < 0.8$) the total current density seems mostly unchanged (Figure 3.20 bottom right), as the reduction/increase of the loop voltage is compensated by increase/reduction of neoclassical conductivity $\sigma_{neo}$ due to the temperature increase/decrease.

To summarize: the excess/lack of bootstrap current driven in the pedestal $\Delta I_{p\ ped}$ due to an increase/decrease of $T_e(\rho = 0.8)$ leads to a respective decrease/increase of the plasma current inside $\rho \sim 0.4$. For a given geometry and on-axis toroidal magnetic field, the $q$ profile is directly proportional to the inverse of the enclosed net plasma current, more specifically, $q \sim \frac{\rho}{I_p(\rho)}$ with $I_p(\rho) = \int j_{par} dA$. When, like for the present scenario, the net $I_p(\rho)$ in the center is relatively small, the redistribution of $\Delta I_{p\ ped}$ due to a changed $T_e(\rho = 0.8)$ can be expected to have a large impact on the central $q$ profile. This is indeed what we observe in Figure 3.20: as $T_e(\rho = 0.8)$ is increased/decreased by 20%, $q_{min}$ is strongly affected, achieving respective values $q_{min} \sim 1.75$ and $q_{min} \sim 1.30$.

## 3.6 Conclusion

This work illustrates how fast inter-discharge modeling and optimization allows to increase understanding of the effects of the various actuators, allowing to develop a stable and reproducible early heating scenario, as experimentally tested in AUG experiments. A framework to perform routine post-discharge simulations of AUG discharges is presented and validated against experimental $T_e$ profiles inferred by IDA [Fischer et al. 2010] and $q$ profiles from the IDE kinetic equilibrium reconstruction [Fischer et al. 2016]. The set-up relies on the IDE toolchain to obtain equilibrium geometry data, neutral beam heating and current drive deposition profiles (RABBIT [Weiland et al. 2018]) and electron cyclotron deposition radii and widths for the individual gyrotrons (TORBEAM [Poli et al. 2001]). Simple analytical formulas for the heat diffusivity and the EC current drive efficiency perform robustly over the range of studied discharges. The $T_e$ boundary condition is imposed at $\rho = 0.8$ and taken from the IDA. While the selected transport model should be sufficiently reliable to predict the main effects of the various actuators and the main inter-dependencies of temperature and $q$ profile, detailed features are of lesser importance for the present work. In Chapter 6 we show how the different transport models available in this framework can be compared.

To allow for a predictive pre-shot simulations and optimization, a simple scaling law based on previous discharges within the same parameter regime was proposed to estimate $n_e T_e(\rho = 0.8)$, with line average density, heating power and plasma current as input variables. Generally this approach resulted in a good agreement between pre- and post-shot simulations of the same scenario that the scaling law was based on, confirming the predictive capability of our framework.

Post-discharge simulations hint that the formation of an off-axis minimum in the $q$ profile, for $q > 1.5$, with $q_{min}$ subsequently decreasing through $q = 1.5$ during the high $\beta_{pol}$ phase, can cause the onset of a confinement-degrading 3/2 tearing mode. Based on simulations, a delay of 200ms was proposed for the onset timing of the NBI heating during ramp-up. Maintaining the relatively cold L-mode plasma longer, $q$ decreases below $q = 1.5$ earlier, at low $\beta_{pol}$ and before the $q$ profile is strongly shaped. When the off-axis $q_{min}$ is formed, $q_{min} < 1.5$, allowing to maintain non-zero shear through the rational 3/2 surface. Post-shot simulation and analysis of the MHD magnetic spectrograms indicate that the robustness of the optimized early heating

scenario against the onset of tearing modes was successfully increased.

Applying a non-linear optimization scheme, RAPTOR was used to assess the maximum $q_{min}$ that can be maintained stable, while achieving the final elevated $q$ profile as early as possible in the discharge. An early stationary elevated $q$ profile with $1.35 < q_{min} < 1.5$ was successfully achieved in AUG experiments using the optimized EC deposition locations predicted by the optimization, allowing to raise $\beta_{pol}$ to its target value early during the flat-top phase. With higher EC power, a further increase of the $q$ profile to $q_{min} > 1.5$ was attempted. According to post-discharge simulations the experimental attempt was unsuccessful due to the combined impact of a reduced pedestal temperature and an increased central peaking of both density and neutral beam current drive.

The fast run-time allows for a quantitative estimate of the impact of model parameter uncertainties on the simulation. The key impact of $T_e(\rho = 0.8)$ has been highlighted: the redistribution of the plasma current due to an increase or reduction of the pedestal temperature strongly impacts the central $q$ profile, as a transport effect leads to small changes of $j_{par}$ at mid radius and since the enclosed plasma current at small radii is relatively small for this scenario.

# 4 Stationary state optimization of ITER hybrid flat-top operating point

In Chapter 2, we introduced a framework for fast, automated optimization of the stationary phase of tokamak plasma discharges. Now, we will apply the QLKNN-hyper-10D transport model [van de Plassche et al. 2020] (in this chapter referred to as QLKNN) within the presented optimization scheme to provide first-principle- based predictions of sets of optimized operation points for the ITER hybrid scenario. These optimization problems are typically solved within minutes on a single CPU.

The performance of ITER hybrid scenarios is investigated at different values of total plasma current, plasma density and pedestal height and for different power contributions in a heating mix consisting of electron cyclotron and neutral beam heating. The stationary state optimization scheme is applied to tailor the safety factor profile $q(\rho)$, optimizing the radial distribution of electron cyclotron current drive (ECCD) deposition.

## 4.1 Introduction

The hybrid scenario achieves improved energy confinement relative to the IPB98(y,2) scaling law eq. (1.4) [ITER Physics Expert Group on Confinement and Transport et al. 1999] by actively tailoring the $q$ profile and its radial derivative, impacting the turbulent transport fluxes by altering the ion temperature gradient (ITG) threshold. QLKNN successfully captures this physics mechanism in its prediction of the ITG-driven heat flux. Various integrated modeling studies have confirmed the potential of hybrid scenarios to provide long-pulse ($t_{burn} > 1000\,\text{s}$) discharges with burning plasma conditions (fusion gain $Q \geq 5$), e.g. [Wagner et al. 2010; Citrin et al. 2010; Polevoi et al. 2020], although simulation results are strongly dependent on the applied heating mix and assumptions like temperature pedestal height and density peaking. The present simulations do not take into account the magnetic flux pumping effect [Petty et al. 2009; Krebs et al. 2017] and rely only on off-axis electron cyclotron co-current drive to shape the $q$ profile, to maximize confinement and maintain $q > 1$.

The obtained scenarios are, by construction, stationary and can hence be maintained throughout the burn phase. Access to these operating points is presently not discussed, although it has been demonstrated how relaxed plasma profiles can be obtained in the early flat-top phase by optimizing actuator trajectories during the ramp-up, as demonstrated in [Felici and Sauter 2012] and [van Dongen et al. 2014] with RAPTOR-based optimization and in [Wehner et al. 2019] with the physics-oriented TRANSP code. Chapter 3 discusses how inter-discharge optimizations in RAPTOR have been used to achieve an early, elevated $q$ profile on ASDEX Upgrade. Early relaxation of the $q$ profile to its stationary solution is important, as the current diffusion time is very long ($\sim 100\,\text{s}$) on ITER and future reactors.

Several works, like [McClenaghan et al. 2020] and [Kim et al. 2021] for ITER, [Hayashi et al. 2017] for JT-60SA and [Rodriguez-Fernandez et al. 2020] for SPARC have used predictive modeling tools to explore the existence of stationary scenarios for current and future devices. The work shown in this chapter has the potential to substantially reduce the effort of such modeling activities by calculating stationary states directly (without requiring iteration between several codes) and allowing the use of numerical optimization tools to find optimal scenarios satisfying constraints. These RAPTOR results can then serve as starting point for more sophisticated analysis using more detailed physics codes.

The subsequent sections extensively apply the non-linear optimization routine described in 2.5.2 and make use of *option 1* of the novel stationary state solver described in Section 2.4.3, treating the plasma loop voltage as an unknown in addition to the requested plasma profiles, while prescribing the auxiliary power sources and plasma current $I_p$. Since the individual optimization problems are solved within minutes on a single CPU, the presented framework provides a versatile tool to explore various operational conditions and perform sensitivity analyses.

## 4.2   The ITER hybrid scenario

Within the ITER scientific mission [ITER Organization 2018], the ITER hybrid scenario provides a potential road to long-pulse discharges ($t_{burn} > 1000\,$s) with a high fusion gain $Q > 5$, providing a compromise between

- the *inductive reference scenario*, pursuing a fusion gain $Q > 10$ for a limited duration $t_{burn} \sim 400\,$s by operating at a high total plasma current ($I_p = 15\,$MA), and

- the *steady state scenario*, achieving an extended discharge duration ($t_{burn} = 3000\,$s, limited by cooling system limits) by operating at a lower total plasma current ($I_p \sim 9\,$MA), driven entirely by non-inductive means (auxiliary current and bootstrap current).

The reduction of the total plasma current $I_p$ requires operation at lower density (Greenwald density limit $n_{e\,Gw} = I_p/(\pi a^2)$ [Greenwald et al. 1988]) and negatively affects the energy confinement time (IPB98(y,2) scaling law eq. (1.4) for ELMy H-mode plasmas [ITER Physics Expert Group on Confinement and Transport et al. 1999] predicts $\tau_E \sim I_p^{0.93} n_e^{0.41}$)[1]. The success of hybrid and steady state scenarios hence rely on enhanced energy confinement, leading to an increase of both the nuclear fusion power and the internally driven bootstrap current. Contrary to some of the scenarios proposed for steady state operation, hybrid scenarios do not rely on the formation of internal transport barriers in the core plasma [Shimada et al. 2007]. Lowering turbulent transport should be achieved through tailoring of the safety factor profile $q$, controlling the auxiliary heating and current density deposition profile. The hybrid scenario envisions a $q$ profile with a wide flat region in the center with $q > 1$ everywhere, avoiding the onset of sawtooth crashes. The absence of sawtooth triggered neoclassical tearing modes (NTMs) allows operation at increased values of $\beta_N$ without confinement degradation (assuming the resistive $\beta_N$ limit for the onset of triggerless NTMs is higher in the absence of sawtooth seed islands). Note that allocation of electron cyclotron current drive to avoid the onset of NTMs [Kong et al. 2019a] is not taken into account in the present work.

The relatively large amount of localized ECCD on ITER allows for a high degree of $q$ profile shaping. The shape of the $q$ profile impacts micro-instabilities driving turbulent transport [Stober et al. 2007; Citrin et al. 2012]. As discussed in [Citrin et al. 2010] and [Hogeweij et al. 2012], hybrid scenario plasmas are characterized by an increased value of $s/q$ at the outer plasma radii, stabilizing ion temperature gradient turbulence (ITG). However, alternative mechanisms have been proposed to explain the improved confinement of hybrid scenarios, including the electromagnetic stabilisation of ITG turbulence, enhanced by both low magnetic shear and fast ions (which are more prevalent at lower density) and increased $\mathbf{E} \times \mathbf{B}$ flow shear turbulence stabilization at lower density [Citrin et al. 2014; Bock et al. 2017; Garcia et al. 2018; Reisner et al. 2020; Han et al. 2022; Citrin and Mantica 2022].

---

[1]A recently published revised energy confinement scaling law ITPA20-IL [Verdoolaege et al. 2021], based on an ITER-like subset of the ITPA global H-mode confinement database (extended with new data from JET with the ITER-like wall and ASDEX Upgrade with the full tungsten wall), predicts a reduced density dependence, while maintaining a strong plasma current dependence: $\tau_E \sim I_p^{1.29} n_e^{0.15}$ (yielding a similar $I_p$ dependence at fixed Greenwald density fraction).
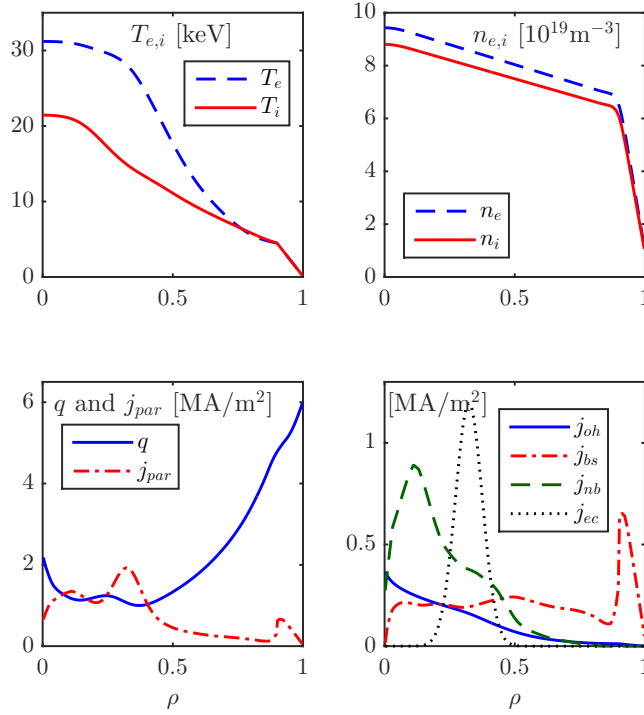
Figure 4.1: **ITER hybrid reference case scenario** Summary of radial profiles of the RAPTOR-QLKNN stationary state simulation referred to henceforth as the ITER hybrid reference case scenario ($I_p$ = 10.5 MA). *Reproduced from [Van Mulders et al. 2021b].*

## 4.3 Modeling assumptions

Table 4.1 and Figure 4.1 present some stationary state quantities and profiles of the RAPTOR-QLKNN simulated plasma scenario referred to henceforth as the ITER hybrid reference case. This scenario is obtained by maximizing the fusion gain $Q$ for a fixed total plasma current $I_p$ = 10.5 MA, by varying the deposition location of the electron cyclotron heating and current drive (modeled as a single gaussian curve with width $\Delta\rho$ = 0.15), while constraining $q > 1$.

### 4.3.1 Stationary diffusion equations and boundary conditions

For the ITER results presented in this chapter, RAPTOR solves for transport of ion and electron heat and poloidal flux (i.e. $T_e$, $T_i$ and $\psi$ stationary diffusion equations). The reference temperature boundary conditions $T_{e\,ped}$ = 4.5 keV and $T_{i\,ped}$ = 4.5 keV are set at the pedestal location $\rho_{ped}$ = 0.9. For $\rho > \rho_{ped}$, a linear temperature pedestal is imposed. The Neumann boundary condition for the $\psi$ diffusion equation depends on the total plasma current $I_p$. A range of different total plasma currents is reviewed, considering $I_p$ = 10.5 MA as the reference case.

Although the addition of particle transport to the set of solved equations is straightforward, fixed density profiles are imposed for the stationary states modeled in this chapter, with the

| | |
|---|---|
| $I_p$ | 10.5 MA |
| $B_0$ | 5.3 T |
| $a$ | 2.0 m |
| $R_0$ | 6.2 m |
| $I_{bs}/I_p$ | 0.43 |
| $I_{ni}/I_p$ | 0.89 |
| $P_{fus}$ | 367 MW |
| $P_{nb}$ | 33 MW |
| $P_{ec}$ | 40 MW |
| $P_{rad\ tot} = P_{brem} + P_{line}$ | 22 MW |
| $P_{sep}$ | 124 MW |
| $P_{LH}$ | 77 MW |
| $W_{th\ tot}$ | 309 MJ |
| $T_{i0}$, $T_{i\ ped}$ | 21 keV, 4.5 keV |
| $T_{e0}$, $T_{e\ ped}$ | 31 keV, 4.5 keV |
| $q_{95}$ | 5.1 |
| $\langle n_e \rangle_{line}/n_{e\ Gw}$ | $7.8 \times 10^{19}\,\mathrm{m}^{-3}/8.5 \times 10^{19}\,\mathrm{m}^{-3}$=0.9 |
| $n_{e0}/n_{e\ ped}$ | $9.4 \times 10^{19}\,\mathrm{m}^{-3}/6.8 \times 10^{19}\,\mathrm{m}^{-3}$=1.4 |
| $H_{y2,98}$ | 1.3 |
| $\beta_N$ | 2.4 |
| $\ell_{i3}$ | 0.84 |
| $U_{pl}$ | 3.7 mV |
| $Q$ | 5.0 |

Table 4.1: **ITER hybrid reference case scenario** Summary of physical quantities of the RAPTOR-QLKNN stationary state simulation referred henceforth as the ITER hybrid reference case scenario. *Reproduced from [Van Mulders et al. 2021b].*

exception of Section 4.8, where the RAPTOR-QLKNN density prediction is presented as part of a density profile sensitivity study. As a result, both Greenwald fraction $f_{Gw} = \langle n_e \rangle_{line}/n_{Gw}$ and the peaking factor $n_{e,i0}/n_{e,i\ ped}$ are directly imposed. The reference density profiles used in this section are constructed by merging two linear segments (respectively for core and pedestal, considering a peaking factor of $n_{e,i0}/n_{e,i\ ped} = 1.4$). The resulting profile is smoothed to avoid a discontinuity in the bootstrap current density, while the first derivative is set to zero at the magnetic axis $\frac{\partial n_e}{\partial \rho}|_{\rho=0} = 0$. The density peaking can be quantified by the ratio $n_{e,i0}/\langle n_{e,i} \rangle_{vol} = 1.3$, which is a conservative value compared to the prediction for the ITER inductive scenario in [Fable et al. 2019]. Since the hybrid scenario operates at lower collisionality, a further increase of density peaking can be anticipated [Angioni et al. 2003; Weisen et al. 2005]. The value of the electron density at the pedestal $n_{e\ ped}$ ($\rho_{ped} = 0.9$) is increased for increasing value of the total plasma current $I_p$, ensuring a line-averaged electron density below the Greenwald density limit ($\langle n_e \rangle_{line}/n_{e\ Gw} = 0.9$). In practice, the density pedestal can be controlled with peripheral pellet fueling on ITER. Note that the use of the line-averaged density to evaluate the Greenwald density fraction is conservative as experimental evidence links the limit to phenomena near the plasma edge, suggesting the potential of plasmas with peaked density profiles to operate at higher densities [Giacomin et al. 2022].
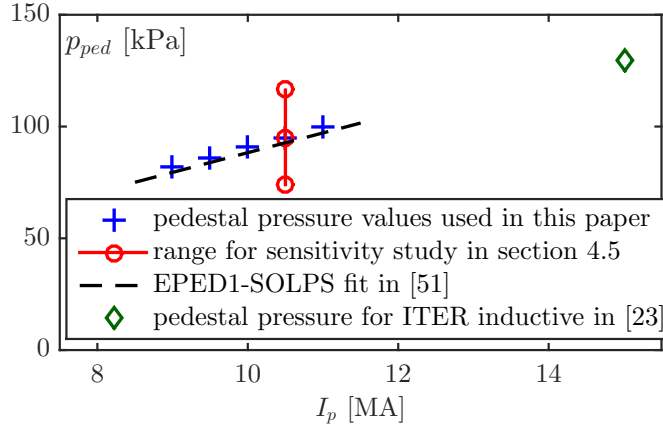
Figure 4.2: **Overview pedestal pressures** The pedestal pressures imposed within the simulations presented in this chapter are compared to the EPED1-based scaling law for ITER moderate pedestal densities with SOLPS-compatible separatrix densities introduced in [Polevoi et al. 2015]. The increased and decreased pedestal pressures applied in the sensitivity study in Section 4.7 are also shown, in addition to the upper pressure 130 kPa for the ITER inductive scenario as reported in [Wagner et al. 2010]. *Reproduced from [Van Mulders et al. 2021b].*

Recent work relates the H-mode density limit to ballooning stability limits at the separatrix, finding $n_{e\ sep}/n_{e\ Gw} \sim 0.4 - 0.5$ as an upper limit [Eich et al. 2018]. This effectively provides an indirect upper limit for $n_{e\ ped}$ due to the stiffness of pedestal transport.

The ion density profile $n_i(\rho)$ (sum over deuterium and tritium species), is inferred from the $n_e(\rho)$ profile by requiring quasi-neutrality (assuming a 50:50 DT mix) and imposing $Z_{eff} = 1.6$, considering Neon ($Z = 10$) as the only impurity, aggregating the impact of He, Be, Ne, W etc. Note that the linear increase of the density pedestal with plasma current $I_p$ results (for constant $T_{e,i\ ped}$) in a linear scaling of the pedestal pressure, which is consistent with EPED1 simulations for ITER [Polevoi et al. 2015]. Figure 4.2 compares the pedestal pressures imposed within the simulations presented in this chapter to the EPED1-based scaling law for ITER moderate pedestal densities with SOLPS-compatible separatrix densities introduced in [Polevoi et al. 2015]. The increased and decreased pedestal pressures applied in the sensitivity study in Section 4.7 are also shown, in addition to the upper pressure 130 kPa for the ITER inductive scenario as reported in [Wagner et al. 2010]. Note that the calculation of consistent separatrix densities is out of the scope of this thesis. The pedestal pressures applied in this chapter are very close to the scaling law projections, giving confidence in the applied boundary conditions.

### 4.3.2 MHD equilibrium geometry

A consistent equilibrium for the $I_p = 10.5$ MA reference case is found by iterative application of the RAPTOR stationary state solver and the CHEASE fixed-boundary ideal MHD equilibrium solver [Lütjens et al. 1996]. The iterative procedure starts from a basic equilibrium, constructed in CHEASE, assuming simple radial profiles and reproducing the shape of the last closed flux surface from [Koechl et al. 2018] (shown in green dotted on Figure 4.3). An automatic
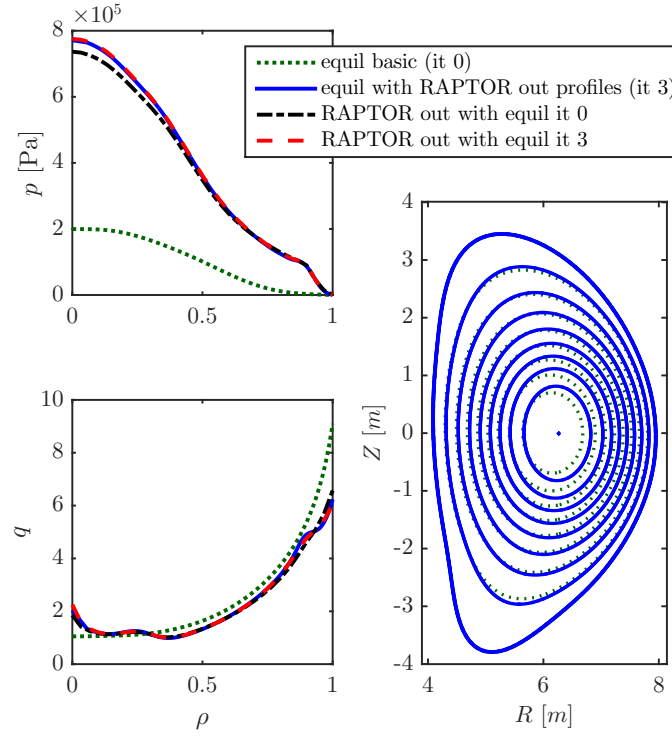
Figure 4.3: Impact of MHD equilibrium consistency on transport solution (magnetic surfaces are shown for both equilibria for 10 equidistant values of the normalized poloidal flux). The pressure and safety factor profiles of the initially used basic equilibrium (green dotted) do not match the resulting RAPTOR profiles (black dash-dotted). After three transport-equilibrium solver iterations, the kinetic profiles in RAPTOR (red dashed) and CHEASE (blue solid) match closely. Note the small adjustment in RAPTOR profiles from iteration 0 to 3. For the equilibrium, the last closed flux surface is maintained fixed, while the inner flux surfaces change due to the updated kinetic profiles.

interfacing between RAPTOR and CHEASE has been implemented, feeding the RAPTOR output profiles $p(\rho)$ and $j_{par}(\rho)$ to CHEASE, to recalculate the equilibrium with a set of profiles consistent with the transport solution. After three RAPTOR-CHEASE iterations, the RAPTOR transport solution converges towards the profiles underlying the CHEASE equilibrium. From Figure 4.3 it is clear that even for a large equilibrium change, the impact on the transport solution is moderate. As a consequence, it is well justified to avoid equilibrium updates during the iterations of the optimizer and only use the final optimized profiles to obtain the consistent equilibria. Including more complex modeling of pedestal stability and turbulent transport, the effect of the equilibrium geometry could become more important and require self-consistent iterations of the equilibrium [Saarelma et al. 2017].

### 4.3.3 Auxiliary heating and current drive

Auxiliary heating and current drive are provided by electron cyclotron waves and neutral beam injection. The combination of these technologies was found to yield the best performance in the optimized ITER hybrid scenario described in [Citrin et al. 2010]. The maximal heating powers are set to $P_{nb} = 33\,\mathrm{MW}$ and $P_{ec} = 40\,\mathrm{MW}$, considering the availability of a 20 MW electron cyclotron upgrade in addition to the ITER baseline heating mix, as proposed in [Wagner et al. 2010] for improved H-mode accessibility margin. Alpha and bremsstrahlung power are calculated by the respective RAPTOR source and sink modules [van Dongen et al. 2014].
The radial deposition profile of electron cyclotron heating and current drive results from an optimization procedure, as described in the subsequent section. The electron cyclotron current drive efficiency is modeled in RAPTOR with a $T_e/n_e$ dependency, resulting in a strong efficiency drop when sweeping the deposition location away from the core (introduced in Section 2.3.3). The efficiency factor is tuned to obtain a dimensionless current drive efficiency (as defined in [Lin-Liu et al. 2003]: $\zeta = \frac{e^3 n I_{ec} R}{\epsilon_0^2 P_{ec} T}$) similar to the efficiency modelled in [Citrin et al. 2010] $\zeta \sim 0.35$.
The JINTRAC integrated modeling suite [Romanelli et al. 2014] with the JETTO transport solver [Cenacchi and Taroni 1988] is used to evaluate consistent neutral beam profiles for the stationary states found at $I_p = 10\,\mathrm{MA}$ and $I_p = 11\,\mathrm{MA}$ with optimized electron cyclotron deposition (applying the QLKNN transport model like in the respective RAPTOR runs). The relaxed final state of time dependent JETTO simulations for $I_p = 10\,\mathrm{MA}$ and $I_p = 11\,\mathrm{MA}$ (with the respective density profiles imposed) converge to a stationary state, with consistent neutral beam profiles evaluated by the PENCIL module [Challis et al. 1989]. Radial profiles of neutral beam deposition for different density profiles are calculated in RAPTOR by interpolating linearly with respect to the density at the magnetic axis $n_{e0}$, e.g. $j_{nb}(\rho) = j_{nb\,10\mathrm{MA}}(\rho) + \frac{n_{e0} - n_{e0\,10\mathrm{MA}}}{n_{e0\,11\mathrm{MA}} - n_{e0\,10\mathrm{MA}}}(j_{nb\,11\mathrm{MA}}(\rho) - j_{nb\,10\mathrm{MA}}(\rho))$, with $n_{e0\,10\mathrm{MA}} = 8.9 \times 10^{19}\,\mathrm{m}^{-3}$ and $n_{e0\,11\mathrm{MA}} = 9.8 \times 10^{19}\,\mathrm{m}^{-3}$ (this is applied over $I_p \in [9\ 11]\mathrm{MA}$). An identical interpolation procedure is applied to evaluate the radial line radiation profiles. Figure 4.4 shows the neutral beam and line radiation profiles obtained from the JETTO predictive runs at $I_p = 10\,\mathrm{MA}$ and $I_p = 11\,\mathrm{MA}$, which provide the inputs to the interpolation procedure in RAPTOR. The proposed linear interpolation based on $n_{e0}$ can be justified by the main dependence of these profiles on
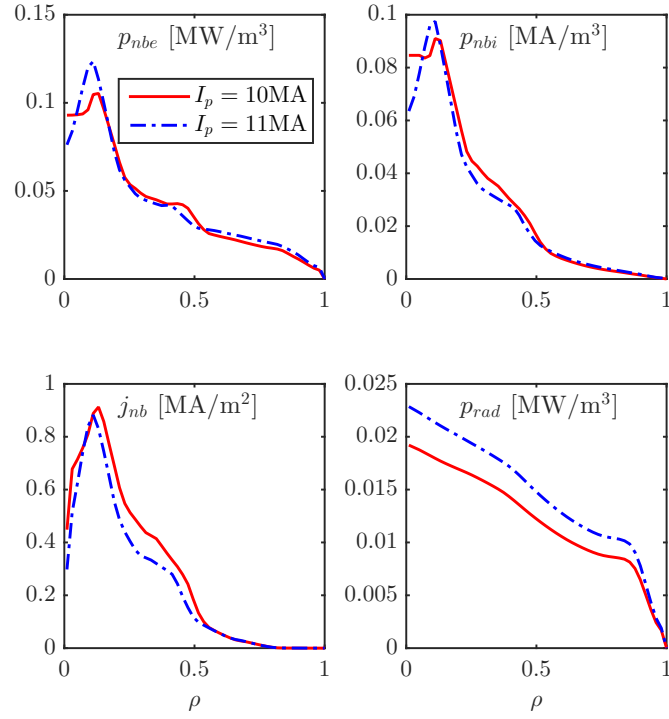
Figure 4.4: **Overview JETTO NBI and line radiation profiles** Neutral beam and line radiation profiles in the relaxed final state of time dependent JETTO-QLKNN simulations for $I_p = 10\,\text{MA}$ and $I_p = 11\,\text{MA}$ (with the respective density profiles profiles imposed). These profiles provide the inputs to the interpolation procedure to evaluate the corresponding source/sink terms in RAPTOR. *Reproduced from [Van Mulders et al. 2021b].*

the density, as well as by the relatively small variation of the respective profiles throughout the explored range of operating points, as apparent from Figure 4.4 (under the present assumption of a fixed density peaking factor). Further efforts for inclusion of (reduced) physics modules to evaluate neutral beam deposition profiles and line radiation profiles are however clearly desirable.

### 4.3.4 Transport flux predictions

Heat diffusivities are modeled with QLKNN [van de Plassche et al. 2020], the QuaLiKiz neural network surrogate described in Section 2.3.4. The model predicts that the ion and electron temperature gradients in the hybrid scenario operating space are dominated by ITG instabilities, with subdominant TEM. Note that the TEM contribution could become more important when the ITG stabilisation by electromagnetic and fast ion effects are accounted for, which is outside the scope of the QuaLiKiz model. For the heat diffusivity predictions in this chapter, only the dominant ITG turbulent transport channel is hence maintained and the other channels (ETG, TEM) are disabled within QLKNN. The inclusion of TEM turbulence may impact the density peaking [Fable et al. 2009], but the bulk of simulations carried out in this work are with heat transport only. The effect of plasma rotation and $\mathbf{E} \times \mathbf{B}$ flow shear on turbulent transport is excluded.

**Ad-hoc effective shear to account for impact of MHD $\alpha$ on transport**

Hybrid scenarios are characterized by a high value of the normalized pressure gradient $\alpha = \frac{d\tilde{\beta}}{d\rho} q^2 R_0$ (where $\beta$ is the ratio of the volume averaged kinetic pressure to the magnetic pressure) towards the edge of the plasma. The standard version of QLKNN does not take into account the impact of $\alpha$ on transport ($\alpha$ is not included in any of the neural network inputs). In the QuaLiKiz geometry model, the quantity $\alpha$ roughly modifies the shear $s \to s - \alpha$. Not taking into account this decrease of the effective shear leads to a systematic over-prediction of temperatures for the ITER hybrid scenario (consider the scaling for the ITG threshold mentioned earlier: $R/L_{T_{i \, crit}} \sim s/q$). Standalone studies with the full QuaLiKiz model show that within the ITER hybrid scenario parameter range, a decent proxy for the impact of $\alpha$ on predicted transport can be obtained by feeding the model an effective shear: $s_{eff} = s - 0.5\alpha$. This ad-hoc rule motivates a transformation of the shear input of the neural network $s \to s - 0.5\alpha$ when modeling hybrid scenarios, leading to excellent agreement of the temperature profiles predicted respectively by JETTO-QuaLiKiz and JETTO-QLKNN with adjusted neural network inputs.

The $s \to s - 0.5\alpha$ transformation is hence applied for ITER hybrid modeling in RAPTOR-QLKNN. To illustrate the validity of this approach, Figure 4.5 compares the temperature and temperature inverse scale length profiles obtained with RAPTOR-QLKNN at the reference plasma current $I_p = 10.5\,\text{MA}$, feeding the neural network shear input with either $s$, $s - 0.5\alpha$ or $s - \alpha$, to relaxed JETTO profiles (time dependent JETTO run, solving solely for electron and ion heat diffusion, ensuring a $q$ profile identical to the RAPTOR run), applying respectively the

Figure 4.5: **Transport model benchmark** A comparison is shown of the temperature and temperature inverse scale length profiles obtained with RAPTOR-QLKNN (*R-QLKNN*) at the reference current $I_p = 10.5$ MA, feeding the neural network shear input with either $s$, $s - 0.5\alpha$ or $s - \alpha$, to relaxed JETTO profiles (time dependent JETTO run, solving solely for electron and ion heat diffusion, ensuring a $q$ profile identic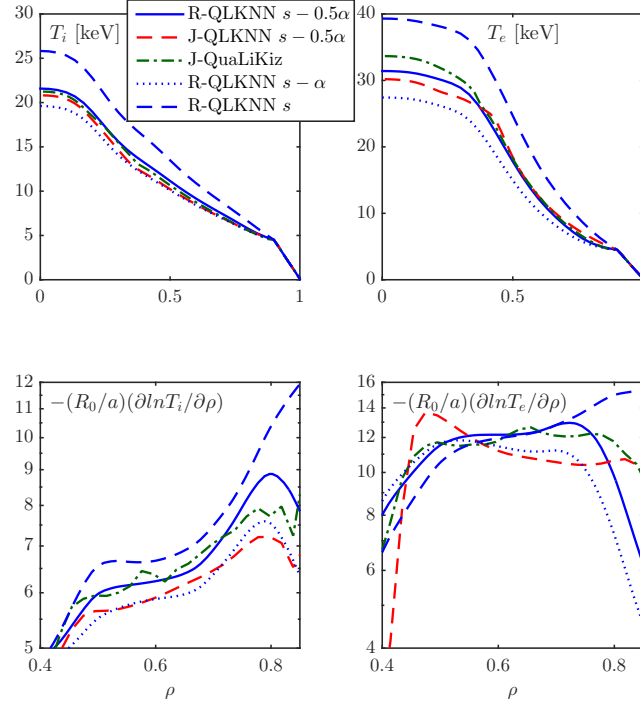al to the RAPTOR run), applying respectively the $s - 0.5\alpha$ corrected QLKNN transport model (*J-QLKNN*) and full QuaLiKiz (*J-QuaLiKiz*). *Reproduced from [Van Mulders et al. 2021b].*

$s - 0.5\alpha$ corrected QLKNN transport model and full QuaLiKiz. The full QuaLiKiz simulation is in close agreement with both JETTO and RAPTOR simulations applying the $s - 0.5\alpha$ correction, as remaining differences can be accounted for to some extent by different smoothing of the predicted heat diffusivity profiles.

**Alternative transport mechanisms**

Although the transport model predicts low transport levels at low radii, flattened temperature profiles toward the magnetic axis are anticipated, even in the absence of sawtooth activity. This statement is motivated by experimental measurements and the results described in [Kumar et al. 2020], where the presence of kinetic ballooning modes in the hybrid plasma core is predicted. This is taken into account by adding a gaussian to the diffusivity predictions, centered at $\rho = 0$, with width $\Delta\rho = 0.1$ and height $\chi_{e,i\,0} = 2\,\mathrm{m}^2/\mathrm{s}$.

As noted above, electromagnetic and fast ion effects are missing in the applied transport model. These effects are seen to increase confinement in present-day hybrid scenarios [Citrin et al. 2014; Jian et al. 2019], while recent work indicates that ITG suppression by fast alphas will also allow improved confinement in ITER [Garcia et al. 2018; Mazzi et al. 2022]. Although the quantitative degree of confinement improvement for ITER due to these effects is uncertain, the levels of core confinement presented in this chapter could hence be under-predicted, providing a conservative lower bound for ITER hybrid performance. Note however that the $s/q$ optimization path is largely independent from these considerations, with the trends seen in ECCD deposition modification and impact of $s/q$ on ITG thresholds holding regardless of the electromagnetic and fast ion effects.

The reference case simulation predicts a strong temperature difference between ions and electrons is maintained in stationary state ($T_{e0}/T_{i0} = 1.46$). In [Stober et al. 2015] the small impact of dominant electron heating on $T_{e0}/T_{i0}$ was illustrated for the ITER inductive scenario. A reduced equipartition heating due to the lower density allows for a stronger temperature ratio in the hybrid scenario. While the stiffness of the ion temperature profile predicted by the present model results in a very weak dependence of the fusion power on the ion heating, the electron profile is notably less stiff, hence resulting in a strong dependence of plasma resistivity, bootstrap current and electron cyclotron current drive efficiency on the level of electron heating.

## 4.4 Optimization of the electron cyclotron deposition profile

The shape of the $q$ profile can be tailored to some extent by optimizing the radial deposition profile of auxiliary current drive sources. The present study considers the optimization of the electron cyclotron current drive profile. Various approaches can be envisioned to parametrize the radially distributed deposition profile in terms of a set of optimization variables. Without making an a priori assumption on the shape of these profiles, the radial deposition profile can be written as the sum of a set of cubic spline basis functions. The procedure for optimizing

a distributed quantity on a basis of splines is discussed in detail in Section 2.5.2. The cost function applied here aims for a maximum fusion gain through minimizing the cost function $J = -Q$, while $q > 1$ is imposed as the constraint $\mathscr{C}_{q>1}$ (2.55).

The optimization problem under consideration is solved on several spline bases, with an increasing number of splines, hence increasing the degrees of freedom available to fine-tune the radial electron cyclotron deposition profile. The behaviour of the resulting optima is presented in Figure 4.6. Increasing the number of splines above 7 has a minor impact on the resulting maximum fusion gain $Q$. This can be understood as follows: to obtain maximum energy confinement, hybrid scenarios maximize the outermost radius with safety factor close to unity, which then results in a maximum magnetic shear further outward. The increased ratio $s/q$ raises the onset threshold for ITG-driven turbulence. The same logic was outlined in [Citrin et al. 2010], where the electron cyclotron current drive distribution was manually tailored to have the $q$ profile clamped to the $q = 1$ constraint at the outermost radius that can be achieved with the available electron cyclotron power. The execution of this procedure is now fully automated. Figure 4.6 shows that with spline bases containing respectively 7 and 9 basis functions, the $q$ profile can be clamped to $q = 1$ at a strikingly similar outermost radius. The outer $s$ and $q$ profiles are virtually identical, yielding similar ITG threshold enhancements and hence fusion gains $Q$.

Further insight is gained by formulating the optimization problem in terms of a single optimization variable: the deposition location of a fixed-width gaussian (width $\Delta\rho = 0.15$). The resulting optimum ($\rho_{ec} = 0.33$) illustrates that a single degree of freedom is sufficient to retrieve the optimum $q$ profile, i.e. the $q$ profile impinging $q = 1$ at the outermost radius that can be achieved with the available electron cyclotron resources. In addition to this optimum, Figure 4.6 also illustrates the $q$ profiles that result from depositing the electron cyclotron current drive further outward ($\rho_{ec} = 0.4$) or inward ($\rho_{ec} = 0.2$). Deposition further out clearly results in a sub-optimal situation: the available electron cyclotron power is not sufficient to pin the $q$ profile down to $q = 1$ (note that the electron cyclotron current drive efficiency degrades when moving to larger radii), resulting in a reduced magnetic shear at outer radii, yielding $Q \sim 4.5$. Although deposition of the electron cyclotron waves further inward results in an increased shear at outer radii, yielding $Q \sim 6.1$, the $q > 1$ constraint is violated.

To check the impact of the assumed deposition width, the optimizer is run with different settings for the width of the gaussian, in a range $\Delta\rho = 0.1 - 0.3$. Reducing the width allows an increase of $s/q$ around mid-radius, improving the confinement enhancement. However, for $\Delta\rho < 0.2$, the fusion gain increase that can be achieved by further reducing $\Delta\rho$ turns out to be negligible.

Now that the consequences of an increase and decrease of the electron cyclotron deposition radius are understood, it is instructive to visualize subsequent optimizer iteration steps. Figure 4.7 shows the heat deposition profile and corresponding $q$ and $T_i$ profiles for every stationary plasma state for which the cost function is evaluated. From the initial deposition radius at $\rho_{ec} = 0.5$, a clear confinement increase can be achieved by reducing $\rho_{ec}$. As the optimizer overshoots into the infeasible operating space with $q < 1$, the constraint gradient guides the state back, by increasing $\rho_{ec}$ until $q > 1$.
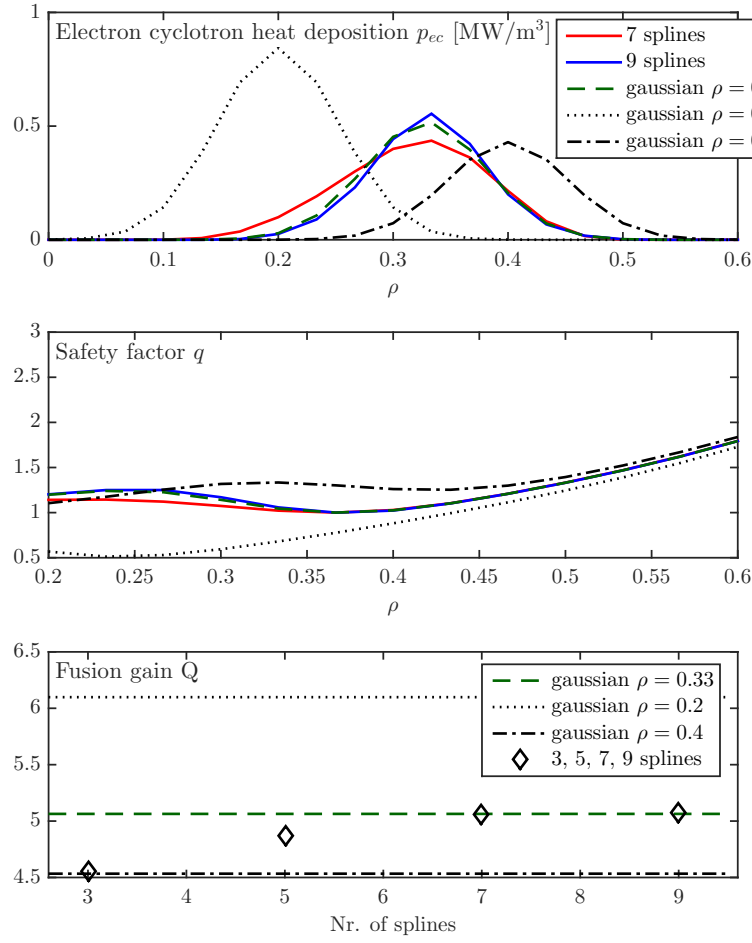
Figure 4.6: *q* **profile tailoring with EC deposition** The optimization problem is solved on several spline bases, with an increasing number of splines, hence increasing the degrees of freedom available to fine-tune the radial electron cyclotron deposition profile. Increasing the number of splines above 7 has a minor impact on the resulting maximum fusion gain *Q*. The figure also presents the performance of the stationary states corresponding to electron cyclotron deposition modeled as a single fixed-width gaussian (width $\Delta\rho = 0.15$), with deposition location at $\rho_{ec} = 0.2$, $\rho_{ec} = 0.33$ (optimum) and $\rho_{ec} = 0.4$. *Reproduced from [Van Mulders et al. 2021b].*
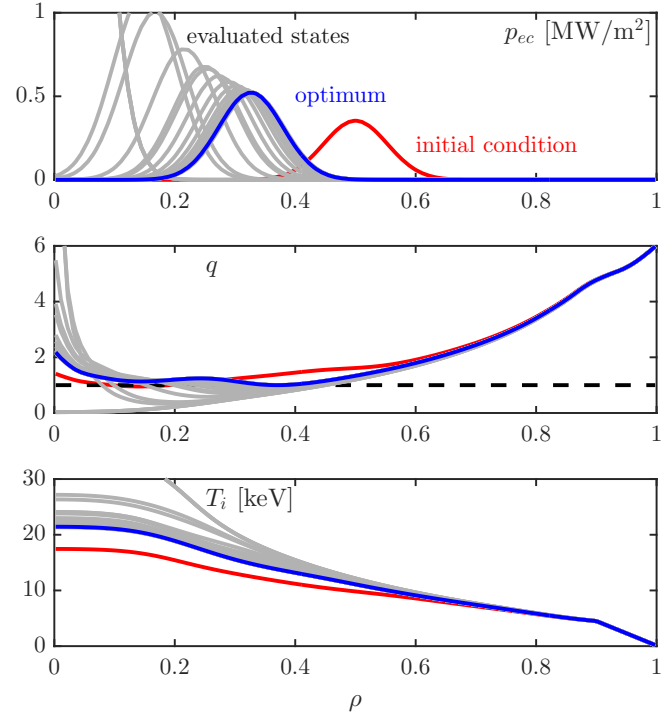
Figure 4.7: **Optimizer iteration steps** The heat deposition profile $p_{ec}$, $q$ profile and $T_i$ profile for every stationary plasma state which the optimization routine has visited are shown. *Reproduced from [Van Mulders et al. 2021b].*

Numerical experiments in which the inputs to the neural network are manipulated can give understanding in the transport physics effects at play when moving $\rho_{ec}$ inward. On the one hand one can expect the $T_{e,i}$ profiles to rise as a result of the increased heat flux passing at low radii (heat flux $q_{e,i} \sim \chi_{e,i} \frac{\partial T_{e,i}}{\partial \rho}$). Due to the stiffness characterizing plasma turbulence, this effect is anticipated to be secondary compared to the impact of the increased $s/q$ (beyond mid-radius) on the ITG threshold. This can be illustrated as follows: the stationary solution for the optimum $\rho_{ec} = 0.33$ can be recalculated while feeding the $q$ and $s$ profile corresponding to the stationary state solution with $\rho_{ec} = 0.5$ to the neural networks. In this way the effect of $q$ profile tailoring is neutralized. The result is presented in Figure 4.8. The profiles corresponding to the stationary state attained for $\rho_{ec} = 0.5$ are shown in red, while the stationary state reached for the optimum $\rho_{ec} = 0.33$ is represented in blue. The green profiles show the temperatures and thermal diffusivities achieved when depositing the electron cyclotron waves at $\rho_{ec} = 0.33$, but providing the $s$ and $q$ profiles of the $\rho_{ec} = 0.5$ simulation to the respective neural network inputs. There is virtually no change in the ion temperature $T_i$ (and hence $Q$) between the red and the green profiles. Although the ion heat flux passing through $\rho \sim 0.33$ is increased through electron-ion equipartitioning, this effect is counteracted by an increased ion heat diffusivity $\chi_i$. Note that the electron temperature profile behaves notably less stiff. However, when the consistent $s$ and $q$ profiles are fed to the neural network, an ion energy confinement enhancement is observed. A rise in the ratio $s/q$ for radii $\rho > 0.4$ results in a drop of the ion heat diffusivity around mid-radius, resulting in a distinct rise of both $T_i$ and $T_e$. Since the temperature equations are not solved within the pedestal region, the local diffusivities are not evaluated for $\rho > 0.9$.

## 4.5 Scan over optima at different total plasma current

The previous section illustrated how the optimization of the deposition location of a single fixed-width gaussian suffices to have the $q$ profile clamped to $q = 1$ as far radially out as possible for a given total electron cyclotron power ($P_{ec} = 40\,\mathrm{MW}$), resulting in maximized fusion gain $Q$ with $q > 1$ for fixed total plasma current ($I_p = 10.5\,\mathrm{MA}$), neutral beam power deposition profiles ($P_{nb} = 33\,\mathrm{MW}$, $p_{nb\,e,i}(\rho)$, $j_{nb}(\rho)$) and plasma density profile ($n_e(\rho)$ with $\langle n_e \rangle_{line}/n_{e\,Gw} = 0.9$ and $n_{e,0}/n_{e\,ped} = 1.4$). This section presents scans over operation points in a total plasma current range bounded on the low side by fully non-inductive operation $I_p = I_{ni}$ and on the high side by the maximum $I_p$ for which $q > 1$ can be sustained (for given density profile and auxiliary powers). Note that operation at lower Greenwald density fraction allows operation at higher plasma currents due to the increased current drive efficiency of auxiliary heating systems.

This scan is repeated at two levels of neutral beam total power injection, respectively 33 MW and 16.5 MW. For each value of $I_p$ and $P_{nb}$, the optimization routine finds the electron cyclotron deposition location $\rho_{ec}$ maximizing fusion gain $Q$, assuming fixed total auxiliary powers ($P_{nb} = 33/16.5\,\mathrm{MW}$ and $P_{ec} = 40\,\mathrm{MW}$), while ensuring $q > 1$. Electron density, neutral beam deposition and line radiation profiles are modeled as outlined in Section 4.3, rendering
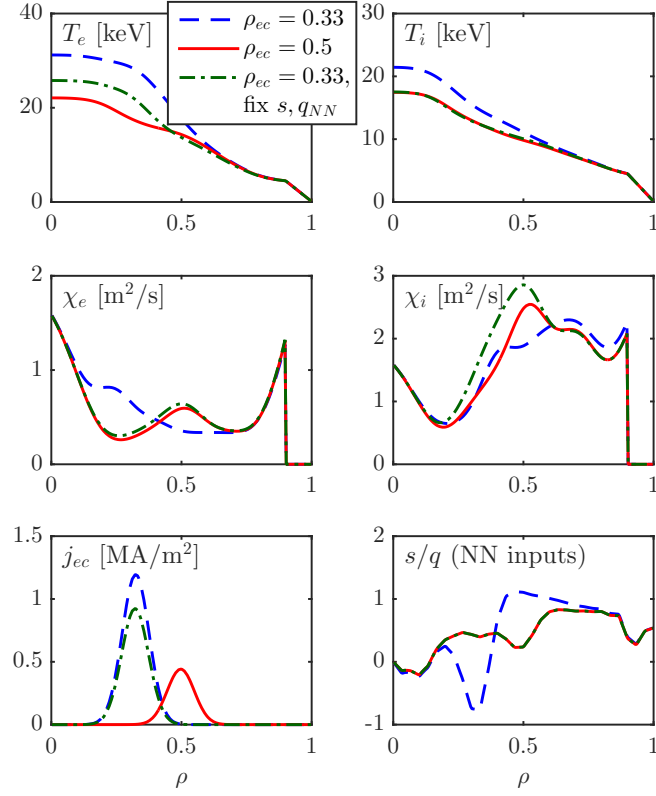
Figure 4.8: **Impact $q$ profile tailoring on transport** The profiles corresponding to the stationary state attained for $\rho_{ec} = 0.5$ are shown in red, while the stationary state reached for the optimum $\rho_{ec} = 0.33$ is represented in blue. The green profiles show the temperatures and thermal diffusivities achieved when depositing the electron cyclotron waves at $\rho_{ec} = 0.33$, but providing the $s$ and $q$ profiles of the $\rho_{ec} = 0.5$ simulation to the respective neural network inputs. *Reproduced from [Van Mulders et al. 2021b].*
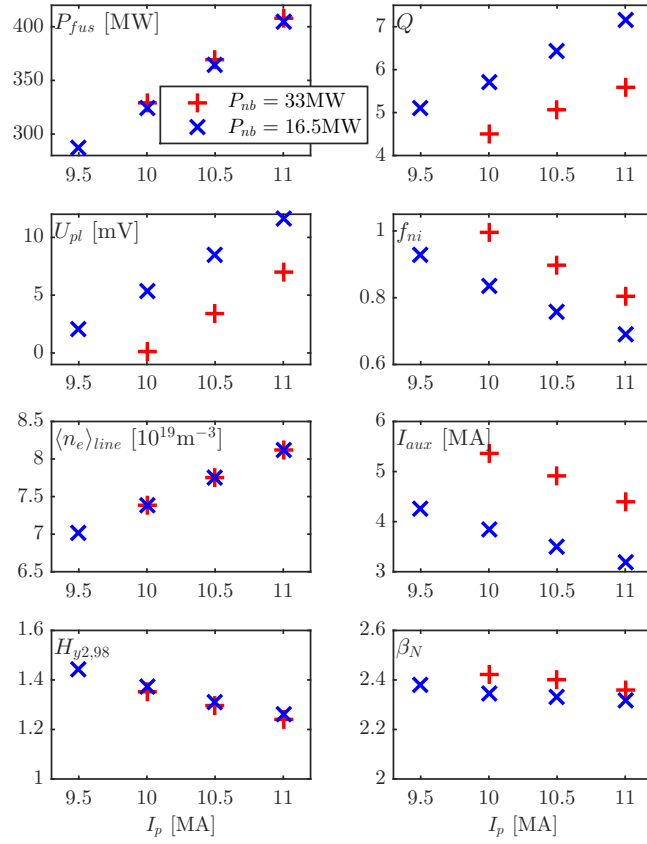
Figure 4.9: **Optimize $\rho_{ec}$ to maximize Q with q > 1 for various $I_p$ and a fixed heating mix** Key performance indicators are shown for the operation points maximizing fusion gain $Q$, assuming fixed total auxiliary powers ($P_{nb} = 33/16.5\,\text{MW}$ and $P_{ec} = 40\,\text{MW}$), while ensuring $q > 1$, with the electron cyclotron deposition location $\rho_{ec}$ as single optimization variable. *Reproduced from [Van Mulders et al. 2021b].*

those profile values simple linear functions of the total plasma current $I_p$. The fusion gain can be further enhanced at given total plasma current and neutral beam power, by reducing the total electron cyclotron power $P_{ec}$. The resulting two-dimensional optimization problems are presented in Section 4.6.

Key physical quantities and performance indicators of the optimal scenarios, obtained at different values of $I_p$, are summarized in Figure 4.9 ($P_{nb} = 33/16.5\,\text{MW}$), Table 4.2 ($P_{nb} = 33\,\text{MW}$) and Table 4.3 ($P_{nb} = 16.5\,\text{MW}$). The electron cyclotron deposition location $\rho_{ec}$ is indicated for each of the scenarios in Table 4.2 and Table 4.3. Note that although this optimization variable only varies modestly between the various optima, it is clear that an increased plasma current $I_p$ requires the deposition of the electron cyclotron current drive at larger radii to avoid the $q$ profile to drop below $q = 1$.

For a given total auxiliary power $P_{aux}$, the increase of plasma current $I_p$ allows an increase of the produced fusion power $P_{fus}$ (and hence an increase of $Q = P_{fus}/P_{aux}$), at the expense of

| $I_p$ | $\rho_{ec}$ | $P_{fus}$ | $P_{aux}$ | $I_{aux}$ | $Q$ | $U_{pl}$ | $f_{ni}$ | $f_{bs}$ | $H_{y2,98}$ | $\beta_N$ |
|---|---|---|---|---|---|---|---|---|---|---|
| [MA] | | [MW] | [MW] | [MA] | | [mV] | | | | |
| | | | nb + ec | | | | | | | |
| 10 | 0.31 | 326 | 33+40 | 5.3 | 4.5 | 0.5 | 0.98 | 0.45 | 1.4 | 2.4 |
| 10.5 | 0.33 | 367 | 33+40 | 4.8 | 5.0 | 3.7 | 0.89 | 0.43 | 1.3 | 2.4 |
| 11 | 0.34 | 404 | 33+40 | 4.3 | 5.5 | 7.4 | 0.80 | 0.40 | 1.2 | 2.4 |

**Table 4.2: Optimize $\rho_{ec}$ to maximize Q with q > 1 for various $I_p$ and a fixed heating mix ($P_{nb}$ = 33MW)** Key performance indicators are shown for the operation points maximizing fusion gain $Q$, assuming fixed total auxiliary powers ($P_{nb} = 33$ MW and $P_{ec} = 40$ MW), while ensuring $q > 1$, with the electron cyclotron deposition location $\rho_{ec}$ as single optimization variable. *Reproduced from [Van Mulders et al. 2021b].*

| $I_p$ | $\rho_{ec}$ | $P_{fus}$ | $P_{aux}$ | $I_{aux}$ | $Q$ | $U_{pl}$ | $f_{ni}$ | $f_{bs}$ | $H_{y2,98}$ | $\beta_N$ |
|---|---|---|---|---|---|---|---|---|---|---|
| [MA] | | [MW] | [MW] | [MA] | | [mV] | | | | |
| | | | nb + ec | | | | | | | |
| 9.5 | 0.29 | 283 | 16.5+40 | 4.2 | 5.0 | 2.4 | 0.92 | 0.48 | 1.4 | 2.4 |
| 10 | 0.30 | 322 | 16.5+40 | 3.8 | 5.7 | 5.5 | 0.83 | 0.45 | 1.4 | 2.3 |
| 10.5 | 0.32 | 363 | 16.5+40 | 3.5 | 6.4 | 8.7 | 0.75 | 0.42 | 1.3 | 2.3 |
| 11 | 0.33 | 402 | 16.5+40 | 3.2 | 7.1 | 12.0 | 0.68 | 0.40 | 1.3 | 2.3 |

**Table 4.3: Optimize $\rho_{ec}$ to maximize Q with q > 1 for various $I_p$ and a fixed heating mix ($P_{nb}$ = 16.5MW)** Key performance indicators are shown for the operation points maximizing fusion gain $Q$, assuming fixed total auxiliary powers ($P_{nb} = 16.5$ MW and $P_{ec} = 40$ MW), while ensuring $q > 1$, with the electron cyclotron deposition location $\rho_{ec}$ as single optimization variable. *Reproduced from [Van Mulders et al. 2021b].*

an increased need for inductive current drive (increase of the loop voltage $U_{pl}$), ultimately limiting the burn phase duration. The achievable burn phase duration is dependent on the flux swing available during the flat-top discharge phase, i.e. the total available central solenoid flux charge ($\psi_0 = 240$ Wb) minus the flux swing consumption during ramp-up. Although the latter is dependent on the ramp-up scenario, a simple estimate is given in [Polevoi et al. 2020]: $\Delta\psi_{ramp} = 14 I_p$. These numbers allow to calculate an approximate value for the loop voltage required for operation over $t_{burn} = 3000s$ at $I_p = 11$ MA:

$$U_{pl\ required} = \frac{\psi_0 - \Delta\psi_{ramp}}{t_{burn}} = 29\,\text{mV} \tag{4.1}$$

This value is higher than any of the stationary state loop voltages obtained in this section. This indicates that any scenario presented in this section can in principle be sustained for the full time window available for an ITER discharge.

The ion core temperatures do not vary significantly over the considered $I_p$ range. This leads to an increasingly large energy confinement enhancement compared to the H98(y,2) scaling law for reducing total plasma current $I_p$. Improved pedestal confinement for higher plasma current is accounted for by the linear pedestal pressure height increase with $I_p$. Nevertheless, QLKNN predicts an improved overall core confinement enhancement for reduced $I_p$, as confirmed by the $H_{y2,98}$ factors in Table 4.2 and 4.3 and Figure 4.9. ECCD tailoring of the $q$

profile with ECCD is more effective at lower $I_p$ with ECCD, while the increased value of $q_{95}$ gives rise to a stronger shear in the outer plasma region (assuming $q \sim 1$ in the center).

An increased plasma current $I_p$ requires increased inductive current drive $I_{ind} = I_p - I_{aux} - I_{bs}$. This is not solely due to the higher total current requirement, but also because of the degrading efficiency of auxiliary current drive at higher densities (i.e. decreasing $I_{aux}$). A fusion gain of $Q = 4.5$ is modeled at virtually steady state conditions for $I_p = 10\,\text{MA}$ and $P_{nb} = 33\,\text{MW}$ ($f_{ni} \sim 1$). The density increase following the plasma current increase to $11\,\text{MA}$ results in a fusion gain $Q = 5.5$, while the non-inductive current fraction drops to $f_{ni} = 0.80$, requiring a loop voltage $U_{pl} = 7.4\,\text{mV}$.

Comparing the optima for both levels of neutral beam power $33\,\text{MW}$ and $16.5\,\text{MW}$, it is clear that a reduced beam power benefits the fusion gain, although the reduced amount of auxiliary driven current needs to be compensated by an increased inductive current drive (loop voltage $U_{pl}$). The optimized off-axis electron cyclotron current drive allows the formation of similar hybrid scenario $q$ profiles for either $P_{nb} = 33\,\text{MW}$ or $16.5\,\text{MW}$, resulting in a similar energy confinement enhancement ($H_{y2,98}$ factors on Figure 4.9). The increased heat flux passing through the plasma barely impacts the fusion power density due to the stiffness of the ion temperature profile. As a result, similar total fusion powers $P_{fus}$ can be achieved with less auxiliary resources $P_{aux}$, giving fusion gains in the range $Q = 5.0 \rightarrow 7.1$, while $U_{pl} = 2.4\,\text{mV} \rightarrow 12.0\,\text{mV}$ and $f_{ni} = 0.92 \rightarrow 0.68$. Furthermore, for steady state operation with $P_{nb} = 16.5\,\text{MW}$, the plasma current needs to be reduced below $I_p = 9.5\,\text{MA}$. Although the fusion gain for this steady state scenario is still around 5, the resulting fusion power drops below $300\,\text{MW}$. Note that for all of the above scenarios $P_{sep} > 1.2 P_{LH}$, where the power crossing the separatrix is $P_{sep} = P_{oh} + P_{alpha} + P_{aux} - P_{rad}$ and the HL threshold power is evaluated with the Martin scaling law [Martin and Takizuka 2008].

## 4.6 Optimization of the heating mix

### 4.6.1 Neutral beam and electron cyclotron power

The previous section illustrates how both an increase of total plasma current and a reduction of neutral beam power give rise to an increasing fusion gain $Q$ at the expense of a reduced maximum burn phase duration $t_{burn} \sim 1/U_{pl}$ (for a fixed electron cyclotron power $P_{ec}$). This result provokes the question whether a further increase of $Q$ can be achieved by reducing the electron cyclotron heating power. This can be investigated quantitatively by formulating an optimization problem in terms of two optimization variables: electron cyclotron deposition location $\rho_{ec}$ and total electron cyclotron power $P_{ec}$. The optimization objective is the maximization of the fusion gain $Q$, while satisfying the constraint $q > 1$. An additional constraint is added to ensure that the power crossing the separatrix $P_{sep}$ remains more than 20% in excess of the HL threshold power $P_{LH}$ [Martin and Takizuka 2008]: $P_{sep} > 1.2 P_{LH}$. Figure 4.10
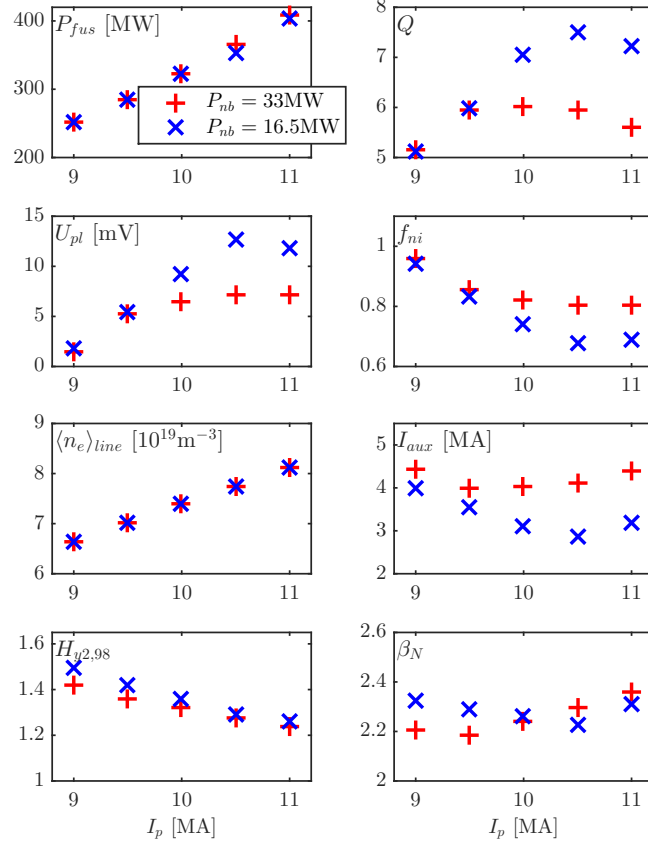
Figure 4.10: **Optimize $\rho_{ec}$ and $P_{ec}$ to maximize Q with q > 1 and $P_{sep}$ > 1.2$P_{LH}$ for various $I_p$** Key performance indicators are shown for the operation points maximizing the fusion gain $Q$ with $q > 1$ and $P_{sep} > 1.2P_{LH}$ for given plasma current and neutral beam power $P_{nb} = 33/16.5$ MW, optimizing the electron cyclotron heating power $P_{ec}$ and deposition location $\rho_{ec}$. *Reproduced from [Van Mulders et al. 2021b].*
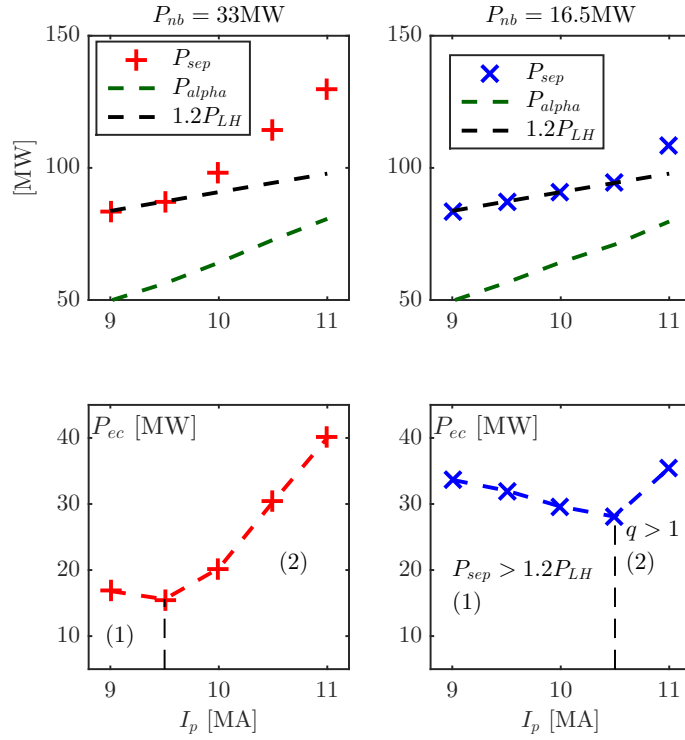
Figure 4.11: **Active constraints when reducing $P_{ec}$ to maximize Q with $q > 1$ and $P_{sep} > 1.2P_{LH}$** In the upper panels, the power crossing the separatrix is shown for the various optima obtained by maximizing the fusion gain $Q$ for given plasma current and neutral beam power $P_{nb} = 33 16.5$ MW, optimizing the electron cyclotron heating power $P_{ec}$ and deposition location $\rho_{ec}$. The $P_{sep} > 1.2P_{LH}$ constraint and alpha heating power are also shown. For scenarios at the lower end of the $I_p$ range the feasible reduction of the electron cyclotron power is clearly limited by the $P_{sep}$ constraint (labeled (1) in the lower panels), while the $q > 1$ constraint limits a further reduction of $P_{ec}$ on the higher end of the $I_p$ range (labeled (2) in the lower panels). *Reproduced from [Van Mulders et al. 2021b].*

| $I_p$ | $\rho_{ec}$ | $P_{fus}$ | $P_{aux}$ | $I_{aux}$ | $Q$ | $U_{pl}$ | $f_{ni}$ | $f_{bs}$ | $H_{y2,98}$ | $\beta_N$ |
|------|------|------|------|------|------|------|------|------|------|------|
| [MA] | | [MW] | [MW] | [MA] | | [mV] | | | | |
| | | | nb + ec | | | | | | | |
| 9 | 0.25 | 249 | 33+17 | 4.4 | 5.0 | 1.3 | 0.96 | 0.47 | 1.4 | 2.2 |
| 9.5 | 0.26 | 281 | 33+16 | 4.0 | 5.8 | 5.1 | 0.86 | 0.44 | 1.4 | 2.2 |
| 10 | 0.29 | 321 | 33+20 | 3.9 | 6.0 | 6.8 | 0.81 | 0.42 | 1.3 | 2.2 |
| 10.5 | 0.32 | 364 | 33+30 | 4.2 | 5.7 | 6.8 | 0.81 | 0.41 | 1.3 | 2.3 |
| 11 | 0.34 | 404 | 33+40 | 4.3 | 5.5 | 7.4 | 0.80 | 0.40 | 1.2 | 2.4 |

Table 4.4: **Optimize $\rho_{ec}$ and $P_{ec}$ to maximize Q with q > 1 and $P_{sep}$ > 1.2$P_{LH}$ for various $I_p$ ($P_{nb}$ = 33MW)** Key performance indicators are shown for the operation points maximizing the fusion gain $Q$ with $q > 1$ and $P_{sep} > 1.2P_{LH}$ for given plasma current $I_p$ and neutral beam power $P_{nb} = 33$ MW, optimizing the electron cyclotron heating power $P_{ec}$ and deposition location $\rho_{ec}$.

| $I_p$ | $\rho_{ec}$ | $P_{fus}$ | $P_{aux}$ | $I_{aux}$ | $Q$ | $U_{pl}$ | $f_{ni}$ | $f_{bs}$ | $H_{y2,98}$ | $\beta_N$ |
|------|------|------|------|------|------|------|------|------|------|------|
| [MA] | | [MW] | [MW] | [MA] | | [mV] | | | | |
| | | | nb + ec | | | | | | | |
| 9.0 | 0.27 | 248 | 16.5+34 | 4.1 | 5.0 | 1.5 | 0.95 | 0.50 | 1.5 | 2.3 |
| 9.5 | 0.28 | 283 | 16.5+32 | 3.6 | 5.8 | 5.2 | 0.84 | 0.46 | 1.4 | 2.3 |
| 10 | 0.29 | 321 | 16.5+30 | 3.1 | 7.0 | 9.1 | 0.74 | 0.43 | 1.4 | 2.3 |
| 10.5 | 0.31 | 355 | 16.5+28 | 2.7 | 7.9 | 13.3 | 0.66 | 0.40 | 1.3 | 2.2 |
| 11 | 0.33 | 399 | 16.5+35 | 2.9 | 7.6 | 13.7 | 0.65 | 0.39 | 1.3 | 2.3 |
| 11 | 0.33 | 396 | 0+42 | 2.1 | 9.4 | 16.5 | 0.58 | 0.39 | 1.3 | 2.3 |

Table 4.5: **Optimize $\rho_{ec}$ and $P_{ec}$ to maximize Q with q > 1 and $P_{sep}$ > 1.2$P_{LH}$ for various $I_p$ ($P_{nb}$ = 16.5MW)** Key performance indicators are shown for the operation points maximizing the fusion gain $Q$ with $q > 1$ and $P_{sep} > 1.2P_{LH}$ for given plasma current $I_p$ and neutral beam power $P_{nb} = 16.5$ MW, optimizing the electron cyclotron heating power $P_{ec}$ and deposition location $\rho_{ec}$. For $I_p = 11$ MA, the optimum obtained without any neutral beam power is also presented.

($P_{nb} = 33/16.5$ MW), Table 4.4 ($P_{nb} = 33$ MW) and Table 4.5 ($P_{nb} = 16.5$ MW) present salient performance indicators of the resulting optimized scenarios, as well as the obtained values for the optimization variables $\rho_{ec}$ and $P_{ec}$.

Comparing Table 4.4 to Table 4.2 and Table 4.5 to Table 4.3, a reduction of the electron cyclotron power indeed results in an increase of the fusion gain $Q$. The reduction of electron cyclotron current drive needs to be compensated by an increased loop voltage driving inductive current. Due to ion temperature profile stiffness, the heating power reduction only moderately affects the produced fusion power, as long as the current drive capability is sufficient to maintain $q > 1$. The increase of $Q$ which can be achieved depends on the magnitude of the decrease of the electron cyclotron power. Depending on the value of the total plasma current, the feasible reduction of the electron cyclotron power is limited by one of the following constraints.

- The current density profiles of scenarios at the *higher end of the $I_p$ range* have a comparatively larger contribution driven inductively and hence require in absolute terms more off-axis non-inductive current drive to maintain $q > 1$, limiting the feasible $P_{ec}$

reduction. Since this effect dominates the increase of fusion power for increased plasma current (due to increased density), *an increase of $I_p$ leads to a decreasing fusion gain Q*.

- For scenarios at the *lower end of the $I_p$ range* the feasible reduction of the electron cyclotron power is limited by the $P_{LH}$ constraint. This is clearly illustrated in Figure 4.11, where the power crossing the separatrix and the constraining lower value are shown for the different scenarios. Although the required threshold power $P_{LH}$ decreases for reduced plasma current $I_p$ (due to reduced density[2]), this does not lead to a reduction of the required total auxiliary power since fusion power is essentially proportional to the square of the density and the plasma self-heating due to fusion-born alphas hence strongly diminishes (also shown in Figure 4.11). Within this range, *an increase of $I_p$ allows for an increasing fusion gain Q*.

Due to these counteracting effects, the achievable increase for the fusion gain $Q$ is most pronounced for intermediate plasma currents, as illustrated in Figure 4.10 and Figure 4.11. For those scenarios where the separatrix power constraint is not active, the loop voltage $U_{pl}$ is virtually constant due to the counteracting effects of increasing total current and reducing current drive efficiency on the one hand and an increased level of maintained electron cyclotron current drive.

It might be surprising to notice that for $I_p = 11\,\text{MA}$ (where the $P_{LH}$ constraint is not active), a lower level of electron cyclotron power is required to maintain $q > 1$ when decreasing the neutral beam power power from $P_{nb} = 33\,\text{MW}$ to $P_{nb} = 16.5\,\text{MW}$ (the required electron cyclotron power decreases from $P_{ec} = 40\,\text{MW}$ to $P_{ec} = 35\,\text{MW}$). Note that violation of the $q > 1$ constraint at low radii is dependent on the particular shape of $j_{oh} + j_{bs} + j_{nb}$, which strongly depends on the imposed neutral beam and density profiles. Since the peak of the neutral beam current density profile is relatively close to the magnetic axis in the present simulations, a reduced neutral beam power can relax the required amount of off-axis electron cyclotron current to maintain $q > 1$.

Finally, one might consider a further reduction of the neutral beam power down to zero. Looking for a maximum fusion gain $Q$, with $q > 1$ and $P_{sep} > 1.2P_{LH}$, an optimum is found with $P_{ec} = 42\,\text{MW}$ (see final row Table 4.5). For the selected density, an electron cyclotron power slightly in excess of the upgraded electron cyclotron power capability is required in absence of any neutral beam power. Although a high fusion gain $Q = 9.4$ is projected, a major contribution of inductive current drive is required ($U_{pl} = 16.5\,\text{mV}$ and $f_{ni} = 0.58$). Note that scenarios without neutral beam injection at lower plasma current would require a further increase of the electron cyclotron power to maintain $P_{sep} > 1.2P_{LH}$, due to the reduced alpha heating.

In conclusion, the fusion power is only modestly impacted by the additional heat flow caused by auxiliary heating, due to the stiffness of the ion temperature profile. Upper limits for the

---

[2]Note that while the Martin scaling law [Martin and Takizuka 2008] reports a dependence $P_{LH} \sim \langle n_e \rangle_{line}^{0.72} B_0^{0.80} S^{0.94}$ ($S$ is the plasma surface area in m$^2$), an increase of $P_{LH}$ with decreasing density is observed below a critical density, as discussed in [Sauter et al. 2011] and refs therein.

fusion gain $Q$ are hence set by either minimum power requirements for the separatrix power flow to maintain H-mode or by minimum current drive requirements for $q$ profile tailoring.

### 4.6.2 ITER baseline heating mix

Many of the above simulations assume the availability of 40 MW electron cyclotron power on ITER. In the present section a brief assessment is made of the hybrid scenario performance that can be achieved with the baseline heating mix foreseen for ITER, including 33 MW of neutral beam power, 20 MW of electron cyclotron power and 20 MW of ion cyclotron power [Shimada et al. 2007]. For a given total plasma current $I_p$, one can envisage two pathways to reduce electron cyclotron heating in the presence of the $q > 1$ and $P_{LH}$ constraints.

- The available ion cyclotron heating power can contribute to the required power flow across the separatrix.

- A reduction of the density, accompanied by a simultaneous increase of temperature pedestal to maintain identical pedestal pressure, renders both constraints less stringent: (1) maintaining $P_{sep} > 1.2 P_{LH}$ requires less electron cyclotron power because the decrease of $P_{LH}$ for reducing density dominates the decrease of alpha heating (the effect of reducing density is partly counteracted by an increasing ion temperature pedestal[3].); (2) maintaining $q > 1$ requires less electron cyclotron power because of the increase in current drive efficiency.

To quantify the potential of these pathways, an optimization problem is constructed in terms of three optimization variables: electron cyclotron deposition location $\rho_{ec}$, total plasma current $I_p$ and ion cyclotron heating power $P_{ic}$. Ion cyclotron heating is modeled as a gaussian centered on the magnetic axis with width $\Delta\rho = 0.2$, depositing equal amounts of power to ions and electrons[4]. The goal is once more maximizing the fusion gain $Q$ with $q > 1$ and $P_{sep} > 1.1 P_{LH}$. The optimization is executed for three levels of neutral beam power ($P_{nb} = 0/16.5/33$ MW) in combination with two different densities ($\frac{\langle n_e \rangle_{line}}{n_{e\ Gw}} = 0.9$ and $0.8$), while the electron cyclotron power is set to $P_{ec} = 20$ MW. The results are summarized in Table 4.6. For each of the six cases, the optimizer attempts to increase the plasma current (and density) to the largest extent as feasible without violating the $q > 1$ constraint with the available 20 MW of electron cyclotron heating power. The increasing fusion power for rising density allows to reduce the ion cyclotron heating as the alpha heating contributes to the threshold separatrix power flow required to maintain H-mode. For a given neutral beam power, a reduced density (with simultaneous increase in pedestal temperature), improves the electron cyclotron current drive efficiency, hence allowing to maintain $q > 1$ for a higher plasma current (corresponding

---

[3]For low core temperatures ($T_i \sim 15-20$ keV), the fusion cross-section scales with $(n_e T_i)^2$; the exponent of the $T_i$ dependence however diminishes for higher temperatures [Fable et al. 2019]

[4]Note that for ion cyclotron heating, the relative heating of the different plasma species depends on the applied heating scheme. These considerations are beyond the scope of this chapter. An even split between electron and ion heating for a DT plasma seems however a reasonable first-order estimate [Dumont and Zarzoso 2012].

| $f_{Gw}$ | $I_p$ | $\rho_{ec}$ | $P_{fus}$ | $P_{aux}$ | $I_{aux}$ | $Q$ | $U_{pl}$ | $f_{ni}$ | $f_{bs}$ |
|---|---|---|---|---|---|---|---|---|---|
| | [MA] | | [MW] | [MW] | [MA] | | [mV] | | |
| | | | | nb + ec + ic | | | | | |
| 0.9 | 9.6 | 0.27 | 286 | 0+20+29 | 1.2 | 5.8 | 15.1 | 0.57 | 0.44 |
| 0.8 | 10.2 | 0.29 | 306 | 0+20+19 | 1.4 | 7.8 | 14.3 | 0.55 | 0.42 |
| 0.9 | 10.1 | 0.28 | 321 | 16.5+20+11 | 2.5 | 6.7 | 12.8 | 0.66 | 0.42 |
| 0.8 | 10.6 | 0.31 | 341 | 16.5+20+1 | 2.8 | 9.1 | 12.0 | 0.65 | 0.39 |
| 0.9 | 10.0 | 0.29 | 319 | 33+20+0 | 3.9 | 6.0 | 6.8 | 0.81 | 0.42 |
| 0.8 | 10.5 | 0.31 | 339 | 33+20+0 | 4.5 | 6.4 | 5.5 | 0.83 | 0.40 |

Table 4.6: **Heating mix** Key performance indicators are shown for the operation points maximizing the fusion gain $Q$ with $q > 1$ and $P_{sep} > 1.2P_{LH}$ by optimizing electron cyclotron deposition location $\rho_{ec}$, total plasma current $I_p$ and ion cyclotron heating power $P_{ic}$ (for given neutral beam power $P_{nb} = 0/16.5/33$ MW, electron cyclotron power $P_{ec} = 20$ MW and density $\frac{\langle n_e \rangle_{line}}{n_{e\,Gw}} = 0.9$ and 0.8).

to a higher fusion gain $Q$). The high density case without neutral beam heating requires 29 MW of ion cyclotron power, beyond the upper limit. Lowering the line-averaged density to $\frac{\langle n_e \rangle_{line}}{n_{e\,Gw}} = 0.8$ allows increasing the plasma current to $I_p = 10.2$ MA, limiting the required ion cyclotron power below 20 MW. While the scenarios with $P_{nb} = 16.5$ MW achieve increased plasma currents compared to the scenarios relying solely on RF wave heating and current drive, a further increase of neutral beam heating and current drive from 16.5 MW to 33 MW does not enable an increase in plasma current, illustrating once more that for neutral beam injection with a deposition profile peaked near the magnetic axis, a power increase is not necessarily beneficial for maintaining $q > 1$. However, neutral beams are clearly a key source of bulk current required to increase the fraction of non-inductively driven current. Furthermore, the two scenarios with $P_{nb} = 33$ MW do not require additional ion cyclotron heating, as the separatrix power flow for combined neutral beam and electron cyclotron heating is in excess of $1.2P_{LH}$ ($P_{sep} - 1.2P_{LH} = 6.8$ MW and 16.8 MW for respectively $\frac{\langle n_e \rangle_{line}}{n_{e\,Gw}} = 0.9$ and 0.8).

### 4.6.3 Electron cyclotron power upgrade

Combining some of the trends uncovered in the previous sections, the operational windows for an ITER hybrid scenario with availability of either $P_{ec} = 20$ MW or $P_{ec} = 40$ MW (while assuming $P_{nb} = 33$ MW and $P_{ic} = 0$ MW) can be compared quantitatively. The maximum plasma current for which $q > 1$ can be maintained is dependent on both the available amount of electron cyclotron power and the plasma density, as both impact the amount of off-axis current drive that can be deposited to tailor the $q$ profile. For a given amount of injected auxiliary power, both fusion power $P_{fus}$ and fusion gain $Q$ increase when increasing plasma current $I_p$, while maintaining the fraction of the line-averaged density to the Greenwald density limit constant. The colored quadrangles in Figure 4.12 circumscribe the operational window with a Greenwald density fraction $f_G = \langle n_e \rangle_{line}/n_{e\,Gw}$ within the range $[0.8, 0.9]$ and a fusion gain $Q > 5$, with the availability of respectively 20 MW (blue) and 40 MW (red) of electron cyclotron power. As discussed in Section 4.3, the pedestal pressure is assumed to
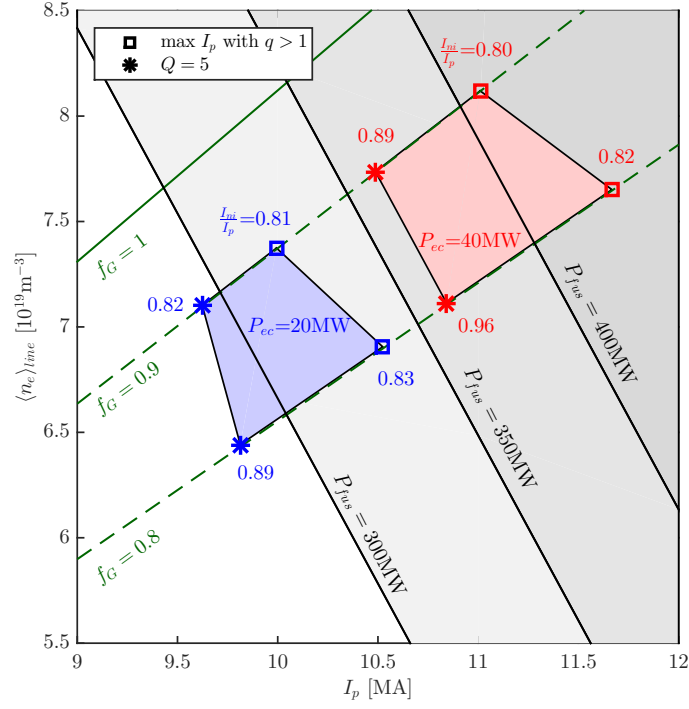
Figure 4.12: **Electron cyclotron power upgrade** The colored quadrangles circumscribe the operational window with a Greenwald density fraction $f_G = \langle n_e \rangle_{line} / n_{e\,Gw}$ within the range $[0.8, 0.9]$ and a fusion gain $Q > 5$, with the availability of respectively 20 MW (blue) and 40 MW (red) of electron cyclotron power. The four vertices of each quadrangle represent the scenarios with optimized electron cyclotron deposition location, corresponding to $Q = 5$ (star symbol on the low $I_p$ side) and the maximum $I_p$ for which $q > 1$ can be maintained (square open symbol on the high $I_p$ side). The relative levels of non-inductively driven current $f_{ni} = I_{ni} / I_p$ of these scenarios are also indicated on the figure. The differences in fusion power $P_{fus}$ are illustrated by a set of diagonal lines. As discussed in Section 4.3, the pedestal pressure is assumed to be linearly increasing with plasma current $I_p$. A density reduction at given plasma current is counteracted by a temperature pedestal increase, keeping the pedestal pressure constant. *Reproduced from [Van Mulders et al. 2021b].*

| $f_{Gw}$ | $I_p$ | $\rho_{ec}$ | $P_{fus}$ | $P_{aux}$ | $I_{aux}$ | $Q$ | $U_{pl}$ | $f_{ni}$ | $f_{bs}$ |
|---|---|---|---|---|---|---|---|---|---|
| | [MA] | | [MW] | [MW] | [MA] | | [mV] | | |
| | | | | nb + ec | | | | | |
| 0.9 | 10.5 | 0.33 | 365 | 33+40 | 4.8 | 5.0 | 3.6 | 0.89 | 0.43 |
| 0.8 | 10.8 | 0.34 | 364 | 33+40 | 5.8 | 5.0 | 1.1 | 0.96 | 0.42 |
| 0.9 | 11.0 | 0.34 | 404 | 33+40 | 4.3 | 5.5 | 7.4 | 0.80 | 0.40 |
| 0.8 | 11.7 | 0.37 | 430 | 33+40 | 5.1 | 5.9 | 5.5 | 0.82 | 0.39 |
| 0.9 | 9.6 | 0.38 | 264 | 33+20 | 3.9 | 5.0 | 7.1 | 0.82 | 0.42 |
| 0.8 | 9.8 | 0.39 | 264 | 33+20 | 4.6 | 5.0 | 3.8 | 0.89 | 0.42 |
| 0.9 | 10.0 | 0.29 | 319 | 33+20 | 3.9 | 6.0 | 6.8 | 0.81 | 0.42 |
| 0.8 | 10.5 | 0.31 | 339 | 33+20 | 4.5 | 6.4 | 5.5 | 0.83 | 0.40 |

Table 4.7: **Electron cyclotron power upgrade** Key performance indicators are shown for the operation points constituting the vertices of the quadrangles in Figure 4.12. The electron cyclotron deposition location $\rho_{ec}$ for each of these scenarios maximizes the fusion gain $Q$, while ensuring $q > 1$.

be linearly increasing with plasma current $I_p$. A density reduction at given plasma current is counteracted by a temperature pedestal increase, keeping the pedestal pressure constant. The four vertices of the quadrangles represent the scenarios with optimized electron cyclotron deposition radius, corresponding to $Q = 5$ (star symbol on the low $I_p$ side) and the maximum $I_p$ for which $q > 1$ can be maintained (rectangle symbol on the high $I_p$ side). The relative levels of non-inductively driven current $f_{ni} = I_{ni}/I_p$ of these scenarios are also indicated on the figure. The $Q = 5$ scenarios with $P_{ec} = 40$ MW clearly achieve a higher $f_{ni}$, with the low density case operating close to steady state conditions. Some performance indicators of these eight scenarios are summarized in Table 4.7. Note that the maximum fusion gains achieved with $P_{ec} = 20$ MW ($Q = 6.0$ for $f_G = 0.9$ and $Q = 6.4$ for $f_G = 0.8$) are higher than the maximum fusion gains achieved with $P_{ec} = 40$ MW ($Q = 5.5$ for $f_G = 0.9$ and $Q = 5.9$ for $f_G = 0.8$), although the increased plasma current yields fusion powers in excess of 400 MW for the latter. The differences in fusion power $P_{fus}$ are illustrated by a set of diagonal lines on Figure 4.12. In summary, one can conclude that increased electron cyclotron power resources widen the hybrid scenario operational space, allowing to achieve higher fusion power, while requiring less inductive current drive for a similar fusion gain $Q$.

## 4.7 Impact of temperature pedestal on scenario performance

Due to the stiff behaviour of the core ion temperature profile, the assumed temperature pedestal height has a strong impact on the predicted fusion power. Furthermore, the $q > 1$ constraint is less restrictive for increased pedestal temperatures, due to the increased off-axis current drive contribution by the bootstrap current driven in both core and pedestal and the enhanced electron cyclotron current drive efficiency at higher $T_e$.

The optimization problem of maximizing the fusion gain $Q$ with $q > 1$ and $P_{sep} > 1.2P_{LH}$, by optimizing both the deposition location and the power level of electron cyclotron heating (for

Figure 4.13: **Pedestal pressure sensitivity** Key performance indicators are shown of stationary states maximizing the fusion gain $Q$ by optimizing both the deposition location and the power level of electron cyclotron heating (for given plasma current $I_p = 10.5\,$MA and neutral beam power $P_{nb} = 33\,$MW), for respective pedestal temperatures $T_{e,i\ ped} = 3.5\,$keV, $4.5\,$keV and $5.5\,$keV, in addition to the respective quantities for stationary states maximizing the fusion gain $Q$ by optimizing the deposition location (for given plasma current $I_p = 10.5\,$MA, electron cyclotron heating $P_{ec} = 45\,$MW and neutral beam power $P_{nb} = 33\,$MW). $q > 1$ and $P_{sep} > 1.2P_{LH}$ are provided as constraints to the optimizer. *Reproduced from [Van Mulders et al. 2021b].*

| $T_{e,i\ ped}$ | $\rho_{ec}$ | $P_{fus}$ | $P_{aux}$ | $I_{aux}$ | $Q$ | $U_{pl}$ | $f_{ni}$ | $f_{bs}$ | $H_{y2,98}$ | $\beta_N$ |
|---|---|---|---|---|---|---|---|---|---|---|
| [keV] | | [MW] | [MW] | [MA] | | [mV] | | | | |
| | | | nb + ec | | | | | | | |
| 3.5 | 0.35 | 273 | 33+45 | 4.7 | 3.5 | 8.6 | 0.79 | 0.35 | 1.1 | 2.0 |
| 4.5 | 0.32 | 364 | 33+30 | 4.2 | 5.7 | 6.8 | 0.81 | 0.41 | 1.3 | 2.3 |
| 5.5 | 0.28 | 448 | 33+18 | 3.6 | 8.8 | 5.6 | 0.83 | 0.48 | 1.4 | 2.5 |

Table 4.8: **Pedestal pressure sensitivity (with variable P$_{ec}$)** Key performance indicators are shown for the operation points maximizing the fusion gain $Q$ with $q > 1$ and $P_{sep} > 1.2 P_{LH}$ by optimizing both the deposition location $\rho_{ec}$ and the power level of electron cyclotron heating $P_{ec}$ (for given plasma current $I_p = 10.5$ MA and neutral beam power $P_{nb} = 33$ MW), for respective pedestal temperatures $T_{e,i\ ped} = 3.5$ keV, 4.5 keV and 5.5 keV.

| $T_{e,i\ ped}$ | $\rho_{ec}$ | $P_{fus}$ | $P_{aux}$ | $I_{aux}$ | $Q$ | $U_{pl}$ | $f_{ni}$ | $f_{bs}$ | $H_{y2,98}$ | $\beta_N$ |
|---|---|---|---|---|---|---|---|---|---|---|
| [keV] | | [MW] | [MW] | [MA] | | [mV] | | | | |
| | | | nb + ec | | | | | | | |
| 3.5 | 0.35 | 273 | 33+45 | 4.7 | 3.5 | 8.6 | 0.79 | 0.35 | 1.1 | 2.0 |
| 4.5 | 0.33 | 365 | 33+45 | 5.2 | 4.7 | 2.4 | 0.92 | 0.43 | 1.3 | 2.4 |
| 5.5 | 0.32 | 457 | 33+45 | 5.6 | 5.9 | -1.6 | 1.06 | 0.53 | 1.4 | 2.8 |

Table 4.9: **Pedestal pressure sensitivity (with fixed P$_{ec}$)** Key performance indicators are shown for the operation points maximizing the fusion gain $Q$ with $q > 1$ and $P_{sep} > 1.2 P_{LH}$ by optimizing the deposition location of electron cyclotron heating (for given plasma current $I_p = 10.5$ MA, neutral beam power $P_{nb} = 33$ MW and electron cyclotron heating $P_{ec} = 45$ MW), for respective pedestal temperatures $T_{e,i\ ped} = 3.5$ keV, 4.5 keV and 5.5 keV.

given plasma current $I_p = 10.5$ MA and neutral beam power $P_{nb} = 33$ MW), as formulated in Section 4.6.1 and presented in Table 4.4, is repeated for increased and reduced temperature (and pressure) pedestal height, as presented in Figure 4.13 and Table 4.8. The result for the reference temperature pedestal ($T_{e,i\ ped} = 4.5$ keV) obtained in the previous parts, is compared to the optimum scenarios obtained for $T_{e,i\ ped} = 3.5$ keV and $T_{e,i\ ped} = 5.5$ keV (corresponding pedestal pressure respectively 74 kPa and 117 kPa). The elevated $T_i$ profile for increased pedestal clearly results in more fusion power. Furthermore, the fusion gain $Q$ is further enhanced as the required level of electron cyclotron heating can be further reduced due to the higher fraction of bootstrap current and the increased electron cyclotron current drive efficiency helping to sustain the hybrid $q$ profile. The lowest pedestal height requires an increase of the available electron cyclotron resources to $P_{ec} = 45$ MW to enable a stationary state with $q > 1$. To disentangle the dual effect on the fusion gain $Q$ of changing both fusion power and auxiliary power, the optimizations at $T_{e,i\ ped} = 4.5$ keV and $T_{e,i\ ped} = 5.5$ keV are repeated with fixed levels of auxiliary power ($P_{nb} = 33$ MW and $P_{ec} = 45$ MW), as shown in Figure 4.13 and Table 4.9.

The assumed temperature pedestal height has clearly a strong impact on the projected scenario performance, highlighting the importance of reliable pedestal stability models to predict ITER performance.
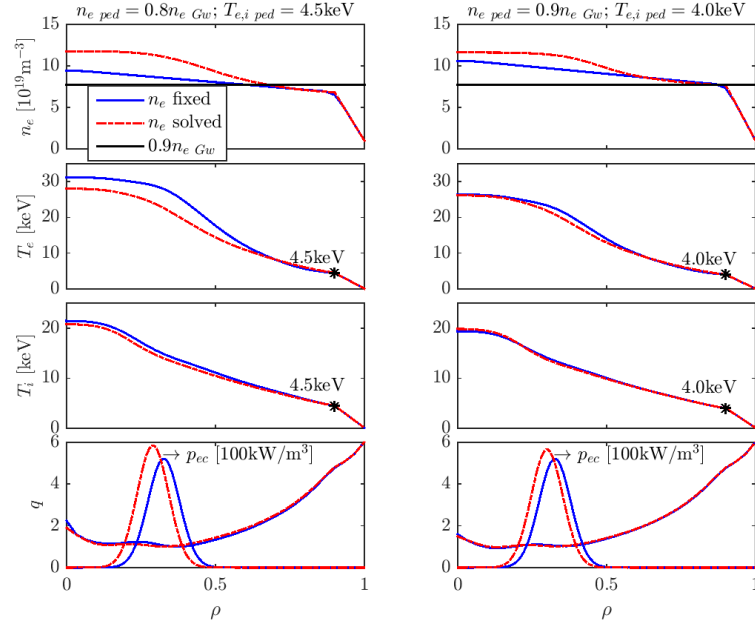
Figure 4.14: **Density peaking** A comparison is shown of the electron density, electron temperature, ion temperature, safety factor and EC heat deposition profiles for a sensitivity study on the impact of the Greenwald density constraint and the density peaking. For the left (right) panels, the pedestal density is respectively set to $n_{e\ ped} = 0.8 n_{e\ Gw}$ ($n_{e\ ped} = 0.9 n_{e\ Gw}$). The density profile is either imposed with a fixed peaking factor or solved for with QLKNN predicted transport. The fixed density profile case with $\frac{n_{e\ ped}}{n_{e\ Gw}} = 0.8$ recovers the hybrid reference case as defined earlier (with $\langle n_e \rangle_{line} = 0.9 n_{e\ Gw}$).

## 4.8 Impact of density peaking and Greenwald density limit

Since the produced fusion power strongly depends on the density, one can anticipate a strong impact of assumptions regarding the peaking of the density profile and the Greenwald density limit. The present section provides a sensitivity study on the impact on the reference case hybrid scenario of different density profiles. The modeling performed in earlier sections provided conservative predictions, considering a limited level of peaking with respect to what is expected for ITER plasmas from modeling and experiments and limiting the line-averaged density to $\langle n_e \rangle_{line} = 0.9 n_{e\ Gw}$. Assuming density limit disruptions mainly originate from phenomena close to the plasma boundary [Greenwald 2002; Giacomin et al. 2022] (as confirmed by the observation of peaked density profiles with line-averaged densities $\langle n_e \rangle_{line} = 1.5 n_{e\ Gw}$ [Lang et al. 2012]), one could release the conservative constraint $\langle n_e \rangle_{line} = 0.9 n_{e\ Gw}$ to a constraint on the pedestal density, i.e. $n_{e\ ped} = 0.9 n_{e\ Gw}$.

The different density profiles considered in this section are presented in Figure 4.14.

- For the left and right panels, the pedestal density is respectively set to $n_{e\ ped} = 0.8 n_{e\ Gw}$ and $n_{e\ ped} = 0.9 n_{e\ Gw}$. The temperature pedestal is adjusted to keep the pedestal pressure unchanged. This can be motivated by the results from EPED1 modeling reported

| $n_e$ | $\frac{n_{e\ ped}}{n_{e\ Gw}}$; $\frac{n_{e,0}}{n_{e\ ped}}$; $\frac{\langle n_e \rangle_{line}}{n_{e\ Gw}}$ | $P_{fus}$ | $P_{aux}$ | $I_{aux}$ | $Q$ | $U_{pl}$ | $f_{ni}$ | $f_{bs}$ | $H_{y2,98}$ | $\beta_N$ |
|---|---|---|---|---|---|---|---|---|---|---|
| | | [MW] | [MW] | [MA] | | [mV] | | | | |
| | | | nb + ec | | | | | | | |
| f | 0.8; 1.4; 0.9 | 367 | 33+40 | 4.8 | 5.0 | 3.7 | 0.89 | 0.43 | 1.3 | 2.4 |
| s | 0.8; 1.7; 1.1 | 502 | 33+40 | 3.3 | 6.9 | 8.3 | 0.79 | 0.48 | 1.2 | 2.5 |
| f | 0.9; 1.4; 1.0 | 377 | 33+40 | 3.5 | 5.1 | 11.2 | 0.74 | 0.41 | 1.2 | 2.3 |
| s | 0.9; 1.5; 1.1 | 461 | 33+40 | 3.1 | 6.3 | 12.0 | 0.74 | 0.44 | 1.2 | 2.4 |

Table 4.10: **Density profile sensitivity** Key performance indicators are shown for four density profile scenarios with $\frac{n_{e\ ped}}{n_{e\ Gw}}$ = 0.8 or 0.9 and the density profile either imposed with a fixed peaking factor ('f'=fixed) or solved for with QLKNN predicted transport ('s'=solved).

in [Polevoi et al. 2015], where for SOLPS consistent separatrix densities and moderate pedestal densities, the predicted pressure pedestal height is independent of the density pedestal height.

- The density profile is either imposed with a fixed peaking factor or solved for with QLKNN predicted transport. The fixed density profile case with $\frac{n_{e\ ped}}{n_{e\ Gw}}$ = 0.8 recovers the hybrid reference case as defined earlier (with $\langle n_e \rangle_{line} = 0.9 n_{e\ Gw}$). Adding the electron density equation to the set of stationary diffusion equations solved by the stationary state solver in RAPTOR, QLKNN provides a prediction of the turbulence-driven inward pinch. Similarly as for the heat transport discussed earlier, the shear input of the neural network is transformed to $s - 0.5\alpha$ and only the ITG prediction is used. Note that these density peaking predictions miss the impact of TEM turbulence [Fable et al. 2009], as well as the electromagnetic effects described in [Hein et al. 2010], shown to reduce density peaking for ITER and DEMO [Fable et al. 2019]. Despite these model deficiencies, the presented density profiles provide a sensitivity study on the impact of the level of density peaking on hybrid scenario performance. Note that pellets will fuel the peripheral ITER plasma, providing effectively an actuator for the pedestal density $n_{e\ ped}$. In the present section, two levels of $n_{e\ ped}$ are compared. A further systematic study of $n_{e\ ped}$ as an optimization variable (acting hence as a proxy for the pellet fueling rate) is left for future work.

Performance indicators of the four resulting scenarios are compared in Table 4.10. Let us first compare the two scenarios with imposed density profiles ('f' in Table 4.10) and a fixed density peaking factor ($n_{e0}/n_{e\ ped} = 1.4$), with the pedestal density respectively $\frac{n_{e\ ped}}{n_{e\ Gw}}$ = 0.8 and 0.9. Since the increase in pedestal density is compensated by a pedestal temperature reduction, lowering the stiff ion temperature profile rigidly, the total fusion power is only impacted modestly. For a fixed pedestal pressure and a fixed density peaking, the fusion gain is weakly dependent on the relative heights of temperature and density pedestal. The loop voltage on the other hand increases by more than a factor three due to the density increase. This is easily explained by the reduced amount of current driven non-inductively due to degrading current drive efficiency, in addition to the increasing plasma resistivity and reducing bootstrap current (lower $T_i$, and lower $T_e/T_i$ for increased density).

Inspecting the QLKNN predicted density profiles in Figure 4.14, it is clear that the peaking is strongly impacted by the varying pedestal boundary conditions for temperature and density. Increasing the pedestal density from $n_{e\ ped} = 0.8 n_{e\ Gw}$ to $0.9 n_{e\ Gw}$, while decreasing the pedestal temperature from $T_{e,i\ ped} = 4.5$ keV to $4.0$ keV as to maintain a constant pedestal pressure, the predicted level of peaking decreases from $\frac{n_{e,0}}{n_{e\ ped}} = 1.7$ to $1.5$. The density profile hence becomes more peaked for reducing collisionality, as expected from theory and experiment [Angioni et al. 2003; Weisen et al. 2005].

For the low pedestal density cases ($\frac{n_{e\ ped}}{n_{e\ Gw}} = 0.8$; left panels Figure 4.14), the QLKNN predicted density profile is notably more peaked compared to the imposed density profile (confirming that $\frac{n_{e,0}}{n_{e\ ped}} = 1.4$ is a conservative assumption). The peaked density profile results in a significant increase of fusion power, and hence fusion gain ($Q = 5.0 \rightarrow 6.9$), while an increased inductive current drive is required ($U_{pl} = 3.7$ mV $\rightarrow 8.3$ mV; $f_{ni} = 0.89 \rightarrow 0.79$). These effects are less pronounced for the high density pedestal cases, since the predicted peaking factor is smaller. Note however that even for similar peaking factor, the radial profile of $n_e(\rho)$ can impact the produced fusion power and local current drive efficiency. Comparing finally the two scenarios with solved density profiles ('s' in Table 4.10), we see that increasing the pedestal density leads to a slight reduction of fusion power due to the predicted drop in density peaking (fusion gain $Q = 6.9 \rightarrow 6.3$), indicating the key importance of the reactivity in the inner core of the plasma. The inductive current drive requirement however increases ($U_{pl} = 8.3$ mV $\rightarrow 12.0$ mV; $f_{ni} = 0.79 \rightarrow 0.74$). Note in Figure 4.14 that the optimized cases with and without predictive density have a similar ion temperature profile: by optimizing the EC deposition radius (self-consistently accounting for the changed EC current drive efficiency and bootstrap current distribution), a similar $q$ profile is obtained, resulting in similar ion transport predictions.

In conclusion, operation at reduced pedestal density appears favorable for the hybrid scenario, under the assumption of an equal pedestal pressure. The increased level of density peaking anticipated for smaller collisionality further reinforces this trend.

## 4.9   Conclusion

The present study confirms that improved energy confinement relative to the H98(y,2) scaling law can be achieved in ITER, by optimizing the electron cyclotron current drive deposition location, pursuing a hybrid scenario $q$ profile with $q > 1$ and maximizing the $s/q$ at radii $\rho > 0.4$. Due to the lack of electromagnetic and fast ion effects in QLKNN, the confinement levels could be systematically under-predicted. Regarding core confinement the presented results can hence be considered as conservative. Note however that the trends seen in ECCD deposition modification and impact of $s/q$ on ITG thresholds hold regardless of the electromagnetic and fast ion effects. As depositing all the available electron cyclotron power in a specific location is shown to be the optimal choice to achieve such $q$ profile, no excessive fine-tuning of electron cyclotron deposition profile is required. For a gaussian deposition profile it suffices to find how close to the magnetic axis the deposition location can be without violating $q > 1$, having the $q$

profile clamped to $q = 1$ at the outermost location that can be achieved for a given electron cyclotron power.

Using this novel combination of tools, ITER hybrid scenarios are projected to be a reliable avenue for long-pulse burning plasmas, with a heating mix $P_{nb} = 33\,\text{MW}$ and $P_{ec} = 40\,\text{MW}$ allowing for $Q = 5$ with $f_{ni} = 0.89$ and $P_{fus} = 365\,\text{MW}$ (assuming $T_{e,i\ ped} = 4.5\,\text{keV}$, $f_G = 0.9$ and $n_{e0}/n_{e\ ped} = 1.4$, and for $I_p = 10.5\,\text{MA}$). A reduced electron cyclotron power $P_{ec} = 20\,\text{MW}$ requires operation at reduced plasma current $I_p = 9.6\,\text{MA}$ and achieves $Q = 5$ at $f_{ni} = 0.82$ and $P_{fus} = 264\,\text{MW}$. Raising the total plasma current allows to reach a higher fusion gain $Q$, at the expense of an increased loop voltage $U_{pl}$ (and hence reduced $f_{ni}$), as presented quantitatively in this work. The stiff behaviour of the ion temperature profile allows to further enhance the achieved fusion gain $Q$ by reducing the amount of injected heat. Depending on the levels of total plasma current, pedestal confinement and neutral beam power, the reduction of electron cyclotron heating and current drive is either limited by the need for enough off-axis current to maintain $q > 1$, or by the need for a sufficient separatrix power flow to maintain H-mode operation, giving rise to an intermediate plasma current maximizing the fusion gain $Q$. Although lowering neutral beam power allows a further increase in fusion gain $Q$, the neutral beams are an important source of auxiliary current drive, required to reach high fractions of non-inductively driven current. Actual scenario performance is strongly dependent on the pedestal pressure and the peaking of the density profile, both having a major impact on fusion power, current drive efficiency and bootstrap current. For a given total pedestal pressure, a lowered pedestal density is favorable: fusion power is only moderately affected due to the simultaneous increase of the stiff ion temperature profile (especially when considering a more peaked density profile can be obtained at reduced collisionality), while current drive efficiency, bootstrap current and plasma conductivity are enhanced by reduced density and increased electron temperature.

# 5 Safe plasma termination strategies for DEMO

Safe termination of a burning plasma in a DEMO reactor is a highly non-trivial task. The high energy content of a reactor-grade plasma and the limited thickness of a reactor first wall (to allow for sufficient tritium breeding), lead to a very small tolerance for plasma disruption events. As safe termination scenarios, both for routine and for emergency shutdown, are critical to any viable tokamak reactor concept, present-day tokamak experiments have started to investigate stable ramp-down solutions, guided by modeling tools.

Modeling and optimization with the RAPTOR code, applied to TCV, ASDEX Upgrade and JET, has allowed to increase the plasma current ramp-down rate while maintaining the plasma radially and vertically stable, by optimizing the time evolution of plasma current and elongation throughout the ramp-down phase [Teplukhina et al. 2017]. On DIII-D, vertical displacement events (VDEs) could be successfully prevented by adjusting the plasma elongation and the inner-gap to the vessel wall, in response to real-time estimators of the proximity to the vertical stability limit [Barr et al. 2021]. Modeling of the ramp-down phase for for ASDEX Upgrade is discussed in [Fable et al. 2013] and [Fietz et al. 2013] and for JET in [Bizarro et al. 2016].

Fast simulators like RAPTOR allow to systematically explore reactor operating points and scenario dynamics, and to automatize the search for optimal control strategies. In [Giruzzi et al. 2015], METIS is used to explore operating points for a pulsed and a steady state DEMO design. Note that the large size and the high temperature of a DEMO plasma core lead to a very slow diffusion time scale of the current density. This clearly illustrates the need for a fast simulation tool to optimize a DEMO scenario.

## 5.1 Challenges for DEMO ramp-down scenarios

Even though the European DEMO strategy aims to maximize its reliance on a conservative physics basis that can be explored on ITER, some fundamentally new challenges will arise.

- Seeded impurities like xenon are required to radiate sufficient heat from the plasma core, maintaining the heat load to the divertor tiles manageable (even in the presence of detachment). Depending on the plasma temperature, the plasma can (locally) be in a

regime where a decrease in $T_e$ leads to an increase in radiated power (from both Xe and W [Siccinio et al. 2020; Ostuni et al. 2022]), triggering a radiative collapse of the plasma. In the DEMO power balance, both the main source term (fusion power) and the main sink term (impurity radiation) are non-linearly dependent on the plasma temperature and density, making the plasma largely self-regulated. Thus, the dynamics of a burning plasma with high radiation fraction is highly non-linear, while external actuators are less effective with respect to present-day machines.

- To maintain the integrity of the thin metal wall (which must be thinner compared to ITER to allow for tritium breeding [Maviglia et al. 2021]), a loss of plasma control at high plasma current $I_p > \sim 5\,\text{MA}$ and stored energy is unacceptable. Developing a reliable ramp-down strategy, both for planned and emergency termination of the plasma, is hence critical for the DEMO mission.

An emergency shutdown scenario in the event of divertor reattachment is discussed in [Siccinio et al. 2020]. Divertor sweeping is proposed to delay the heat flux to the coolant becoming critical. While maintaining this emergency measure, temporarily averting target plate damage [Siccinio et al. 2019], a fast plasma current ramp-down is paramount. Furthermore, a fast reduction of plasma current is beneficial to reduce the forces experienced by the vacuum vessel in case of a disruption, which are proportional to $I_p^2$. However, note that for non-emergency ramp-up and ramp-down scenarios, slower ramp phases with a slow density evolution might be preferred to allow the turbine to follow slow changes in fusion power, to maximize exploitation for electric energy production [Siccinio et al. 2020; Del Nevo 2018].
In this chapter the feasibility of different plasma current ramp-down rates is investigated. Through action of the central solenoid, the loop voltage at the edge of the plasma is controlled to maintain the imposed $I_p$ time evolution. The reduced loop voltage at the edge then provides a driving force for outward current diffusion. However, due to the high temperatures and the large size of a DEMO plasma, current diffusion is extremely slow. A fast current ramp-down will hence tend to peak the current density profile, or equivalently, increase the plasma internal inductance $\ell_{i3}$, resulting in reduced controllability of the vertical position of the plasma. Since a loss of position control of the plasma column needs to be avoided throughout the entire ramp-down, the minimum time window required to safely terminate the discharge is constrained by the *vertical stability limit*. For the work presented in this chapter, CREATE-NL simulations [Albanese et al. 2015] of the vertical position stabilization control loop for DEMO [Mattei et al. 2016] are used to obtain upper limit for the internal inductance. Note that vertical stabilization of the plasma column is projected to become more challenging for future tokamak reactors with respect to present-day devices. Future tokamaks like DEMO aim to maximize performance by strongly elongating the plasma. Compared to present devices, the current diffusion time scale is very long, while conductive walls are further away from the plasma due to the presence of tritium breeding blankets. Furthermore, measurements are complicated by the presence of 14.1 MeV neutrons and control will be less efficient due to the difficulty of putting internal coils inside the vessel and the comparatively long distance to the poloidal field coils (which are located outside of the toroidal field coils [Federici et al. 2019]).

In addition to the vertical position control, a set of further constraints limits the operation space of feasible ramp-downs.

- In order to ensure stable *radial position control*, the maximum rate of change of poloidal field coil currents impose an upper limit on the time derivative of the vertical magnetic field $B_v$, which can be written as:

$$B_v = \frac{\mu_0 I_p}{4\pi R}\left(\ln\left(\frac{8R}{a\kappa^{0.5}}\right) + \beta_p + 0.5\ell_{i3} - 1.5\right) \tag{5.1}$$

  Rapid changes of any of the parameters in eq. (5.1) can hence potentially cause a loss of radial position control.

- Since the *Greenwald density limit* [Greenwald et al. 1988], the upper limit on the plasma (edge) density [Lang et al. 2012; Giacomin et al. 2022], is proportional to the plasma current, the density has to be decreased throughout the ramp-down phase. While in the present work full control over the plasma density is assumed, in practice the particle confinement time limits the achievable density ramp-down rate and may impose an early HL back transition.

- While terminating a burning plasma, the fusion power is reduced, by changing the isotope DT concentration and by bringing down the density ($P_{fus} \sim n_e^2$). The presence of the inherent W impurity and the seeded Xe impurity to boost core radiation make the plasma prone to a *radiative collapse*: while the alpha heating drops, the average cooling factor of W and Xe increases for decreasing $T_e$. Methods for the removal of Xe and W or large auxiliary heating power resources are required to maintain a positive power balance throughout the entire ramp-down phase.

Both the vertical and the radial position control problem illustrate the impact of the time evolution of internal plasma profiles on the magnetic control, through parameters like $\ell_{i3}$ and $\beta_{pol}$. Conversely, the plasma shape evolution can be used as an actuator to drive changes to the plasma profile evolution: in [Teplukhina et al. 2017], it was found that a fast decrease in plasma elongation allows to limit the increase of the internal inductance (while simultaneously widening the margin for vertical controllability). Furthermore, the plasma shape impacts the thermal confinement quality of the plasma. These examples illustrate the inherently coupled nature of the kinetic ($q$, $T_e$, $n_e$) and magnetic (position and shape) control problems.
The constraints mentioned in this section, non-linearly dependent on the plasma state itself, have to be simultaneously met. A fast transport solver like RAPTOR captures some of these non-linearities and can hence assist in the design process of safe ramp-down strategies, as will be presented in the remainder of this chapter. The set-up of the RAPTOR simulations is described in Section 5.2, highlighting the various non-linearities captured by the model. In Section 5.3, a stationary operating point for a DEMO reactor is established, which will serve as the initial state for the ramp-down simulations. The time traces of auxiliary heating and Xe impurity concentration are manually optimized to find a feasible ramp-down scenario, avoiding a

radiative collapse, in Section 5.4. The upper limit for the internal inductance, obtained from CREATE-NL vertical stability calculations, is introduced in Section 5.5. For various ramp-down rates, L-mode confinement quality assumptions and HL transition timings, the feasibility with respect to vertical and radial position control is assessed. Optimization with respect to vertical stability is studied in Section 5.6. The RAPTOR non-linear optimization algorithms are used to optimize the ramp-down time traces of plasma current and elongation to ensure operation within the vertically stable operating envelope extracted from CREATE-NL calculations, while avoiding decreasing values of $q_{95}$ that could compromise MHD stability. Conclusions are formulated in Section 5.7.

## 5.2 Simulation set-up for DEMO simulations

The termination simulations in this chapter cover a plasma current ramp from $I_{p\ flat\ top} = 17.75$MA down to $I_{p\ final} = 5.00$MA. Depending on the $I_p$ ramp-down rate, different simulation time windows result, with $t_{final} = \frac{I_{p\ final} - I_{p\ flat\ top}}{dI_p/dt}$.

### 5.2.1 Stationary state (initial state ramp-down)

Since the gradient-based transport model with feedback on the pedestal gradient is not yet compatible with the stationary state solver[1], a time dependent simulation with constant actuator inputs is run. Due to the slow current diffusion time scale, a long simulation time ($t_{final} = 2000$s) is required for the loop voltage profile $U_{pl}$ to relax to its final, radially flat state. The obtained stationary state is used as the initial state $x_0$ for the ramp-down simulations.

### 5.2.2 Transport equations and heat sources

- The transport equations solved for are electron heat transport ($T_e(\rho, t)$), electron density transport ($n_e(\rho, t)$) and current diffusion ($\psi(\rho, t)$). These equations are evolved from $t_0 = 0$s to $t_{final}$ on the full radial domain $\rho \in [0\ 1]$. The ion temperature is set equal to the electron temperature.

- For the main ions, a 50/50 deuterium/tritium fuel mix is assumed. A set of three impurities is assumed, as discussed later, with an impurity density set proportional to $n_e$, with a user-defined, time-dependent factor. $n_D + n_T$ and $Z_{eff}$ is solved for by imposing quasi-neutrality and evaluating the effective charge equation for $Z_{eff}$.

- The flat-top neutral beam deposition profiles $p_{nbi,e}$ and $j_{nbi}$ are taken from a METIS DEMO simulation, with a volume-dependent factor scaling the profiles to match the

---

[1]An additional equation could be added to the non-linear set of stationary state equations, imposing a global metric for confinement and line average density, adding the transport model edge gradient parameters as unknowns. Alternatively, an outer loop could adapt the transport parameters until convergence, leveraging the fast speed of the stationary state solver.

requested total power evolution $P_{nbi}(t)$.

- The EC heating is deposited in the center $\rho_{dep} = 0$ with $w_{dep} = 0.1$, without any current drive.

- The alpha power density is evaluated with the formula described in [van Dongen et al. 2014], consistently calculating the electron and ion heating contributions, according to the formula derived in [Wesson 2004]. Since this alpha power model is relatively simplistic (not taking into account fast ion losses due to orbit and ripple effects and diffusion across the plasma during the slowing down time), a multiplicative factor $c_\alpha = 0.73$ was introduced to obtain the DEMO RAPTOR simulations reported in [Siccinio et al. 2018], benchmarked against more complete ASTRA simulations.

### 5.2.3 Heat and density transport model

The transport model employed is the gradient-based model developed in [Teplukhina et al. 2017], introduced in Section 2.3.4. We use this model because its prediction is well-defined, based on the $H_{98,y2}$ scaling factor ($H_{98,y2} = 1$ is assumed here in H-mode, allowing for a conservative prediction), and it models the whole plasma radius for both L- and H-mode plasmas. The values used for the logarithmic gradients $\lambda_{T_e, n_e}$ are inspired by the available literature on predictive DEMO modeling, as described later in this chapter.

The time traces $\mu_{T_e, n_e}(t)$, governing the pedestal confinement quality, are set as the sum of a feedforward and a feedback contribution. The feedforward contribution provides an initial estimate of the time evolution of the pedestal gradient. The feedback controller, with a proportional and an integral term, adds a corrective term to bring the plasma confinement time and line-averaged density towards pre-defined reference traces $\tau_E \sim H_{ref} \tau_{E\,scl}$ and $n_{el} \sim n_{el\,ref}$, making use of the error terms defined in eq. (5.2).

$$\mu_X(t) = \mu_X^{ff}(t) + g_p e(t) + g_i \int e(t) dt \text{ with } \begin{cases} e(t) = H_{ref} - \tau_E / \tau_{E\,scl} \text{ for } X = T_e \\ e(t) = n_{el\,ref} - n_{el} \text{ for } X = n_e \end{cases} \tag{5.2}$$

In the present work, the line-averaged density reference $n_{el\,ref}$ is set proportional to the Greenwald density limit $n_{e,Gw} = I_p / (\pi a^2)$, with a user-defined factor $f_{Gw} = n_{el\,ref} / n_{e,Gw}$ that can be time-dependent. Different confinement time scaling $\tau_{E\,scl}$ could be applied; in this study the IPB98(y, 2) scaling law is used [ITER Physics Expert Group on Confinement and Transport et al. 1999].

#### Evaluating $\tau_E$ and $\tau_{E\,scl}$ in plasma with high levels of radiated power

It is important to note that the IPB98(y, 2) scaling law is derived based on the data available on present-day machines, with modest levels of radiated power from the core plasma compared to a DEMO plasma. This raises the question of how radiated power should be correctly accounted
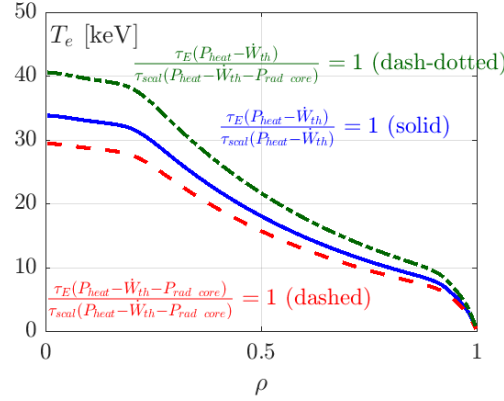
Figure 5.1: A comparison is shown between $T_e$ profiles for the DEMO stationary state calculated in RAPTOR, for different assumptions regarding the way radiated power is taken into account when calculating the loss power. The three profiles have an H factor equal to unity $H_{98y,2} \sim (P_L)^{0.69}_{\tau_E\,scl} W_{th}/(P_L)_{\tau_E} = 1$. For the blue profile $(P_L)_{\tau_E} = (P_L)_{\tau_E\,scl} = P_{heat} - \dot{W}_{th}$, corresponding to the standard implementation of the gradient-based model as applied in this chapter. For the red profile $(P_L)_{\tau_E} = (P_L)_{\tau_E\,scl} = P_{heat} - \dot{W}_{th} - P_{rad\,core}$, as proposed in [Lux et al. 2016]. For the green profile, $(P_L)_{\tau_E\,scl} = P_{heat} - \dot{W}_{th} - P_{rad\,core}$, while $(P_L)_{\tau_E} = P_{heat} - \dot{W}_{th}$.

| $(P_L)_{\tau_E}$ | $(P_L)_{\tau_E\,scl}$ | $H_{98y,2}$ (no $P_{rad\,core}$) | $P_{rad\,core}$ | $W_{th}$ |
|---|---|---|---|---|
| $-\cancel{P_{rad\,core}}$ | $-\cancel{P_{rad\,core}}$ | 1.01 | 102 MW | 1257 MJ |
| $-P_{rad\,core}$ | $-P_{rad\,core}$ | 0.92 | 105 MW | 1093 MJ |
| $-\cancel{P_{rad\,core}}$ | $-P_{rad\,core}$ | 1.15 | 102 MW | 1508 MJ |

Table 5.1: The stationary DEMO operating points obtained in RAPTOR are presented, for different assumptions regarding the way radiated power is taken into account when calculating the loss power. The three cases have an H factor equal to unity $H_{98y,2} = (P_L)^{0.69}_{\tau_E\,scl} W_{th}/(P_L)_{\tau_E} = 1$. The first two columns indicate whether or not $P_{rad\,core}$ is subtracted, respectively in the loss power terms $(P_L)_{\tau_E}$ and $(P_L)_{\tau_E\,scl}$.

for in the calculation of confinement time and in the scaling law evaluation. More specifically, a proper definition of the loss power $P_L$ is required, present both in the confinement time formula $\tau_E = W_{th}/P_L$, and in the scaling law dependency $\tau_{E\,scl} = \tau_{E\,98y,2} \sim P_L^{-0.69}$. The standard implementation of the gradient-based transport model assumes $P_L = P_{heat} - \dot{W}_{th}$, with $P_{heat}$ the total plasma heating power (ohmic, alpha and auxiliary) and $\dot{W}_{th} = dW_{th}/dt$. This definition of the loss power does not subtract any fraction of the power radiated directly from the core plasma. In [Lux et al. 2016], IPB98(y, 2) confinement scaling predictions are compared to ASTRA-TGLF simulations to come up with a proper $P_L$ correction term accounting for the core radiated power. By subtracting 60% of the radiated power inside $\rho = 0.75$, the best agreement between simulation and scaling law is obtained, i.e. $P_L = P_{heat} - \dot{W}_{th} - P_{rad\,core}$ with $P_{rad\,core} = 0.6 \int_{\rho=0}^{0.75} p_{rad} dV$.

Applying these corrections in the gradient-based model impacts the predicted temperatures and stored thermal energies. For a given H factor, e.g. equal to unity, one can write $\tau_E = W_{th}/P_L \sim \tau_{E\,scl} = \tau_{E\,98y,2} \sim P_L^{-0.69}$, hence for the resulting stored energy one can write $W_{th} \sim (P_L)_{\tau_E}(P_L)^{-0.69}_{\tau_E\,scl}$. While applying the $P_{rad\,core}$ subtraction in $(P_L)_{\tau_E}$ leads to a reduced $W_{th}$, the loss power correction in the scaling law tends to increase $W_{th}$ (since confinement degrades with increasing power). Depending on which of both loss power factors $(P_L)_{\tau_E}$ and

$(P_L)_{\tau_E\,scl}$ is corrected with a radiated power subtraction, we can hence distinguish four cases[2] (the three cases for which a RAPTOR stationary state is found are shown in Figure 5.1 and Table 5.1):

- The net effect of the double loss power correction proposed in [Lux et al. 2016] leads to a reduced $W_{th}$. This can be illustrated by comparing the blue and the red $T_e$ profiles in Figure 5.1.

- Subtracting $P_{rad\,core}$ only in the scaling law evaluation would lead to the green profile in Figure 5.1, with improved confinement.

- No stationary operating point was found for the case where $P_{rad\,core}$ is only subtracted for the confinement time evaluation. This can be understood by considering the corresponding expression:

$$H_{98y,2} = \frac{\tau_E}{\tau_{E\,98y,2}} \sim \frac{W_{th}}{P_{heat} - \dot{W}_{th} - P_{rad\,core}}(P_{heat} - \dot{W}_{th})^{0.69} \tag{5.3}$$

  Evaluating this expression with the $T_e$ profile obtained with the standard settings of the gradient-based model (no $P_{rad\,core}$ subtraction, blue profile in Figure 5.1), leads to an H factor above one (confinement is degraded, the blue $T_e$ is too optimistic). However, by decreasing $T_e$, both numerator and denominator decrease, respectively due to a reduced $W_{th}$ and an increased $P_{rad\,core}$. Interestingly, this leads to the fact that, when reducing $T_e$ (by reducing $\mu_{T_e}$), no profile satisfying $H_{98y,2} = 1$ is found.

Later in this chapter, the H factor is calculated without subtracting $P_{rad\,core}$ in $(P_L)_{\tau_E}$ and $(P_L)_{\tau_E\,scl}$. Not applying the $P_{rad\,core}$ corrections as proposed in [Lux et al. 2016] in the gradient-based transport model is equivalent to assuming a confinement enhancement of about 10%.

### 5.2.4 Application of the gradient-based transport model

Strengths of the gradient-based transport model include the fact that the diffusion equations are solved up to the last closed flux surface; pedestal boundary conditions are replaced by global confinement quantities like an H factor or a line-averaged density. Furthermore, through provision of the time evolution of the H factor, the timing (and duration) of the LH/HL transition can be easily adjusted. For ramp-down studies this allows to assess the impact of early versus late transition timings on the time evolution of the internal inductance $\ell_{i3}$. While the lack of predictive models for heat and particle transport are obviously a limitation, this approach allows for a robust evaluation of the current profile dynamics. Employing cautious H factor assumptions allows to perform DEMO simulations that are conservative with respect to the assumed confinement quality.

---

[2]While $(P_L)_{\tau_E} = (P_L)_{\tau_E\,scl}$ is the most consistent assumption [Lux et al. 2016], we include all four cases to provide a more complete overview of the impact of the different definitions on the predicted temperature and stored thermal energy.

|  | Fine $t$ grid | Coarse $t$ grid |
|---|---|---|
| $g_{i\ \chi_e}$ | $75\ 10^3$ | $50\ 10^3$ |
| $g_{p\ \chi_e}$ | $75\ 10^3$ | $50\ 10^3$ |
| $g_{i\ V_{n_e}}$ | $1.8\ 10^{20}$ | $1.2\ 10^{20}$ |
| $g_{p\ V_{n_e}}$ | $3.6\ 10^{20}$ | $2.4\ 10^{20}$ |
| $\Delta t_{init}$ | $10\,\text{ms}$ | $200\,\text{ms}$ |
| $\Delta t$ | $100\,\text{ms}$ | $200\,\text{ms}$ |
| $\Delta t_{HL}$ | $50\,\text{ms}$ | $200\,\text{ms}$ |

Table 5.2: Controller gain values of the transport model and the time grid step. A two-staged approach is applied, where the resulting $\mu_{T_e,n_e\ result}(t) = \mu_{T_e,n_e}^{ff} + \mu_{T_e,n_e}^{fb}$ traces of a fine $t$ grid simulation are used to inform a faster coarse $t$ grid simulation.
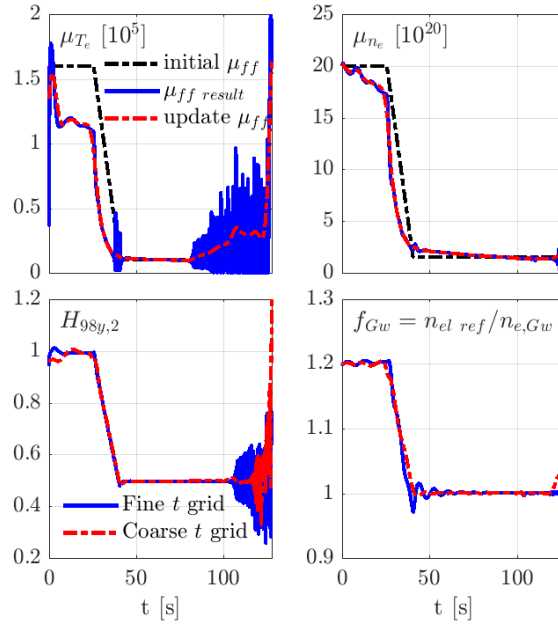


Figure 5.2: The feedforward $\mu_{T_e,n_e}(t)$ traces of the fine and coarse $t$ grid simulations are shown, as well as the resulting $H_{ref}$ and $n_{el\ ref}$ reference-tracking.

We summarize the controller gain values of the transport model and the time grid step that have been applied in the present work in Table 5.2. Note that finding a good set of gain values is a heuristic trial-and-error process, searching for controller gains that are large enough to ensure a good tracking of the reference $H_{ref}$ and $n_{el\ ref}$, while avoiding numerical oscillations that occur for values that are too large. To obtain fast simulations that can be used within a non-linear optimization framework, we use a two-staged approach:

- First, a simulation is run with a small time step $\Delta t$ and relatively large transport controller gains. The $\mu_{T_e,n_e}(t)$ traces are initialized with an educated guess for the time evolution of the pedestal gradient (the black dash-dotted lines in Figure 5.2). The first 100 time steps are performed with a reduced time step $\Delta t_{init}$. Furthermore, a reduced time step $\Delta t_{HL}$ is applied during the HL transition. A good tracking of the reference $H_{ref}$ and $n_{el\ ref}$ is obtained, as shown by the blue traces in the bottom panels in Figure 5.2. The resulting time traces $\mu_{T_e,n_e\ result}(t) = \mu_{T_e,n_e}^{ff} + \mu_{T_e,n_e}^{fb}$ (the blue traces in the top panels in Figure 5.2) are saved.

- A second simulation can be run with an increased and uniform time step and with reduced controller gains, by using the smoothed $\mu$ time traces from the previous simulation $\mu_{T_e,n_e\ result}(t)$ as feedforward reference $\mu_{T_e,n_e}^{ff}$ (the red traces in the top panels in Figure 5.2), leading again to a good tracking of the reference $H_{ref}$ and $n_{el\ ref}$, as shown by the red traces in the bottom panels in Figure 5.2, even for the coarser time grid, enabling a speed-up of the simulation by about a factor three.

### 5.2.5 Impurity concentrations and line radiation

Three impurity species are considered: (1) an intrinsic tungsten influx is assumed since W is envisioned as plasma-facing component armour material; (2) xenon is seeded in the core to enhance the radiated power, limiting the divertor heat load; (3) as alpha particles born from fusion reactions thermalise, heating the plasma, they constitute a source of helium impurities. At present, RAPTOR does not solve for impurity transport[3]. Within the simulation, the radial distribution of the impurities is taken proportionally to the electron density $n_e$, with a user-defined time-dependent concentration factor (the resulting time evolution of $Z_{eff}$ is calculated self-consistently).

Impurity radiation of the three impurity species is evaluated with the formula 5.4, with $L_{imp}(T_e)$ the impurity cooling factor taken from the ADAS database [ADAS; Maget et al. 2022; Ostuni et al. 2022].

$$P_{rad} = n_e n_{imp} L_{imp}(T_e) \tag{5.4}$$

---

[3]Note that the lack of impurity transport is an important limitation for ramp-down studies, as avoiding a radiative collapse caused by impurity accumulation poses an important constraint. The impurity concentration profiles and time evolution imposed in RAPTOR should be verified by higher fidelity integrated modeling codes. Alternatively, reduced analytical models [Fajardo et al. 2023] for (heavy) impurity transport could be integrated in the code.
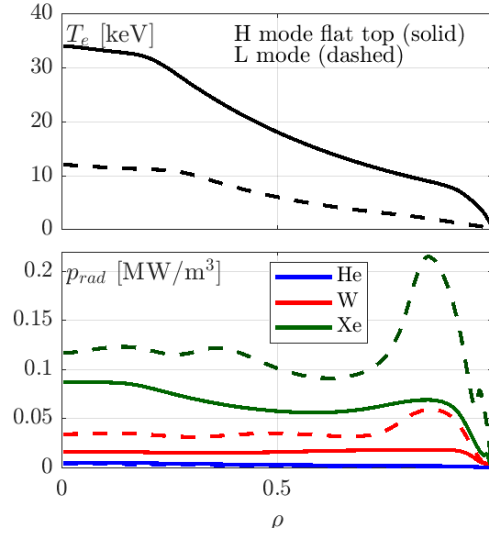
Figure 5.3:  Radiated power from three impurities, for concentrations $n_{He}/n_e = 0.05$, $n_W/n_e = 3\,10^{-5}$, $n_{Xe}/n_e = 5\,10^{-4}$, as evaluated with ADAS cooling factor data, with respectively the end of flat-top $T_e$ profile and a L-mode $T_e$ profile. Xenon, the seeded core impurity, is the dominant radiator. Note how the HL transition during the ramp-down leads to a strong increase in radiated power, from both W and Xe. A combination of plasma heating and Xe removal is required to avoid a radiative collapse, as studied later in this chapter.

Note that impurities affect the plasma power balance both by dilution of the main ions, impacting the fusion power, and by the emitted line radiation. The second process is highly non-linear with respect to temperature since the average cooling factor increases throughout the plasma core for decreasing $T_e$ (as illustrated in Figure 5.3). Under the modeling assumption $T_i = T_e$, the fusion power, and the alpha self-heating of the plasma, will decrease simultaneously. This dynamical process clearly has the potential of triggering a runaway process, with increased radiation and decreased fusion power further decreasing $T_e$.

## 5.2.6   MHD equilibrium geometry

The equilibrium geometry used for the RAPTOR simulations is based on the free boundary equilibrium calculations in CREATE-NL. The plasma boundary shapes at different times in the plasma ramp-down, at different values of the plasma current, are shown in Figure 5.4. The geometry metrics corresponding to these equilibria are assigned to the time in the RAPTOR simulation when the corresponding plasma current is reached. For intermediate times, the geometry metrics are interpolated linearly. The CREATE-NL calculations have also been used to obtain an operating envelope for vertically stable operation during the DEMO ramp-down phase, as explained in Section 5.5.2.

The equilibria have a lower single null configuration. The elongation is reduced during the ramp-down, while the LCFS shape close to the X-point remains mostly unchanged, easing the heat exhaust challenge for the divertor by maintaining the magnetic geometry in the strike point regions.
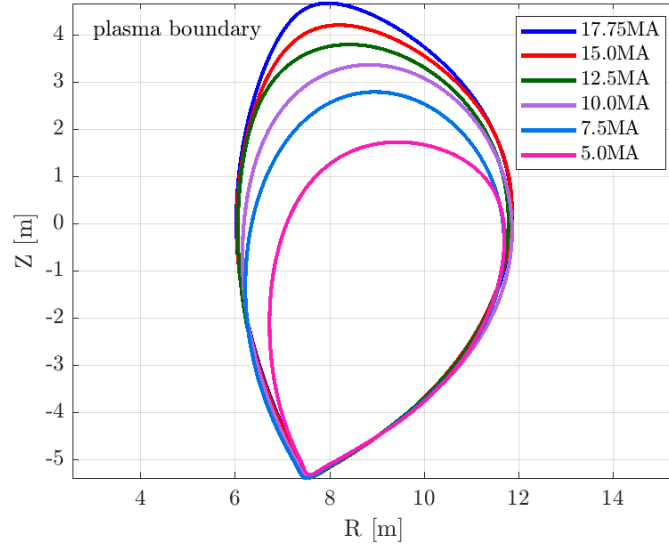
Figure 5.4: Plasma boundary shapes at different values of the plasma current during the ramp-down phase, simulated with the free boundary equilibrium solver CREATE-NL [Albanese et al. 2015], as reported in [Mattei et al. 2016]. The equilibrium geometry of these equilibria is used for the RAPTOR simulations in this chapter.

## 5.3 Stationary DEMO operating point

The stationary operating point established here is mainly based on considerations reported in [Zohm et al. 2013], [Giruzzi et al. 2015] and [Siccinio et al. 2020]. The operating parameters are summarized in Table 5.3. A central feature of a burning DEMO plasma is the high degree of self-regulation of the plasma profiles: the power balance is dominated by the plasma self-heating by the fusion-born alpha fast particles, dependent on $T_i(\rho)$, $n_{D,T}(\rho)$ and fuel dilution, and the radiated power from heavy impurities, both intrinsic (W) and seeded (Xe), with a non-linear dependence on $T_e$. Reliance on auxiliary current drive to tailor the $q$ profile is minimized to maintain a high fusion gain $Q$.

- In [Giruzzi et al. 2015], the physics-based transport model TGLF is used to predict critical temperature and density gradients. Based on those values, we set $\lambda_{T_e} = 2$ ($R/L_{T_e} \sim 6$) and $\lambda_{n_e} = 0.67$ ($R/L_{n_e} \sim 2$). In the L-mode phase, discussed in the next section, we assume $\lambda_{T_e\ L\ mode} = (3/2.3)\lambda_{T_e\ H\ mode}$ and $\lambda_{n_e\ L\ mode} = (1/0.5)\lambda_{n_e\ H\ mode}$, assuming the same factors $\lambda_{T_e,n_e\ L\ mode}/\lambda_{T_e,n_e\ H\ mode}$ as were obtained for JET and AUG in [Teplukhina et al. 2017]. The ion temperature is set $T_i = T_e$. Even though electron heating is dominant for the simulated DEMO plasma, $T_e \sim T_i$ is assumed due to the high confinement time scale with respect to the equipartition time scale in a DEMO device [Stober et al. 2015; Fable et al. 2019].

- The W concentration is set to $3\ 10^{-5}$, like in [Giruzzi et al. 2015]. The Xe concentration is set to $5\ 10^{-4}$, allowing for a total radiated power of 242 MW, which is about 54% of the total heating power. This allows to limit $P_{sep}/R_0$ to 22.9 MW/m (close to

Figure 5.5: Radial profiles for stationary (flat loop voltage profile) flat-top burning plasma DEMO operating point, as evaluated by RAPTOR.

| | |
|---|---|
| $I_p$ | 17.75 MA |
| $B_0$ | 5.86 T |
| $a$ | 2.93 m |
| $R_0$ | 8.95 m |
| $V$ | 2318 m$^3$ |
| $\kappa_e$ | 1.67 |
| $\delta_e$ | 0.37 |
| $I_{bs}/I_p$ | 0.46 |
| $I_{ni}/I_p$ | 0.57 |
| $P_{fus}$ | 1732 MW |
| $P_{nb}$ | 50 MW |
| $P_{ec}$ | 50 MW |
| $P_{rad\ tot} = P_{brem} + P_{line}$; $f_{rad} = \frac{P_{rad\ tot}}{P_{heat\ tot}}$ | 242 MW; 54% |
| $P_{sep}$ | 205 MW |
| $P_{LH}$ | 121 MW |
| $W_{th\ tot}$ | 1279 MJ |
| $T_{i0}$, $T_i(\rho = 0.8)$ | 38.1 keV, 7.9 keV |
| $T_{e0}$, $T_e(\rho = 0.8)$ | 38.1 keV, 7.9 keV |
| $q_{95}$ | 4.26 |
| $q_{min}$ | 1.05 |
| $\langle n_e \rangle_{line}/n_{e\ Gw}$ | $7.9 \times 10^{19}$ m$^{-3}$/$6.6 \times 10^{19}$ m$^{-3}$=1.20 |
| $n_{e0}/\langle n_e \rangle_{vol}$ | $10.3 \times 10^{19}$ m$^{-3}$/$7.1 \times 10^{19}$ m$^{-3}$=1.45 |
| $H_{y2,98}$ | 1.00 |
| $\beta_N$ | 2.57 |
| $l_i$ | 0.64 |
| $U_{pl}$ | 22.5 mV |
| $Q$ | 17.3 |
| $\langle Z_{eff} \rangle_{vol}$ | 2.32 |
| $n_{helium}/n_e$ | 0.05 |
| $n_{xenon}/n_e$ | $5 \times 10^{-4}$ |
| $n_{tungsten}/n_e$ | $3 \times 10^{-5}$ |
| $P_{sep}/R_0$ | 22.9 MW/m |

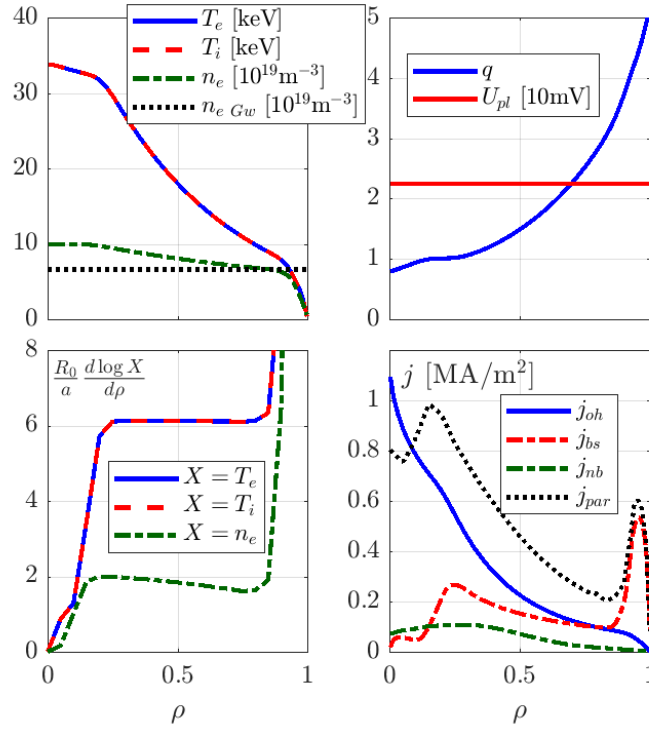Table 5.3: Operating parameters for stationary (flat loop voltage profile) flat-top burning plasma DEMO operating point, as evaluated by RAPTOR.

$P_{sep}/R_0$=18.9 MW/m in the EU-DEMO 2018 design point reported in [Siccinio et al. 2020]), while a margin $P_{sep} - P_{LH} \sim 80$ MW is maintained, to achieve good confinement and avoid any unwanted HL back transition. The helium concentration is set to 0.05, inspired by the COREDIV [Zagorski et al. 2013] simulation results in [Giruzzi et al. 2015], and below the maximum He concentration of 0.075 mentioned in [Siccinio et al. 2018].

- The fusion power is $P_{fus}$=1732 MW, below the 2 GW of the EU-DEMO 2018 design point. Note that this value is sensitive to assumptions regarding temperature and density peaking (higher reactivity in the center), Greenwald fraction, $H_{98y,2}$ factor, impurity concentrations (diluting the DT fuel). The impurity concentrations will also impact the discharge duration through the impact of $Z_{eff}$ on the neoclassical conductivity, and hence on the loop voltage to be provided by the central solenoid to sustain the required ohmic plasma current.

- For the applied $R/L_{n_e}$, a density peaking $n_{e0}/\langle n_e \rangle_{vol} = 1.45$ results, close to what has been reported in [Fable et al. 2019]. With this density peaking a Greenwald fraction $\langle n_e \rangle_{line}/n_{e\ Gw} = 1.2$ can be achieved, while maintaining the pedestal density about 5% below the Greenwald density (the density constraint is assumed to be active at the pedestal top location [Zohm et al. 2013]).

- It is interesting to note that RAPTOR predicts that bootstrap current is about half of the total plasma current. As illustrated in Figure 5.5, the bootstrap current density is a strong source of off-axis current density (with a notable peak in the pedestal region). As a consequence, $q_{min}$ is relatively close to unity, with a region of low magnetic shear extending to $\rho \sim 0.25$ (sawteeth model not activated).

## 5.4 Heating throughout ramp-down to avoid a radiative collapse

In this section, we explore manually optimized time traces of auxiliary heating and the Xe impurity concentration, aiming for a feasible ramp-down scenario, avoiding a radiative collapse. Optimization with respect to vertical stability is presently not considered, but will be addressed in Section 5.6.

The plasma current is reduced with a constant ramp rate $dI_p/dt = -100$ kA/s. A time trace of the evolution of $H_{98,y2}$ is pre-defined, setting both the timing of the HL transition and assumptions regarding the confinement quality during H- and L-mode. For the simulation presented in this section, the HL transition is initialized at $t = 0.2 t_{final}$ ($t_0 = 0$ s at the end of flat-top). The H factor transitions linearly from $H_{98y,2} = 1$ to $H_{98y,2} = 0.5$, over a duration[4] $\Delta t_{duration\ HL} = 15$ s. Note that these choices are relatively arbitrary at this stage. In the next section we will however perform a sensitivity study, changing the HL timing and L-mode confinement factor. An overview of the evolution of various parameters during the ramp-down

---

[4]The duration of the transition phase depends on the characteristic time required to decrease the pedestal and depends on a variety of plasma parameters. In [Teplukhina et al. 2017], $\Delta t_{duration\ HL} = 0.1$ s, 0.5 s and 1 s have been derived, based on Thomson and $H_\alpha$ measurement, for respectively TCV, AUG and JET.
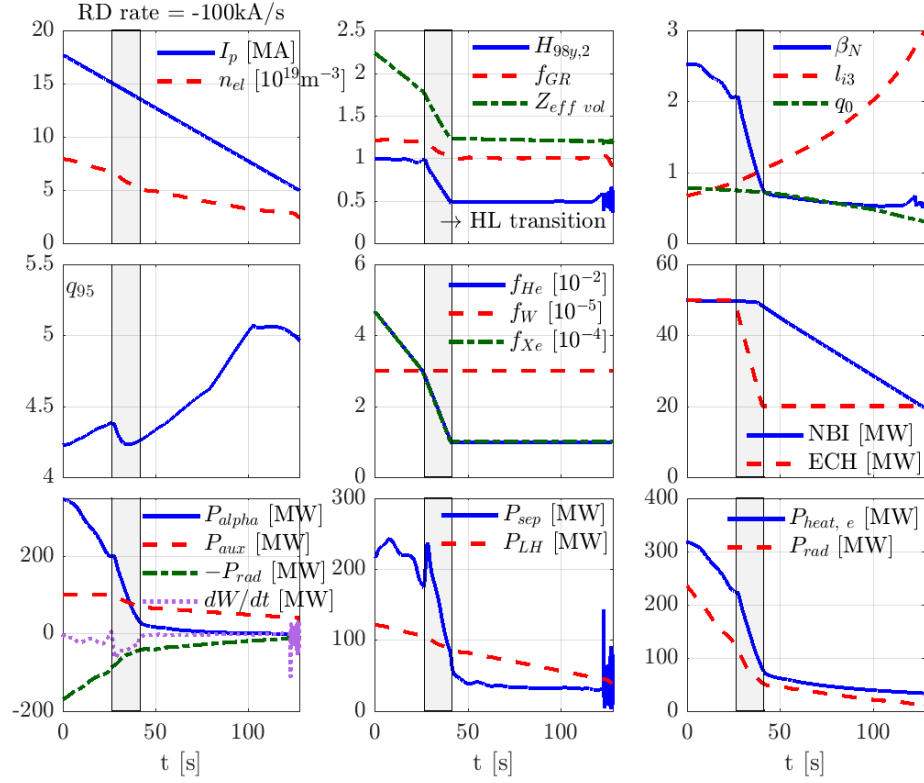
Figure 5.6: Key time traces for DEMO ramp-down RAPTOR simulation with $dI_p/dt = -100\,\text{kA/s}$, $t_{HL} = 0.2t_{final}$, $H_{98y,2} = 1$ in H-mode, $H_{98y,2} = 0.5$ in L-mode. The time evolution of auxiliary heating and Xe concentration are optimized to avoid a radiative collapse.

simulation is given in Figure 5.6.

### 5.4.1   Power balance and impurity concentrations

We list some of the constraints and considerations that have been taken into account when designing these ramp-down traces.

**Strong auxiliary heating required throughout the entire ramp-down phase**

Even if the Xe concentration can be efficiently reduced during the ramp-down (which is far from obvious and needs to be assessed in more sophisticated codes), strong auxiliary heating of the plasma throughout the entire modeled ramp-down phase (i.e. the diverted phase down to $I_p = 5\,\text{MA}$) is mandatory to avoid a radiative collapse. This is due to the combined effect of an increasing cooling factor for W and Xe for reducing $T_e$, and a simultaneous sharp decrease of the alpha power with reducing $T_i$ and $n_e$ (the density has to be reduced simultaneously with the plasma current to avoid an increasing violation of the Greenwald density limit). Note that higher fidelity simulations are required to assess the feasibility of the proposed ramp-down

rates of density and Xe impurity concentration, taking into account the expected particle confinement time (usually the particle confinement time is 5-10 times larger compared to the energy confinement time [Becker 1988]), impurity confinement time and pump efficiency. To conclude: the plasma needs to be strongly heated while being terminated ($P_{ec} = 50\,\text{MW} + P_{nb} = 50\,\text{MW}$ at the beginning of ramp-down, maintaining $P_{ec} = 20\,\text{MW} + P_{nb} = 20\,\text{MW}$ by $t = t_{final}$, when $I_p = 5\,\text{MA}$). The margin with respect to radiative instability can be evaluated from the bottom right plot in Figure 5.6: the heating power to the electrons $P_{heat\ e}$ should be maintained above the radiated power $P_{rad}$, throughout the ramp-down. The margin is relatively small at the end of the HL transition: with $P_{aux} \sim 70\,\text{MW}$, a margin $P_{heat\ e} - P_{rad} \sim 20\,\text{MW}$ can be maintained. Note that the heating of discharges with high radiation during ramp-down is already common practice on present-day devices.

### Self-consistent triggering of HL transition

While enough heating power needs to be maintained throughout the L-mode phase of the ramp-down, the reduction of heating power during the HL transition power should obviously be significant enough to actually trigger the transition to an L-mode plasma. Note that the strong reduction of stored thermal energy provides an effective heating term $-\dot{W}_{th} = -dW_{th}/dt > 0$, as the stored thermal energy crosses the separatrix, contributing to $P_{sep} = P_{heat} - \dot{W}_{th} - P_{rad}$, delaying the timing when $P_{sep} < P_{LH}$, with $P_{LH}$ the LH threshold power predicted by the Martin scaling law [Martin and Takizuka 2008].

In the present simulation, self-consistency of the HL transition is ensured by making sure $P_{sep}$ drops below $P_{LH}$ during the HL transition time window between $t = t_{HL}$ and $t = t_{HL} + \Delta t_{duration\ HL}$. The H factor reference trace is linearly reduced during this time window, leading to a decreasing alpha heating. In reality, the fusion power would be reduced by adjusting the DT fuel ratio. Furthermore the density is reduced, by adjusting the Greenwald fraction $f_{Gw}$ from 1.2 to 1 (as mentioned before, the particle confinement time limits the density ramp-down rate). The power conducted over the separatrix $P_{sep}$ comes down to $P_{LH}$ only by the end of the HL transition time window, due to the effective $\dot{W}_{th}$ heating term. In the simulation, reducing the Greenwald fraction during the HL transition is found to increase the margin with respect to a radiative collapse, as calculated self-consistently from the various species densities (assuming the pre-defined impurity concentration traces).

### The effect of $Z_{eff}$

Note that by ramping down the impurity concentrations, to avoid radiative collapse, $Z_{eff}$ decreases throughout the ramp-down (the He concentration is reduced, which is consistent with the reducing number of fusion reactions, reducing the source term for He ions; the W concentration is maintained constant). The resulting $Z_{eff}$ evolution is evaluated self-consistently in RAPTOR. A reduced $Z_{eff}$ leads to a reduced resistivity of the plasma, slowing down current diffusion. This raises an interesting trade-off between the margins with respect to radiative and vertical instabilities: by reducing $Z_{eff}$, margin with respect to a radiative
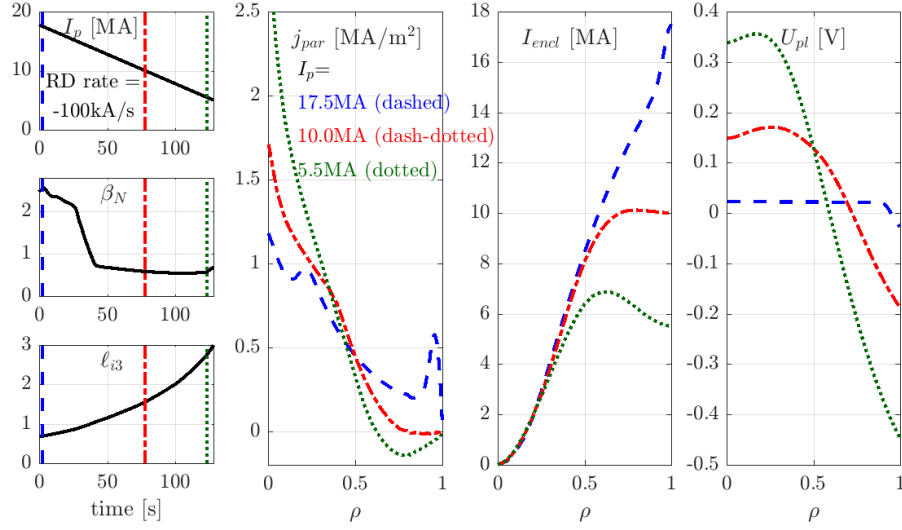
Figure 5.7: The (integrated) parallel current density and the loop voltage profile are shown at three different timings during the ramp-down.

instability can be improved, at the expense of a slower current diffusion, leading to a stronger increase of $\ell_{i3}$, making the plasma more vertically unstable. Tailoring the plasma current density to limit the increase of $\ell_{i3}$, by optimization of the time traces of plasma current and elongation, is discussed in Section 5.6.

**Heat exhaust constraints**

Finally, the reduction of impurity concentrations should not lead to a large increase in the power crossing the separatrix, that needs to be handled by the divertor. Even though this heat load would be transient, a reduced $P_{sep}$ with respect to flat-top values might be required due to the difficulty of maintaining the plasma detached during the ramp-down phase, at lower plasma densities. In the present simulation $P_{sep}$ is maintained below 240 MW throughout the H-mode phase (compared to $P_{sep} = 205$ MW during flat-top burning plasma phase). Further modeling studies into the simultaneous reduction of alpha power and radiated power, including quantitative heat exhaust constraints, are left for future work.

### 5.4.2 Current diffusion dynamics

**Peaking of the current density**

In Figure 5.7, the current density $j_{par}$, integrated current density $I_{encl}$ and the loop voltage profile $U_{pl}$ are shown at various times during the ramp-down simulation, first during H-mode and subsequently at two times during the L-mode phase. Close to the initial state of the simulation, the current density profile is relatively broad, with a strong contribution from the bootstrap current driven within the pedestal region. The simulation starts from a stationary

state with a fully relaxed current density profile, characterized by a radially flat loop voltage profile. As a consequence, the ohmic current density is self-similar with the neoclassical conductivity profile.

Note that to follow the imposed $dI_p/dt$, the edge loop voltage is continuously reduced. The internal current distribution of the plasma changes with a diffusion time scale that increases with the size of the device and the plasma electron temperature, leading to large values in DEMO with respect to present-day devices. As the ramp-down is fast with respect to the current diffusion time scale, the current density evolves into an increasingly non-equilibrated state ($U_{pl0}$-$U_{pl,edge}$ increases). As the loop voltage is strongly peaked, the ohmic current density (which is the dominant contribution, especially during L-mode), can have a strongly different shape with respect to the neoclassical conductivity profile (and hence $T_e^{3/2}$).

The plot showing the integrated plasma current profiles ($I_{encl}$), shows that the enclosed plasma current at small radii decreases very slowly, due to the slow outward current diffusion. As the plasma volume reduces throughout the ramp-down phase, the central current density rises. Alternatively formulated, the central current density resists fast reductions (with respect to the current diffusion time scale) of the neoclassical conductivity and bootstrap current by raising the central loop voltage. Nevertheless, the total plasma current evolution (imposed as a Neumann boundary condition for eq. (2.16)), needs to be satisfied, leading to a negative current density in the outer plasma. The MHD stability of suchlike current density profiles has not been investigated.

As the current density evolves on a slow time scale with respect to the plasma current, the plasma current ramp-down rate $dI_p/dt$ is an effective control parameter to tailor the evolution of the internal inductance $\ell_{i3}$, as has been discussed in [de Vries et al. 2017]. In Section 5.6, this feature will be leveraged to maintain the internal inductance below an upper limit given by vertical stability calculations in CREATE-NL.

In [Romero and JET-EFDA Contributors 2010], a lumped parameter model for the time evolution of the tokamak plasma current and internal inductance has been proposed, with plasma resistance, non-inductive current and boundary voltage or poloidal field coil currents as inputs. The circumstances for a correlation between $d\ell_{i3}/dt$ and $dI_p/dt$ are analytically derived, supporting the use of $I_p$ as a virtual actuator to control the internal inductance.

### 5.4.3   The impact of sawteeth on current density peaking

The peaking of the current density, as described in the previous section, leads to a decrease of $q_0$ below unity, even though $q_{95}$ is increasing throughout the ramp-down, as shown in Figure 5.6. As a consequence, sawteeth instabilities will likely be triggered at some time during ramp-down. In the present section, we assess the impact of sawteeth on the time evolution of $\ell_{i3}$. In Figure 5.8, the early HL, cold L-mode $-100\,\text{kA/s}$ ramp-down simulation is compared to a simulation where the RAPTOR sawtooth model, first presented in [Piron et al. 2015], is applied, using the sawtooth models described in [Porcelli et al. 1996; Sauter et al. 1998]. A sawtooth crash is triggered when the magnetic shear at $q = 1$ exceeds a user-defined critical value. In this simulation we set $s_{q=1,crit} = 0.4$, inspired by the values mentioned for a burning
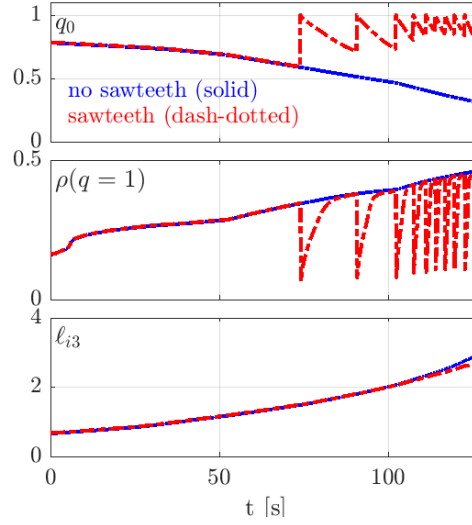
Figure 5.8: The impact of the sawtooth model on the early HL, cold L-mode, $-100\,$kA/s ramp-down simulation is illustrated. Only a minor impact on the $\ell_{i3}$ evolution is observed.

plasma in [Kim et al. 2014]. The red traces in Figure 5.8 show that the first sawtooth crash is triggered only in the second half of the ramp-down phase, after the plasma transitions to low confinement mode. The long sawtooth period during the H-mode phase of the plasma is consistent with the fast particle stabilization of sawteeth expected in a burning plasma [Eriksson et al. 2004; Porcelli et al. 1996] (resulting in a higher expected value of $s_{q=1,crit}$ compared to present-day devices).

Note that the impact of the sawtooth crashes on the time evolution of the internal inductance is minor and leads to a slight reduction, hence increasing the margin with respect to vertical instability. This can be understood as follows: after a sawtooth crash, the temperature profile broadens, hence broadening the neoclassical conductivity profile and eventually the current density profile (tending to reduce $\ell_{i3}$). However, this change of profiles occurs mostly in the center, while the outer $j_{par}$ profile remains mostly unaffected. Furthermore, after the sawtooth crash the $\rho(q = 1)$ radius moves inward. In the gradient-based transport model this leads to a peaking of the temperature profile: the region with stiff transport and a high temperature gradient extends further into the core. This effect counteracts the broadening effect mentioned earlier. Since the impact of sawtooth with the present modeling assumptions is small, and tends to ease the burden on vertical control, the sawtooth model is not used in the feasibility and optimization studies discussed further in this chapter. Once an optimum ramp-down trajectory is found, this conservative assumption can be relaxed to assess the potential of sawteeth to further reduce $\ell_{i3}$.

## 5.5 Vertical stability for different $I_p$ ramp-rate, HL transition timing and L-mode confinement assumptions

### 5.5.1 Modeling results

With the set-up discussed in the previous section, a range of different ramp-down simulations has been performed, with each of the following $I_p$ ramp-down rates: $dI_p/dt = -50\,\text{kA/s}$, $-100\,\text{kA/s}$, $-150\,\text{kA/s}$, $-200\,\text{kA/s}$. Note that $dI_p/dt = -200\,\text{kA}$ was used as the starting point of this study, as it is the DEMO reference design value that was also used for the CREATE-NL free boundary equilibrium control simulation in [Mattei et al. 2016]. For each of these ramp-down rates, two simulations are run, differing from one another in HL transition timing and the assumed L-mode confinement quality:

- *Early HL, cold L:* the HL transition is initialized at $t = 0.2\,t_{final}$ ($t_0 = 0\,\text{s}$ at the end of flat-top). The H factor transitions linearly from $H_{98y,2} = 1$ to $H_{98y,2} = 0.5$, over a duration $\Delta t_{duration\ HL} = 15\,\text{s}$. These are the same assumptions that have been applied for the simulation in Section 5.4.

- *Late HL, hot L:* the HL transition is initialized at $t = 0.4\,t_{final}$. The H factor transitions linearly from $H_{98y,2} = 1$ to $H_{98y,2} = 0.75$, over a duration $\Delta t_{duration\ HL} = 15\,\text{s}$.

By running the ramp-down simulations for both of these assumptions, a case with a more significant confinement transition earlier in the discharge can be compared with a more gradual confinement transition later in the discharge (giving a rough estimate for the sensitivity to the assumed H factor trace).

The resulting RAPTOR simulations are presented in Figure 5.9. As expected, increasing the absolute value of the $I_p$ ramp-down rate leads to an faster growth of the internal inductance $\ell_{i3}$. Furthermore, for each of the ramp-down rates, a delayed HL transition combined with an improved L-mode confinement quality leads to a stronger growth of $\ell_{i3}$. As higher temperatures are maintained for a longer time, the outward diffusion of the central plasma current is slowed down, causing a further peaking of the current density.

To ensure radial position control, the time derivative of the vertical magnetic field must stay below an upper limit, depending on coil voltage limits imposed by power supplies and/or the superconductor. While we have presently no upper limit value available, we evaluate $dB_v/dt$ with eq. (5.1) for the different simulations, as shown in Figure 5.9. The time derivative $dB_v/dt$ reaches the largest absolute values during the HL transition (as expected from the $\beta_p$ dependence in eq. (5.1)). Furthermore, note that the best-case scenario $H_{98y,2}$ trace regarding vertical stability (early HL, cold L) is the most demanding regarding radial position control, with the strongest peak in the $dB_v/dt$ trace.
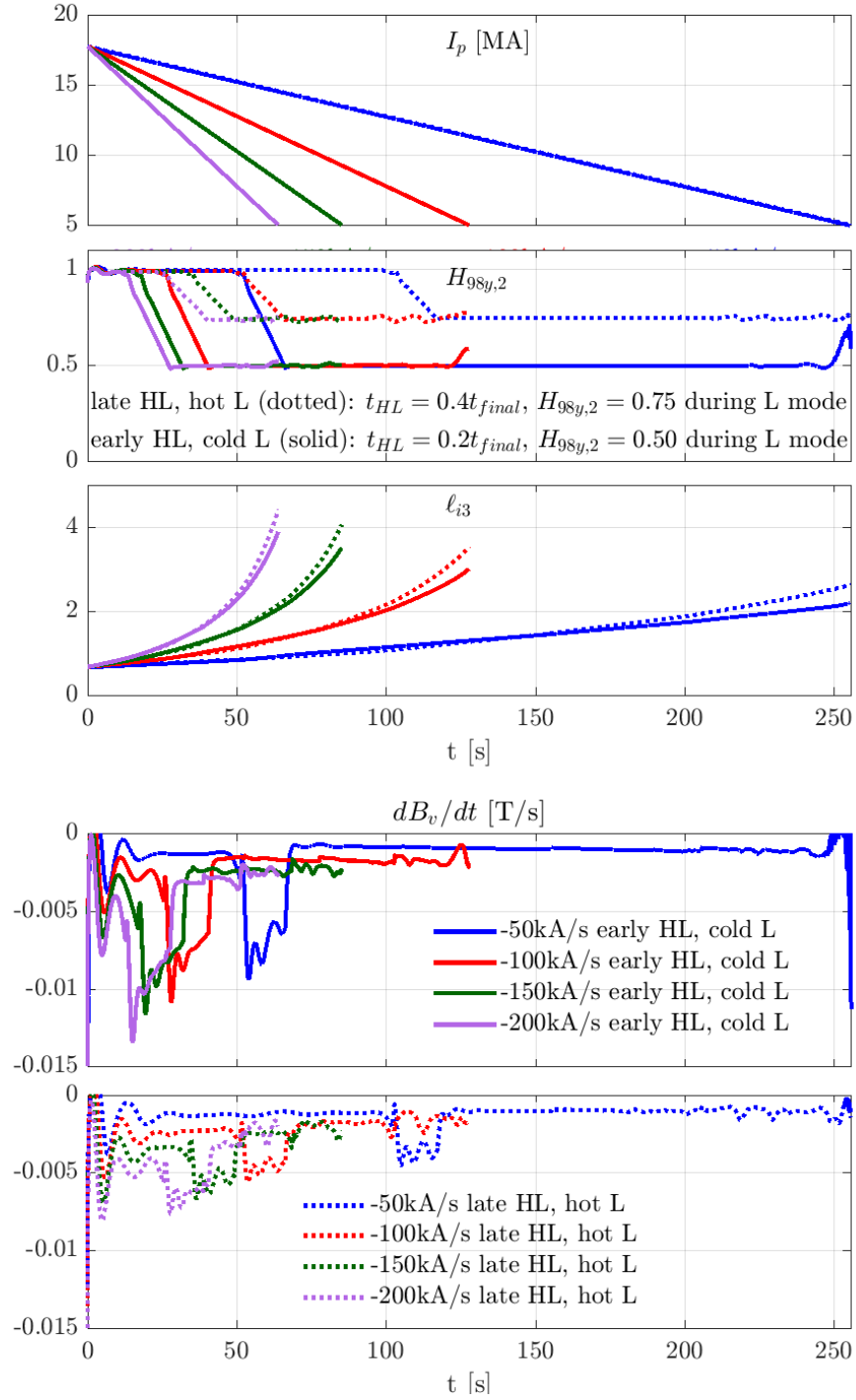
Figure 5.9: A set of RAPTOR simulations for different ramp-down rates $dI_p/dt = -50\,\text{kA/s}, -100\,\text{kA/s}, -150\,\text{kA/s}, -200\,\text{kA/s}$. For each ramp-down rate, two assumptions for the $H_{98y,2}$ time evolution are considered.

| $I_p$ [MA] | $\ell_{i3}$ | $\beta_{pol}$ | $\kappa$ |
|---|---|---|---|
| 19.6 | < 0.90 | 1.10 | < 1.68 |
| 17.5 | < 1.00 | 1.10 | < 1.56 |
| 15.0 | < 1.10 | 1.05 | < 1.50 |
| 12.5 | < 1.25 | 1.00 | < 1.45 |
| 10.0 | < 1.40 | 1.00 | < 1.40 |
| 7.5 | < 1.60 | 0.10 | < 1.40 |
| 5.0 | < 1.70 | 0.10 | < 1.35 |

Table 5.4: From free boundary equilibrium control calculations with CREATE-NL [Albanese et al. 2015], the above combinations of $(I_p, \kappa, \ell_{i3})$ are considered controllable, as reported in [Mattei et al. 2016]. For a given plasma current, the elongation and internal inductance values provide an upper constraint on the stable operating envelope.

### 5.5.2 Comparison RAPTOR-predicted $\ell_{i3}$ versus CREATE-NL vertical stability limit

**CREATE-NL vertical stability limit**

In [Mattei et al. 2016], free boundary equilibrium control calculations with CREATE-NL [Albanese et al. 2015] are presented for the diverted phase of the DEMO plasma ramp-up and ramp-down. For the ramp-down, the limits to a vertically stable operating envelope are mapped out with respect to the plasma current $I_p$, elongation $\kappa$ and internal inductance $\ell_{i3}$. The resulting sequence of triplets $(I_p, \kappa, \ell_{i3})$ of controllable operating parameters is repeated in Table 5.4. Each of these three parameters play an important role in the assessment of vertical stability: while a degraded vertical control efficiency can be anticipated for an increased internal inductance $\ell_{i3}$, corresponding to a stronger peaking of the current density, this tendency can be counteracted by adjusting the plasma shape, reducing the elongation. Furthermore, controllability of the vertical position improves at lower plasma current, as the coil currents for vertical stability control in the CREATE-NL model for DEMO are more effective to counteract vertical position excursions at lower plasma current [Mattei et al. 2016]. Considering the upper limits for internal inductance $\ell_{i3}$ and elongation $\kappa$ for a given plasma current $I_p$ (as summarized in Table 5.4), the potential of different ramp-down rates to maintain the internal inductance below the upper limit for vertical controllability can now be assessed. For the purpose of the feasibility study presented here and the optimization introduced in the next section, we employ these values to extract a constraint on the internal inductance, dependent on the plasma current value. We assume that the plasma can be maintained vertically stable if $\ell_{i3} < f_{margin} \ell_{i3\ CREATE}(I_p)$. We include a margin factor $f_{margin} > 1$, as the present constraint $\ell_{i3\ CREATE}(I_p)$ is a conservative assessment, not an optimized limit. Various considerations could increase the maximum allowed $\ell_{i3}$.

- Optimizing position and shape control, while using the consistent kinetic profile evolution, is expected to provide some improvement with respect to vertical controllability.

- Inclusion of in-vessel coils in the DEMO design would facilitate more effective vertical control.
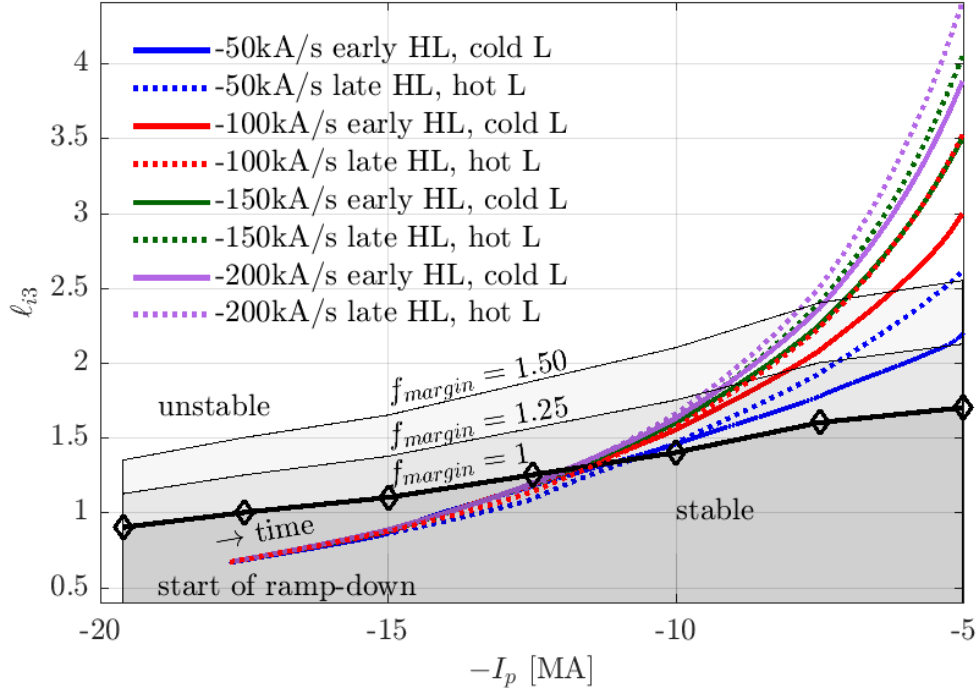
Figure 5.10: Time traces of $\ell_{i3}$ within the $(-I_p, \ell_{i3})$ plane, for the RAPTOR simulations shown in Figure 5.9. The stability limit $f_{margin}\ell_{i3\ CREATE}(I_p)$ allows to assess the margin with respect to the vertical stability limit obtained in CREATE-NL.

- A faster decrease of elongation $\kappa$ with respect to the reference in [Mattei et al. 2016] improves vertical controllability for a given plasma current.

The vertical stability constraint $\ell_{i3\ CREATE}(I_p)$ is indicated in Figure 5.10, with the diamond symbols representing the equilibria from CREATE-NL that are introduced in Table 5.4. Allowing for some margin with respect to this CREATE-NL result, the lines with margin factor $f_{margin} = 1.25$ and 1.50 are also shown. The dark grey region with $\ell_{i3} < \ell_{i3\ CREATE}(I_p)$ is the region where vertical stability can be guaranteed, while the white region $\ell_{i3} > 1.5\ell_{i3\ CREATE}(I_p)$ contains operating points that can likely not be maintained vertically stable. Note that the x-axis is $-I_p$, so that moving to the right on the abscissa corresponds to progressing time during the ramp-down phase. Later in the ramp-down, at lower plasma currents, a larger internal inductance can be maintained vertically stable.

**Comparison to modeled $\ell_{i3}$ traces**

Let us now superimpose the $\ell_{i3}$ traces modeled in RAPTOR on the $(-I_p, \ell_{i3})$ plot in Figure 5.10. For each of the considered ramp-down rates $dI_p/dt = -50\,\text{kA/s}, -100\,\text{kA/s}, -150\,\text{kA/s}, -200\,\text{kA/s}$, the two assumptions for the $H_{98y,2}$ time evolution introduced in Section 5.5 are considered: early HL transition to cold L-mode versus late HL transition to hot L-mode. The maximum values of $\ell_{i3}$ reached at the final time of the simulation (for $I_p = 5\,\text{MA}$) are shown

| $dI_p/dt$ [kA/s] | $t_{final}$ [s] | $\ell_{i3\ final}$ (early HL, cold L) | $\ell_{i3\ final}$ (late HL, hot L) |
|---|---|---|---|
| −50 | 256 | 2.20 | 2.61 |
| −100 | 128 | 3.00 | 3.53 |
| −150 | 85 | 3.50 | 4.05 |
| −200 | 64 | 3.88 | 4.41 |

Table 5.5: Final (maximum) value of the internal inductance $\ell_{i3}$ for the RAPTOR simulations shown in Figure 5.9.

in Table 5.5. As a first conclusion, we can observe that the tendency of the plasma to peak the current density during the ramp-down phase leads to a stronger increase of $\ell_{i3}$ compared to the increase of the constraining value $\ell_{i3\ CREATE}$, even for a conservative ramp-rate of $dI_p/dt = -50\,\text{kA/s}$. However, allowing for some margin on the vertical stability constraint (justified by the reasons listed earlier), the $dI_p/dt = -50\,\text{kA/s}$ ramp-down simulations stay below upper limits with $f_{margin}$ respectively 1.25 and 1.50. For the fastest ramp-down assumption ($dI_p/dt = -200\,\text{kA/s}$), both H factor trace assumptions lead to a severe violation of the upper $\ell_{i3}$ limit with $f_{margin} = 1.50$. We conclude that this ramp-down rate is likely overly ambitious for a reliable DEMO design.

Also for the simulations with intermediate $I_p$ ramp-down rates ($dI_p/dt = -150\,\text{kA/s}, -100\,\text{kA/s}$), the upper $\ell_{i3}$ limit with $f_{margin} = 1.50$ is violated. In the following section, we will attempt to optimize the plasma current trace and the plasma shaping evolution to bring the $\ell_{i3}$ trace below the upper constraint, with $f_{margin}$ either 1.25 and 1.50, for these intermediate ramp rates.

## 5.6 Optimized $I_p$ and shaping evolution to avoid vertical instability

In the present section, feasible DEMO ramp-down scenarios are searched for by numerical solution of an optimal control problem for the ramp-down phase. The mathematical formulation and solution procedure is discussed in Section 5.6.1, while the actual results are presented in Section 5.6.2.

### 5.6.1 Formulation of the optimization problem

**Cost function**

Loosely speaking, the aim is to ramp down the plasma current as quickly as possible, while satisfying all physical and technical constraints. Since the plasma density should decrease proportionally to $I_p$ to avoid a density limit violation, and since the fusion power is proportional to the square of the plasma density, a fast decrease of $I_p$ corresponds to a fast decrease of the plasma thermal energy. A fast $I_p$ decrease hence reduces the potential impact of depositing the stored thermal energy on the reactor vessel first wall. Furthermore, the electromagnetic forces acting on the vessel after plasma disruption are proportional to $I_p^2$. To reflect these

considerations, the time integal of the plasma current is chosen as a cost function:

$$J_{I_p} = \nu_{I_p} \int_0^{t_{final}} I_p(t) dt \tag{5.5}$$

The factor $\nu_{I_p}$ is chosen to have a cost function around unity for the initial condition for the ramp-down traces.

**Constraint functions**

An extensive set of physical and technical limits constrain the ramp-down phase:

- *Density limit:* as the time evolution of the plasma current $I_p(t)$ is adjusted during the optimization, the reference density trace $n_{el, ref}(t)$ (Section 5.2.3) is updated after each iteration step, to keep the allowed Greenwald fraction unchanged throughout the optimization procedure.

- *Vertical stability limit:* $\ell_{i3} < f_{margin} \ell_{i3, CREATE}(I_p)$, as discussed before. Note that by optimizing the plasma current, both the internal inductance $\ell_{i3}$ and the upper limit $\ell_{i3, CREATE}(I_p)$ can be adjusted.

- *Ideal MHD stability:* a constraint can be added to maintain $dq_{95}/dt = \dot{q}_{95} > 0$, while $q_{95} < 4.5$, to avoid the onset of ideal MHD instabilities. Generally, plasmas with a lower $q_{95}$ value are more prone to MHD instabilities, since they operate closer to the ideal MHD limit. Hence we choose to avoid $q_{95}$ decreasing when $q_{95} < 4.5$, although this is not a hard limit and could be further relaxed.

**Optimization variables**

The actuator traces that are optimized to minimize the cost function while satisfying the constraints are the plasma current $I_p(t)$ and the elongation of the plasma edge $\kappa(t)$. These variables have been introduced as optimization variables for the ramp-down phase in [Teplukhina et al. 2017]. Within the optimization problem formulation, the actuator traces $u_i(t) = I_p(t), \kappa(t)$ are parametrized by a set of optimization variables $p_{i,j}$. The optimization variables contain the values of the actuator time traces on a set of $n_i$ free knot points, as described by eq. (5.6): by multiplication with a set of piecewise linear basis functions, followed by summation, the actuator traces $u_i(t)$ are recovered (for the actuators $i$ and the corresponding optimization variables $p_{i,j}$, more detail can be found in [Felici and Sauter 2012]).

$$u_i(t) = \sum_j^{n_i} P_{ij}(t) p_{i,j} \tag{5.6}$$

157

**Using the elongation trace $\kappa$ as an optimization variable**

As the equilibrium impacts the radial transport equations through geometric coefficients in the diffusion PDEs (eq. (2.16), eq. (2.24) and eq. (2.25)), the time evolution of the elongation $\kappa$ can be used as an optimization variable, to impact the plasma state dynamics. In RAPTOR, these metrics, stacked together in the vector $\mathbf{g}$, are calculated from the output files of a CHEASE equilibrium solution. From the CREATE-NL equilibrium solutions introduced in Section 5.2.6, a sequence of metrics $\mathbf{g}_\kappa$ for seven different values of plasma elongation $\kappa$ is obtained. During a ramp-down with constant ramp rate $dI_p/dt$, $\mathbf{g}$ for intermediate time points is evaluated through linear interpolation in time.

We attempt to optimize the time evolution of the plasma shape, by finding the optimum time trace of the elongation $\kappa(t)$. The fact that the dependencies of the geometric factors $\mathbf{g}$ on $\kappa$ are not analytically available, has consequences for the optimization routine:

- Cost and constraint function gradients $\frac{\partial J}{\partial \mathbf{p}}$ and $\frac{\partial \mathscr{C}}{\partial \mathbf{p}}$ have to be evaluated numerically with finite differencing and cannot be evaluated analytically, slowing down the optimization.

- Lacking a coupled Grad-Shafranov solver, a consistent evaluation of the updated metrics $\mathbf{g}$ for a changed $\kappa$ cannot be obtained within the optimization routine.

After each iteration step, the geometric factors $\mathbf{g}$ have to be recalculated to match the new trial of the time evolution of the elongation $\kappa$. A linear interpolation scheme is applied to update the metrics $\mathbf{g}$. The two reference equilibria with most similar elongation $\kappa$ are identified (out of the set of CREATE-NL equilibria $\kappa_{ref,i}$): $\kappa_{ref\ 1} < \kappa_{opt} < \kappa_{ref\ 2}$. Then, a linear interpolation in $\kappa$ is applied to obtain the metric vector $\mathbf{g}$:

$$\mathbf{g}_{\kappa_{opt}} = \mathbf{g}_{\kappa_{ref\ 1}} + \frac{\kappa_{opt} - \kappa_{ref\ 1}}{\kappa_{ref\ 2} - \kappa_{ref\ 1}}\left(\mathbf{g}_{\kappa_{ref\ 2}} - \mathbf{g}_{\kappa_{ref\ 1}}\right) \tag{5.7}$$

Once an optimized ramp-down scenario is found, the adequacy of this linear interpolation scheme can be checked by running a set of CHEASE simulations for time points along the optimized trajectory, as illustrated in Section 5.6.4.

**Ramp-down optimal control problem**

To summarize, the ramp-down optimal control problem can be written as:

$$\min_{\mathbf{p}} \quad J_{I_p}(u(t)) \quad \forall t \in [t_0, t_{RD}] \text{ (cost)} \tag{5.8a}$$

$$\text{subject to} \quad f(\dot{x}(t), x(t), u(t)) = 0 \quad \forall t \in [t_0, t_{RD}] \text{ (state)} \tag{5.8b}$$

$$u_i(t) = \sum_j^{n_i} P_{ij}(t) p_{i,j} \text{ (actuator parametrization)} \tag{5.8c}$$

$$A_{ineq}\mathbf{p} \le b_{ineq} \text{ (actuator limits)} \tag{5.8d}$$

$$\mathscr{C}_{\ell i3 < f_{margin}\ell i3\ CREATE(I_p)} \le 0 \text{ and } \mathscr{C}_{\dot{q}_{95}>0} \le 0 \text{ (state constraints)} \tag{5.8e}$$

The actuator limits 5.8d are included to impose both $I_p(t)$ and $\kappa(t)$ to be monotonically decreasing. At this stage, no minimum time derivative is set. Position and shape control studies including the field coil currents are required to establish how fast plasma current and plasma shaping can be changed during the ramp-down phase.

The algorithm applied to solve the non-linear, constrained optimization problem formulated in 5.8a - 5.8e is sequential quadratic programming (SQP) [Nocedal and Wright 2006], as implemented in the Matlab function `fmincon`. This algorithm was applied before in [Felici and Sauter 2012] and [Teplukhina et al. 2017]. Even though cost and constraint function gradient information has to be obtained numerically, the fast run time of a single RAPTOR simulation allows to maintain the full solution of the non-linear optimization problem computationally tractable (a few hours on a single CPU).

Generally speaking there is no guarantee that the obtained optimum trajectory is a global optimum. Rerunning the optimization from different initial conditions allows to increase confidence in the obtained optimum solution. Finally, the selection of the number of optimization variables needs to give the optimizer enough degrees of freedom to be able to find an optimum, while a too high dimensionality leads to the risk of overfitting with respect to specific settings of model parameters. Verifying the obtained optimum trajectory with more complete integrated modeling tools can increase confidence in the obtained optimum.

### 5.6.2 Optimized DEMO ramp-down scenarios

A set of optimized DEMO ramp-down scenarios is summarized in Figure 5.11, with different assumptions regarding the total ramp-down time window and the time evolution of the reference $H_{98y,2}$:

1. $dI_p/dt = -100\,\text{kA/s}$; early HL transition, cold L-mode;

2. $dI_p/dt = -100\,\text{kA/s}$; late HL transition, hot L-mode;

3. $dI_p/dt = -150\,\text{kA/s}$; early HL transition, cold L-mode (for late HL transition, hot L-mode, no feasible solution could be found).
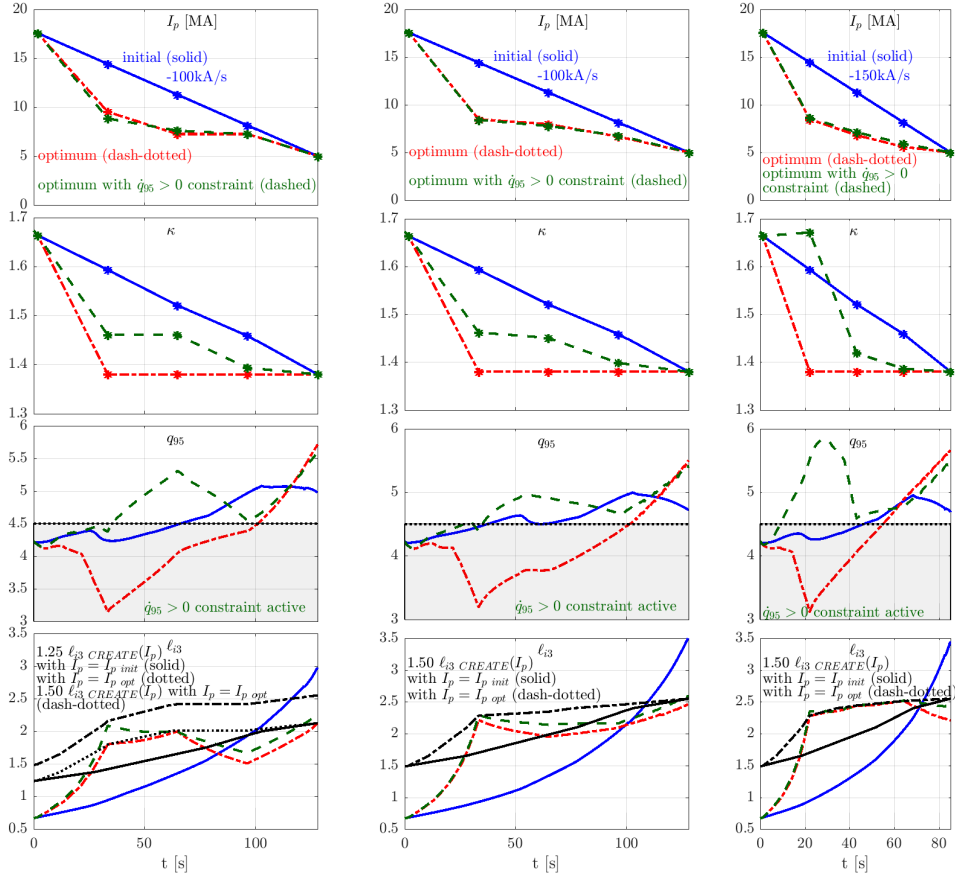
Figure 5.11: Initial and optimized time traces for three DEMO ramp-downs: (1) $dI_p/dt = -100\,\text{kA/s}$; early HL transition, cold L-mode; (2) $dI_p/dt = -100\,\text{kA/s}$; late HL transition, hot L-mode; (3) $dI_p/dt = -150\,\text{kA/s}$; early HL transition, cold L-mode. Feasible ramp-down traces are found with $f_{margin} = 1.25$ for (1) and with $f_{margin} = 1.50$ for (2) and (3).

The respective trajectories given as initial conditions to the optimizer are the corresponding RAPTOR simulations shown in Figures 5.9 and 5.10.

**Constraint on $\ell_{i3}$**

The red dash-dotted traces in Figure 5.11 represent the optimum found for the optimization problem formulated in 5.8a - 5.8e, with $\mathscr{C}_{\ell_{i3} < f_{margin} \ell_{i3\ CREATE}(I_p)} \leq 0$ active as the only constraint (so no constraint on the time evolution of $q_{95}$). For case (1), a feasible solution is found with $f_{margin} = 1.25$, while for cases (2) and (3), $f_{margin}$ has to be raised to 1.50 to find a feasible solution. Both $I_p$ and $\kappa$ are approximated by linear segments, parametrized by three intermediate knot points (at the intersection of linear segments). The end points are maintained equal to the initial condition, while the values of the knot points constitute the optimization variables (6 optimization variables in total).

For each of the three cases, the optimized $I_p(t)$ and $\kappa(t)$ trajectories feature both a sharp initial decrease in the first segment of the ramp-down. For the elongation $\kappa$, an immediate ramp-down to the final, minimum elongation is proposed. The proposed changes in plasma current ramp-rates $dI_p/dt$ allow to maintain $\ell_{i3} < f_{margin} \ell_{i3\ CREATE}(I_p)$. The initial fast reduction of $I_p$ leads to a very fast increase of $\ell_{i3}$. However, the fast decrease of $I_p$ also leads to a fast increase of the upper limit $f_{margin} \ell_{i3\ CREATE}(I_p)$. Furthermore, the decrease of the $I_p$ ramp-rate at the first knot point leads to a knee point in the $\ell_{i3}(t)$ trace. For the three cases, an optimum trajectory is found that avoids a violation of the vertical stability constraint throughout the entire ramp-down phase.

**Constraints on $\ell_{i3}$ and $\dot{q}_{95}$**

A strong reduction of the elongation during the early ramp-down can lead to low $q_{95}$ values that could compromise ideal MHD stability. To counteract this effect, an additional constraint, $\mathscr{C}_{\dot{q}_{95} > 0} \leq 0$, imposing $\dot{q}_{95} > 0$ when $q_{95} < 4.5$, is added, ensuring $q_{95}$ increases monotonically. The green dashed traces in Figure 5.11 represent the optimum found for the optimization problem formulated in 5.8a - 5.8e, with both $\mathscr{C}_{\ell_{i3} < f_{margin} \ell_{i3\ CREATE}(I_p)} \leq 0$ and $\mathscr{C}_{\dot{q}_{95} > 0} \leq 0$ active as constraints. For the three cases, an optimum plasma current similar to the optimization problem with single non-linear constraint is found. The early decrease of $q_{95}$ is avoided by limiting the early reduction of the elongation $\kappa$.

Note that for scenario 1 ($dI_p/dt = -100\,\mathrm{kA/s}$; early HL transition, cold L-mode), no feasible solution satisfying both constraints is found: the $\ell_{i3}$ trace exceeds the CREATE-NL limit by the end of the first segment. In a case like this, where the optimizer did not achieve a feasible solution, it is still interesting to evaluate how close the final iteration of the optimizer approaches a feasible ramp-down trajectory.
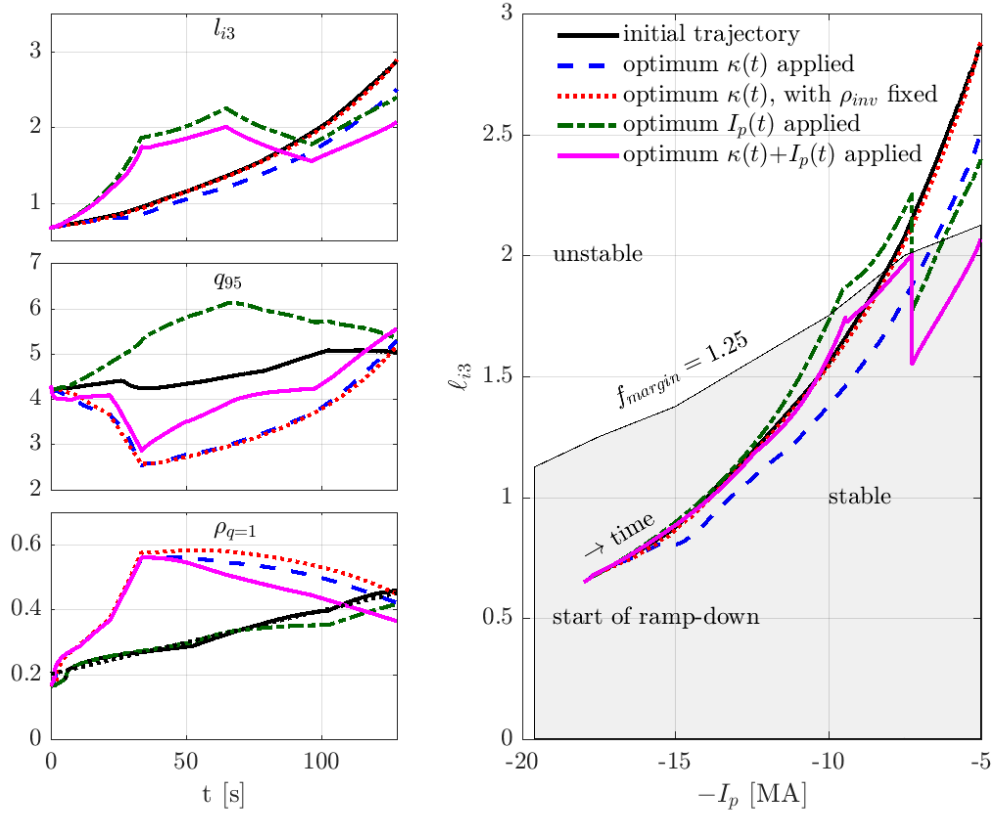
Figure 5.12: A set of ramp-down simulations is presented to improve our understanding of the dynamics underlying the obtained optimum trajectory (for the case with $dI_p/dt = -100\,\text{kA/s}$, late HL transition, hot L-mode in Figure 5.11), as explained in Section 5.6.3.

### 5.6.3 Interpretation impact optimum $I_p$ and $\kappa$ on $\ell_{i3}$

To understand better the dynamics underlying the obtained optimum trajectory, we study in more detail the optimized $I_p$ and $\kappa$ traces for the case with $dI_p/dt = -100\,\mathrm{kA/s}$, late HL transition, hot L-mode in Figure 5.11. We consider the case without the additional constraint on $\dot{q}_{95}$. Various simulations are performed to understand both the individual and the joint impact of the optimized $I_p$ and $\kappa$ traces, as presented in Figure 5.12 and explained below.

- **Initial ramp-down trajectory with constant $dI_p/dt$ and $d\kappa/dt$** (black solid trace in Figure 5.12)

- **Optimized shaping evolution $\kappa(t)$, while maintaining the initial $I_p(t)$ evolution with constant $dI_p/dt$** (blue dashed trace in Figure 5.12)
  The fast reduction of elongation $\kappa$ leads to a reduction of $\ell_{i3}$. Note however that the value of $q_{95}$ reduces to values below 3, compromising ideal MHD stability. The $\rho_{q=1}$ trace illustrates that the fast decrease of $q_{95}$ pushes the inversion radius $\rho_{q=1}$ further outward. Since the transport model applied in these simulations enhances flattening within the $q = 1$ surface, temperature and density profiles are broadened. Since a large fraction of the current density is ohmic and bootstrap current, this will also lead to a broader current density profile, hence a reduced internal inductance $\ell_{i3}$.

- **Optimized shaping evolution $\kappa(t)$, while maintaining the initial $I_p(t)$ evolution with constant $dI_p/dt$, with the inversion radius applied in the transport model kept fixed at $\rho_{inv} = 0.1$** (red dotted trace in Figure 5.12)
  To confirm the hypothesis discussed under the previous item, a RAPTOR simulation is performed where the inversion radius trajectory applied in the transport model is maintained fixed to the same time evolution of $\rho_{q=1}$ that was observed for the initial trajectory. In this case, the mechanism of a reduced $q_{95}$ pushing out the inversion radius cannot broaden the temperature and density profiles. As a consequence, the $\ell_{i3}(t)$ trace is no longer reduced with respect to the initial simulation. Rather, the simulated internal inductance evolution is very similar to the original time trace. Note however that in Chapter 6, a direct impact of a fast compression of the plasma shape on the internal inductance will be observed (both in experiment and simulation).

- **Optimized plasma current evolution $I_p(t)$, while maintaining the initial $\kappa(t)$ evolution with constant $d\kappa/dt$** (green dash-dotted trace in Figure 5.12)
  The plasma current $I_p(t)$ is clearly an effective actuator to shape the time evolution of the internal inductance $\ell_{i3}(t)$, even when keeping the plasma shaping evolution unchanged. Note how after the first change in $I_p$ ramp-rate, the increase of $\ell_{i3}$ is significantly slowed down. After the second change in ramp-rate even a reduction of $\ell_{i3}$ is predicted. For the same shaping trajectory, the lower plasma currents lead to a stronger increase of $q_{95}$.

- **Optimized plasma current $I_p(t)$ and shaping evolution $\kappa(t)$** (magenta solid trace in Figure 5.12)
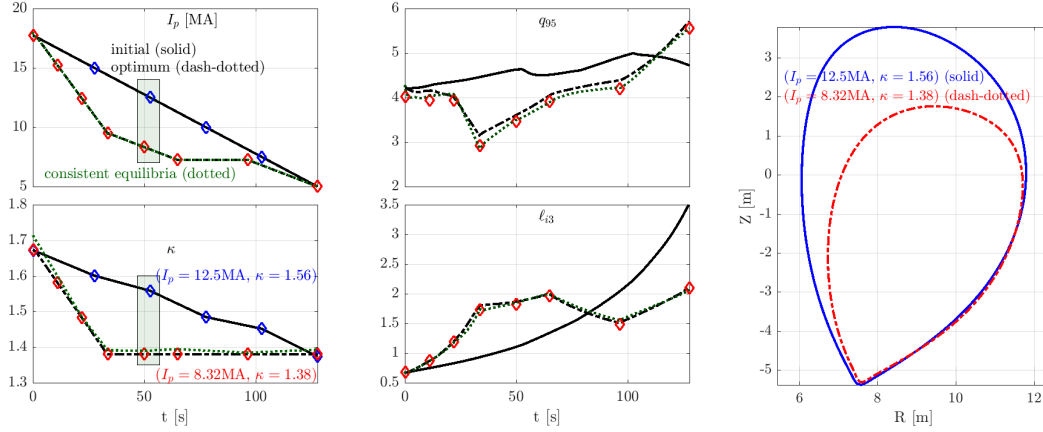
Figure 5.13: Initial and optimized time traces are shown for $I_p(t)$, $\kappa$, $q_{95}$ and $\ell_{i3}$ (for the case with $dI_p/dt = -100\,\text{kA/s}$, late HL transition, hot L-mode in Figure 5.11). The values of plasma current and elongation of the equilibria initially obtained from CREATE-NL are indicated by the blue diamonds. The red diamond symbols indicate the equilibria calculated during post-processing of the optimized results. These equilibria are calculated with values of $I_p$, $\kappa$ and kinetic profiles consistent with the optimal trajectory. For an equilibrium around $t = 50\,\text{s}$ (identified by the green boxes): the initial equilibrium obtained from CREATE-NL is compared to the updated, consistent equilibrium.

Combining the optimum $I_p(t)$ and $\kappa(t)$ traces, the internal inductance can be maintained below the constraint value $\ell_{i3} < 1.25\ell_{i3\ CREATE}(I_p)$. This can be verified by plotting the time trace in the $(-I_p, \ell_{i3})$ plane, on the right hand side of Figure 5.12. Note that the vertical line in the time trace does not correspond to a discontinuity in time: the internal inductance reduces while the plasma current is maintained at a constant value.

## 5.6.4 Consistency optimized evolution shaping and kinetic profiles with MHD equilibria

**Routine to calculate consistent equilibria for optimum trajectory**

Once an optimized ramp-down scenario is found, a consistent set of CHEASE equilibria can be calculated for time points along the optimized trajectory. This way, one can validate whether the impact of the optimized $\kappa$ trace on the plasma state evolution has been correctly captured by the naive interpolation scheme introduced in Section 5.6.1.

An automated function allows the user to provide the time points for which a consistent equilibrium is desired. For these times, equilibria are calculated with consistent plasma current, elongation (the last closed flux surface of the equilibrium from the original sequence with elongation $\kappa$ closest to the desired value $\kappa_{opt}$ is rescaled) and kinetic profiles (pressure $p$ and current density $j_{par}$ from the RAPTOR simulation).

The initial sequence of CREATE-NL equilibria and a sequence of equilibria along an optimized ramp-down trajectory are indicated by sets of diamond symbols in Figure 5.13. The boundary
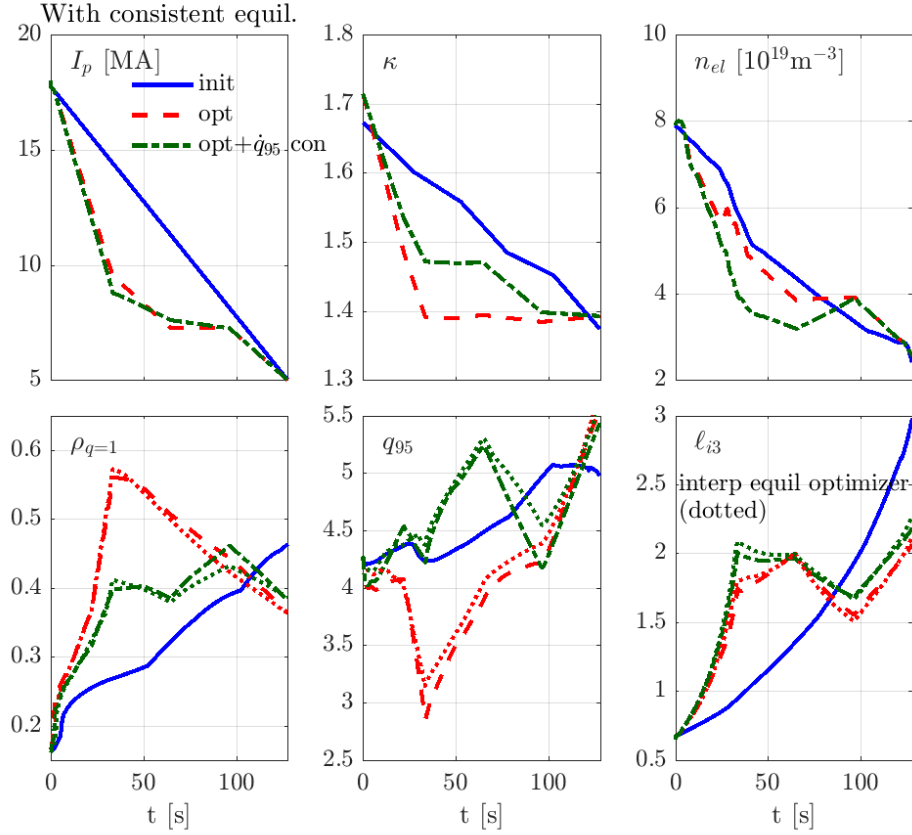
Figure 5.14: Time traces of the initial and optimized ramp-down trajectory (with and without an additional constraint imposing $\dot{q}_{95} > 0$ for $q_{95} < 4.5$), for the case $dI_p/dt = -100\,\text{kA/s}$, early HL, cold L-mode presented in Figure 5.11. The optimum trajectories are obtained with the metric data of a set of consistent CHEASE equilibria (consistent $I_p$, $\kappa$ and kinetic profile evolution), and differ slightly from the dotted lines that represent the final simulation performed by the optimizer (with interpolated metric terms based on the initial sequence of CREATE-NL equilibria).

shape for an equilibrium around $t = 50\,\text{s}$ (identified by the green boxes in the $I_p$ and $\kappa$ time trace plots) is compared between the original equilibrium and the updated, consistent equilibrium.

Let us now compare the $\ell_{i3}$ and $q_{95}$ traces obtained with the optimizer (applying a simple, linear interpolation technique to evaluate **g**) with the respective values obtained with a RAPTOR simulation using the fully consistent CHEASE results as underlying equilibria. Both for $\ell_{i3}$ and $q_{95}$ the changes are modest, justifying the applied linear interpolation procedure.

**Optimum trajectory including consistent equilibria**

In Figure 5.14, a set of traces are compared for the initial ramp-down trajectory and the optimized ramp-down trajectories, with respectively the $\mathscr{C}_{\ell_{i3} < f_{margin} \ell_{i3\ CREATE}(I_p)} \leq 0$ constraint and both constraints $\mathscr{C}_{\ell_{i3} < f_{margin} \ell_{i3\ CREATE}(I_p)} \leq 0$ and $\mathscr{C}_{\dot{q}_{95} > 0} \leq 0$ (for the case $dI_p/dt = -100\,\text{kA/s}$,

early HL, cold L-mode presented in Figure 5.11). These simulations are obtained by rerunning the optimum trajectories with the metric data of a set of consistent CHEASE equilibria (consistent $I_p$, $\kappa$ and kinetic profile evolution). The dotted lines in Figure 5.14 represent the final simulation performed by the optimizer (with interpolated metric terms based on the original sequence of CREATE-NL equilibria). The impact on $\ell_{i3}$ of rerunning the simulation with the metrics of a fully consistent set of CHEASE equilibria is limited, while the minimum in the $q_{95}$ traces is somewhat lower for the consistent simulation. This has to be taken into account when setting the $q_{95}$ value above which no $\dot{q}_{95} < 0$ is allowed (i.e. one can include some additional margin to account for a reduced value in the simulation with consistent equilibria).

Note that while the dashed red and dash-dotted green ramp-down traces in Figure 5.14 operate at identical plasma current $I_p$ and Greenwald fraction throughout the ramp-down phase, the second scenario requires a faster ramp-down of the effective line-averaged density. This can be understood as follows: for the set of equilibria outer shapes applied for this work, the plasma minor radius $a$ is decreased simultaneously with the plasma elongation $\kappa$. A faster decrease of elongation hence leads to a slower decrease of the Greenwald density $n_{Gw} = I_p/\pi a^2$, which eases the density ramp-down challenge. In the first-principles scaling law recently proposed in [Giacomin et al. 2022], $n_{lim} \sim (1+\kappa)^{-1/3} a^{-79/42}$, confirming that faster decrease of $\kappa$ and $a$ would allow for a slower reduction of the plasma density.

## 5.7 Conclusion

The safe termination of burning plasmas is of crucial importance for the exploitation of DEMO, as very few disruption events can be tolerated (especially at plasma currents above $I_p \sim 5\,\mathrm{MA}$). The high radiated power fraction of DEMO, to limit the heat load to be handled by the divertor, will make the scenario sensitive to excursions from a nominal scenario, both in stationary state and during transient phases like ramp-down: a decrease of electron temperature leads to increasing average cooling factors for the intrinsic W species and the seeded Xe species, potentially triggering a runaway process towards a radiative collapse. To avoid a radiative collapse during the ramp-down phase, strong plasma heating needs to be maintained (with the level of heating depending on how efficiently impurities can be removed from the plasma). The present chapter applies the gradient-based transport model introduced in [Teplukhina et al. 2017]. A stationary RAPTOR reference for the DEMO stationary operating point is established, based on operating conditions discussed in the literature [Zohm et al. 2013; Giruzzi et al. 2015; Siccinio et al. 2020]. The simulation includes the effect of plasma dilution by the fusion-born helium species as well the radiation from W and Xe, making use of ADAS cooling factor data [ADAS]. We discussed the various non-linearities to be considered when setting a reactor operating point, considering the active contraints on performance, as well as physics limits. Importantly, a DEMO plasma is characterized by a high degree of self-regulation of the kinetic profiles (posing a challenge for kinetic profile control): the power balance is dominated by the plasma self-heating by the alpha fast particles, dependent on temperature and density profiles and fuel dilution, and the radiated power from heavy impurities, with a non-linear

dependence on $T_e$. Reliance on auxiliary current drive to tailor the q profile is minimized to maintain a high fusion gain Q.

The stationary operating point is used as initial condition for a series of ramp-down simulations. The technical and physical constraints that need to be simultaneously satisfied throughout the entire ramp-down phase raise a set of trade-offs when setting the actuator time traces. Leveraging the fast run time of the code, feasible DEMO ramp-down scenarios are developed in RAPTOR. A quantitative estimate is presented of the strong auxiliary heating required throughout the ramp-down phase, to avoid a radiative collapse.

Fast ramp-down scenarios are critical for emergency shutdown of the burning plasma, e.g. in case of divertor reattachment [Siccinio et al. 2020]. Ramping down the plasma current tends to cause a peaking of the current density profile, with a faster plasma current ramp-down rate leading to a stronger peaking. In our simulations, strong peaking of $j_{par}$ with inversion of the plasma current direction near the plasma edge is routinely observed after the HL transition. The corresponding increase of the plasma internal inductance $\ell_{i3}$ poses a challenge for the vertical position controllability of the plasma column, as thoroughly assessed in this chapter. An upper limit on the internal inductance from CREATE-NL [Albanese et al. 2015] free boundary equilibrium control calculations is introduced [Mattei et al. 2016], dependent on plasma current $I_p$ and elongation $\kappa$. The feasibility of different plasma current ramp-down rates with respect to this vertical control limit is assessed: while a ramp-rate of $dI_p/dt = -50\,\text{kA/s}$ seems conservative, a ramp-rate of $dI_p/dt = -200\,\text{kA/s}$ seems overly optimistic. For a given ramp-rate, the increase of $\ell_{i3}$ can be limited by enhancing the outward diffusion of the current density: a lower temperature (e.g. early HL transition) or an increased $Z_{eff}$ allows for a faster current diffusion time scale. Furthermore, the plasma current $I_p(t)$ time evolution, within a given ramp-down time window, is an effective actuator to tailor the internal inductance trace $\ell_{i3}(t)$. A simultaneous reduction of the plasma elongation $\kappa$ allows to enhance the vertical controllability of the plasma column, while potentially inducing a further reduction of $\ell_{i3}$ by broadening $j_{par}(\rho)$ by pushing the $q = 1$ radius further outward. A simultaneous reduction of the minor radius leads to a slower decrease of the Greenwald density, allowing for a slower plasma density ramp-down. Note however that shape control calculations should verify how fast the elongation can be adjusted. Furthermore, a strong decrease of $q_{95}$ during the ramp-down should be avoided, to avoid compromising ideal MHD stability of the plasma. Applying the RAPTOR automated optimization routines introduced in [Teplukhina et al. 2017], feasible ramp-down trajectories could be obtained for average ramp-down rates of $dI_p/dt = -100\,\text{kA/s}$ and $dI_p/dt = -150\,\text{kA/s}$.

# 6 Analysis and modeling of ramp-down scenarios on ASDEX Upgrade

In Chapter 5, the development of safe ramp-down strategies is identified as a critical challenge for a DEMO reactor. While integrated simulations of magnetic control and the kinetic profile evolution can improve confidence in the performance of optimized ramp-down strategies, it is crucial to test the applied models and observe the complex dynamics at play on present-day devices. The delicate operating space that has to be navigated in order to avoid physics limits has been described in [de Vries et al. 2017], studying a multi-machine database. For various tokamaks, scenarios with dimensionless parameters matching the ITER baseline scenario are under development, including TCV and ASDEX Upgrade (AUG) [Sauter et al. 2021]. In these experiments, the available control techniques and modeling frameworks can be validated over the different operating phases, including the ramp-down.

## 6.1 Introduction

**Relation to earlier RAPTOR results for TCV, AUG and JET**

In [Teplukhina 2018; Teplukhina et al. 2017], ramp-down optimizations have been performed for TCV, AUG and JET. A faster plasma current ramp-down rate was successfully executed on TCV for an ohmic L-mode: simultaneous reduction of the plasma elongation with the plasma current allows to avoid an increase of $dB_v/dt$, which would cause a violation of the radial position control constraint. For AUG, a ramp-down scenario, starting from H-mode, was optimized towards a faster $I_p$ ramp. These optimized trajectories feature a simultaneous reduction of the plasma elongation, to limit the increase of the internal inductance $\ell_{i3}$. While experimental validation of these ramp-down traces was hampered by technical machine limitations, some experimental ramp-down traces have been shown in [Teplukhina 2018], hinting towards a positive impact of a fast reduction of the elongation on the increase of $\ell_{i3}$.

**Aim of the present work**

In the present work, an extensive set of AUG ramp-downs is considered. Most of these discharges belong to the AUG ITER baseline program, with nominal flat-top parameters for the on-axis magnetic field $B_0 = -1.9\,\mathrm{T}$, the plasma current $I_p = 1.1\,\mathrm{MA}$ and the upper triangularity $\delta_{top} \sim 0.3$. A set of interesting ramp-downs that have been performed within the H-mode density limit program (flat top: $B_0 = -2.5\,\mathrm{T}$, $I_p = 0.8\,\mathrm{MA}$ and $\delta_{top} \sim 0.0 - 0.3$) is also shown.

Pre-programmed actuator time traces for heating, plasma current and shaping have been varied, to understand their relative importance in designing a safe ramp-down strategy, allowing us to make recommendations regarding the respective role of these various actuator traces in the balancing act of designing a reliable ramp-down scenario. Furthermore, the capability of the RAPTOR simulator to capture the relevant effects is validated, providing experimental support for the simulation results obtained in the previous chapter. The plasma shape is controlled in feedforward, setting the poloidal field coil currents for the expected evolution of plasma current $I_p$ and $\beta_{pol}$, while $\beta_{pol}$ is controlled in feedback.

The focus of this work is modeling the impact of various physics drivers like plasma current, shaping and heating traces on the time evolution of the internal inductance $\ell_{i3}$. As explained in Section 5.1, the current density profile tends to become increasingly more peaked during the ramp-down phase, increasing the value of $\ell_{i3}$ and making vertical position control of the plasma position more challenging. While on AUG, vertical stability is usually ensured by the presence of internal control coils and passive stabilization loops, vertical stability is projected to be an important operating constraint for ramp-downs of future machines (as discussed in Section 5.1). The importance of an optimized time evolution for $\ell_{i3}$ for DEMO has been illustrated in Chapter 5.

## 6.2   Workflow for post-discharge simulations

The RAPTOR set-up applied in this section to model AUG ramp-downs is similar to the set-up described in Chapter 3, although a different transport model is applied. Electron heat and density transport and current diffusion are solved for, applying a gradient-based transport model, for which the implementation is reported in [Teplukhina et al. 2017] and Section 2.3.4. Note that the same set-up is used for the DEMO simulations in Chapter 5.

Sawteeth are modeled with the Porcelli sawtooth model described in [Piron et al. 2015], triggering sawtooth crashes when the magnetic shear at $q = 1$ exceeds the critical value $s_{q=1,crit} = 0.2$. The critical shear $s_{q=1,crit}$ is user-defined and can be adjusted to match the experimentally observed sawtooth period.

### 6.2.1   Heat and density transport model

Statistical analysis reported in [Teplukhina et al. 2017] derived characteristic logarithmic gradients for the stiff region of $T_e$ and $n_e$ profiles during AUG shots, both for H- and L-mode plasmas. In the present work, we attempt to apply the same parameters, i.e. for H-mode:

$\lambda_{T_e} = 2.3$, $\rho_{ped,T_e} = 0.9$, $\lambda_{n_e} = 0.5$ and $\rho_{ped,n_e} = 0.9$; and for L-mode $\lambda_{T_e} = 3.0$, $\rho_{ped,T_e} = 0.8$, $\lambda_{n_e} = 1.5$ and $\rho_{ped,n_e} = 0.8$.

However, in Section 6.3 we will find that a sudden transition from H-mode to an ohmic L-mode can cause a broad region with comparatively low temperature $T_e \sim 10\,\text{eV}$, that in some cases extends to radii $\rho \sim 0.65$ (edge cooling). The modeling of $T_e$ and $n_e$ profiles during this regime is improved by adjusting the gradient-based transport model characteristic logarithmic gradients to $\lambda_{T_e} = 4.5$, $\lambda_{n_e} = 1.5$, while maintaining $\rho_{ped} = 0.8$. These settings are applied for those discharges where a direct transition from H-mode to an L-mode without auxiliary heating is programmed.

As mentioned before, the gradient-based transport model implementation in RAPTOR does not rely on boundary conditions set at the pedestal top. Rather, a gradient parameter $\mu$ in the edge region is feedback controlled to match global confinement metrics, namely a reference for the line-averaged density and a reference for the $H_e$ factor[1].

The feedback control reference for the line-averaged density is set equal to the H-1 FIR measurement (in case the measurement is corrupted by fringe jumps, a synthetic line-averaged density is calculated from the IDA profile). For $H_e$, the same references are applied as in [Teplukhina et al. 2017], namely $H_e = 0.4$ during H-mode and $H_e = 0.2$ during L-mode. In the following sections we will see that this assumption leads to excellent agreement of the modeled $T_e(\rho = 0.8, t)$ trace with the experimental time trace.

### 6.2.2   Equilibrium geometry

Geometry metrics are taken from a sequence of reconstructed MHD equilibria from the IDE code. A dense equilibrium time grid with a time step of 0.1s is selected (for the experiments where the plasma column is rapidly compressed, the time step is reduced to 0.05s). This allows to capture the effect of changing equilibrium on the diffusion equations solved by RAPTOR.

### 6.2.3   Heating and current drive sources

Ion cyclotron heating is modeled with a gaussian deposition profile centered at $\rho_{dep} = 0$, assuming full absorption and equal heating to ion and electron species. NBI heating and current density profiles are extracted from the RABBIT run performed within the IDE code.

### 6.2.4   Post-discharge simulations

A summary of the performed ramp-down experiments is presented in Appendix D, to accompany the discussion in the following sections. Comparisons are shown between RAPTOR post-shot simulations of $T_e(\rho, t)$, $n_e(\rho, t)$ and $q(\rho, t)$, and IDA/IDE reconstructions, to validate the performance of the applied set-up over a variety of ramp-down scenarios.

---

[1] $H_e$ is the $H_{98y,2}$ confinement factor using solely the stored thermal energy of the electrons $W_{th,e}$. Note the difference with Chapter 5, where the total $H_{98y,2}$ factor is controlled, summing the stored thermal energy of all ion species to $W_{th,e}$.
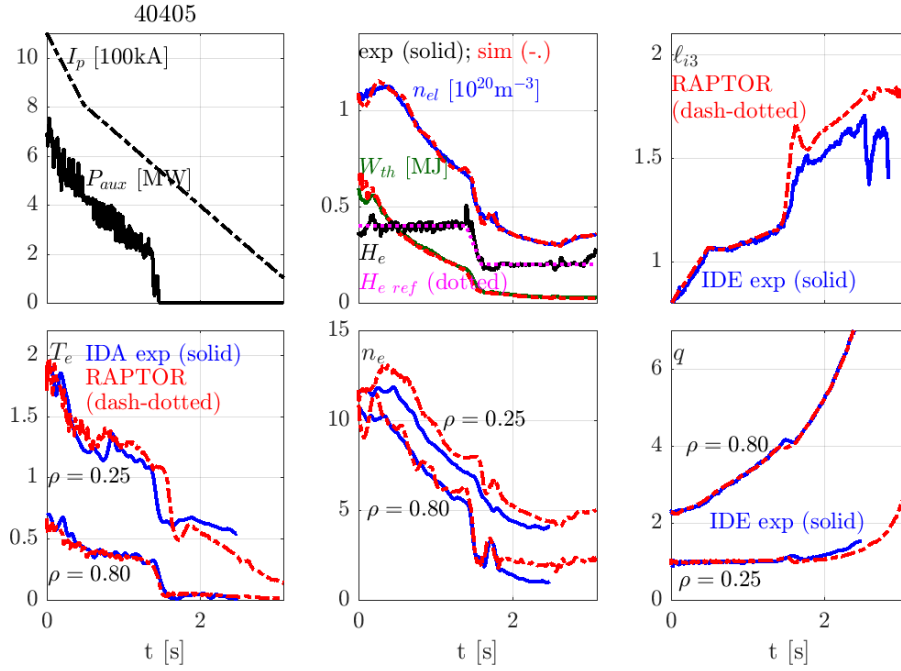
Figure 6.1: IDE/IDA reconstruction and RAPTOR simulation for discharge 40405.

## 6.3 The importance of L-mode heating and HL transition timing

Let us consider the comparison between the experimental IDE/IDA reconstruction and RAP-TOR (with gradient-based model) for discharge 40405, shown in Figure 6.1. The ramp-down features a change in $I_p$ ramp-rate around 0.5s (note: in this chapter we define t=0s at the start of the plasma current ramp-down). Two effects on the time evolution of $\ell_{i3}$ are pronounced:

- The reduction of $dI_p/dt$ during the H-mode phase leads to a flattening of the $\ell_{i3}$ time evolution, both in the simulation and in the IDE reconstruction. The effect of the $I_p$ trace on $\ell_{i3}$ is studied in Section 6.4.

- The HL transition around 1.4s leads to a distinct increase of $\ell_{i3}$. In the following subsection, this distict rise of $\ell_{i3}$ is investigated.

### 6.3.1 Observation of edge cooling in AUG experiments

In Figure 6.2, the L-mode electron temperature (and density) profile is shown for two discharges that transition from H-mode to an ohmic L-mode (41388: HL transition initiates around 0.7s; 40405: HL transition initiates around 1.4s; for both discharges the HL transition is initiated by turning off the auxiliary heating). In the absence of auxiliary heating, a broad relatively cold outer region is formed in the plasma. The magnetic spectrograms indicate the presence of an n=1 mode, even though no disruption is triggered. Further analysis is required to see if the low edge $T_e$ is MHD or transport-driven.
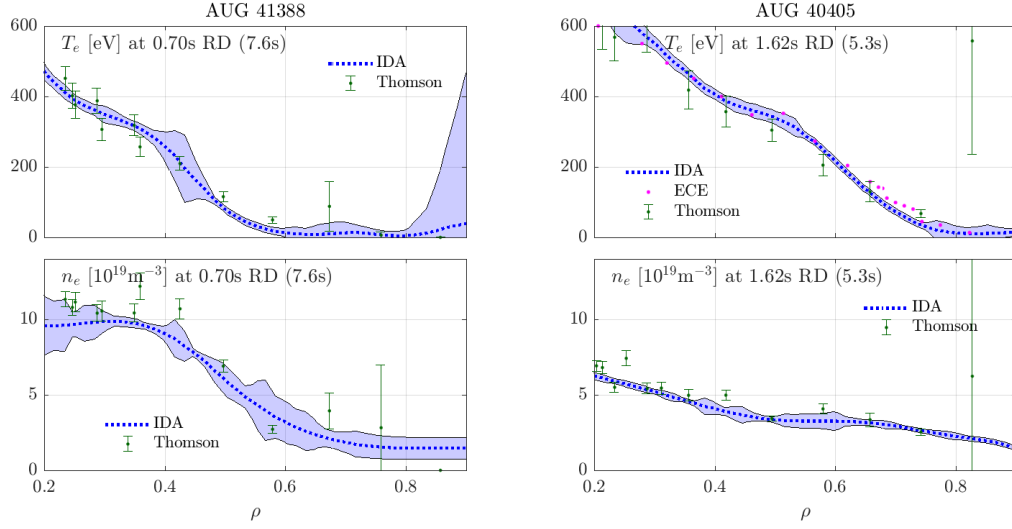
Figure 6.2: $T_e$ and $n_e$ profiles for discharges 41388 and 40405, after the transition from H-mode to an ohmic L-mode.

The observed dynamics are reminiscent of the edge cooling dynamics observed in JET termination phases [Pucella et al. 2021]. Both central temperature hollowing or peripheral cooling of the plasma give rise to a steepened current density profile through the $q = 2$ surface, increasing the probability of triggering a 2/1 tearing mode that can lead to plasma disruption [Sykes and Wesson 1980; Wesson et al. 1989]. Whilst the former is more common due to central impurity accumulation at lower density and for a flatter $q$ profile, the latter is more prevalent due to edge cooling under the conditions of a peaked $q$ profile and a higher density [Pucella et al. 2021].

In the previous chapter we found that a DEMO reactor requires high levels of auxiliary heating throughout the full ramp-down phase, to avoid a radiative collapse. In the present chapter, the impact of a flattened outer $T_e$ profile on the internal inductance is modeled. Stability analysis of the current density profile with respect to the onset of a 2/1 mode, as performed in [Pucella et al. 2021], or the self-consistent modeling of edge cooling with ADAS cooling factor data [ADAS], is outside the scope of this work.

### 6.3.2   Modeling the impact of edge cooling

**Gradient-based transport model**

As the plasma conductivity scales like $\sim T_e^{3/2}$, a strong impact of the electron temperature on the predicted current density profile during an ohmic L-mode phase can be anticipated. Applying the default setting of the gradient-based transport model for AUG L-mode plasmas (i.e. $\lambda_{T_e} = 3.0$, $\rho_{ped,T_e} = 0.8$ [Teplukhina et al. 2017]), the increase of $\ell_{i3}$ during the HL transition is under-predicted, as shown in Figure 6.3 (green dashed line). The electron temperature in the outer region is over-predicted, while the average logarithmic gradient $\lambda_{T_e}$ is below
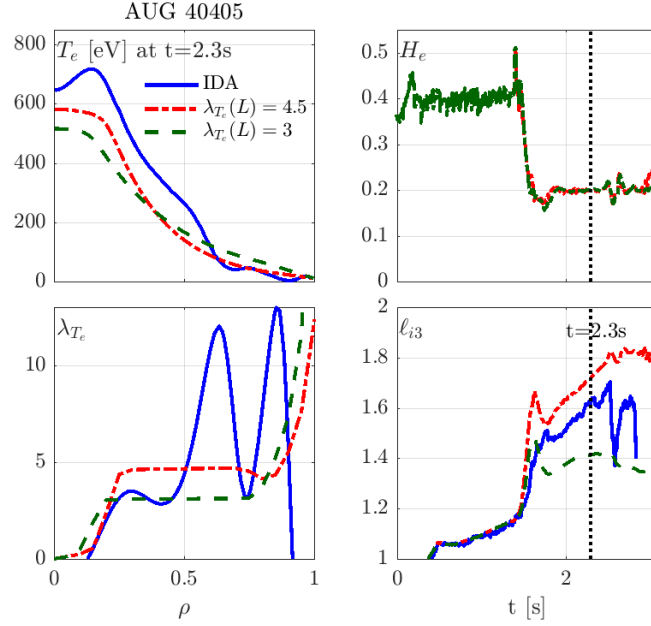
Figure 6.3: IDE/IDA versus RAPTOR with gradient-based model, with L-mode logarithmic gradient $\lambda_{T_e} = 3$ (default) or $\lambda_{T_e} = 4.5$, for discharge 40405, with late HL transition to ohmic L-mode: (a) $T_e$; (b) $H_e$; (c) $\lambda_{T_e} = -d \log T_e / d\rho$; (d) $\ell_{i3}$.

the experimentally observed core gradients. A better match with the experimental traces can be obtained by raising the logarithmic gradient used by the model, to $\lambda_{T_e} = 4.5$, while maintaining $\rho_{ped,T_e} = 0.8$. To match the same $H_e$ factor, the edge temperature is reduced, while $T_e$ rises more steeply towards the center of the plasma. The rise of the internal inductance is more pronounced, as observed in experiment. As the observed dynamics are captured more accurately, $\lambda_{T_e} = 4.5$ is applied for modeling those discharges that feature a direct transition from H-mode to an ohmic L-mode (for all these discharges, a strong cooling of the edge has been observed).

From these initial simulations, we can identify the key impact of $T_e$ peaking and the height of the outer $T_e$ profile on the peaking of the current density profile and the resulting value of the internal inductance $\ell_{i3}$. While for $\lambda_{T_e} = 3.0$, $\ell_{i3\ max} \sim 1.4$, for $\lambda_{T_e} = 4.5$, $\ell_{i3\ max} \sim 1.8$. The actual cause of this low edge temperature is outside of the scope of this study. However to counter this effect, it is proposed to keep finite auxiliary heating during the L-mode phase, to avoid radiative collapse (as discussed in Chapter 5 for DEMO) and to control the increase of $\ell_{i3}$ by avoiding an excessively fast reduction of the edge $T_e$.

**Comparison of transport models**

To gain further insight in the L-mode regime with edge cooling, we compare the performance of the different transport models applied in this thesis, to predict the ramp-down of discharge 40405, as presented in Figure 6.4:
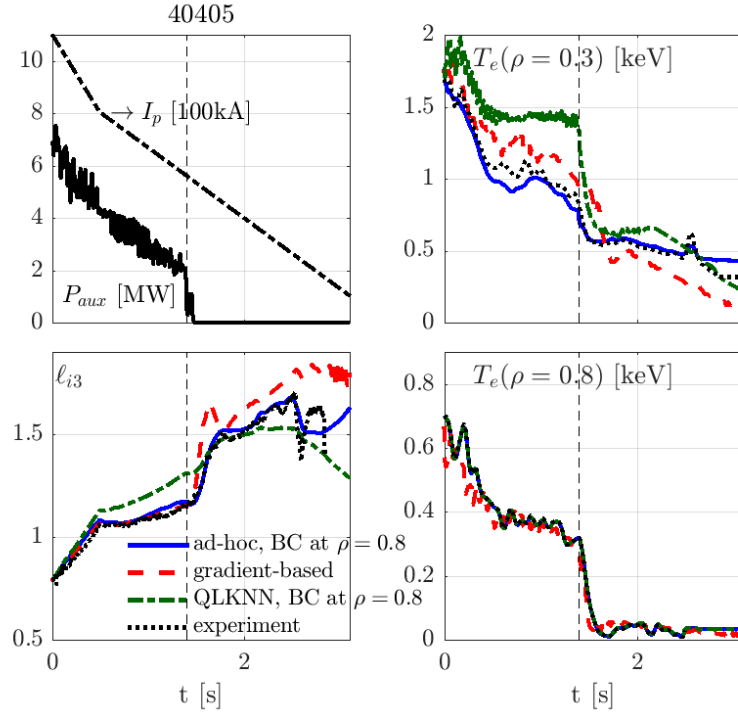
Figure 6.4: The ramp-down phase of discharge 40405 is simulated in RAPTOR with three different transport models. (a) $I_p$ and $P_{aux}$; (b) $T_e(\rho = 0.3)$; (c) $\ell_{i3}$; (d) $T_e(\rho = 0.8)$.

- the gradient-based model, with non-standard settings for the L-mode phase, as described previously; $T_e$, $n_e$ and $q$ are solved for,

- the ad-hoc empirical formula eq. (2.30), with model settings identical to those applied in Chapter 3; $n_e(\rho, t)$ and the $T_e(\rho = 0.8, t)$ boundary condition are imposed based on experimental data, $T_e$ and $q$ are solved for,

- the QuaLiKiz neural network surrogate QLKNN-hyper-10D [van de Plassche et al. 2020]; $n_e(\rho, t)$ and $T_{e,i}(\rho = 0.8, t)$ are imposed based on experimental data, $T_e$, $T_i$ and $q$ are solved for.

The following observations can be made, based on Figure 6.4.

- While the ad-hoc empirical formula and QLKNN-hyper-10D require a boundary condition $T_e(\rho = 0.8, t)$, the gradient-based model only requires an estimate for the global electron heat confinement in H- and L-mode. The $T_e(\rho = 0.8, t)$ trace predicted by the simulation agrees well with the IDA measurement that is used as boundary condition for the simulations with the alternative transport models.

- Applying the ad-hoc empirical formula leads to an excellent agreement of the predicted $\ell_{i3}$ trace with the experimental reconstruction. This is remarkable since the parameters of the transport model are taken identical to those used to model advanced scenarios in
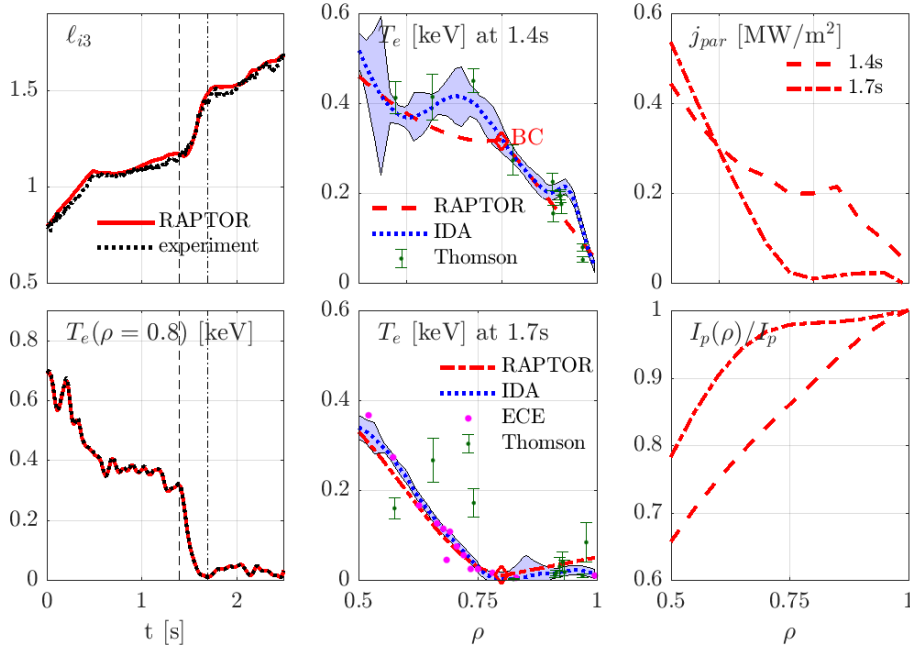
Figure 6.5: Comparison of experimental data with RAPTOR simulation with ad-hoc empirical formula and boundary condition at $\rho = 0.8$ (shown within the range $\rho = [0.5\ 1]$).

Chapter 3 ($c_{ano} = 0.15$, $c_{neo} = 0.50$, $c_{T_e} = 1.2$, $\chi_c = 0$). It should however be emphasized that the time evolution of $T_e(\rho = 0.8, t)$ is set based on the experimental time trace.

- QLKNN-hyper-10D seems to overpredict the core temperature during the H-mode phase[2], leading to an overprediction of the internal inductance. Note that in this case the predicted $\Delta \ell_{i3}$ during the HL transition is reduced.

Since the ad-hoc empirical formula recovers the observed $\ell_{i3}$ evolution most accurately, this simulation can be used to understand the origins of the increased internal inductance in more detail. Figure 6.5 illustrates how the sudden collapse of temperature in the outer plasma region ($\rho > 0.75$) at the HL transition leads to a strong reduction of ohmic and bootstrap driven current in this region, causing a strong peaking of the current density profile. the electron temperature profile $T_e$ is plotted before (1.4s) and after (1.7s) the HL transition, as measured by Thomson and ECE diagnostics, and inferred by the IDA. The bottom right plot, showing the enclosed plasma current integral, shows that after the HL transition, about 80% of the plasma current is driven inside $\rho = 0.5$.

---

[2]Further investigation is required to understand whether QuaLiKiz under-estimates transport in this regime or whether the QLKNN fit becomes less accurate for the increasing $T_e > T_i$ during ramp-down. Alternatively, destabilization by density peaking might be under-estimated due to insufficient accuracy of the measurements.
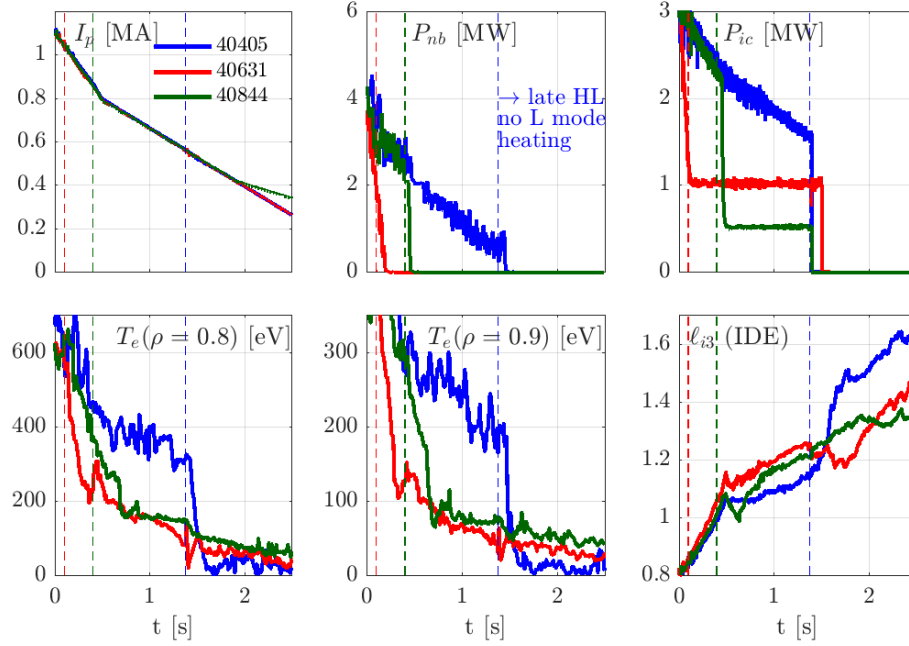
Figure 6.6: Ramp-down traces of discharges with different HL timings and different amounts of L-mode heating.

### 6.3.3 Early HL transition to a heated L-mode phase

**Experiment**

To investigate whether the strong rise of internal inductance that has been observed for a late HL transition to an ohmic L-mode (40405) can be avoided, new discharges have been designed that feature an earlier HL transition and an auxiliary heated L-mode phase, while the $I_p$ trace is identical. The HL transition of discharges 40631 and 40844 is respectively around the start of ramp-down and around 0.4s (which is right before the kneepoint in the $I_p$ trace). Both discharges maintain IC heating during the L-mode phase[3], respectively 1 MW and 0.5 MW. The temperature traces ($T_e(\rho = 0.8)$ and $T_e(\rho = 0.9)$) in Figure 6.6 clearly indicate that the peripheral electron temperature in the L-mode heated discharges decreases more gradually, leading to a reduced internal inductance $\ell_{i3}$. Note that discharges 40631 and 40844 maintain higher $T_e(\rho = 0.8)$ and $T_e(\rho = 0.9)$ even in the phase when all discharges are in an ohmic L-mode. As the ramp-down phase is highly transient, understanding of the plasma state at a given point requires to consider the full dynamic state evolution.

---

[3]An attempt (discharge 40851) maintaining 0.4 MW of NBI power until 1.5s likewise resulted is a gradual decline of $T_e(\rho = 0.8)$ rather than a sudden collapse. One discharge (40848) has been performed with an early HL transition to an ohmic L-mode. The time traces (shown in Figure D.10 of Appendix D) indicate that while a radiative collapse of the outer $T_e$ profile initially took place, the $T_e(\rho = 0.8, t)$ trace recovers, halting a further rise of $\ell_{i3}$. Note that the reduction of the $I_p$ ramp-down rate reduces the likelihood of termination due to a density limit violation, as the edge density has more time to reduce for a given $I_p$.
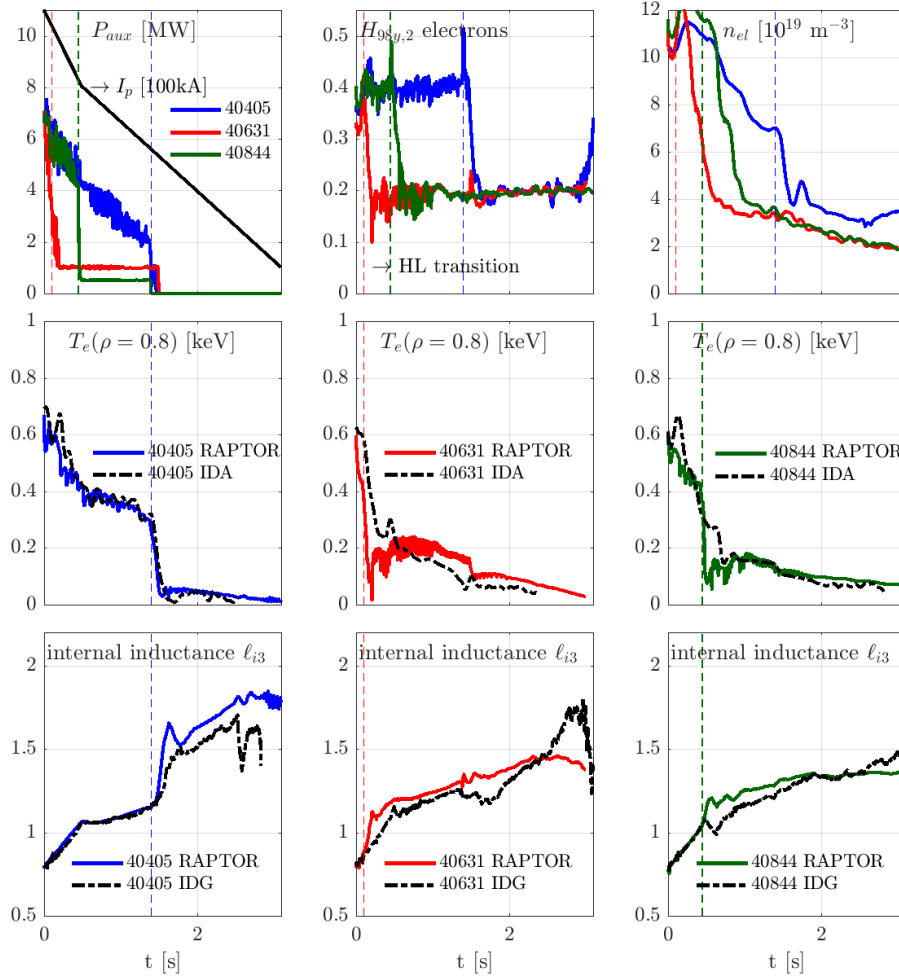
Figure 6.7: RAPTOR simulations for the discharges 40405, 40631 and 40844, with an HL timing respectively around 1.4s, 0.1s and 0.4s.

**Modeling**

The discharges 40405, 40631 and 40844 have been simulated with the gradient-based transport model in RAPTOR, as illustrated in Figure 6.7. While the three discharges are simulated with an identical $I_p$ trace, with a knee point around 0.5s, the HL transition is initiated at respectively 1.4s, 0.1s and 0.4s. For discharge 40405, with a direct transition to a cold L-mode phase, the transport model uses $\lambda_{T_e} = 4.5$ during L-mode, as discussed in Section 6.3.2. The two other discharges maintain some auxiliary heating directly after the HL transition and apply the standard setting $\lambda_{T_e} = 3$ throughout the entire L-mode phase. Applying these settings, $T_e(\rho = 0.8, t)$ is predicted reasonably well for all three shots. During the ohmic L-mode phase of discharges 40631 and 40844, the $\ell_{i3}$ values predicted by RAPTOR differ from the
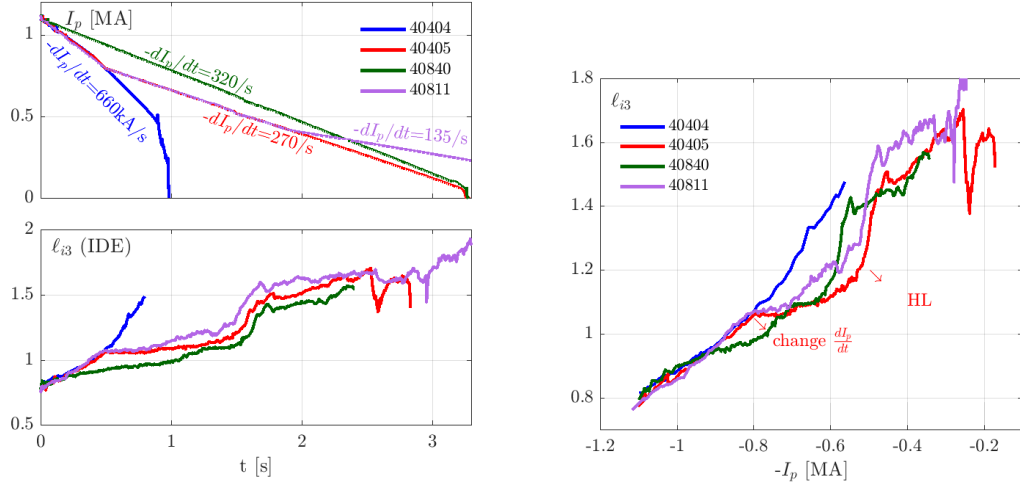
Figure 6.8: Ramp-down traces of discharges with different traces of the plasma current $I_p$.

IDE reconstructed data, which show a further rise of $\ell_{i3}$ to values above $\ell_{i3} = 1.5$. Further investigation into the dynamics of $\ell_{i3}$ in this phase is required, ideally with the assistance of more complete integrated modeling codes.

## 6.4 Plasma current as an actuator to tailor the $\ell_{i3}$ time evolution

**Experiment**

In Chapter 5, the time evolution of the plasma current $I_p$ has been identified as an effective actuator to tailor the time evolution of the internal inductance $\ell_{i3}$. More specifically, starting from a fast ramp down rate and subsequently reducing the plasma current ramp-down rate allows to reduce the growth rate of the internal inductance, while allowing to reach lower $I_p$ values relatively quickly.

In Figure 6.8, four discharges with different plasma current time traces are shown, each maintaining a relatively constant volume throughout the ramp-down phase. Discharge 40404 has the fastest ramp-down rate, $dI_p/dt \sim 660$kA/s, resulting in a rapid rise of the internal inductance $\ell_{i3}$, until the discharge disrupts with a plasma current $I_p \sim 500\,$kA[4] .

Discharges 40405 and 40840 feature new ramp-down traces, that implement a strong reduction of the absolute value of $dI_p/dt$, while having an identical evolution in the first segment of the ramp-down phase. For discharge 40405, the absolute value of $dI_p/dt$ is essentially halved at 0.5s. The impact on $\ell_{i3}(t)$ is strong: the internal inductance remains more or less constant around $\ell_{i3} \sim 1.3$ during the time window between the $I_p$ knee point and the HL transition

---

[4]The disruption of discharge 40404 is incurred after the HL transition. Due to the dynamics described in Section 6.3, the sudden transition to an ohmic L-mode leads to collapse of the outer electron temperature, leading to a density limit excursion.

(1.4s). Likewise, in the $(-I_p, \ell_{i3})$ plane in Figure 6.8 the change of gradient of the $\ell_{i3}$ trace is clearly pronounced.

Discharge 40811 features a second halving of the $I_p$ ramp-down rate during the L-mode phase, around 2s. 40405 and 40811 have a similar $\ell_{i3}(t)$ evolution (after the first $I_p$ knee point, $\ell_{i3}$ is slightly higher for 40811, potentially due to differences in elongation). Whether the second $I_p$ knee point causes a further reduction in the growth rate of $\ell_{i3}$, is not clear from the IDE data. Discharge 40840 has a constant ramp-down rate, while covering the same total ramp-down time window as discharge 40405. Comparing the respective traces in Figure 6.8, both discharges reach similar $\ell_{i3}$ values after the HL transition.

### Modeling

The quantitative effect of a change of $dI_p/dt$ is well captured in RAPTOR. The good match between experiment and simulation can be illustrated by comparing the IDE and RAPTOR $\ell_{i3}$ traces in Figure 6.1 for discharge 40405. Also for discharge 40631, where the same $I_p$ trace is applied, but the change of $dI_p/dt$ occurs during L-mode rather than H-mode, the time evolution of $d\ell_{i3}$ is rather well recovered (Figure 6.7). These successful benchmarks of the model increase the confidence in the optimization procedure applied in the previous chapter.

## 6.5 The effect of the plasma shape evolution

### 6.5.1 Scan over plasma shape quantities

**Experiment**

In Figure 6.9, a set of three ramp-downs with a similar plasma current ramp-down rate is compared ($dI_p/dt \sim -700\,\text{kA/s}$). This discharge scan was performed to study the effect of shaping. Discharge 40236 is an attempt to maintain the shape constant throughout ramp-down. A reduction of triangularity $\delta$ at constant elongation $\kappa$ is the aim of discharge 40238. Conversely, the ramp-down phase of discharge 40239 attempts to maintain triangularity $\delta$ constant, while reducing the elongation $\kappa$.

Control over these individual shaping parameters was only partly successful, as can be seen in Figure 6.9.

- Discharge 40236 maintains a relatively constant volume (and triangularity), while the elongation however decreases ($a_{minor}$ increases from about 0.52m to 0.55m).

- Discharge 40238 does achieve a reduction of triangularity, while the elongation evolution is similar to discharge 40236, resulting in a moderate volume reduction.

- Discharge 40239 has only a moderately stronger elongation reduction compared to the other two shots, combined with some decrease of the triangularity, resulting in the strongest volume reduction (a reduction of about 15%).
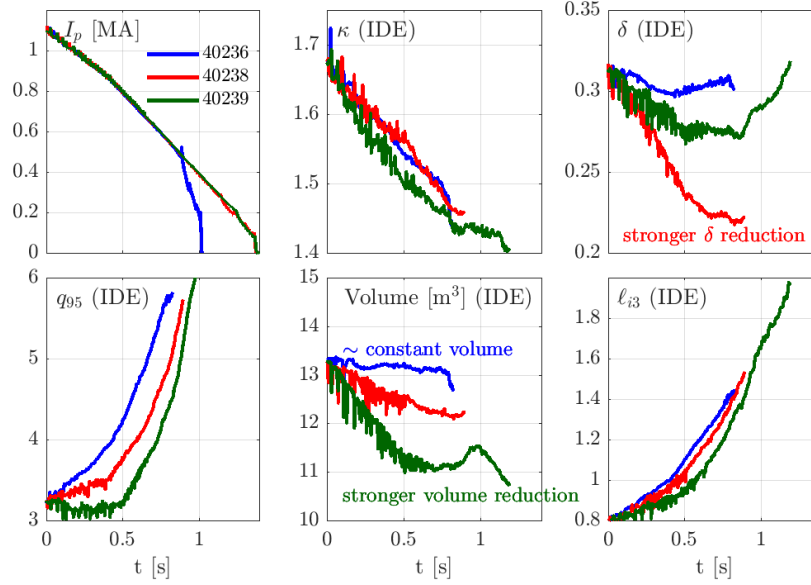
Figure 6.9: Ramp-down traces to study the effect of shaping on $\ell_{i3}$ and $q_{95}$.

Based on these experiments, limited conclusions can be drawn regarding the impact of individual shaping parameters. It can be observed that a reduction of the plasma volume results in a slower increase of $q_{95}$ and $\ell_{i3}$. Note that the disruption of discharge 40236 is not caused by loss of vertical controllability, but by a radiative collapse, due to a lack of auxiliary heating after the HL transition, as described in Section 6.3.

**Modeling**

We perform a set of RAPTOR simulations for discharges 40236 and 40239 to investigate whether the model can capture the impact of the equilibrium evolution on $\ell_{i3}(t)$. The RAPTOR simulations are shown in Appendix D: while for discharge 40236, the predicted $\ell_{i3}$ trace matches closely the value reconstructed by IDE (Figure D.1), RAPTOR seems to over-predict $\ell_{i3}$ for discharge 40239, thus under-predicting the impact of the shape adjustments (Figure D.3).

In addition to the standard simulations, additional simulations are performed, swapping the underlying equilibrium data used for the RAPTOR simulations amongst each other, as presented in Figure 6.10. Repeating the simulation of discharge 40236 with the geometry evolution of discharge 40239 (with the decreasing volume), leads to a decrease of the predicted $\ell_{i3}$ by RAPTOR, matching the $\ell_{i3}$ trace simulated for 40239. Conversely, repeating the simulation of 40239 with the geometry evolution of discharge 40236, leads to an increase of the predicted $\ell_{i3}$ by RAPTOR, matching the $\ell_{i3}$ trace simulated for 40236. For a smaller plasma volume at a given plasma current, the lower $q_{95}$ value causes a broader $j_{par}$ profile and hence a lower $\ell_{i3}$ value. For reducing $q_{95}$, the $q = 1$ radius moves outward, which, when applying the gradient-based transport model, leads to broader temperature and density profiles.
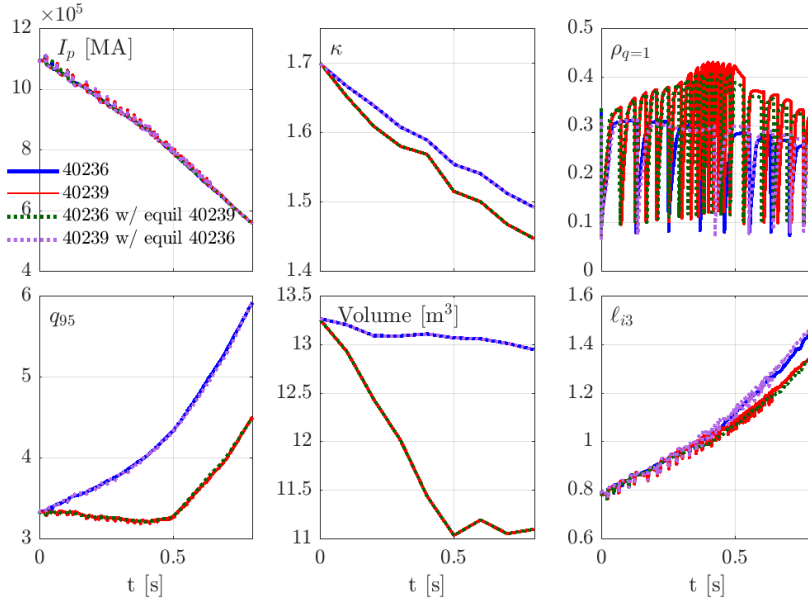
Figure 6.10: RAPTOR simulations for discharges 40236 and 40239, including a simulation of both discharges with swapped equilibrium data (the equilibrium geometry data of discharge 40239 is used for the simulation of 40236 and vice versa).

### 6.5.2 Rapid compression of the plasma column

**Experiment**

During the termination of H-mode density limit experiments on AUG, a rapid compression of the plasma column has been executed, in an attempt to counter the increase of the internal inductance $\ell_{i3}$, as applied in discharge 41388. Halfway through the ramp-down phase, the plasma transitions from a diverted to a limited phase, and the cross-section is compressed and moved towards the inner limiter (some plasma boundary shapes are illustrated in Figure 6.13). The evolution of various shaping parameters are shown in Figure 6.11. Note the rapid reduction of volume and elongation as the plasma poloidal cross-section is contracted and the shaping is reduced, resulting in a circular cross-section. A fast reduction of both $q_{95}$ and the internal inductance $\ell_{i3}$ during the compression phase is observed in the IDE reconstruction. When the plasma current reaches $I_p \sim 110\,\text{kA}$, the plasma disrupts as the excessive reduction of $q_{95}$ results in an MHD instability.

The second discharge shown in Figure 6.12 (40750), remains diverted throughout the ramp-down. While the plasma volume and the elongation reduce significantly, there is no fast compression phase and both $q_{95}$ and $\ell_{i3}$ increase monotonically.

**Modeling**

To understand the dynamics of the ramp-down phases of discharges 41388 and 40750 in more detail, RAPTOR simulations have been performed for both discharges. As both discharges have
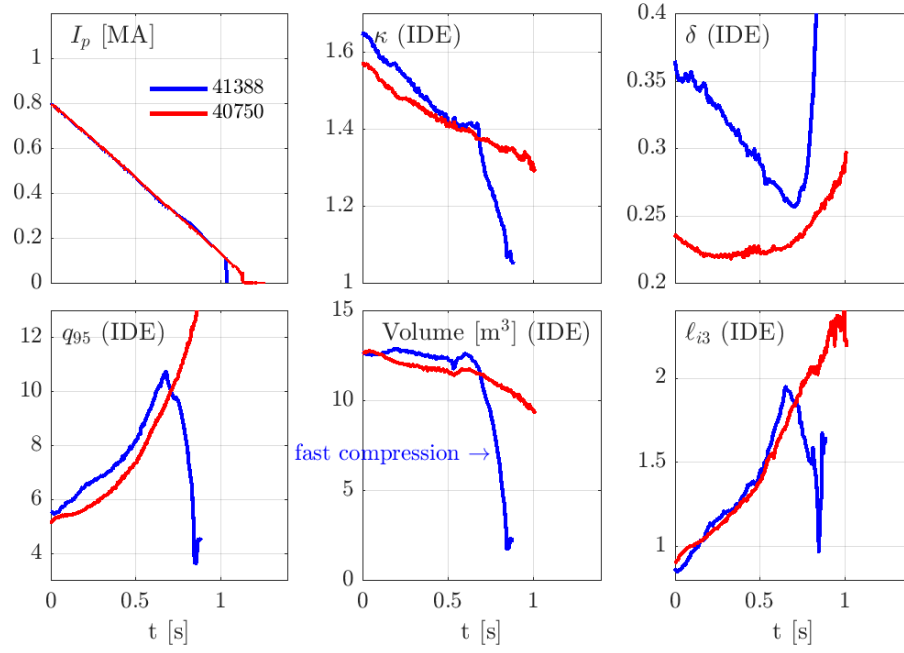
Figure 6.11: Ramp-down traces to study the effect of plasma compression on $\ell_{i3}$ and $q_{95}$.
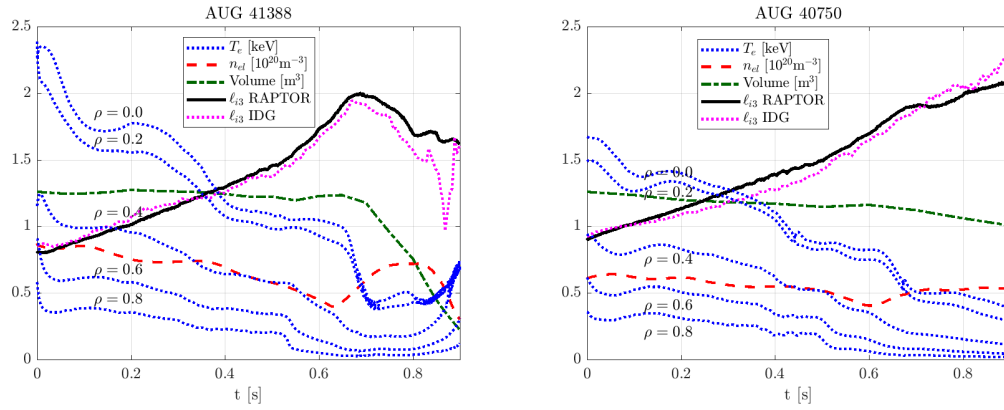


Figure 6.12: Time traces $T_e$, $n_{el}$, volume and $\ell_{i3}$ for RAPTOR simulations of discharges 41388 and 40750.
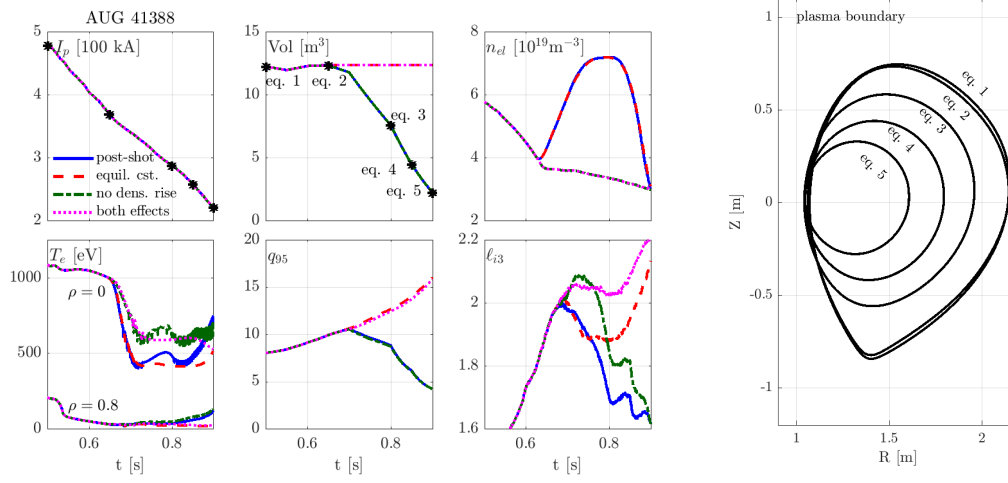
Figure 6.13: Sensitivity study in RAPTOR on the effect of plasma column compression and density on the internal inductance $\ell_{i3}$ and $q_{95}$.

an HL transition to an ohmic L-mode, the non-standard L-mode setting of the gradient-based transport model with $\lambda_{T_e} = 4.5$ is applied. Furthermore, for these two discharges, an electron H-factor $H_e = 0.3$ (instead of default value $H_e = 0.4$) leads to an improved agreement with the experimental data (during H-mode).

Figure 6.12 gives an overview of some of the modeled traces in RAPTOR, including electron temperature at various radii ($\rho = [0\ 0.2\ 0.4\ 0.6\ 0.8]$), the line average density, the plasma volume and the internal inductance $\ell_{i3}$. For both discharges, the RAPTOR-simulated $\ell_{i3}$ evolution recovers closely the experimentally observed trace. The dynamics of the internal inductance can be understood by considering the $T_e$ traces at various radii. Both discharges have an HL transition shortly after t=0.5s, leading to a distinct decrease of the outer $T_e$ traces (no auxiliary heating is maintained), increasing the growth rate of the $\ell_{i3}$ trace. At a later time during the L-mode phase, around t=0.6s, an increase of the line-averaged density occurs (due to central impurity accumulation). Note that the line average density reference for the gradient-based transport model is the experimentally observed trace. The density rise is most pronounced for discharge 41388. The observed density peaking causes a reduction of the central electron temperature traces. This effect is recovered by the RAPTOR simulation, as visible in Figure 6.12. As the temperature profile and the (dominantly ohmic) current density profile broaden, the observed reduction of the internal inductance $\ell_{i3}$ results. Note however that an additional impact from the changing equilibrium geometry can be expected, as the plasma column is compressed.

To isolate the effects of the density rise and the plasma compression on the internal inductance evolution, three additional simulations have been performed, as presented in Figure 6.13. The initial post-shot simulation, applying the line average density trace and the equilibrium sequence observed in the experiment, is shown in blue.

- The first sensitivity study, shown in red, maintains the observed density increase, but

keeps the underlying equilibrium geometry constant from t=0.65s onward. As a first, obvious consequence, we can see that the value of $q_{95}$ continues to increase as the plasma current reduces. While the initial $\ell_{i3}$ reduction after t=0.65s is little affected, the absence of the plasma compression leads to an increase of $\ell_{i3}$ towards the end of the simulated time window.

- A second simulation maintains the original equilibrium evolution, with the plasma compression, while imposing an artificial density reference without the density rise observed in experiment. In this case the initial reduction of $\ell_{i3}$ after t=0.65s is less pronounced. However, the plasma compression still leads to a strong decrease of $\ell_{i3}$ by the end of the simulation.

- Finally, a simulation is run with a constant equilibrium geometry from t=0.65s and the artificial density trace without density increase. The strongest increase of $\ell_{i3}$ is observed for this simulation.

We conclude that, according to these simulations, rapid compression of the plasma column leads to a significant reduction of the internal inductance, due to the impact of the changing geometry, which can be reinforced by a simultaneous density rise.

## 6.6 Conclusion

The ramp-down phases of a series of ITER baseline and H-mode density limit discharges performed on AUG are analysed and modeled with the same gradient-based transport model for heat and density transport that has been applied for the DEMO ramp-down studies in Chapter 5.

Continued auxiliary heating after the HL transition allows for a gradual decrease of the outer $T_e$ profile, rather than a sudden collapse (edge cooling). Even in cases where a density limit disruption can be avoided, the radiative collapse causes a sharp rise of the internal inductance $\ell_{i3}$, which would endanger vertical stability on future machines. Interestingly, the higher outer $T_e$ for an auxiliary heated L-mode plasma persists after the auxiliary heating is eventually turned off, highlighting the inherently dynamic nature of the ramp-down plasma state evolution. The abrupt increase of $\ell_{i3}$ can be captured by RAPTOR, applying either the gradient-based model with an increased logarithmic gradient parameter $\lambda_{T_e}$, or a simple ad-hoc transport formula with boundary condition provided at $\rho = 0.8$.

The role of the plasma current ramp-down rate $dI_p/dt$ as an effective actuator to tailor the time evolution of the internal inductance $\ell_{i3}$, as proposed for DEMO ramp-down optimizations in Chapter 5, has been confirmed in experiment. A reduction of $dI_p/dt$ has a strong and immediate impact, limiting the subsequent growth rate of $\ell_{i3}$.

For a given $I_p$ trace, reducing volume and shaping during ramp-down seems beneficial to limit the increase of $\ell_{i3}$ (and $q_{95}$). While the effect of individual shaping parameters ($\kappa$, $\delta$) is unclear, the slower increase of $q_{95}$ due to a reduction of the plasma cross-section allows for a

slower increase of $\ell_{i3}$, both in simulation and experiment.

A rapid compression of the plasma column has been attempted during the ramp-down of H-mode density limit experiments. The fast dynamics of this highly transient phase are captured by RAPTOR simulations, imposing the time-varying equilibrium geometry and the line average density measured in experiment. Simulations have quantified the respective impact of a density rise due to central impurity accumulation, broadening the $T_e$ profile, and the changing geometry during the plasma compression phase. While plasma compression seems a promising technique to limit the $\ell_{i3}$ increase during ramp-down, further simulations and experiments would help to further understand the interplay between individual shaping parameters and the $\ell_{i3}$ evolution. Furthermore, an excessive compression should be avoided, as a sharp decrease of $q_{95}$ causes the onset of MHD instabilities.

# 7 Conclusion and outlook

Reliable control over the current density, temperature and density profiles throughout the entire tokamak discharge, from the ramp-up phase to the flat-top and the ramp-down phases, is paramount to reliably achieve high performance scenarios in future fusion reactors, while retaining a safe margin to physics instabilities and engineering limits of the machine. The dynamic response of these profiles to the available actuators is governed by a coupled, non-linear set of diffusion equations. The RAPTOR code combines an efficient numerical implementation with a set of reduced physics models to evaluate transport coefficients and source and sink terms, thus allowing for fast evaluation of the plasma dynamical response, or the stationary operating point.

In this thesis, we have further developed the numerical and physical capabilities of the RAPTOR code. By routinely simulating ASDEX Upgrade (AUG) discharges, we have shown that rapid simulations of the plasma state evolution enable an improved physical interpretation of the observed phenomena. Furthermore, the fast computation time then allows to optimize actuator time traces for following discharges, allowing for more efficient physics-model-based scenario development. Exploring the full space of potential stationary working points and dynamical operation strategies, we have shown how RAPTOR can be used to optimize scenarios for ITER and DEMO, identifying active constraints and effective actuators to navigate the plasma state in the desired operating envelope. The obtained optimized scenarios can subsequently be tested in more complete simulators with improved physics fidelity and a full set of integrated models for the whole device.

## 7.1 Summary of the main results

### 7.1.1 RAPTOR upgrade: a framework for fast, automated optimization of the stationary state

RAPTOR has been extended with a non-linear solver that rapidly evaluates the stationary set of plasma profiles for a selected number of the transport channels $\psi(\rho, t)$, $T_{e,i}(\rho, t)$, $n_{e,i}(\rho, t)$. Leveraging the availability of analytical Jacobians, the equations are robustly solved, even

in conjunction with a stiff transport model (like QuaLiKiz-hyper-10D [van de Plassche et al. 2020]).

The new solver has been embedded in a framework for fast, automated optimization of the stationary phase of tokamak plasma discharges. Cost and constraint functions, reflecting respectively plasma performance indicators and limitations on the desired plasma state, can be generically implemented and their respective gradients are calculated analytically. Both scalar variables (e.g. heating powers) and radially distributed quantities (e.g. electron cyclotron deposition profile) can be optimized.

The numerical implementation of both the stationary state solver and the optimization routine have been discussed in detail in Chapter 2.

### 7.1.2 Stationary state optimization for the ITER hybrid scenario

Coupling the stationary state optimization scheme to the QuaLiKiz neural network surrogate model QLKNN-hyper-10D [van de Plassche et al. 2020], the ITER hybrid scenario has been investigated, as presented in Chapter 4. Safety factor $q(\rho)$, ion temperature $T_i(\rho)$ and electron temperature $T_e(\rho)$ are solved for. To take into account the effect of $\alpha = \frac{d\beta}{d\rho}q^2 R_0$ on confinement, the shear input to the transport model is adjusted to $s_{eff} = s - 0.5\alpha$, as indicated by a dedicated QuaLiKiz standalone study for the ITER hybrid regime.

The fusion gain $Q$ can be maximized by optimizing the deposition of electron cyclotron current drive. We found that adequate tailoring of the hybrid $q$ profile, with $q \sim 1$ in the core and high $s/q$ in the outer region, can be achieved without excessive fine-tuning of electron cyclotron deposition profile. The confinement can be maximized by clamping the $q$ profile to $q = 1$ at the most outward location that can be achieved for a given electron cyclotron power. For a gaussian deposition profile this corresponds to finding the innermost deposition radius for which $q > 1$ is not violated. Whilst these results are consistent with [Citrin et al. 2010], the procedure has been fully automatized, with a surrogate first-principles-based model, greatly accelerating the optimization. The full, non-linear optimization problem is solved within minutes on a single CPU.

With a heating mix $P_{nb} = 33\,\mathrm{MW}$ and $P_{ec} = 40\,\mathrm{MW}$, $Q = 5$ is predicted with non-inductive current fraction $f_{ni} = 0.89$ and fusion power $P_{fus} = 365\,\mathrm{MW}$ (assuming $T_{e,i\ ped} = 4.5\,\mathrm{keV}$, $f_G = 0.9$ and $n_{e0}/n_{e\ ped} = 1.4$, and for $I_p = 10.5\,\mathrm{MA}$). Optimal operating points have been compared for different values of plasma current, density and pedestal height and for varying heating mix.

Due to the stiffness of the QLKNN-predicted transport, an increase of fusion gain can be achieved by reducing the electron cyclotron power. Depending on the levels of plasma current and neutral beam power, the reduction of electron cyclotron heating and current drive is either limited by the need for enough off-axis current to maintain $q > 1$, or by the need for a sufficient separatrix power flow to maintain H-mode operation, giving rise to an intermediate plasma current maximizing the fusion gain Q. Similarly, a reduction of neutral beam heating allows to increase the fusion gain, at the expense of lowering the non-inductive current fraction.

The strong impact of pedestal pressure and density profile peaking on fusion power, current drive efficiency and bootstrap current is quantified. For a given pedestal pressure, a lowered

pedestal density allows for better performance as the non-inductive current fraction can be boosted while the fusion power remains essentially the same. Including the density equation to the set of solved equations, RAPTOR-QLKNN predicts a stronger density peaking for reduced pedestal density.

Optimizing the set of radial plasma profiles for a variety of operating regimes, the presented workflow naturally lends itself for integration into reactor design system codes.

### 7.1.3  Ramp-up optimization for ASDEX Upgrade advanced scenario

A fast, reliable and reproducible early heating scenario at $I_p = 1\,\text{MA}$ has been developed for AUG, guided by inter-discharge simulations and optimizations in RAPTOR, as described in Chapter 3. Fast access to a stationary state is important for future reactors, as current diffusion is orders of magnitude slower than in present-day devices.

A framework has been presented to routinely simulate AUG discharges from ramp-up to ramp-down, both before and after the pulse is executed. Simple, reduced models for transport and electron cyclotron current drive are applied, with $\chi_{e\ ano} \sim \rho q T_e^{1.2}$ and $\eta_{cd\ ECCD} \sim e^{-\rho^2/0.5^2} T_e/n_e$. Therefore, the present validated simulations are real-time compatible. Imposing the $T_e$ boundary condition at $\rho = 0.8$, this set-up is able to recover the dynamics of $T_e(\rho, t)$ and $q(\rho, t)$ in the plasma core, as validated against experimental reconstructions from IDA [Fischer et al. 2010] (for $T_e$) and IDE [Fischer et al. 2016] (for $q$). Model parameters are maintained constant to simulate the range of discharges discussed. The IDE tool-chain is used to obtain equilibrium geometry data, neutral beam heating and current drive deposition profiles (RABBIT [Weiland et al. 2018]) and electron cyclotron deposition radii and widths for the individual gyrotrons (TORBEAM [Poli et al. 2001]). To set the $T_e$ pedestal top boundary condition in pre-discharge simulations, a simple scaling law based on previous discharges within the same parameter regime has been proposed. The electron pressure at $\rho = 0.8$ is estimated, with line average density, heating power and plasma current as input variables. For the advanced scenario regime studied, we obtained: $n_e T_e(\rho = 0.8) = 0.51\, n_{el\ 10^{19}\,m^{-3}}^{0.82} (P_{oh}(I_{p\ MA}, P_{aux\ MW}) + P_{aux\ MW})^{0.53} I_{p\ MA}^{1.71}$. In the presence of data from previous discharges which feature roughly a similar pedestal transport regime, this approach leads to a reasonable prediction of $T_e(\rho = 0.8, t)$, during the full discharge.

The good agreement between pre- and post-shot simulations has allowed us to run inter-discharge optimizations and to predict the impact of actuator adjustments before discharge execution. Post-discharge simulations led to the hypothesis that a 3/2 tearing mode in the early flat-top phase could be causally linked to the formation of an off-axis $q_{min} > 1.5$, with $q_{min}$ and the related region of low magnetic shear subsequently decreasing through $q = 1.5$. Running predictive, pre-shot simulations, a 200 ms delay of the early heating (by NBI), has been proposed, allowing $q_{min}$ to drop through $q = 1.5$ earlier in the discharge, during the ramp-up, at reduced values of $\beta_N$ and radius. The updated actuator recipe has been tested and subsequent post-shot simulation and analysis of the MHD magnetic spectrograms indicate that the robustness of the early heating scenario against the onset of tearing modes was successfully increased.

Automated optimization of the deposition radii of the ECCD sources has been attempted, aiming to achieve an early, elevated, stationary $q$ profile, both for $q_{min} < 1.5$ and $q_{min} > 1.5$. Applying the ECCD deposition proposed by RAPTOR simulations, relaxation of the $q$ profile immediately after reaching the flat-top phase, with $q_{min} < 1.5$, has been accomplished, as confirmed by IDE reconstruction and post-discharge simulations with ASTRA [Schramm et al. 2022] and RAPTOR. Maintaining $q_{min} > 1.5$ has been hampered by the onset of disruptions due to locked 2/1 modes, reduced pedestal temperature and a central peaking of density and neutral beam current drive. Enhanced robustness against 2/1 modes has been achieved by reducing the plasma current to $I_p = 900\,\text{kA}$, aiming to move the location of $q = 2$ inward, reducing the probability of ELM-triggered NTMs.

Scenario development clearly benefits from both pre- and post-discharge simulations, improving the interpretation of the observed dynamics, considering the non-linear interplay of $T_e$ and $q$. The impact of model parameter uncertainties are quantitatively estimated. The key impact of the achieved pedestal temperature $T_e(\rho = 0.8, t)$ has been identified: a strong impact on the central $q$ profile is observed when the pedestal temperature is increased or reduced, due to the small total current enclosed at small radii for the studied scenario.

### 7.1.4 Ramp-down optimization for DEMO

A safe ramp-down scenario is essential for the exploitation of a DEMO reactor, as close to zero disruption events can be tolerated at plasma currents above $\sim 5\,\text{MA}$. In Chapter 5, we have proposed an optimized set of actuators to achieve safe discharge termination. The strongly non-linear coupling of the kinetic profiles to the main heat sources and sinks (alpha power and impurity radiation), is self-consistently captured in RAPTOR. Coupling to the [ADAS] database is used to model the non-monotonic cooling factor dependence on $T_e$. Decreasing $T_e$, a radiative collapse can be triggered. We have applied the RAPTOR code to assess the levels of auxiliary heating that need to be maintained throughout the ramp-down, to maintain the discharge stable. Even if xenon can be efficiently extracted, a strong heating of more than 20 MW is needed during the L-mode phase. Feasible ramp-down trajectories are obtained, meeting a variety of constraining limits.

A fast landing scenario is critical for emergency shutdown of a burning plasma. A fast ramp-down leads to a strong peaking of the parallel current density $j_{par}$, leading to a high value of the internal inductance $\ell_{i3}$ and, according to our RAPTOR simulations for DEMO, inversion of the plasma current near the edge. The $\ell_{i3}$ increase corresponding to a range of different ramp-down rates has been analysed, and compared against a $(\kappa, I_p)$-dependent upper limit from free boundary equilibrium control calculations [Mattei et al. 2016] in CREATE-NL [Albanese et al. 2015]. A fast ramp-down with $dI_p/dt = -200\,\text{kA/s}$ is found to be overly optimistic. It is also shown that an early HL transition or a limited reduction of the impurity content (hence $Z_{eff}$) can limit the increase of $\ell_{i3}$, as the outward diffusion of current density is enhanced. Automated numerical optimization of the ramp-down phase has been performed in RAPTOR, optimizing the time evolution of plasma current and elongation, imposing the CREATE-NL limit on $\ell_{i3}$ as a constraint. The time evolution of $\ell_{i3}$ can be effectively tailored by the

plasma current evolution. Reducing the plasma elongation can potentially cause a further reduction of $\ell_{i3}$, as the $q = 1$ radius is moved to a larger radius. If the plasma minor radius is reduced simultaneously, the Greenwald density decrease is counteracted, allowing for a slower reduction of the plasma density. The RAPTOR optimizations include a constraint on $q_{95}$, as a reduction due to strong shaping adjustment compromises MHD stability. With the optimized time traces of plasma current and elongation, feasible termination strategies have been obtained for average ramp-down rates up to $dI_p/dt = -150\text{kA/s}$ (or $dI_p/dt = -100\text{kA/s}$ with more conservative assumptions). Due to the coupled nature of magnetic control and profile control, this result should be verified with a free boundary equilibrium solver.

### 7.1.5  Ramp-down optimization for ASDEX Upgrade

A series of ramp-down experiments have been performed on ASDEX Upgrade, to explore safe termination strategies. In Chapter 6, the same gradient-based transport that has been applied to model the DEMO ramp-down, has been successfully applied to model the transport of electron heat and density, following the approach introduced in [Teplukhina et al. 2017].
Both simulation and experiment confirm that the increase of the internal inductance $\ell_{i3}$ can be limited by a reduction of volume and elongation, hence increasing the margin towards vertical instability, although the impact of individual shaping parameters like elongation $\kappa$ and triangularity $\delta$ remains unclear. Rapid compression of the plasma column during the ramp-down has been executed in experiment and modeled in RAPTOR, imposing the time-varying equilibrium geometry and the line average density measured in experiment. Simulations have quantified the respective impact of a density rise due to central impurity accumulation, broadening the $T_e$ profile, and the changing geometry during the plasma compression phase. Excessive compression should be avoided, as a sharp decrease of $q_{95}$ causes the onset of MHD instabilities.
A sudden collapse of the peripheral electron temperature, causing a sharp rise of $\ell_{i3}$ and in some cases a density limit excursion followed by a disruption, has been avoided by continued auxiliary heating during the L-mode phase. The abrupt rise of $\ell_{i3}$ has been successfully modeled in RAPTOR.
The plasma current trace $I_p$ has been identified as an effective actuator to tailor the time evolution of the internal inductance $\ell_{i3}$, as proposed for DEMO ramp-down optimizations in Chapter 5, both in simulation and experiment. A reduction of $dI_p/dt$ has a strong and immediate impact, limiting the subsequent growth rate of $\ell_{i3}$. Our results demonstrate how the optimization procedure can take advantage of this effect to find trajectories satisfying a vertical stability constraint which itself depends on $I_p$.

## 7.2 Outlook

### 7.2.1 Further development of the RAPTOR code

Continued integration of reduced physics models in the RAPTOR code can be envisioned, although it is paramount that the code remains lightweight. Some options include:

- **Auxiliary heating and current drive:** The coupling of the RABBIT code [Weiland et al. 2018] is envisioned, allowing fast evaluation of neutral beam deposition profiles of heat, current and fast ions. Integrating a fast NBI model to evaluate the heating and current drive sources consistently with the plasma profiles would further increase the fidelity of RAPTOR predictions. Including the modeling of particle transport and neutral beam deposition allows to solve self-consistently the non-linear coupling between neutral beam deposition profiles, density peaking and thermal confinement.

- **Pedestal confinement:** Reliable pedestal height predictions are of central importance to correctly predict the global confinement of the discharge, as well as local features of the $q$ profile. In Chapter 3, we applied simple scaling laws based on earlier discharges to estimate the pedestal height predictively. Extending this work with a more advanced pedestal model, like proposed in [Luda et al. 2021] and [Meneghini et al. 2017], would allow extrapolation to different scenarios, as well as different machines, hence generalizing the applicability.

- **Transport:** New generations of neural network emulations of the QuaLiKiz transport model, including characteristics of turbulent transport physics in the network architecture, are currently under development [Horn 2020].

- **Impurity transport:** Reduced analytical models [Fajardo et al. 2023] for (heavy) impurity transport could be integrated in the code.

- **Flux pumping:** Inclusion of a simplified model for magnetic flux pumping, e.g. following the approach proposed in [de Blank and Krebs 2022], would allow to explore the potential of this mechanism to tailor the central $q$ profile.

Novel features that could be implemented include:

- **Automated sensitivity analysis:**
    - The availability of analytic Jacobians could be leveraged to obtain estimates of the sensitivity of the outputs of simulations to model inputs.
    - Alternatively, the fast forward modeling capability of the RAPTOR code could be used to estimate error bars on modeled output quantities with a Monte Carlo method, propagating the uncertainties on input quantities measured in experiment.

Suchlike sensitivity metric would allow to automatically assess the impact of non-modeled physics variables, like $Z_{eff}$, the initial $q$ profile, the (pedestal top) boundary conditions etc.

Regarding *transport model tuning parameters*, a sensitivity metric could be used to avoid overfitting. Strong changes in the predicted state for small adjustments of the tuning parameters should be avoided.

Within the RAPTOR *optimization routines*, one could also propagate sensitivities and evaluate the sensitivity of the cost function to model parameters and to the optimization variables themselves. When the value of the cost function changes strongly due to a small variation of an optimization variable, the problem is overfitted and the number of optimization variables should be reduced.

- **Extension gradient-based transport model:** An additional equation could be added to the non-linear set of (stationary) state equations, imposing a global metric for confinement and line average density, adding the transport model edge gradient parameters as unknowns. Alternatively, an outer loop of the implicit time solver and/or the stationary state solver could adapt the transport parameters until convergence.

### 7.2.2 Further optimization of elevated $q$ profile scenarios

A degraded pedestal temperature can hamper our efforts to maintain $q_{min} > 1.5$, as has been quantified in Chapter 3. If the pedestal is well diagnosed, we could use a linearized model around the nominal non-linear RAPTOR simulation to calculate the change in EC power and deposition radii required to maintain $q_{min} > 1.5$, accounting for the difference between the expected $T_e(\rho = 0.8, t)$ and the measured trace in the previous discharge. An ILC approach would be well suited to iteratively approach the reference $q_{min}$, even in the presence of small model-reality mismatches, given that shot-to-shot variations of the pedestal are not too strong. Eventually, one could control the ECCD deposition in real-time, based on the effective pedestal height and the estimated $q$ profile (from real-time equilibrium reconstruction and RAPTOR simulation), using an MPC controller.

### 7.2.3 Further optimization of ramp-down scenarios

**Validating DEMO termination strategies**

The inherently coupled nature of the kinetic ($q$, $T_e$, $n_e$) and magnetic (position and shape) control problems demands integrated simulations to test the feasibility of established ramp-down strategies. The kinetic profile evolution of the optimum ramp-down trajectory should be confirmed with higher fidelity integrated modeling tools (including impurity transport, pedestal model etc.). Ideally, whole-device modeling should be envisioned, including SOL dynamics and pumping efficiency. Iteration or coupling between a transport solver and a free boundary equilibrium control model (like CREATE-NL [Albanese et al. 2015]) is required to

assess controllability.

More specifically: for the optimized ramp-down trajectories proposed in Chapter 5, it should be verified whether the poloidal field coils allow for the proposed changes in plasma elongation, and whether the plasma column can be maintained radially and vertically stable (for the modeled kinetic profile evolution, plasma elongation and for a given DEMO design, e.g. with or without in-vessel coils).

**Understanding radiative collapse during AUG ramp-down**

Applying integrated modeling tools with higher physics fidelity, better insight could be obtained in the dynamics leading to a radiative collapse of the outer $T_e$ profile during the ohmic L-mode phase of the ramp-down in AUG. In RAPTOR, simulations including impurity radiation estimates from ADAS cooling factor data [ADAS], could be attempted, similar to the DEMO simulations in Chapter 5 of this thesis and the WEST simulations presented in [Maget et al. 2022; Ostuni et al. 2022].

### 7.2.4 Towards real-time control

The successful validation of rapid, reduced physics models in RAPTOR to model AUG discharges encourages further application of RAPTOR in real-time. An accurate real-time estimate of the plasma state, including the safety factor $q$ profile, will ultimately make scenarios more robust for inevitable shot-to-shot variations and allow for increasingly advanced physics-based control strategies.

By ensuring reproducible access to high performance operating points, as well as reliable discharge termination, adequate modeling and control solutions will play a key role in the operation of reactor-class tokamaks, hopefully bringing us closer to achieving a controlled burning plasma.

# A Ad-hoc formula for pre-shot estimate of ohmic power

In Chapter 3, a scenario-dependent scaling law eq. (3.4) has been proposed to evaluate a pre-discharge estimate of the time evolution of the electron pressure pedestal $n_e T_e(\rho = 0.8, t)$. The total heating power is selected as one of the input variables to the scaling law. To enable application of the scaling law also during ohmic or low power L-mode phases (when ohmic power is dominant), a pre-shot estimate of the ohmic heating power is required.

$$P_{oh\ MW} = c_{I_p} I_{p\ MA} e^{-c_P P_{aux\ MW}} + c_{oh}(1 - e^{-c_P P_{aux\ MW}}) \tag{A.1}$$

We attempt to estimate the ohmic heating power based on formula eq. (A.1), transitioning from a linear dependency on the plasma current $I_p$ in the ohmic heated phase to a constant value $c_{oh}$ when $P_{aux\ MW}$ becomes large. The relative magnitude of both terms is set by the exponential $e^{-c_P P_{aux\ MW}}$. Note that the linear dependence during the ohmic phase was also found on TCV [Sauter et al. 2014]. Even though $P_{oh} \sim I_p^2$ for constant resistivity, an increase of confinement with $I_p$ will impact the resistivity through its $T_e^{-3/2}$ dependency.

To verify formula eq. (A.1) and estimate the parameters $c_{I_p}$, $c_P$ and $c_{oh}$, time dependent predictions of $P_{oh}$ are compared to RAPTOR post-shot simulations for four different shots (1MA early and late heating, 900kA early heating). With the parameter setting summarized in Table A.1, a reasonable estimate of the RAPTOR $P_{oh}(t)$ trace is obtained, based solely on the input variables $I_p$ and $P_{aux}$. Note that the parameters $c_{I_p}$, $c_P$ and $c_{oh}$ applied in Chapter 3 are not generally valid and should be reassessed for a different scenario with alternative density, heating or plasma current.

| $P_{oh}$ model | |
| --- | --- |
| $c_{I_p}$ | 0.90 |
| $c_P$ | 0.28 |
| $c_{oh}$ | 0.05 |

Table A.1: Setting of tuning parameters of formula eq. (A.1), based on the four simulated discharges shown in Figure A.1.

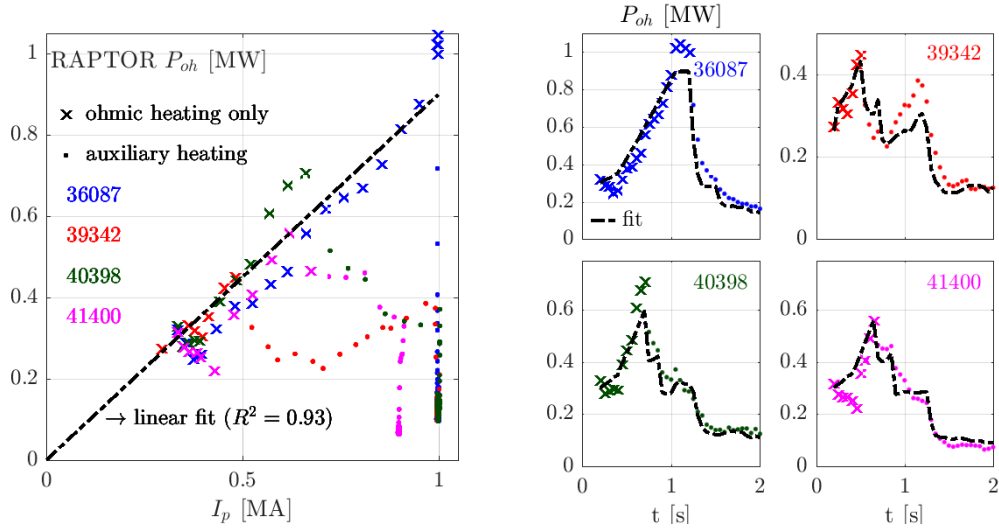# Appendix A.  Ad-hoc formula for pre-shot estimate of ohmic power



Figure A.1:  Data of four RAPTOR post-shot simulations are presented, to illustrate the application of formula eq. (A.1) to estimate the ohmic power $P_{oh\ MW}$, with plasma current $I_{p\ MA}$ and total auxiliary heating $P_{aux\ MW}$ as input variables.  During the ohmic heating phase, a linear relation $P_{oh\ MW} = c_{I_p} I_{p\ MA}$ captures well the dependency of the ohmic power predicted in RAPTOR on the plasma current.  For an externally heated plasma, the $P_{oh\ MW}$ prediction transitions to a constant value for high $P_{aux\ MW}$, with the exponential $e^{-c_P P_{aux\ MW}}$ setting the relative importance of both terms.  The time dependent plots on the right show how the formula (with fixed tuning parameters) performs well for various AUG advanced scenario shots studied in Chapter 3.

# B Overview of AUG advanced scenario data and simulations

This appendix accompanies Chapter 3, providing additional data and RAPTOR simulation results. Experimental data regarding the performance of the various discharges shown in Section B.1. Post-discharge simulations for most of the discharges presented in Chapter 3 are shown in Section B.2, as well as magnetic spectrograms loaded from pyspecview (a Python tool at AUG to visualise Fourier spectrograms for several diagnostics, settings Cross-phaseogram, Diag: Elm_coils, Sig: BCoils). The color of the signature visible in the spectrogram corresponds to the detected toroidal mode number, as indicated on the color bar.

## B.1   Experimental data on discharge performance
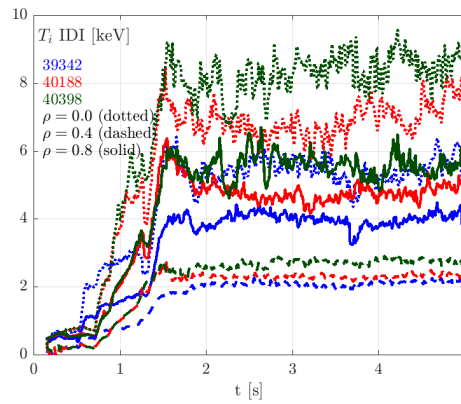


Figure B.1: Ion temperature traces at $\rho$ = [0.0 0.4 0.8], as applied in IDE based on CXRS data. The optimized early heating discharge achieves high, steady ion temperature from $t$ = 1.5s.
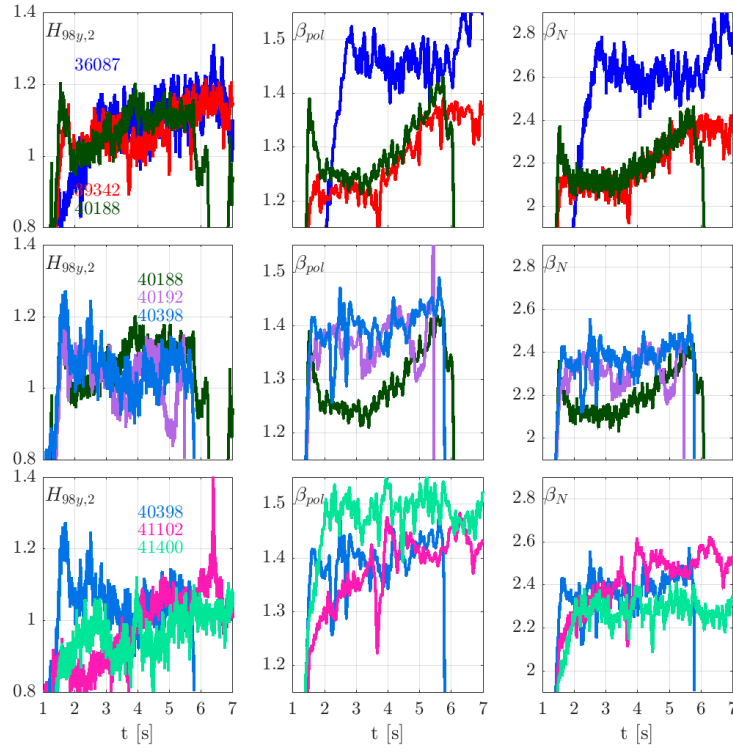
Figure B.2: The time traces $H_{98y,2}$, $\beta_{pol}$ and $\beta_N$ for the late heating discharges 36087 and the early heating discharges 39342, 40188, 40192, 40398, 41102 and 41400. For $H_{98y,2}$, the TTR post-processed diagnostic signal is used, applying a RABBIT run to subtract fast ion energy.

| Shot nr. (time) | IDE; IDA vsn. | $I_p$ [MA]; $q_{95}$ | $P_{net}$ | NBI onset timing [s] | $\beta_{pol}$; $\beta_N$ | $H_{98y,2}$ (subtr. fast ion) | $T_{e0}$; $T_e(\rho=0.8)$ [keV] | $T_{i0}$; $T_i(\rho=0.8)$ [keV] | $\frac{n_{e0}}{n_e(\rho=0.8)}$ | MHD activity ($t<2.5$s) |
|---|---|---|---|---|---|---|---|---|---|---|
| 36087 (5.0s) | 4; 2 | 1.0; 3.9 | 12.5 | 1.2 | 1.45; 2.6 | 1.15 | 11.0; 1.9 | 6.0; 2.2 | 1.3 | quiescent |
| 39342 (6.0s) | 3; 4 | 1.0; 3.9 | 10.0 | 0.5 | 1.35; 2.1 | 1.15 | 7.5; 1.6 | 6.0; 1.9 | 1.6 | **3/2@1.7s**, 2/1@2.2s |
| 40029 (2.0s) | 2; 3 | 1.0; 3.9 | 10.5 | 0.7 | 1.25; 2.1 | 0.90 | 7.0; 1.5 | 8.0; 1.8 | 1.7 | quiescent |
| 40030 (2.0s) | 4; 3 | 1.0; 3.9 | 9.5 | 0.7 | 1.20; 2.1 | 1.00 | 7.5; 1.5 | 8.0; 2.0 | 1.9 | quiescent |
| 40187 (2.5s) | 1; 2 | 1.0; 3.9 | 8.0 | 0.7 | 1.25; - | - | 3.5; 1.2 | 7.0; 1.7 | 2.0 | 3/2@0.8s, N=3@1.0s |
| 40188 (*1.6, 4.0s*) | 1; 2 | 1.0; 3.9 | 12.0 | 0.7 | 1.35; 2.3 | 1.10 | 7.5; 1.6 | 7.0; 2.0 | 1.5 | 3/2@1.0s, N=4@1.6s |
| 40192 (2.0s) | 3; 4 | 1.0; 3.9 | 10.5 | 0.7 | 1.35; 2.3 | 1.10 | 8.5; 1.8 | 8.5; 2.1 | 1.5 | 3/2@1.1s |
| 40398 (1.6s) | 1; 2 | 1.0; 3.9 | 11.0 | 0.7 | 1.40; 2.4 | <1.20 | 8.5; 1.8 | 8.5; 2.3 | 1.5 | 3/2@1.1s, N=4,3@t>1.9s |
| 40825 (1.6s) | 1; 2 | 1.0; 3.9 | 11.0 | 0.7 | 1.40; 2.4 | 1.00 | 8.5; 1.8 | 7.5; 2.0 | 1.6 | 3/2@1.1s, 2/1@2.1s |
| 41102 (5.0s) | 3; 3 | 1.0; 3.9 | 12.0 | 0.7 | 1.40; 2.5 | 1.05 | 9.5; 1.6 | 6.5; 2.0 | 1.7 | quiescent |
| 41400 (2.0s) | 1; 3 | 0.9; 4.1 | 11.5 | 0.7 | 1.45; 2.3 | 1.00 | 7.5; 1.3 | 6.0; 1.8 | 2.2 | quiescent |

Table B.1: Parameters of the AUG advanced scenario discharges discussed in Chapter 3. MHD activity during $t<2.5$s is summarized, with **boldface** indicating a clear impact on core $T_e$, and underline indicating a subsequent disruption. The timing is chosen to select the best performance phase (for 40188 at 1.6s, the indicated performance is achieved transiently due to a $\beta_{pol}$ overshoot, and later recovered after a pre-programmed $\beta_{pol}$ ramp).

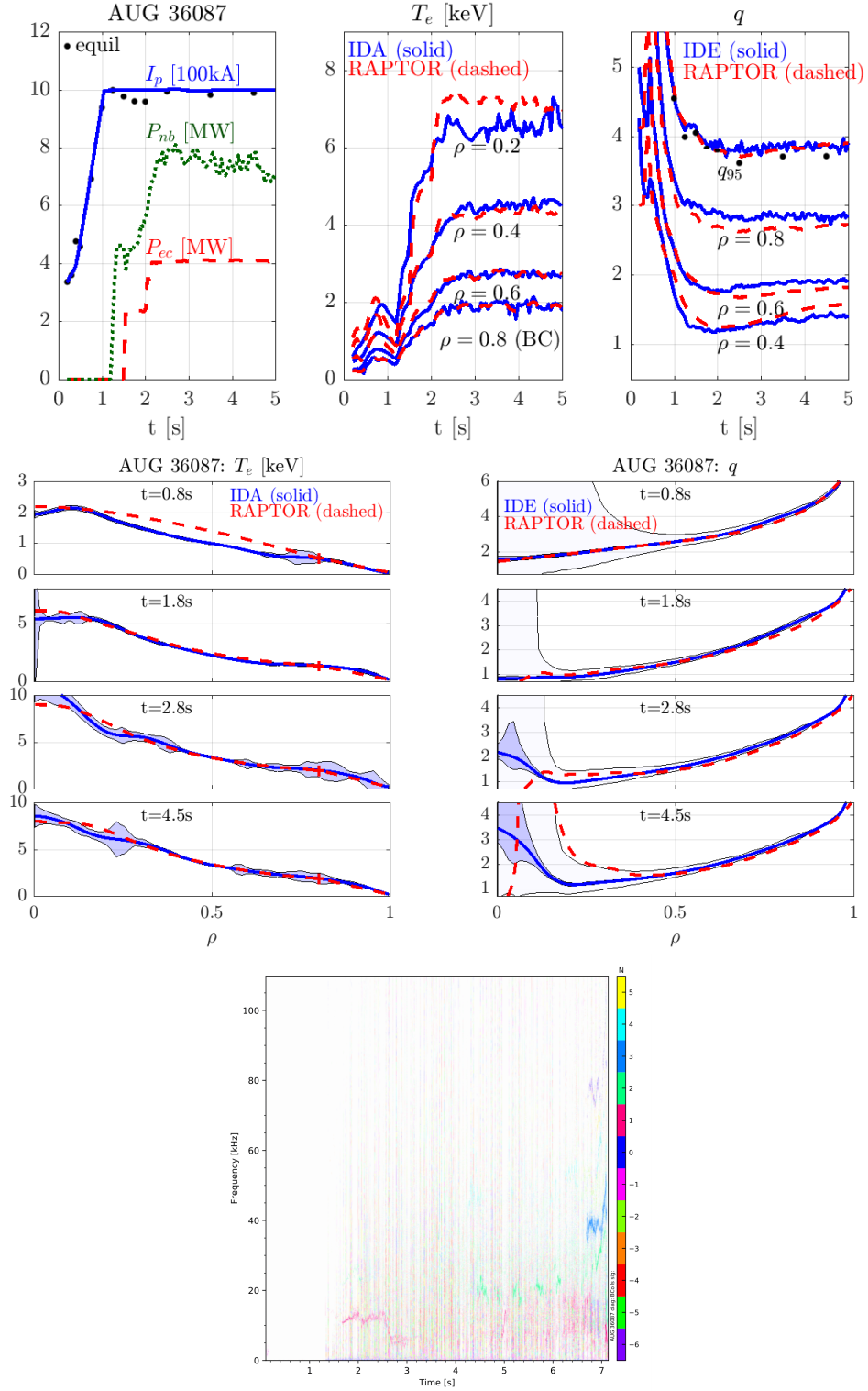## B.2 Full-discharge simulations of AUG advanced scenarios and magnetic spectrograms

Figure B.3: 36087: RAPTOR vs IDA/IDE and magnetic spectrogram. Note that IDE has a substantially lower final $q_{min}$, even though $T_e(\rho, t)$ and the outer $q$ profile are rather similar.
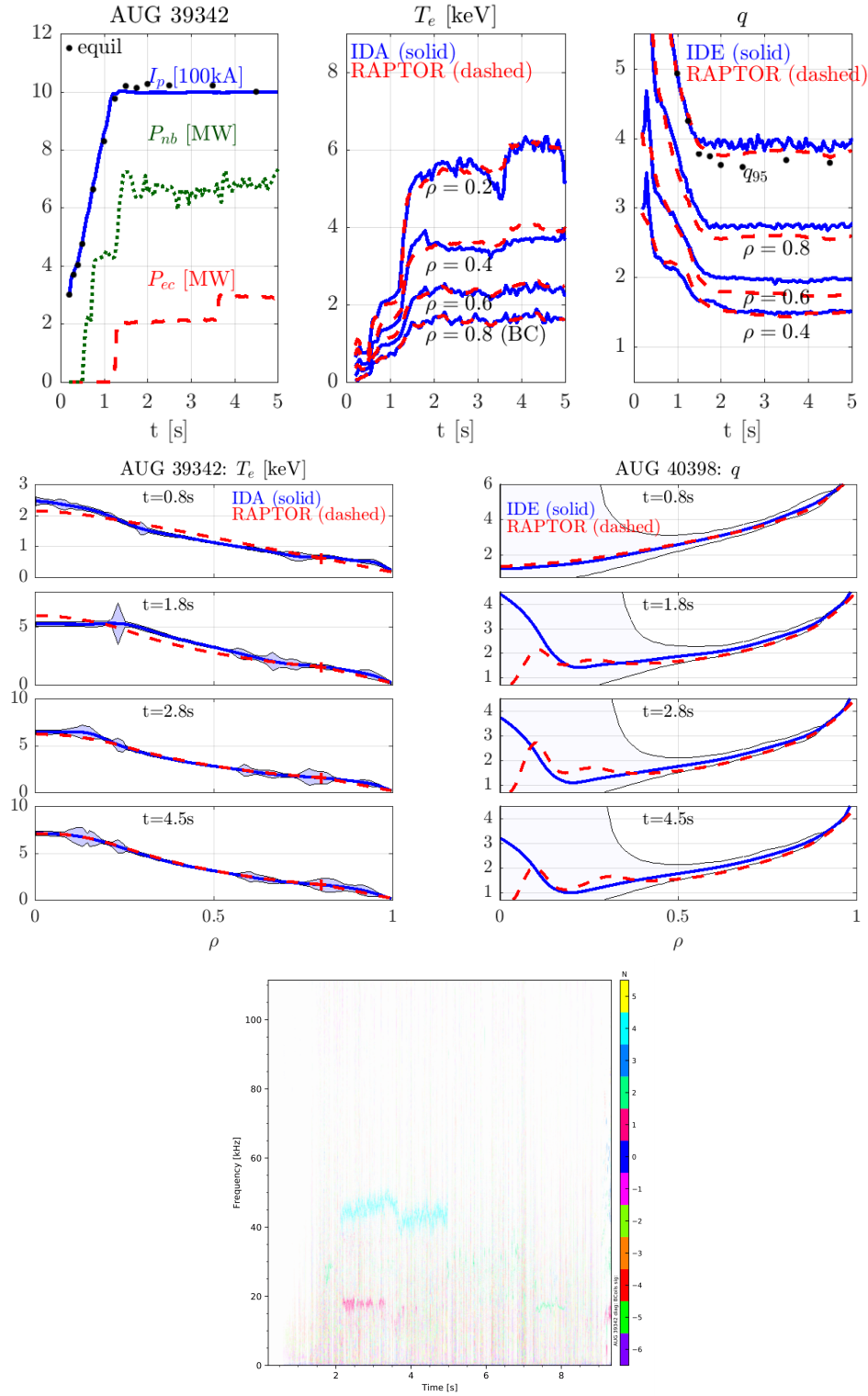
Figure B.4: 39342: RAPTOR vs IDA/IDE and magnetic spectrogram.
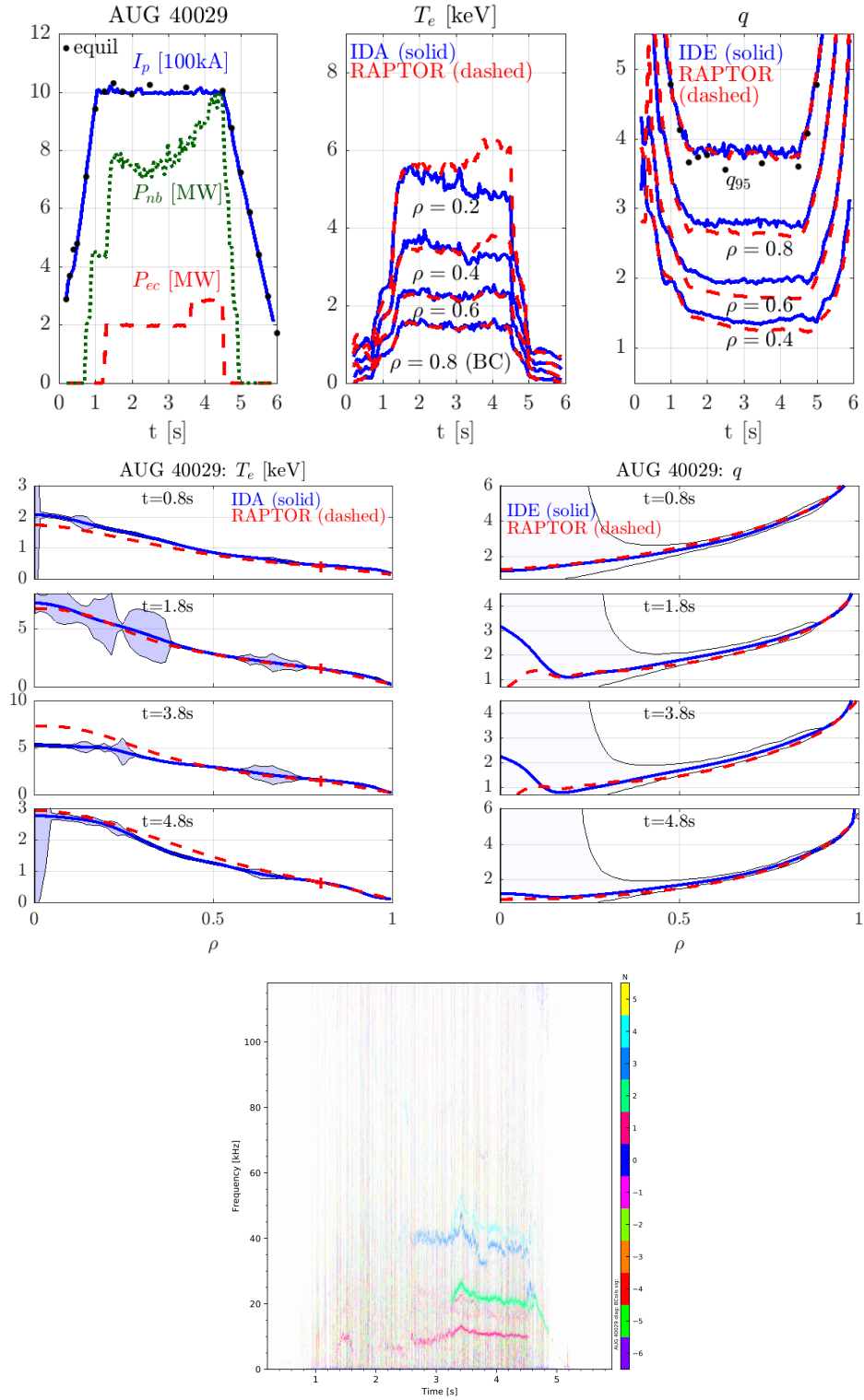
Figure B.5: 40029: RAPTOR vs IDA/IDE and magnetic spectrogram.

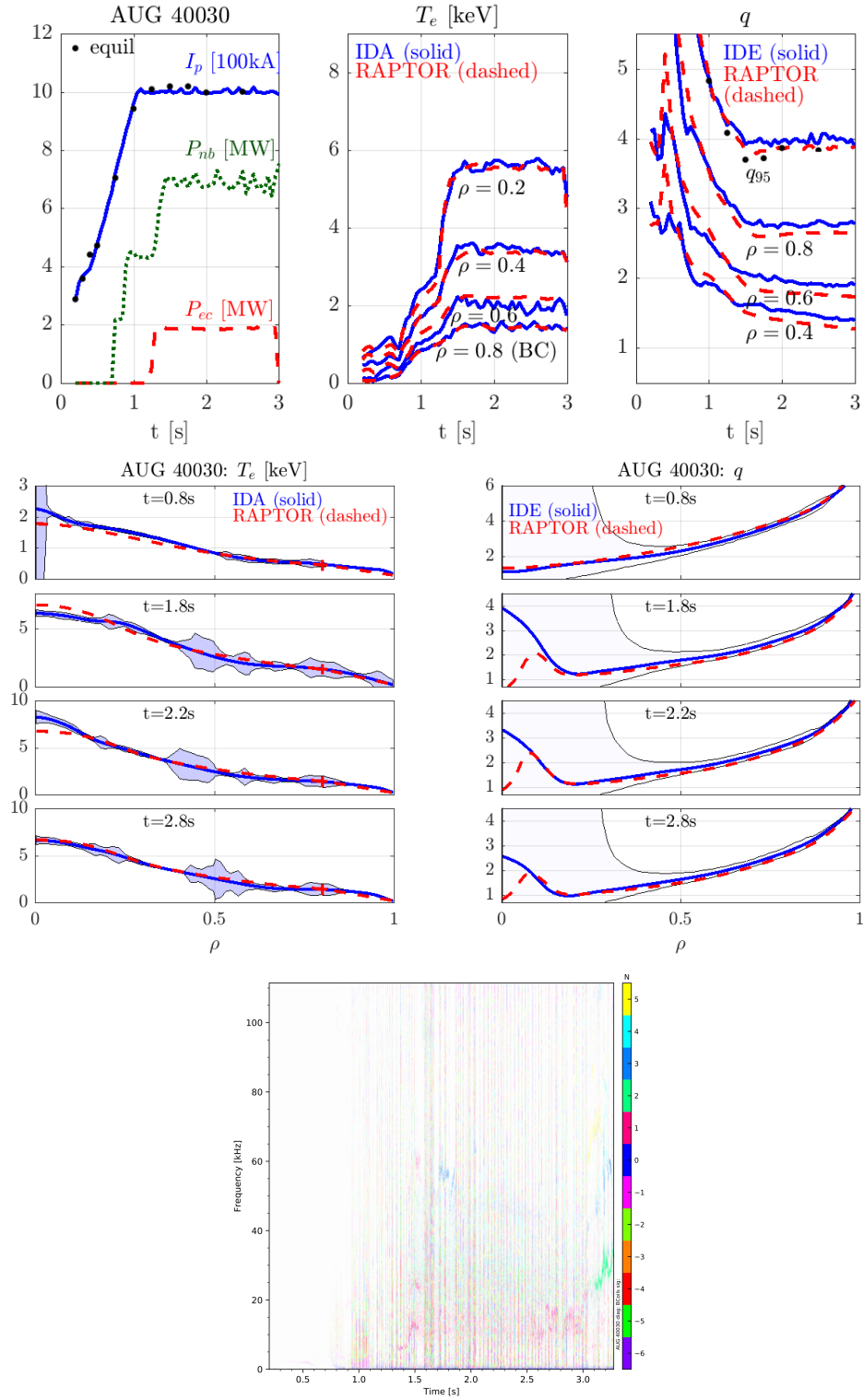Figure B.6: 40030: RAPTOR vs IDA/IDE and magnetic spectrogram. The premature termination of this discharge is due to a false locked mode alarm.

Figure B.7:   40187:  RAPTOR vs IDA/IDE (core $T_e$ and $q$ are significantly different) and magnetic spectrogram. Due to a technical failure this discharge runs essentially without ECCD.
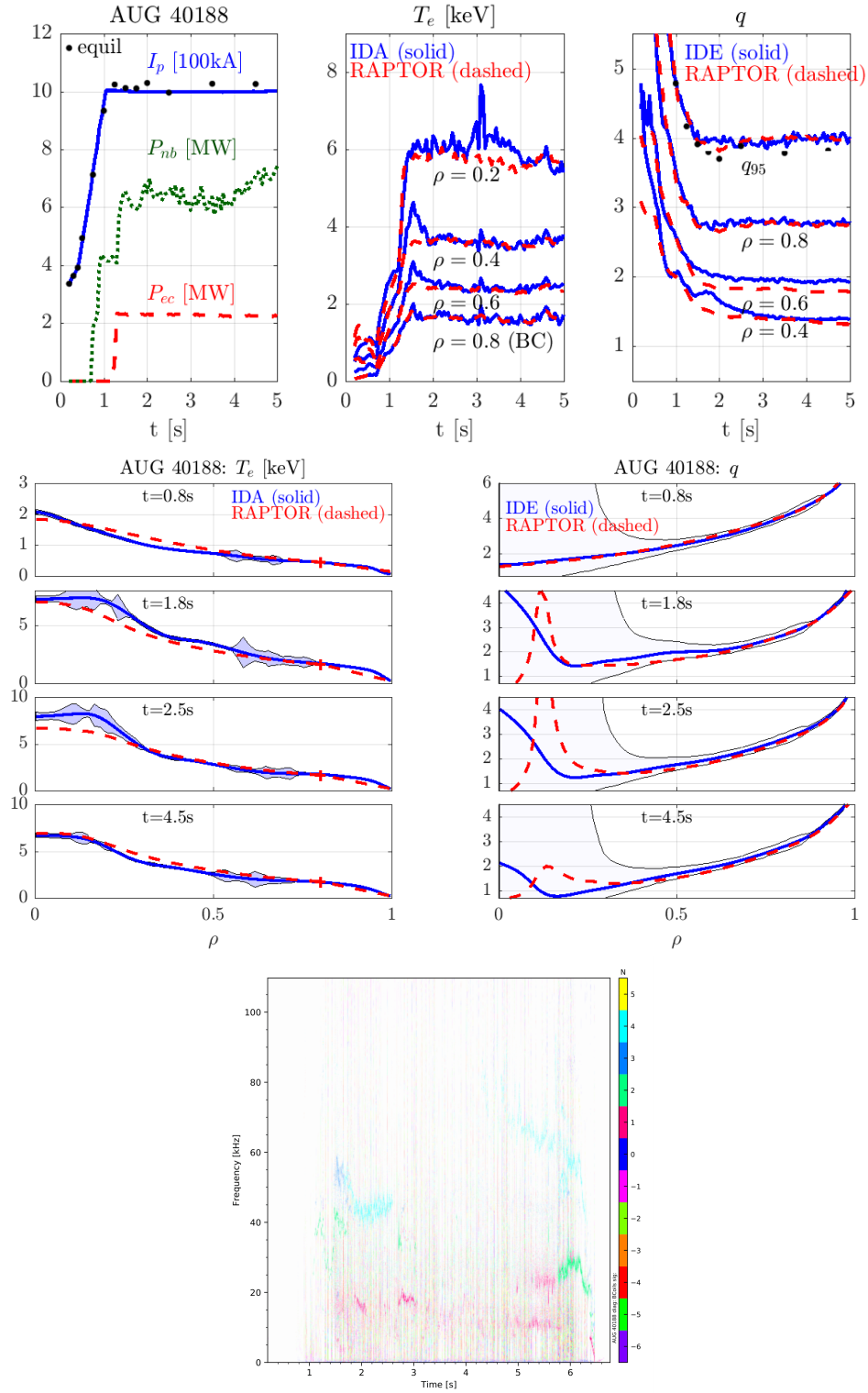
Figure B.8: 40188: RAPTOR vs IDA/IDE and magnetic spectrogram.

Figure B.9: 40192: RAPTOR vs IDA/IDE and magnetic spectrogram. 3/2 NTMs strongly affect core $T_e$ between 3s and 4s, indicating marginal stability.

Figure B.10:  40398: RAPTOR vs IDA/IDE and magnetic spectrogram. The core $T_e$ (and the $H_{98y,2}(t)$ trace) is decreasing after 2.5s.

Figure B.11: 40825: RAPTOR vs IDA/IDE and magnetic spectrogram. A locked 2/1 mode terminates the discharge at 2.1s.
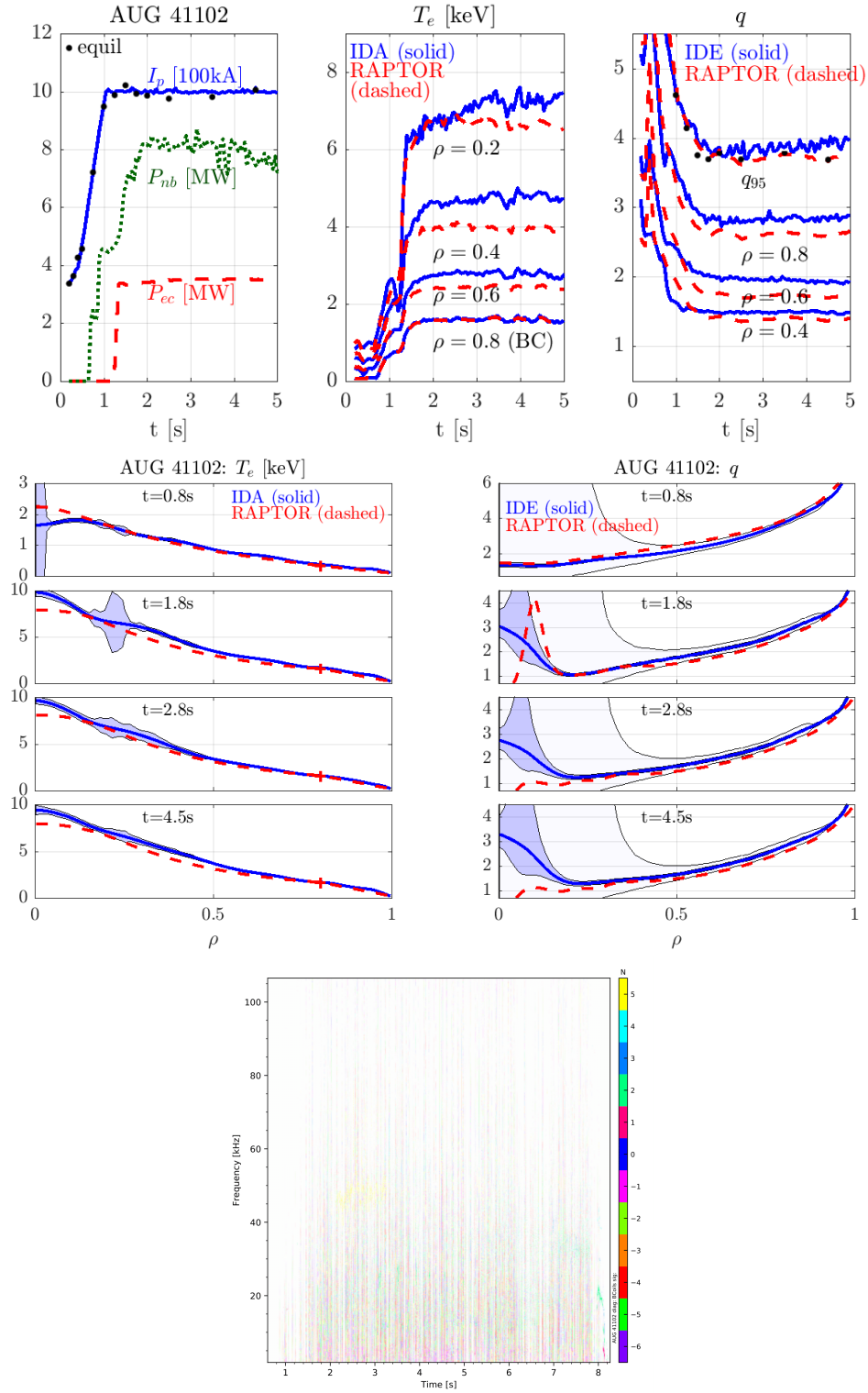
Figure B.12: 41102: RAPTOR vs IDA/IDE and magnetic spectrogram.

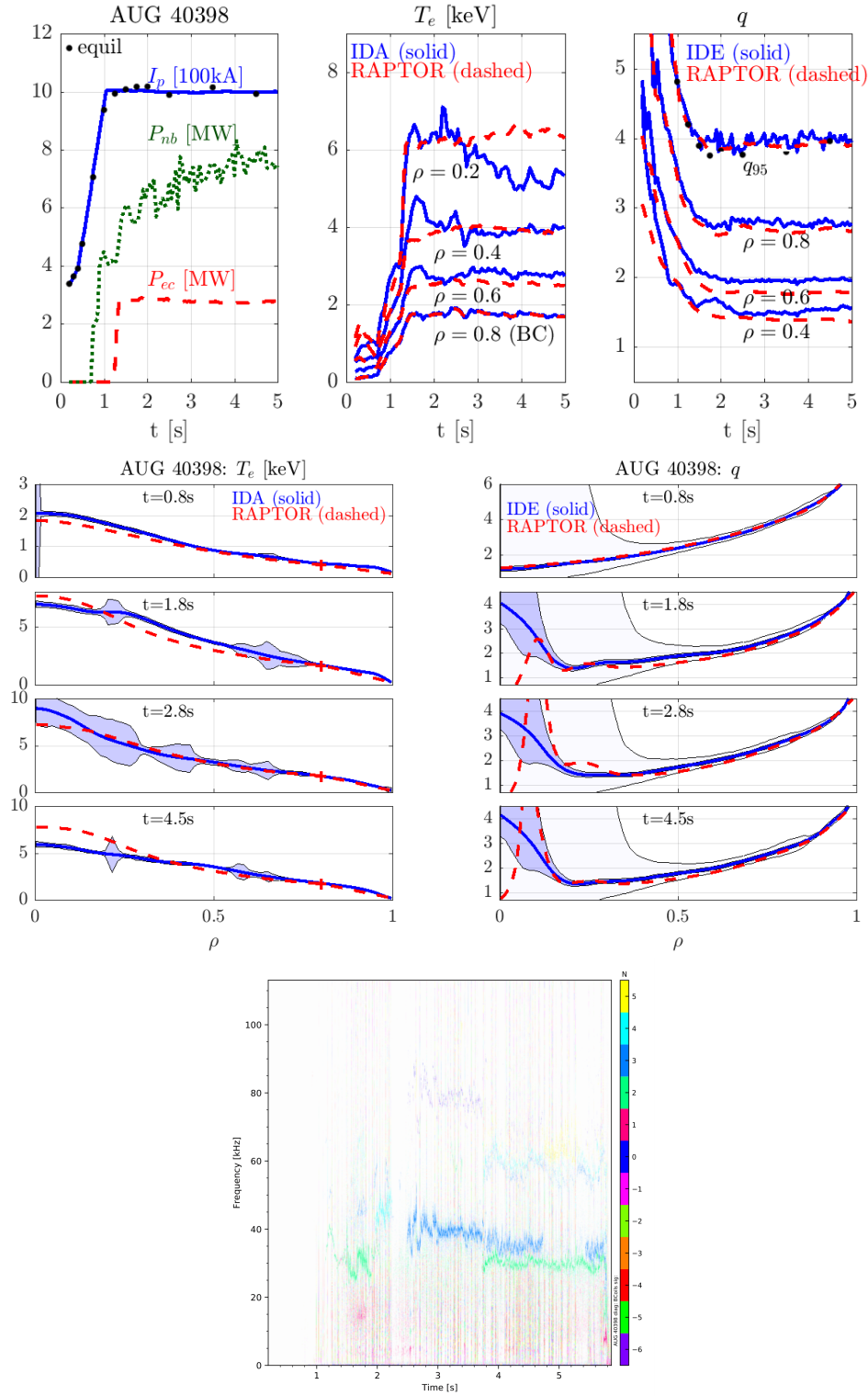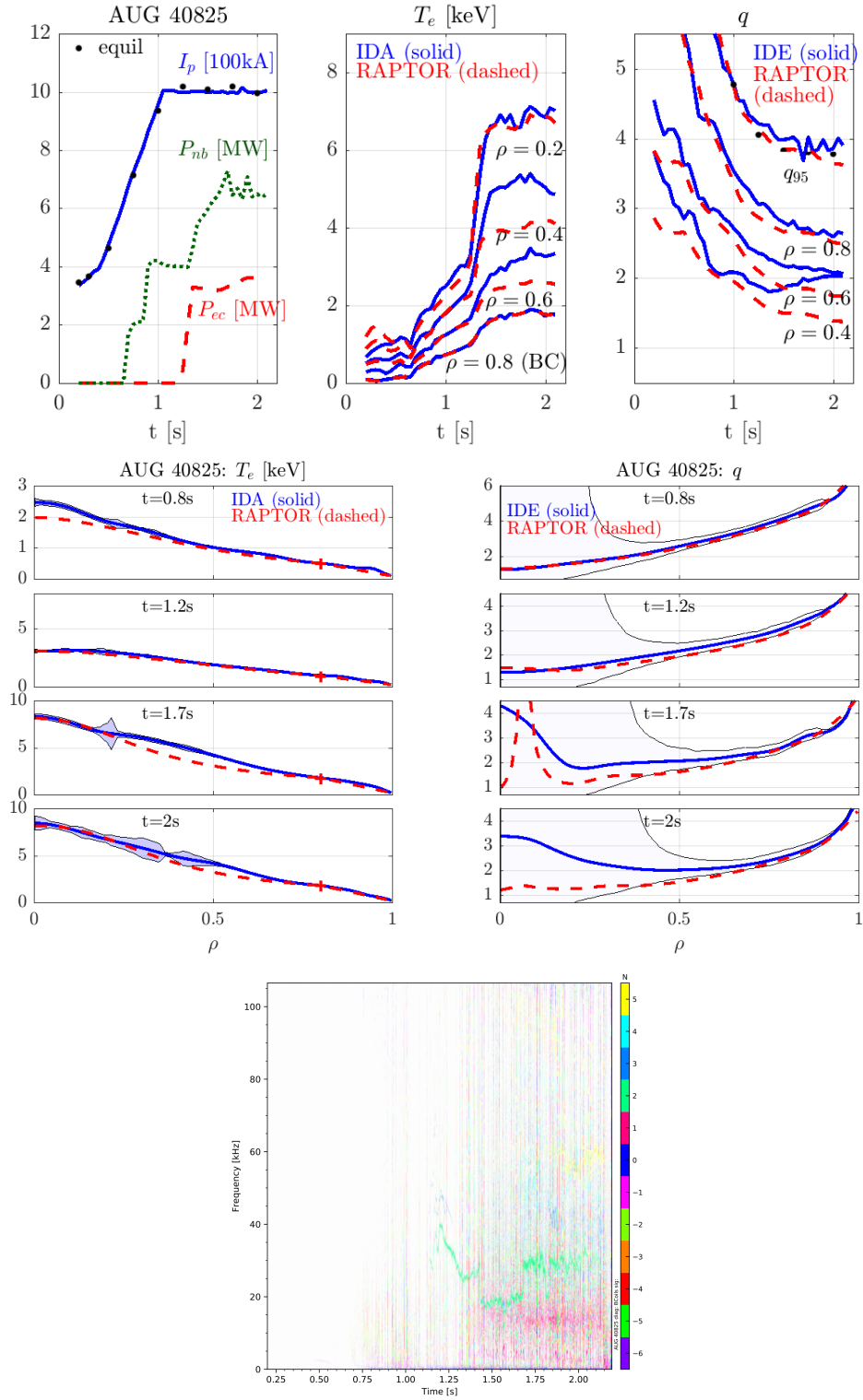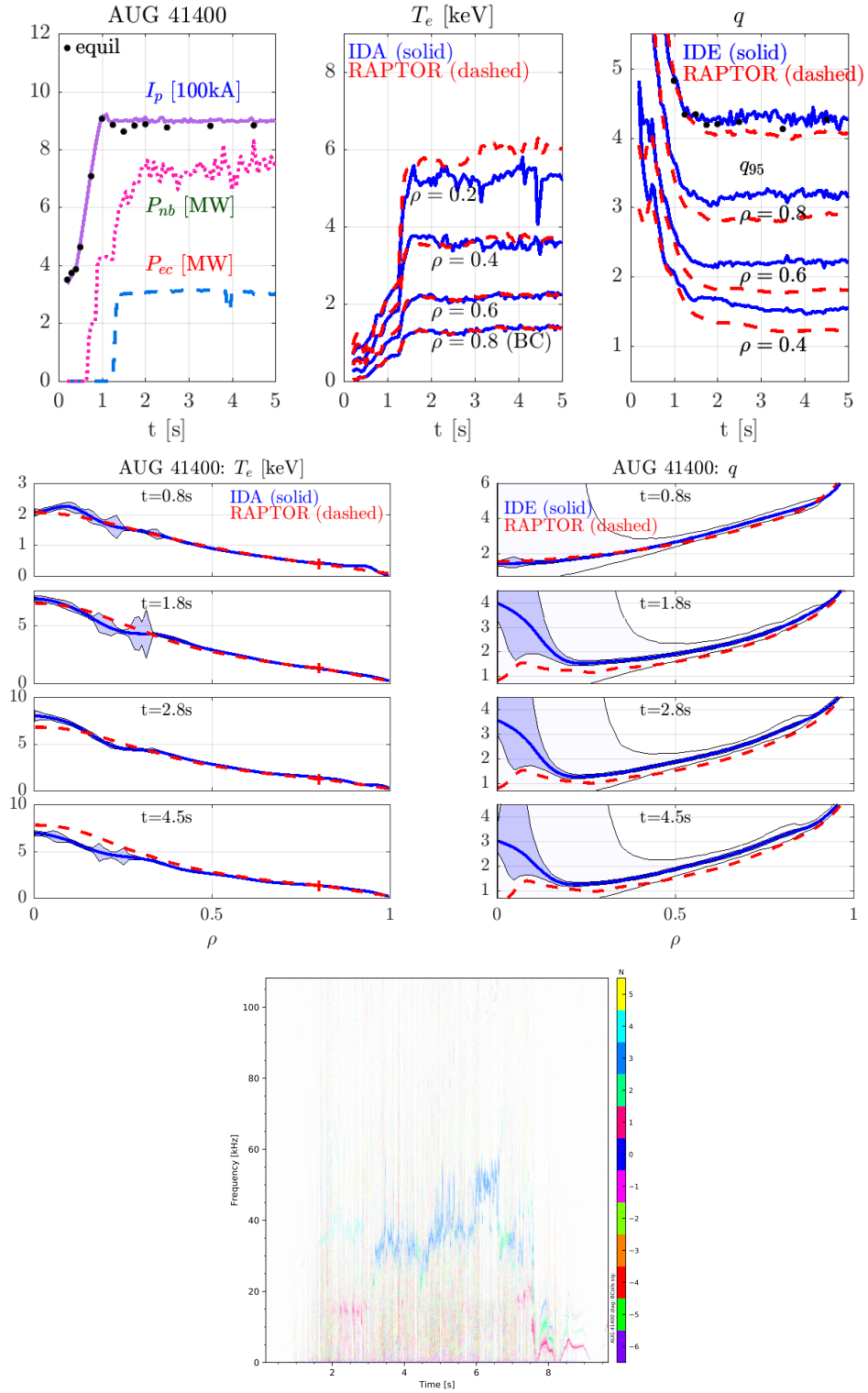Figure B.13: 41400: RAPTOR vs IDA/IDE and magnetic spectrogram. Reduced plasma current $I_p = 900$kA

# C Feasibility study for replacement current-drive NBI source for ASDEX Upgrade advanced scenario

The beamline geometry of the neutral beam injectors on ASDEX Upgrade allows to distinguish two radial sources (1 and 4), four tangential sources (2,3,5 and 8) and two current drive sources (6 and 7)[1]. The strong off-axis current driven by source 6 and 7 is important for the advanced scenario described in Chapter 3, which aims for an off-axis peak in the current density profile. By the end of 2021, a leak in the ion dump impeded further use of NBI source 7 in the ongoing AUG campaign. To assess whether the scenario could still be run with the remaining sources, the modeling frameworks in ASTRA and RAPTOR were used to make a quantitative assessment of the situation [Schramm et al. 2022].

To obtain source profiles for the individual NBI sources, interpretative ASTRA [Fable et al. 2013, 2022] runs are performed for the various NBI sources, applying the RABBIT code [Weiland et al. 2018] to calculate the deposition profiles. Figure C.1 shows the current density contributions of the individual NBI sources at 3.5s.

Summing different combinations of these source profiles, assuming the absence of non-linear effects, the impact of the loss of an individual source can rapidly be explored in RAPTOR. Firstly, it is checked that the RAPTOR simulation using the NBI sources present in 39342 (NBI 3, 6 and 7) properly recovers the RAPTOR post-shot simulation making use of the total NBI deposition profiles from IDE. Comparing the blue and red dotted traces in Figure C.3, it is clear that the simulation making use of the summed ASTRA NBI deposition profiles successfully recovers the post-shot run.

The next step is to assess the impact of the loss of NBI source 7 on the ability to maintain the $q$ profile elevated. A RAPTOR simulation is performed with a newly proposed NBI heating mix, combining NBI sources 2, 6, 8, while maintaining the original mix NBI 3, 6 before 1.27s. For this NBI heating mix, only minor differences in $q$ profile evolution are observed with respect to

---

[1]More specifications can be found on https://www.aug.ipp.mpg.de/foswiki/bin/view/ITED/NiauGeometry

## Appendix C. Feasibility study for replacement current-drive NBI source for ASDEX Upgrade advanced scenario
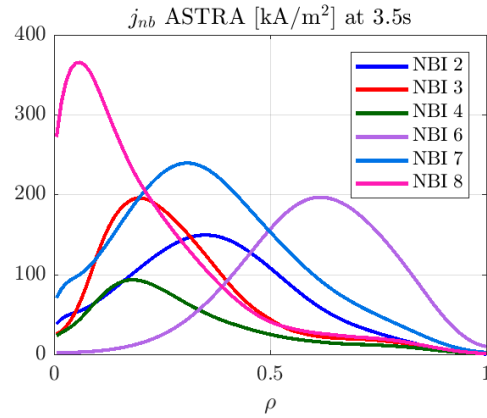


Figure C.1: Individual current density contributions of the different NBI sources, calculated by RABBIT in an interpretative ASTRA run of discharge 39342 at 3.5s; NBI sources 6 and 7 provide the strongest off-axis current drive contribution.
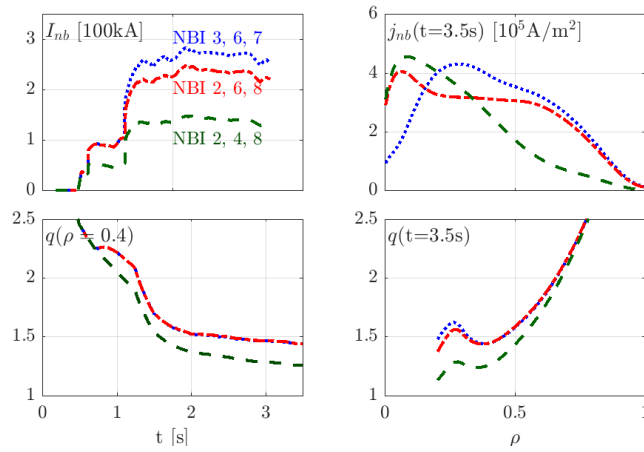


Figure C.2: Using the deposition profiles of individual neutral beams, as obtained from interpretative ASTRA-RABBIT simulations, RAPTOR simulations for different combinations of NBI sources can be run, testing the impact on the $q$ profile evolution.
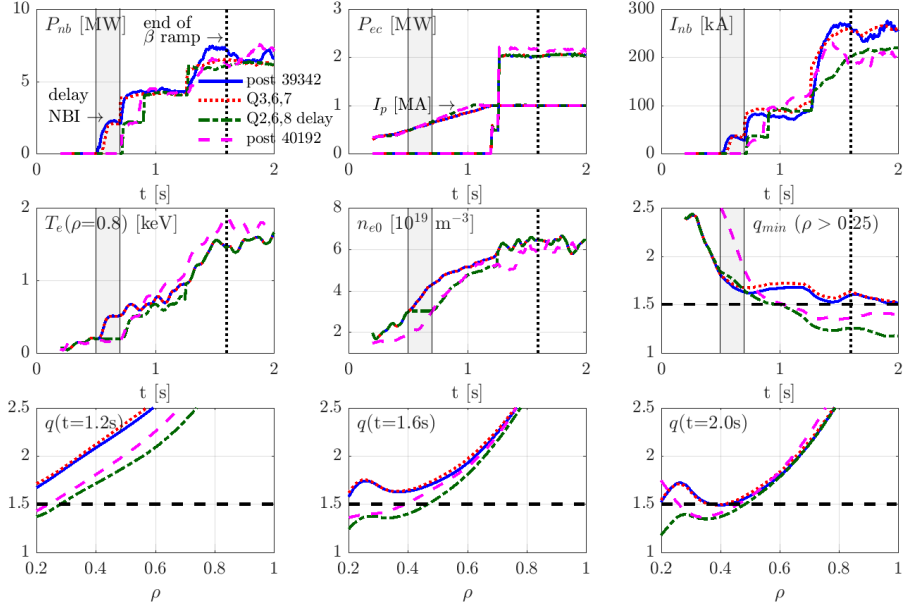
Figure C.3: The blue and red dashed traces illustrate how the post-shot simulation of discharge 39342 can successfully be recovered by summing the individual NBI source profiles from the active NBI sources. Furthermore, a delay of 200ms is proposed for the onset timing of the NBI, to avoid $q_{min}$ dropping through $q = 3/2$ at large radius and high $\beta_N$. The green dashed-dotted and magenta dashed traces illustrate how the RAPTOR pre-shot run successfully matches salient features of the post-shot simulation of the discharge with delayed NBI onset timing (40192).

the initial NBI set-up, as illustrated in Figure C.2. For comparison, we also simulate the impact in case of additional loss of NBI source 6, the source with the largest off-axis current drive. Note that the original set-up relies on source 6 from 0.7s onwards. Replacing this source by source 4, we can see that the impact of losing source 6 is much stronger compared to the loss of source 7. A strong reduction in the neutral beam driven current $I_{nb}$ leads to a significant drop in the $q$ profile. It is however interesting to note that even in this case a $q_{min} > 1.2$ seems feasible to maintain.

# D Overview of AUG ramp-down scenario data and simulations

To accompany the discussion of the ramp-down experiments presented in Chapter 6, an overview Table D.1 is presented, as well as a series of ramp-down traces ($I_p$, $\beta_{pol}$, heating traces, shaping traces, $T_e(\rho = 0.8)$ from IDA, gas flux and $I_{pol,SOL}$ to characterize the ELMs).

For those discharges that have been simulated in RAPTOR, on overview figure is shown to validate whether the post-discharge simulation with the gradient-based transport model leads to a good agreement with $T_e(\rho, t)$, $n_e(\rho, t)$, $q(\rho, t)$ and the internal inductance $\ell_{i3}(t)$, as inferred from experiment by IDA/IDE.

The figures for the individual discharges are presented in the same order as they are mentioned in Table D.1.

| Shot nr. (t_RD [s]) | IDE; IDA | $I_{p,flattop}$; $I_{p,final}$ [MA] | $I_p$ trace | $t_{HL}$ [s]; L-mode heating | remark shaping |
|---|---|---|---|---|---|
| **IBL** | | | | | |
| 40236 (3.7) | 1; 1 | 1.1; **0.5** | fast | 0.8; ohmic | attempt for constant shape |
| 40238 (3.7) | 1; 1 | 1.1; <0.1 | fast | 0.8; ohmic | keep $\kappa$, reduce $\delta$ |
| 40239 (3.7) | 1; 1 | 1.1; <0.1 | fast | 0.8; ohmic | keep $\delta$ reduce $\kappa$ |
| 40404 (3.7) | | 1.1; **0.50** | 0.8; fast | ohmic | |
| 40405 (3.7) | 2; 1 | 1.1; <0.1 | double | 1.4; ohmic | |
| 40631 (3.7) | 2; 3 | 1.1; <0.1 | double | 0.1; IC heated | |
| 40811 (3.7) | | 1.1; <0.1 | triple | 1.4; ohmic | |
| 40840 (5.2) | | 1.1; <0.1 | moderate | 1.5; ohmic | |
| 40844 (3.7) | 3; 2 | 1.1; <0.1 | triple | 0.4; IC heated | |
| 40848 (3.7) | 3; 2 | 1.1; <0.1 | triple | 0.4; ohmic | |
| 40851 (3.7) | | 1.1; <0.1 | triple | 0.4; NBI heated | |
| **HDL** | | | | | |
| 40750 (3.6) | 2; 3 | 0.8; <0.1 | fast | 0.5; ohmic L | gradual vol. reduction ($n_{el}$ rise) |
| 41388 (6.9) | 2; 3 | 0.8; <u>0.1</u> | fast | 0.5; ohmic L | rapid compression ($n_{el}$ rise) |

Table D.1: An overview is given of the ramp-down experiments discussed in Chapter 6. In this chapter, t=0s is redefined as the final time point of the flat-top phase, i.e. $t = t_{shot} - t_{RD}$. The final plasma current $I_{p,final}$ indicates whether the ramp-down was completed without disruption (<0.1), or whether a disruption ended the ramp-down prematurely, either due to radiative collapse (in **boldface**) or due to an MHD instability due to a strong decrease of $q_{95}$ (underlined). The $I_p$ ramp-down rate is indicated; *fast*: $d_{I_p}/dt \sim -660kA/s$; *moderate*: $d_{I_p}/dt \sim -320kA/s$; *double*: $d_{I_p}/dt \sim -660kA/s$ to $d_{I_p}/dt \sim -270kA/s$ at 0.5s; *triple*: $d_{I_p}/dt \sim -660kA/s$ to $d_{I_p}/dt \sim -270kA/s$ at 0.5s to $d_{I_p}/dt \sim -135kA/s$ at 2s. The timing for the HL transition is specified, as well as whether auxiliary heating is initially maintained during the L-mode phase. Finally, some remarks are given regarding the shaping evolution strategy.
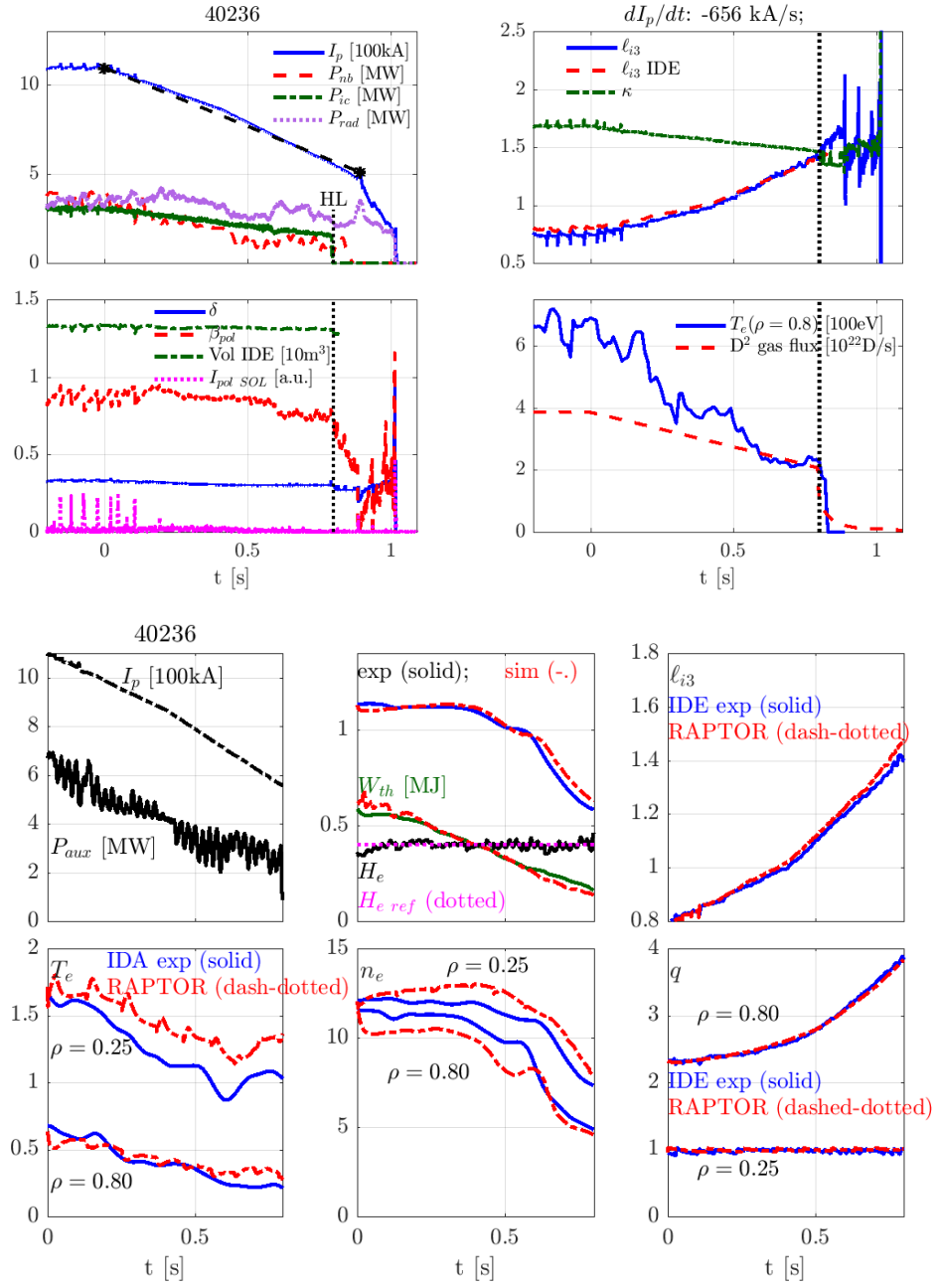
**40236**



Figure D.1: 40236: experimental traces and RAPTOR simulation.

**40238**
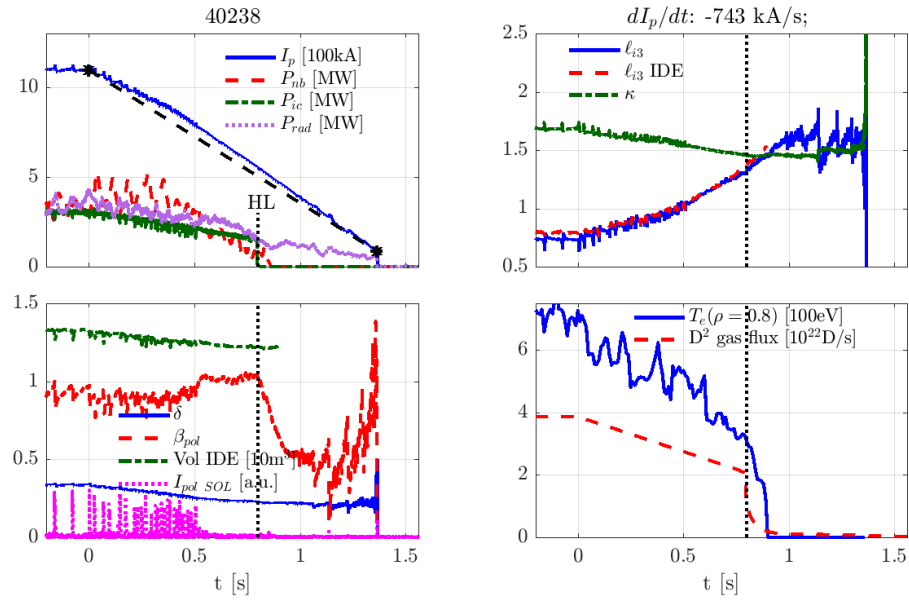


Figure D.2: 40238: experimental traces.
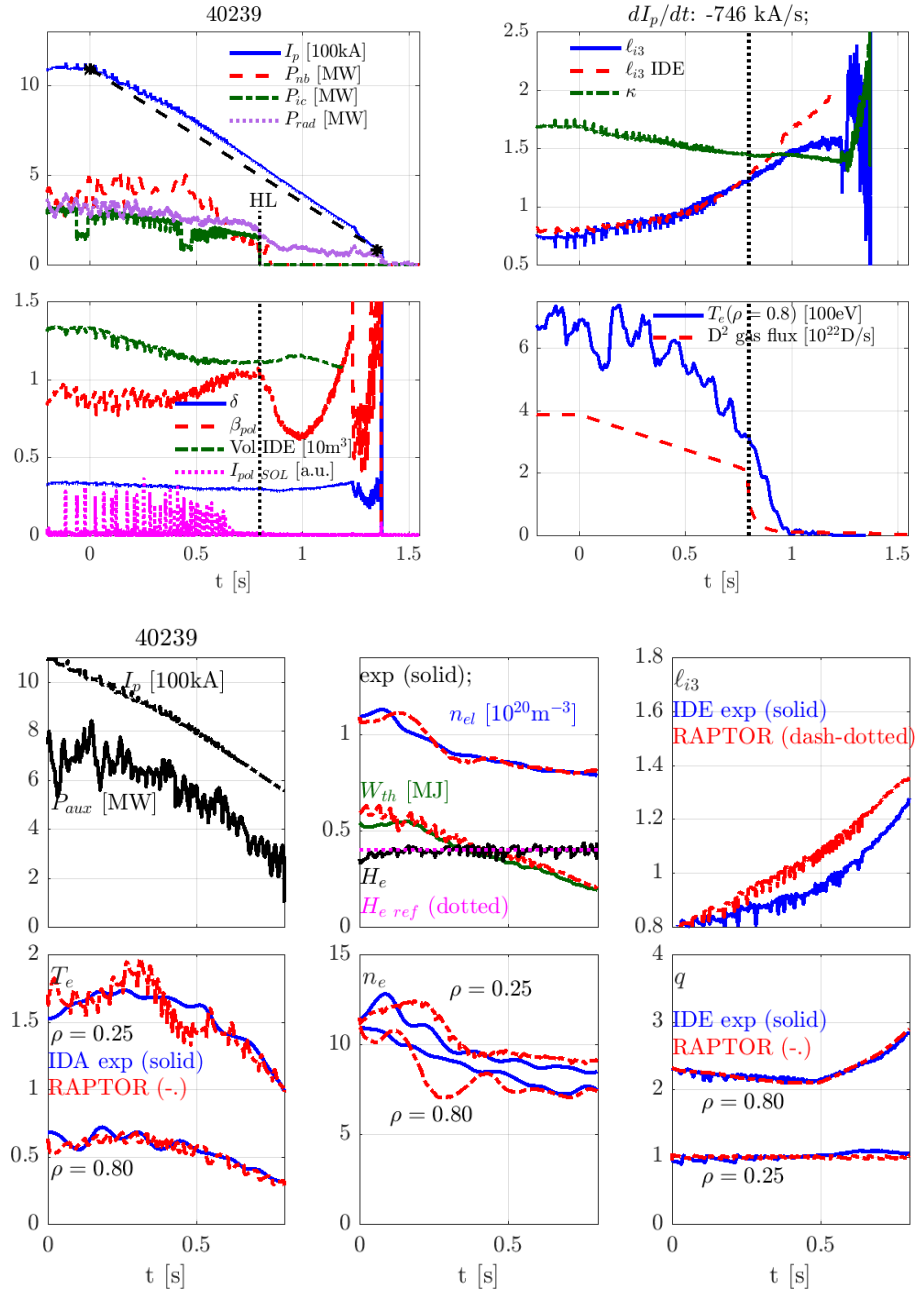
**40239**



Figure D.3: 40239: experimental traces and RAPTOR simulation; RAPTOR over-prediction $\ell_{i3}$ with respect to IDE.

**40404**
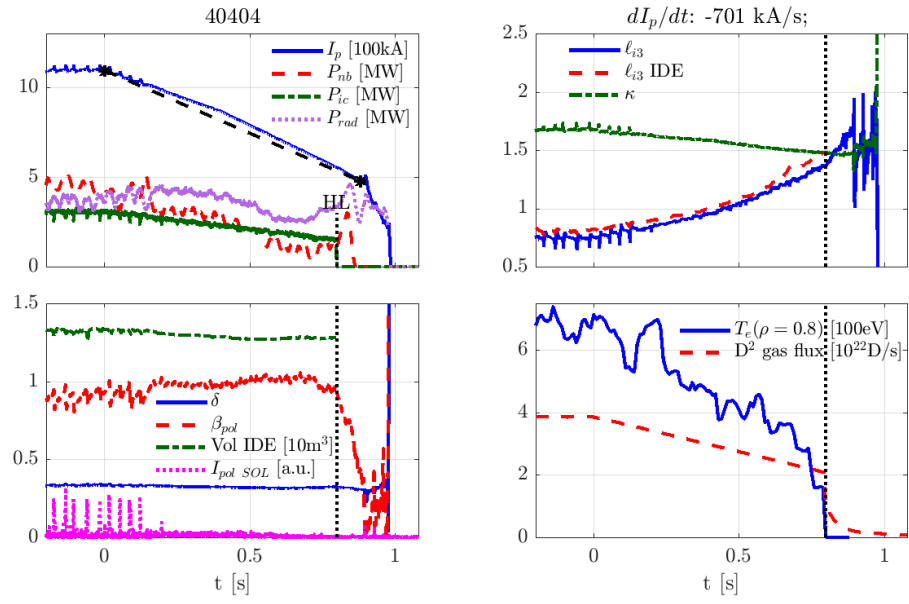


Figure D.4: 40404: experimental traces.
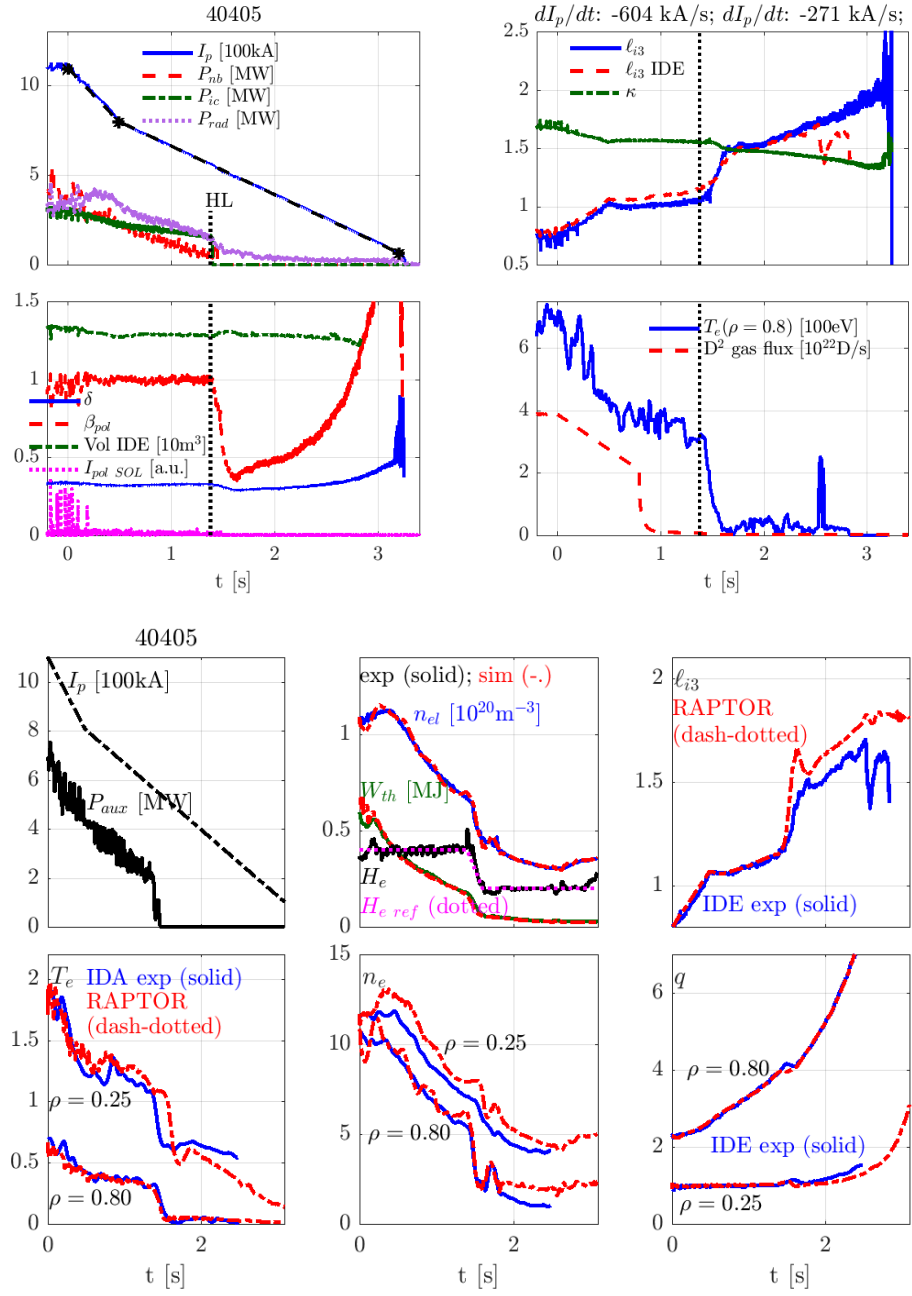
Figure D.5: 40405: experimental traces and RAPTOR simulation.

**40631**
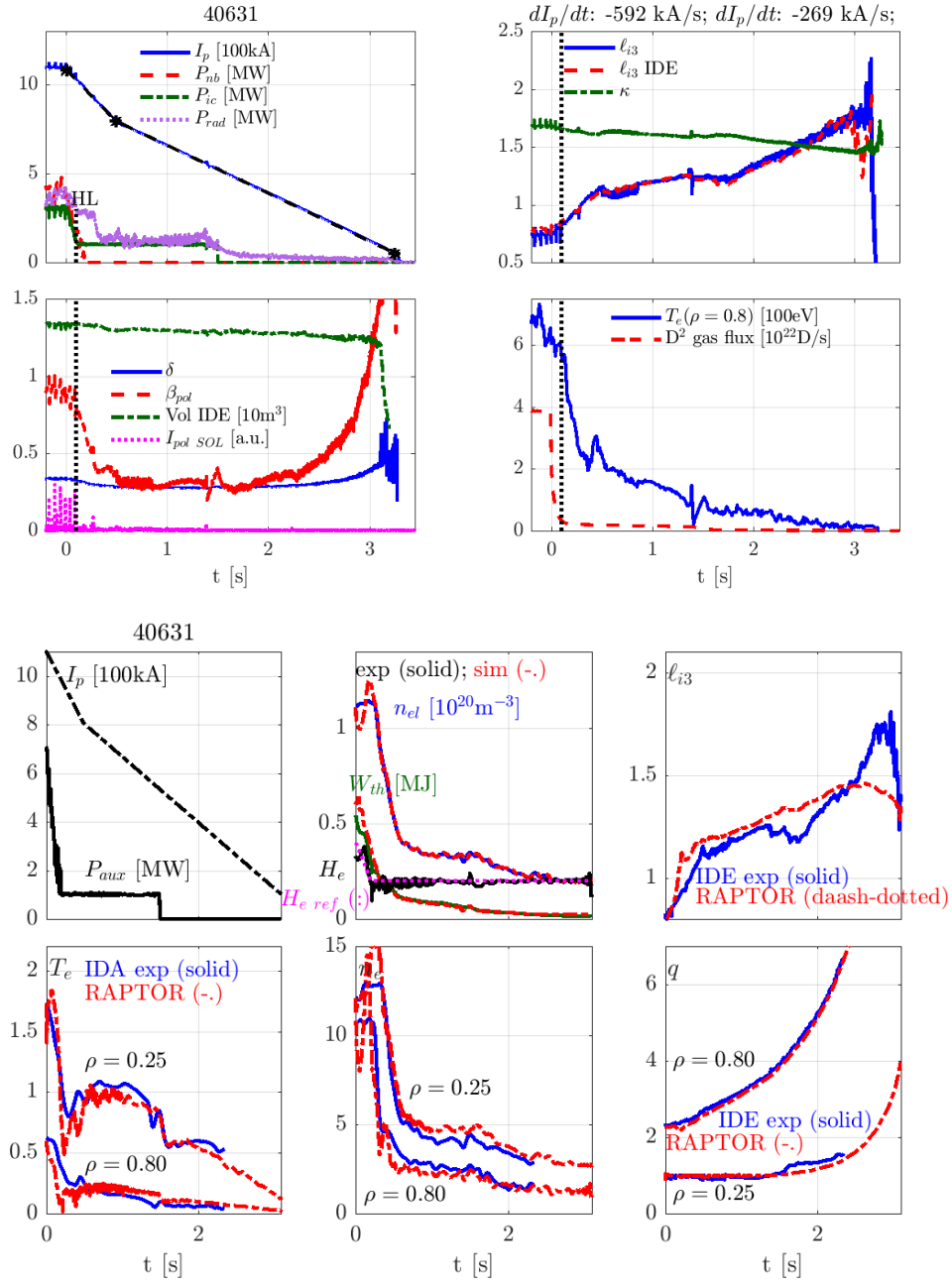


Figure D.6: 40631: experimental traces and RAPTOR simulation.

**40811**
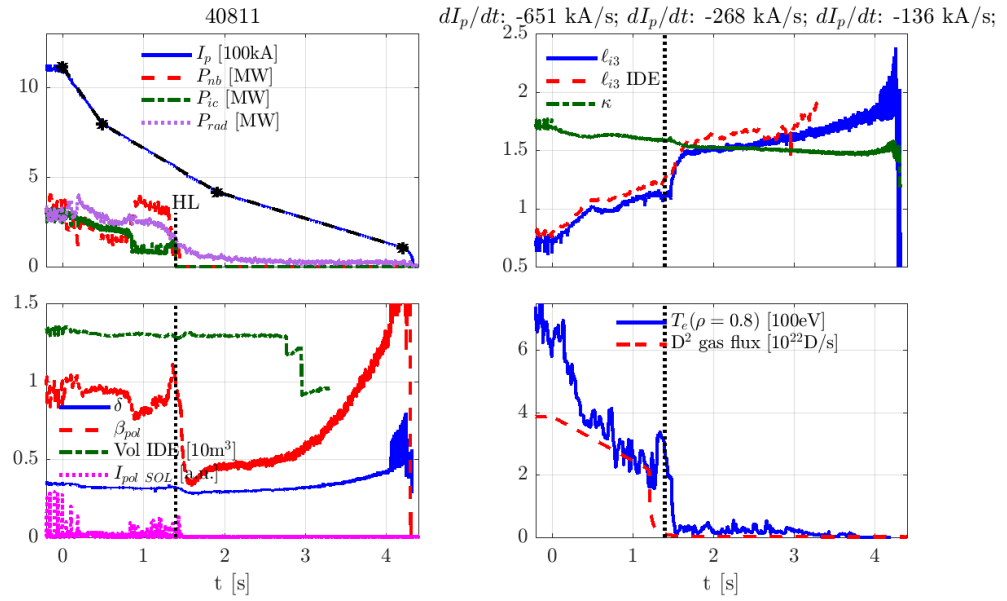


Figure D.7: 40811: experimental traces.

**40840**
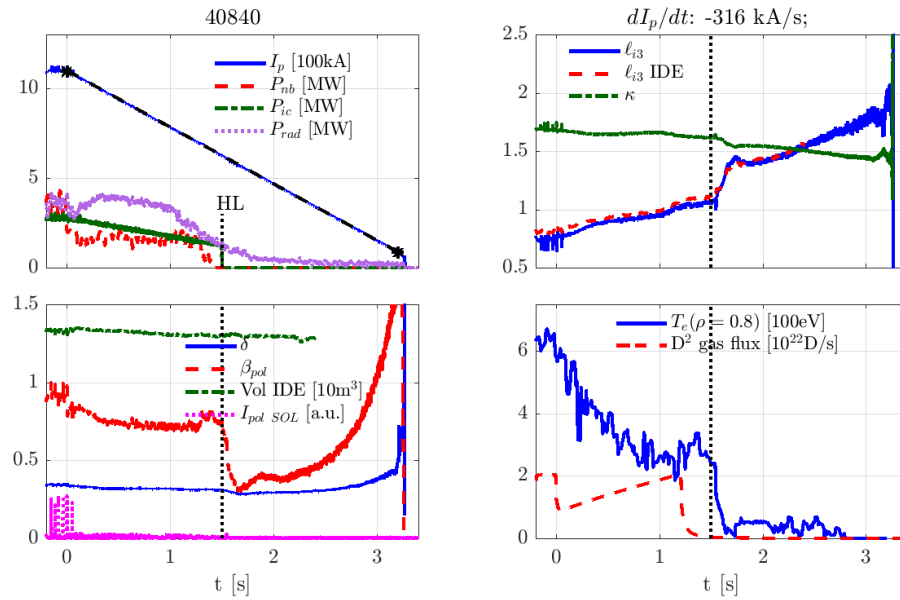


Figure D.8: 40840: experimental traces.

**40844**



Figure D.9: 40844: experimental traces and RAPTOR simulation.
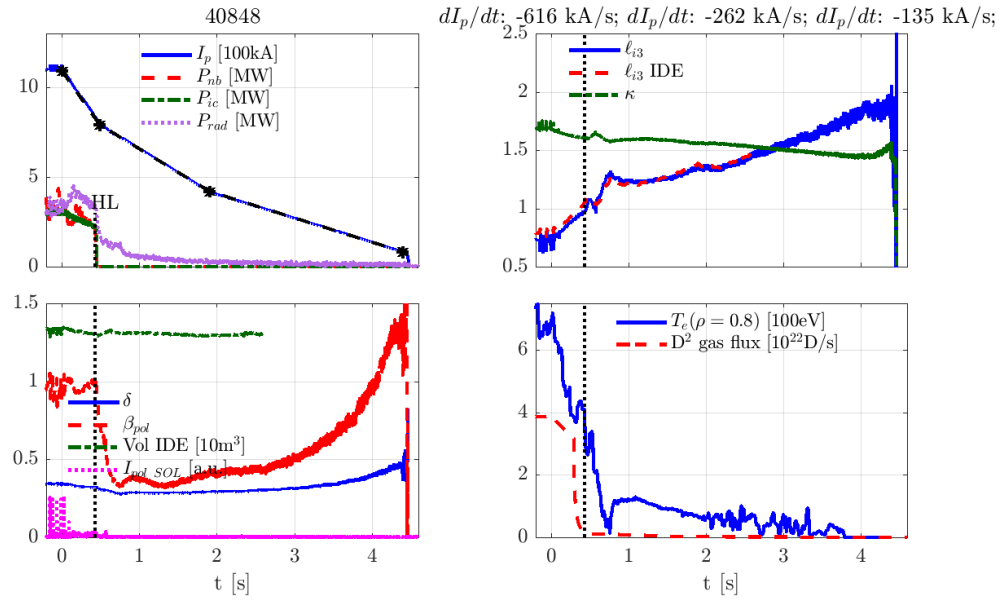
**40848**



Figure D.10: 40848: experimental traces.

**40851**
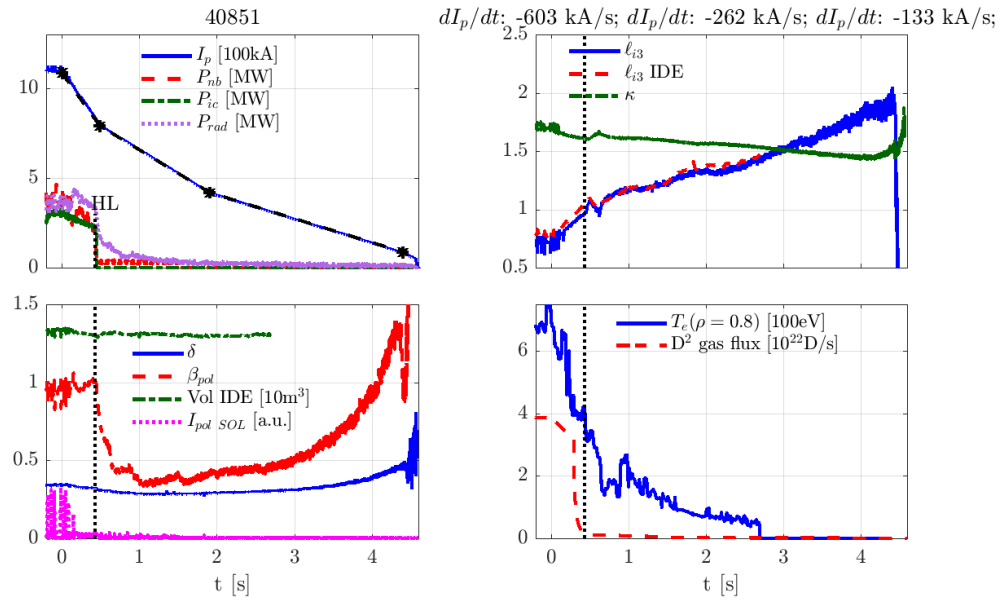


Figure D.11: 40851: experimental traces.

**40750**
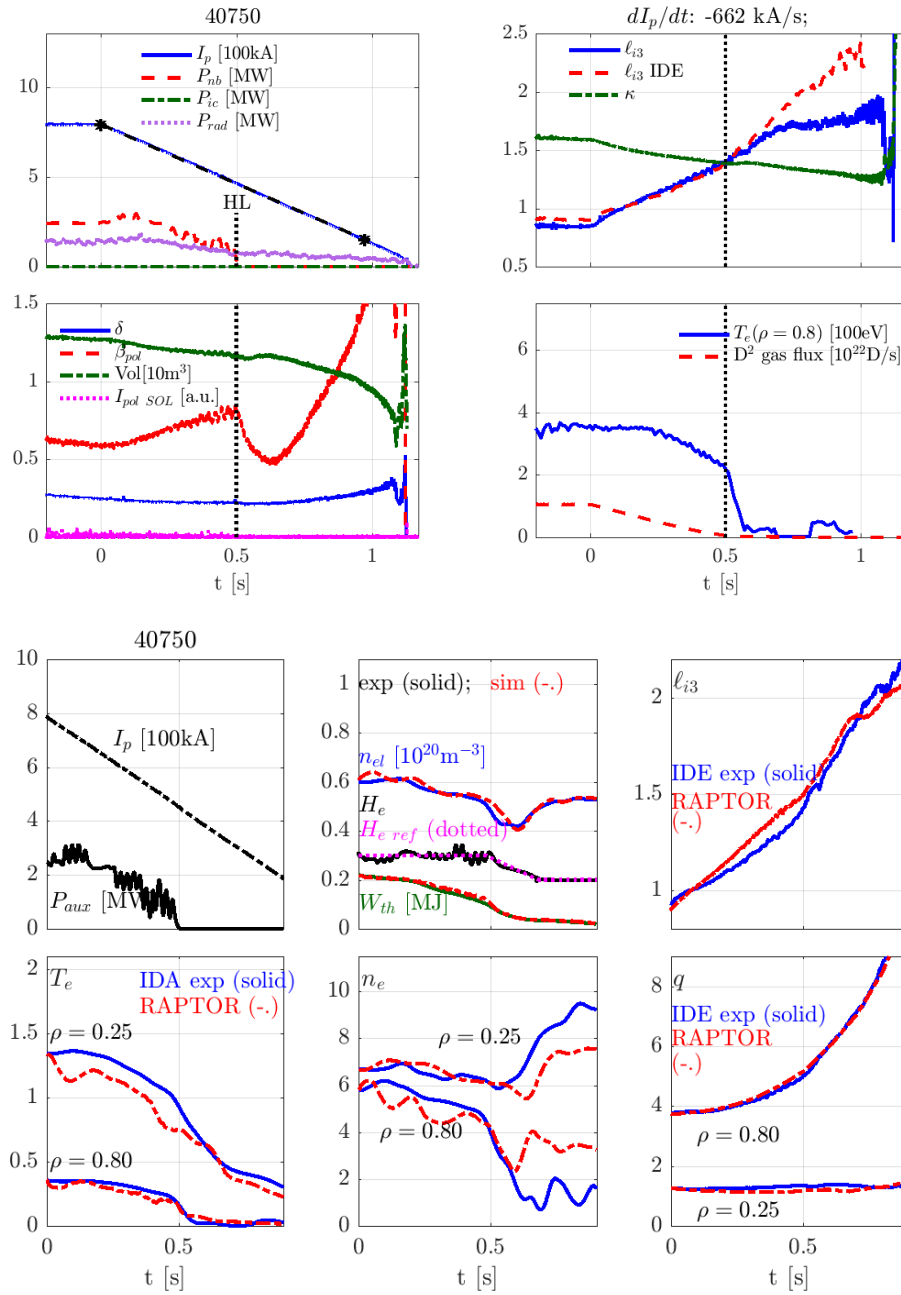


Figure D.12: 40750: experimental traces and RAPTOR simulation.
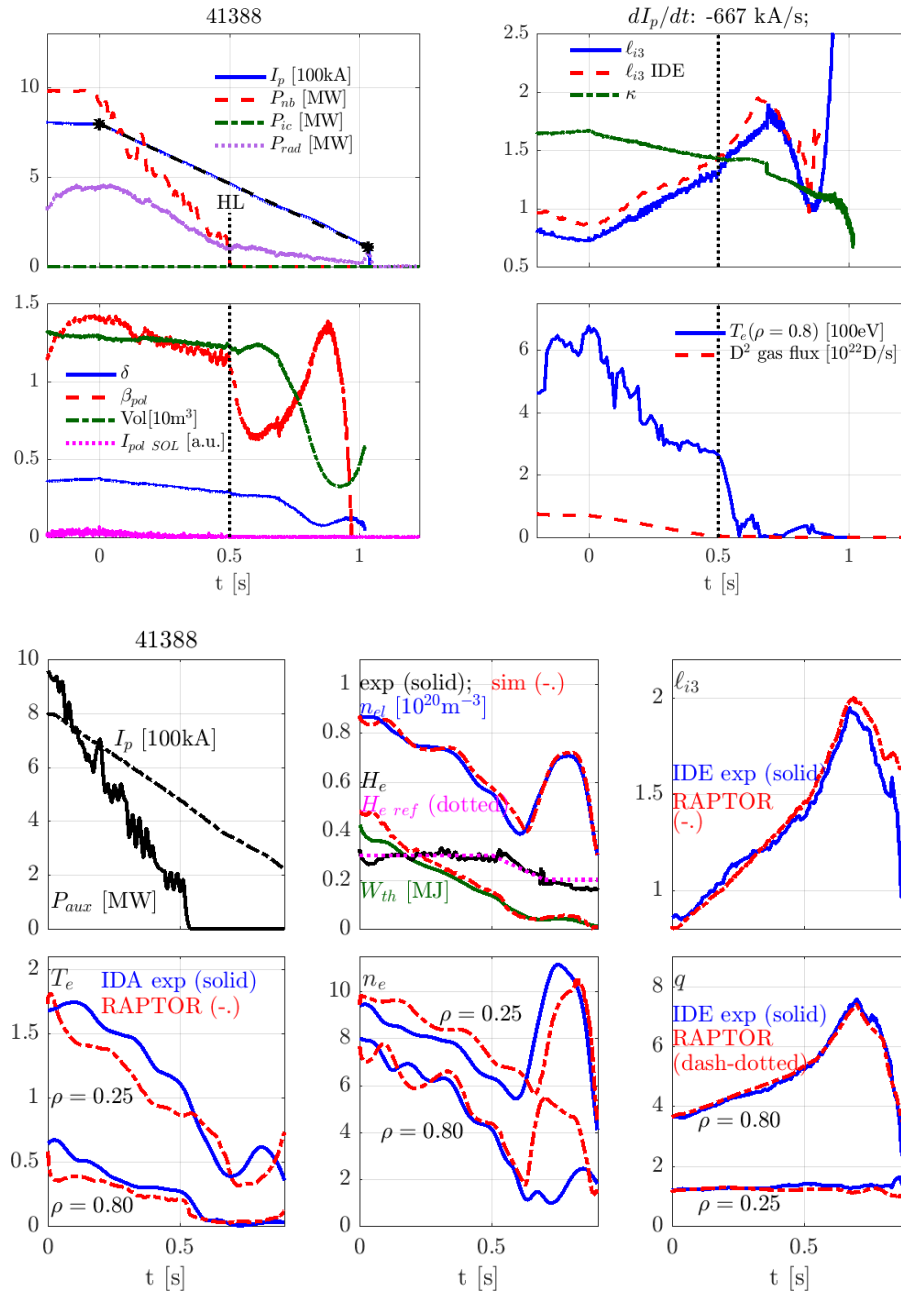
Figure D.13: 41388: experimental traces and RAPTOR simulation.

# Acknowledgements

When I started this journey in the Autumn of 2018, I could have never imagined the road ahead, full of unexpected twists and turns, like an Alpine mountain pass. I want to thank the many people accompanying and supporting me along the way.

Merci Olivier, for being my mentor, for your tireless optimism and for always being available for a chat. After our discussions I always felt enlightened by your intuition and excited about what to do next. Throughout some turbulent years, you have been a constant support, both on a personal and a scientific level.

Federico, thank you for always pushing me to learn new things, from clean coding to surfing. Your help has been essential to tame RAPTOR.

To everyone in the modeling and control group, it has been a pleasure to work during these years among such talented and warm-hearted people.

Cassandre, thank you for taking over this project with so much motivation. It is reassuring to leave while knowing that my work will be continued by someone as skillful as you.

The collaboration with IPP Garching has been a very rewarding experience. Jörg Stober, Alex Bock and Hartmut Zohm, thank you for giving me the opportunity to contribute to the ASDEX Upgrade advanced scenario program, to test modeling predictions in experiment, and for inviting me to a castle in the Bavarian Alps. I am grateful to Raphael Schramm for the regular discussions and exchange of simulations, to Thomas Puetterich and Bernhard Sieglin for helping me collect data on plasma ramp-down scenarios and to Ondřej Kudláček for involving me in the ion temperature ILC experiments early during my PhD.

I would like to thank Jonathan Citrin, Karel van de Plassche, Aaron Ho and Michele Marin (in his previous life as a PhD student) from the DIFFER team in Eindhoven for inviting me several times over and for introducing me to the fascinating world of turbulent transport and neural networks.

I would also like to express my gratitude towards the members of the thesis committee, Francis Casson, Jörg Stober and Olivier Février, for their helpful suggestions which improved the quality of this document.

The PhD started with me walking into an office with a Swiss, a Cameroonian and a Mexican. Baptiste, thank you for the great times, from going out in Lausanne to running through the streets of Rome. Arsène, you are an inspiration to all of us, brightening the institute with your passionate attitude. Guillermo, your patient explanations of basic plasma physics and MHD

have helped me through the first year. Then at some point a French guy arrived in the office: Jean, thanks for the great times we had at our first conference in Zürich, where we learned about giant planets, and for all the interesting coffee break conversations!

To my office mates in PPB210. Aylwin, thank you for coming everyday with a smile to work, for being a steadfast support and travel companion. Nico, you challenge every dull moment with your adventurous nature and give me fresh insights whenever I'm lost. Where are we going for our next office trip?

To the members of the cinéforum: Alessandro G, Antonia, Davide G, Davide M, Francesco R, Giovanni, Luke, Madeleine and Michele: I'm truly going to miss our weekly dinner+movie at Château Vallar.

Now, let's go alphabetically:

André, I will never forget our countless Alpine and Jurassic expeditions. You made me discover this beautiful country on two wheels and taught me that even the highest mountain passes can be climbed ... by bike ... through a storm ... in winter ...

Antoine B, thank you for introducing me into trail running and for the fun we had during the conference in Zürich (remember the horrendous Hotel California?)[1].

Antoine H, I was great to ride a Tour de France stage together (too bad the publicity caravan caught up with us ...).

Bigsteomitico (you were looking for the S right? ... idiot). Thank you for feeding me whenever I was working late in the lab to write this thesis. I'm still finishing the food you left at my place after your b-day party. Although you are stubborn and annoying, you are still a great friend.

Curdin, our discussions on sustainable energy, accompanied by your home-brewed beers, made me remember why our work matters. Twenty!

Federico P, thank you for the nights at No Name and the hikes in the Alps, soon you'll show me around in the Calanques.

Francesco P, I loved singing out loud together during our US road trip. Life is a highway! Continue to make RAPTOR fly and RAPDENS dance!!

Jesús, I really enjoyed the Spanish food you prepared (even though I almost froze to death). Be careful in the darkness of the basement of PPB!

Jia, thank you for the Christmas tree, I won't tell anyone where you stole the decoration (by the way, when are you picking it up?).

Lorenzo M, I am honored you introduced me into the sacred Italian art of making tiramisù.

Lorenzo S, thank you for waiting for me at the end of each descent.

Mateusz, Gran Maestro, I hope we can continue combining our skiing and cycling adventures with enjoying la bella vita.

Matteo, I'm grateful for the hikes, for the dinners at your Château and for your warmth as a friend, I'll think of you whenever I hear our song.

Mengdi, thank you for showing me the best line of sight to check on Olivier's office.

Mike, it was a lot of fun skiing together during my first day on the slopes, when we got away from the rest of the group.

---

[1] First I wrote: "thank you for not inviting me to your wedding", but then I removed it because it sounds a bit passive aggressive.

Reinart, I'm glad someone takes over the important role of 'Flemish person at SPC'.

Renat, thank you for making that spectacular Russian honey cake for Christmas. It was absolutely worth the six hours of preparation.

Samuele, mec, it was a pleasure to study together the convergence of the Giro d'Italia. See you soon in Aix-en-Provence!

Sophie, thank you for the after-party pasta that time when I fell asleep while standing.

To the other members of the SPC PhD/postdoc community: don't forget to organize your welcome apéro and enjoy the bbq-by-the-lake season that will start soon.

To my Antwerp friends. Lucas, our travels and periodical chats mean a lot to me. Raphaël and Vincent, I often remember the great times we had in the House in Leuven. Frederik, thank you for all the council you gave me over a beer in the Reynaert bar. David, Jurgen, Maxime, I cherish our decades-stretching friendships. Wouter, thank you for the memorable cycling adventures in Flanders and Switzerland.

Claudia, over these years you have been a source of strength and happiness for me. With you, everyday activities like cooking and going to the market become special. While my time in Switzerland has been full of beautiful surprises, meeting you has been the most fortunate event of all.

Mama en papa, none of this would have been possible without your unconditional love and support. This thesis is dedicated to you.

*Lausanne, March 29, 2023*                                                                 Simon

# Bibliography

[ADAS ] : *Atomic Data and Analysis Structure (ADAS).* www.adas.ac.uk/

[Albanese et al. 2015] ALBANESE, R. ; AMBROSINO, R. ; MATTEI, M.: CREATE-NL+: A robust control-oriented free boundary dynamic plasma equilibrium solver. In: *Fusion Engineering and Design* 96-97 (2015), 664–667. – URL https://www.sciencedirect.com/science/article/pii/S0920379615302167. – Proceedings of the 28th Symposium On Fusion Technology (SOFT-28). – ISSN 0920-3796

[Alfvén 1950] ALFVÉN, H: *Cosmical Electrodynamics.* Oxford: Claredon Press (UK), 1950

[Alonso et al. 2022] ALONSO, J.A. ; CALVO, I. ; CARRALERO, D. ; VELASCO, J.L. ; GARCIA-REGANA, J.M. ; PALERMO, I. ; RAPISARDA, D.: Physics design point of high-field stellarator reactors. In: *Nuclear Fusion* 62 (2022), feb, 3, 036024. – URL https://dx.doi.org/10.1088/1741-4326/ac49ac

[Angioni et al. 2003] ANGIONI, C ; PEETERS, A G. ; PEREVERZEV, G V. ; RYTER, F ; TARDINI, G: Density Peaking, Anomalous Pinch, and Collisionality in Tokamak Plasmas. In: *Physical Review Letters* 90 (2003), May, 205003. – URL https://link.aps.org/doi/10.1103/PhysRevLett.90.205003

[Angioni et al. 2023] ANGIONI, Clemente ; BONANOMI, Nicola ; FABLE, Emiliano ; SCHNEIDER, Philip A. ; TARDINI, Giovanni ; LUDA, Teobaldo ; STAEBLER, Gary M.: The dependence of tokamak L-mode confinement on magnetic field and plasma size, from a magnetic field scan experiment at ASDEX Upgrade to full-radius integrated modelling and fusion reactor predictions. In: *Nuclear Fusion* (2023). – URL http://iopscience.iop.org/article/10.1088/1741-4326/acc193

[Antonsen et al. 1996] ANTONSEN, T. M. ; DRAKE, J. F. ; GUZDAR, P. N. ; HASSAM, A. B. ; LAU, Y. T. ; LIU, C. S. ; NOVAKOVSKII, S. V.: Physical mechanism of enhanced stability from negative shear in tokamaks: Implications for edge transport and the L-H transition. In: *Physics of Plasmas* 3 (1996), 6, 2221–2223. – URL https://doi.org/10.1063/1.871928

[Artaud et al. 2018] ARTAUD, J F. ; IMBEAUX, F ; GARCIA, J ; GIRUZZI, G ; ANIEL, T ; BASIUK, V ; BÉCOULET, A ; BOURDELLE, C ; BURAVAND, Y ; DECKER, J ; DUMONT, R ; ERIKSSON, L G. ; GARBET, X ; GUIRLET, R ; HOANG, G T. ; HUYNH, P ; JOFFRIN, E ; LITAUDON, X ; MAGET, P ;

MOREAU, D ; NOUAILLETAS, R ; PÉGOURIÉ, B ; PEYSSON, Y ; SCHNEIDER, M ; URBAN, J: METIS: a fast integrated tokamak modelling tool for scenario design. In: *Nuclear Fusion* 58 (2018), 10, 105001. – URL https://doi.org/10.1088/1741-4326/aad5b1

[Artsimovich 1969] ARTSIMOVICH, L. A.: Summary on closed plasma systems. In: *Plasma Physics and Controlled Nuclear Fusion Research (Proc. 3rd Int. Conf. Novosibirsk, 1968)* (1969), 11

[Artsimovitch et al. 1964] ARTSIMOVITCH, L A. ; MIRNOV, S V. ; STRELKOV, V S.: Investigation of ohmic heating of the plasma in the "Tokamak-3" toroidal assembly. In: *Soviet Atomic Energy* 17 (1964), 886

[Atkinson and Houtermans 1929] ATKINSON, R. ; HOUTERMANS, F. G.: Transmutation of the Lighter Elements in Stars. In: *Nature* 123 (1929), 567–568

[Barr et al. 2021] BARR, J.L. ; SAMMULI, B. ; HUMPHREYS, D.A. ; OLOFSSON, E. ; DU, X.D. ; REA, C. ; WEHNER, W.P. ; BOYER, M.D. ; EIDIETIS, N.W. ; GRANETZ, R. ; HYATT, A. ; LIU, T. ; LOGAN, N.C. ; MUNARETTO, S. ; STRAIT, E. ; WANG, Z.R. et al.: Development and experimental qualification of novel disruption prevention techniques on DIII-D. In: *Nuclear Fusion* 61 (2021), oct, 12, 126019. – URL https://dx.doi.org/10.1088/1741-4326/ac2d56

[Barton et al. 2015] BARTON, J.E. ; BOYER, M.D. ; SHI, W. ; WEHNER, W.P. ; SCHUSTER, E. ; FERRON, J.R. ; WALKER, M.L. ; HUMPHREYS, D.A. ; LUCE, T.C. ; TURCO, F. ; PENAFLOR, B.G. ; JOHNSON, R.D.: Physics-model-based nonlinear actuator trajectory optimization and safety factor profile feedback control for advanced scenario development in DIII-D. In: *Nuclear Fusion* 55 (2015), jul, 9, 093005. – URL https://dx.doi.org/10.1088/0029-5515/55/9/093005

[Becker 1988] BECKER, G.: Empirical scaling laws for local transport in neutral beam heated plasmas. In: *Nuclear Fusion* 28 (1988), aug, 8, 1458. – URL https://dx.doi.org/10.1088/0029-5515/28/8/013

[Bickerton et al. 1971] BICKERTON, R. J. ; CONNOR, J. W. ; TAYLOR, J. B.: Diffusion Driven Plasma Currents and Bootstrap Tokamak. In: *Nature Physical Science* 229 (1971), 4, 110–112. – URL https://doi.org/10.1038/physci229110a0. ISBN 2058-1106

[Biglari et al. 1990] BIGLARI, H. ; DIAMOND, P. H. ; TERRY, P. W.: Influence of sheared poloidal rotation on edge turbulence. In: *Physics of Fluids B: Plasma Physics* 2 (1990), 1, 1–4. – URL https://doi.org/10.1063/1.859529

[Bizarro et al. 2016] BIZARRO, Joao P S. ; KOECHL, Florian ; VOITSEKHOVITCH, Irina et al.: Modelling the Ohmic L-mode ramp-down phase of JET hybrid pulses using JETTO with Bohm-gyro-Bohm transport. In: *Plasma Physics and Controlled Fusion* 58 (2016), sep, 10, 105010. – URL https://dx.doi.org/10.1088/0741-3335/58/10/105010

[Blum et al. 2019] BLUM, Jacques ; HEUMANN, Holger ; NARDON, Eric ; SONG, Xiao: Automating the design of tokamak experiment scenarios. In: *Journal of Computational*

*Physics* 394 (2019), 594–614. – URL https://www.sciencedirect.com/science/article/pii/S0021999119303985. – ISSN 0021-9991

[Bock et al. 2021]    BOCK, A ; BURCKHART, A ; DUNNE, M ; FISCHER, R ; KREBS, I ; REISNER, M ; SILVAGNI, D ; STOBER, J ; PÜTTERICH, T et al.: Non-Inductive High-beta H-Modes in Full-Tungsten ASDEX Upgrade. In: *47th European Physical Society Conference on Plasma Physics*, 2021

[Bock et al. 2018]    BOCK, A. ; DOERK, H. ; FISCHER, R. ; RITTICH, D. ; STOBER, J. ; BURCKHART, A. ; FABLE, E. ; GEIGER, B. ; MLYNEK, A. ; REICH, M. ; ZOHM, H.: Advanced tokamak investigations in full-tungsten ASDEX Upgrade. In: *Physics of Plasmas* 25 (2018), 5, 056115. – URL https://doi.org/10.1063/1.5024320

[Bock et al. 2017]    BOCK, A. ; FABLE, E. ; FISCHER, R. ; REICH, M. ; RITTICH, D. ; STOBER, J. ; BERNERT, M. ; BURCKHART, A. ; DOERK, H. ; DUNNE, M. ; GEIGER, B. ; GIANNONE, L. ; IGOCHINE, V. ; KAPPATOU, A. ; MCDERMOTT, R. ; MLYNEK, A. ; ODSTRCIL, T. ; TARDINI, G. ; ZOHM, H. et al.: Non-inductive improved H-mode operation at ASDEX Upgrade. In: *Nuclear Fusion* 57 (2017), oct, 12, 126041. – URL https://dx.doi.org/10.1088/1741-4326/aa8967

[Bottino et al. 2006]    BOTTINO, A ; SAUTER, O ; CAMENEN, Y ; FABLE, E: Linear stability analysis of microinstabilities in electron internal transport barrier non-inductive discharges. In: *Plasma Physics and Controlled Fusion* 48 (2006), jan, 2, 215. – URL https://dx.doi.org/10.1088/0741-3335/48/2/004

[Bourdelle et al. 2015]    BOURDELLE, C ; CITRIN, J ; BAIOCCHI, B ; CASATI, A ; COTTIER, P ; GARBET, X ; IMBEAUX, F: Core turbulent transport in tokamak plasmas: bridging theory and experiment with QuaLiKiz. In: *Plasma Physics and Controlled Fusion* 58 (2015), 1, 014036. – URL https://doi.org/10.1088/0741-3335/58/1/014036

[Brunetti et al. 2014]    BRUNETTI, D ; GRAVES, J P. ; COOPER, W A. ; WAHLBERG, C: Fast growing resistive two fluid instabilities in hybrid-like tokamak configuration. In: *Plasma Physics and Controlled Fusion* 56 (2014), jun, 7, 075025. – URL https://dx.doi.org/10.1088/0741-3335/56/7/075025

[Burrell et al. 1992]    BURRELL, K H. ; CARLSTROM, T N. ; DOYLE, E J. ; FINKENTHAL, D ; GOHIL, P ; GROEBNER, R J. ; HILLIS, D L. ; KIM, J ; MATSUMOTO, H ; MOYER, R A. ; OSBORNE, T H. ; RETTIG, C L. ; PEEBLES, W A. ; RHODES, T L. ; STJOHN, H ; STAMBAUGH, R D. ; WADE, M R. ; WATKINS, J G.: Physics of the L-mode to H-mode transition in tokamaks. In: *Plasma Physics and Controlled Fusion* 34 (1992), dec, 13, 1859. – URL https://dx.doi.org/10.1088/0741-3335/34/13/014

[Cacuci 1981]    CACUCI, D. G.: Sensitivity theory for nonlinear systems. I. Nonlinear functional analysis approach. In: *Journal of Mathematical Physics* 22 (1981), 12, 2794–2802. – URL https://doi.org/10.1063/1.525186

# Bibliography

[Camenen et al. 2007]   CAMENEN, Y. ; POCHELON, A. ; BEHN, R. ; BOTTINO, A. ; BORTOLON, A. ; CODA, S. ; KARPUSHOV, A. ; SAUTER, O. ; ZHUANG, G. et al.: Impact of plasma triangularity and collisionality on electron heat transport in TCV L-mode plasmas. In: *Nuclear Fusion* 47 (2007), jun, 7, 510. – URL https://dx.doi.org/10.1088/0029-5515/47/7/002

[Canal et al. 2013]   CANAL, G.P. ; DUVAL, B.P. ; FELICI, F. ; GOODMAN, T.P. ; GRAVES, J.P. ; POCHELON, A. ; REIMERDES, H. ; SAUTER, O. ; TESTA, D. et al.: Fast seeding of NTMs by sawtooth crashes in TCV and their preemption using ECRH. In: *Nuclear Fusion* 53 (2013), sep, 11, 113026. – URL https://dx.doi.org/10.1088/0029-5515/53/11/113026

[Candy et al. 2009]   CANDY, J ; HOLLAND, C ; WALTZ, R E. ; FAHEY, M R. ; BELLI, E: Tokamak profile prediction using direct gyrokinetic and neoclassical simulation. In: *Physics of Plasmas* 16 (2009), 6, 060704. – URL https://doi.org/10.1063/1.3167820

[Carpanese et al. 2020]   CARPANESE, F. ; FELICI, F. ; GALPERTI, C. ; MERLE, A. ; MORET, J.M. ; SAUTER, O. et al.: First demonstration of real-time kinetic equilibrium reconstruction on TCV by coupling LIUQE and RAPTOR. In: *Nuclear Fusion* 60 (2020), may, 6, 066020. – URL https://dx.doi.org/10.1088/1741-4326/ab81ac

[Carpanese 2021]   CARPANESE, Francesco: *PhD thesis no. 7914 Development of free-boundary equilibrium and transport solvers for simulation and real-time interpretation of tokamak experiments.* École Polytechnique Fédérale de Lausanne (EPFL), CH-1015 Lausanne, Switzerland, 2021. – URL http://infoscience.epfl.ch/record/283775

[Cenacchi and Taroni 1988]   CENACCHI, G ; TARONI, A: Jetto a free boundary plasma transport code. In: *ENEA-RT-TIB–88-5* (1988)

[Challis et al. 1989]   CHALLIS, C D. ; CORDEY, J G. ; HAMNÉN, H ; STUBBERFIELD, P M. ; CHRISTIANSEN, J P. ; LAZZARO, E ; MUIR, D G. ; STORK, D ; THOMPSON, E: Non-inductively driven currents in JET. In: *Nuclear Fusion* 29 (1989), 4, 563–570. – URL https://doi.org/10.1088/0029-5515/29/4/002

[Chang and Callen 1990]   CHANG, Z. ; CALLEN, J.D.: Global energy confinement degradation due to macroscopic phenomena in tokamaks. In: *Nuclear Fusion* 30 (1990), feb, 2, 219. – URL https://dx.doi.org/10.1088/0029-5515/30/2/003

[Citrin et al. 2010]   CITRIN, J ; ARTAUD, J-F ; GARCIA, J ; HOGEWEIJ, G M D. ; IMBEAUX, F: Impact of heating and current drive mix on the ITER hybrid scenario. In: *Nuclear Fusion* 50 (2010), 11, 115007. – URL https://doi.org/10.1088/0029-5515/50/11/115007

[Citrin et al. 2017]   CITRIN, J ; BOURDELLE, C ; CASSON, F J. ; ANGIONI, C ; BONANOMI, N ; CAMENEN, Y ; GARBET, X ; GARZOTTI, L ; GÖRLER, T ; GÜRCAN, O ; KOECHL, F ; IMBEAUX, F ; LINDER, O ; VAN DE PLASSCHE, K ; STRAND, P ; SZEPESI, G: Tractable flux-driven temperature, density, and rotation profile evolution with the quasilinear gyrokinetic transport model QuaLiKiz. In: *Plasma Physics and Controlled Fusion* 59 (2017), 12, 124005. – URL https://doi.org/10.1088/1361-6587/aa8aeb

[Citrin et al. 2015]   CITRIN, J ; BRETON, S ; FELICI, F ; IMBEAUX, F ; ANIEL, T ; ARTAUD, J F. ; BAIOCCHI, B ; BOURDELLE, C ; CAMENEN, Y ; GARCIA, J: Real-time capable first principle based modelling of tokamak turbulent transport. In: *Nuclear Fusion* 55 (2015), 9, 092001. – URL https://doi.org/10.1088/0029-5515/55/9/092001

[Citrin et al. 2014]   CITRIN, J ; GARCIA, J ; GOERLER, T ; JENKO, F ; MANTICA, P ; TOLD, D ; BOURDELLE, C ; HATCH, D R. ; HOGEWEIJ, G M D. ; JOHNSON, T ; PUESCHEL, M J. ; SCHNEIDER, M: Electromagnetic stabilization of tokamak microturbulence in a high-$\beta$ regime. In: *Plasma Physics and Controlled Fusion* 57 (2014), 1, 014032. – URL https://doi.org/10.1088/0741-3335/57/1/014032

[Citrin et al. 2012]   CITRIN, J ; HOBIRK, J ; SCHNEIDER, M ; ARTAUD, J F. ; BOURDELLE, C ; CROMBE, K ; HOGEWEIJ, G M D. ; IMBEAUX, F ; JOFFRIN, E ; KOECHL, F ; STOBER, J: Predictive analysis of q-profile influence on transport in JET and ASDEX Upgrade hybrid scenarios. In: *Plasma Physics and Controlled Fusion* 54 (2012), may, 6, 065008. – URL https://doi.org/10.1088/0741-3335/54/6/065008

[Citrin and Mantica 2022]   CITRIN, Jonathan ; MANTICA, Paola: Overview of tokamak turbulence stabilization by fast ions. In: *Plasma Physics and Controlled Fusion* (2022). – URL http://iopscience.iop.org/article/10.1088/1361-6587/acab2b

[Clery 2013]   CLERY, D: *A piece of the Sun.* Overlook Duckworth, Peter Mayer Publishers, Inc., 2013

[Coda et al. 2000]   CODA, S ; GOODMAN, T P. ; HENDERSON, M A. ; HOFMANN, F ; PIETRZYK, Z A. ; SAUTER, O et al.: High-power ECH and fully non-inductive operation with ECCD in the TCV tokamak. In: *Plasma Physics and Controlled Fusion* 42 (2000), 12B, B311–B321. – URL https://doi.org/10.1088/0741-3335/42/12B/323

[Coppi 1980]   COPPI, B.: Comments on Plasma Physics and Controlled Fusion. In: *Nuclear Fusion* 5 (1980), mar, 6, 261–269. – URL https://dx.doi.org/10.1088/1741-4326/ac1654

[Coppi et al. 1980]   COPPI, B. ; FERREIRA, A. ; RAMOS, J. J.: Self-Healing of Confined Plasmas with Finite Pressure. In: *Phys. Rev. Lett.* 44 (1980), Apr, 990–993. – URL https://link.aps.org/doi/10.1103/PhysRevLett.44.990

[de Blank and Krebs 2022]   DE BLANK, H.J. ; KREBS, I.: Analytic model of $m = 1$ magnetic flux pumping. In: *Poster at the Joint Varenna-Lausanne Int. Workshop on Theory of Fusion Plasmas, Varenna, Italy, September, 2022,* 2022, P. 18

[de Vries et al. 2009]   DE VRIES, P.C. ; JOFFRIN, E. ; BRIX, M. ; CHALLIS, C.D. ; CROMBE, K. ; ESPOSITO, B. ; HAWKES, N.C. ; GIROUD, C. ; HOBIRK, J. ; LOENNROTH, J. ; MANTICA, P. ; STRINTZI, D. ; TALA, T. ; VOITSEKHOVITCH, I. et al.: Internal transport barrier dynamics with plasma rotation in JET. In: *Nuclear Fusion* 49 (2009), may, 7, 075007. – URL https://dx.doi.org/10.1088/0029-5515/49/7/075007

## Bibliography

[de Vries et al. 2017]    DE VRIES, P.C. ; LUCE, T.C. ; BAE, Y.S. ; GERHARDT, S. ; GONG, X. ; GRIBOV, Y. ; HUMPHREYS, D. ; KAVIN, A. ; KHAYRUTDINOV, R.R. ; KESSEL, C. ; KIM, S.H. ; LOARTE, A. ; LUKASH, V.E. ; LUNA, E. de la ; NUNES, I. ; POLI, F. ; QIAN, J. ; REINKE, M. ; SAUTER, O. ; SIPS, A.C.C. ; SNIPES, J.A. ; STOBER, J. ; TREUTTERER, W. ; TEPLUKHINA, A.A. ; VOITSEKHOVITCH, I. ; WOO, M.H. ; WOLFE, S. ; ZABEO, L. et al.: Multi-machine analysis of termination scenarios with comparison to simulations of controlled shutdown of ITER discharges. In: *Nuclear Fusion* 58 (2017), dec, 2, 026019. – URL https://dx.doi.org/10.1088/1741-4326/aa9c4c

[Debye and Hückel 1923]    DEBYE, P ; HÜCKEL, E: The theory of electrolytes I. The lowering of the freezing point and related occurrences. In: *Physikalische Zeitschrift* 24 (1923), 185–206

[Del Nevo 2018]    DEL NEVO, A: *Direct Coupling of WCLL BB PHTS to PCS feasibility study - Preliminary PCS design with an internal source of energy to operate at a minimum load the steam turbine and the power cycle in dwell.* Eurofusion, 2018. – URL http://idm.euro-fusion.org/?uid=2MN55V

[Dnestrovski and Kostomarov 1969]    DNESTROVSKI, Y. N. ; KOSTOMAROV, D. P.: In: *International Conference on Plasma Confinement in Closed Systems, Dubna, 1969, Abstracts of Contributed Papers, Moscow* (1969), 41

[Doyle et al. 2007]    DOYLE, E.J. ; HOULBERG, W.A. ; KAMADA, Y. ; MUKHOVATOV, V. ; OSBORNE, T.H. ; POLEVOI, A. ; BATEMAN, G. ; CONNOR, J.W. ; CORDEY, J.G. ; FUJITA, T. ; GARBET, X. ; HAHM, T.S. ; HORTON, L.D. ; HUBBARD, A.E. ; IMBEAUX, F. ; JENKO, F. ; KINSEY, J.E. ; KISHIMOTO, Y. ; LI, J. ; LUCE, T.C. ; MARTIN, Y. ; OSSIPENKO, M. ; PARAIL, V. ; PEETERS, A. ; RHODES, T.L. ; RICE, J.E. ; ROACH, C.M. ; ROZHANSKY, V. ; RYTER, F. ; SAIBENE, G. ; SARTORI, R. ; SIPS, A.C.C. ; SNIPES, J.A. ; SUGIHARA, M. ; SYNAKOWSKI, E.J. ; TAKENAGA, H. ; TAKIZUKA, T. ; THOMSEN, K. ; WADE, M.R. ; WILSON, H.R. ; ITPA TRANSPORT PHYSICS TOPICAL GROUP ; ITPA CONFINEMENT DATABASE AND MODELLING TOPICAL GROUP ; ITPA PEDESTAL AND EDGE TOPICAL GROUP: Chapter 2: Plasma confinement and transport. In: *Nuclear Fusion* 47 (2007), jun, 6, S18. – URL https://dx.doi.org/10.1088/0029-5515/47/6/S02

[Dumont and Zarzoso 2012]    DUMONT, R J. ; ZARZOSO, D: Heating and current drive by ion cyclotron waves in the activated phase of ITER. In: *Nuclear Fusion* 53 (2012), dec, 1, 013002. – URL https://doi.org/10.1088/0029-5515/53/1/013002

[Eddington 1920]    EDDINGTON, A. S.: The Internal Constitution of the Stars. In: *Nature* 106 (1920), 14–20

[Eich et al. 2018]    EICH, T ; GOLDSTON, R J. ; KALLENBACH, A ; SIEGLIN, B ; SUN, H J.: Correlation of the tokamak H-mode density limit with ballooning stability at the separatrix. In: *Nuclear Fusion* 58 (2018), jan, 3, 034001. – URL https://doi.org/10.1088/1741-4326/aaa340

[Ellis et al. 2018]    ELLIS, K V. ; LUX, H ; FABLE, E ; KEMBLETON, R ; SICCINIO, M.: The next step in systems modelling: The integration of a simple 1D transport and equilibrium solver. In: *EPS Conference, Prague (2018)* (2018)

[Erba et al. 1998]   ERBA, M. ; ANIEL, T. ; BASIUK, V. ; BECOULET, A. ; LITAUDON, X.: Validation of a new mixed Bohm/gyro-Bohm model for electron and ion heat transport against the ITER, Tore Supra and START database discharges. In: *Nuclear Fusion* 38 (1998), jul, 7, 1013. – URL https://dx.doi.org/10.1088/0029-5515/38/7/305

[Eriksson et al. 2004]   ERIKSSON, L.-G. ; MUECK, A. ; SAUTER, O. ; CODA, S. ; MANTSINEN, M. J. ; MAYORAL, M.-L. ; WESTERHOF, E. ; BUTTERY, R. J. ; MCDONALD, D. ; JOHNSON, T. ; NOTERDAEME, J.-M. ; DE VRIES, P.: Destabilization of Fast-Ion-Induced Long Sawteeth by Localized Current Drive in the JET Tokamak. In: *Phys. Rev. Lett.* 92 (2004), Jun, 235004. – URL https://link.aps.org/doi/10.1103/PhysRevLett.92.235004

[Fable et al. 2019]   FABLE, E ; ANGIONI, C ; BOBKOV, V ; STOBER, J ; BILATO, R ; CONWAY, G D. ; GOERLER, T ; MCDERMOTT, R M. ; PUETTERICH, T ; SICCINIO, M ; SUTTROP, W ; TESCHKE, M ; ZOHM, H: The role of the source versus the collisionality in predicting a reactor density profile as observed on ASDEX Upgrade discharges. In: *Nuclear Fusion* 59 (2019), 7, 076042. – URL https://doi.org/10.1088/1741-4326/ab1f28

[Fable et al. 2013]   FABLE, E ; ANGIONI, C ; CASSON, F J. ; TOLD, D ; IVANOV, A A. ; JENKO, F ; MCDERMOTT, R M. ; MEDVEDEV, S Y. ; PEREVERZEV, G V. ; RYTER, F ; TREUTTERER, W ; VIEZZER, E et al.: Novel free-boundary equilibrium and transport solver with theory-based models and its validation against ASDEX Upgrade current ramp scenarios. In: *Plasma Physics and Controlled Fusion* 55 (2013), nov, 12, 124028. – URL https://dx.doi.org/10.1088/0741-3335/55/12/124028

[Fable et al. 2009]   FABLE, E ; ANGIONI, C ; SAUTER, O: The role of ion and electron electrostatic turbulence in characterizing stationary particle transport in the core of tokamak plasmas. In: *Plasma Physics and Controlled Fusion* 52 (2009), dec, 1, 015007. – URL https://doi.org/10.1088/0741-3335/52/1/015007

[Fable et al. 2018]   FABLE, E ; ANGIONI, C ; SICCINIO, M ; ZOHM, H: Plasma physics for fusion reactor system codes: Framework and model code. In: *Fusion Engineering and Design* 130 (2018), 131–136. – URL https://www.sciencedirect.com/science/article/pii/S0920379618302801

[Fable et al. 2022]   FABLE, E ; JANKY, F ; TREUTTERER, W ; ENGLBERGER, M ; SCHRAMM, R ; MURACA, M ; ANGIONI, C ; KUDLACEK, O ; POLI, E ; REICH, M ; SICCINIO, M ; TARDINI, G ; WEILAND, M ; WU, C ; ZOHM, H et al.: The modeling of a tokamak plasma discharge, from first principles to a flight simulator. In: *Plasma Physics and Controlled Fusion* 64 (2022), feb, 4, 044002. – URL https://dx.doi.org/10.1088/1361-6587/ac466b

[Fajardo et al. 2023]   FAJARDO, Daniel ; ANGIONI, Clemente ; CASSON, Francis J. ; FIELD, Anthony R. ; MAGET, Patrick ; MANAS, Pierre: Analytical model for the combined effects of rotation and collisionality on neoclassical impurity transport. In: *Plasma Physics and Controlled Fusion* (2023). – URL http://iopscience.iop.org/article/10.1088/1361-6587/acb0fc

# Bibliography

[Faugeras 2020]   FAUGERAS, Blaise:  An overview of the numerical methods for tokamak plasma equilibrium computation implemented in the NICE code. In: *Fusion Engineering and Design* 160 (2020), 112020. – URL https://www.sciencedirect.com/science/article/pii/S0920379620305688. – ISSN 0920-3796

[Federici et al. 2019]   FEDERICI, G. ; BACHMANN, C. ; BARUCCA, L. ; BAYLARD, C. ; BIEL, W. ; BOCCACCINI, L.V. ; BUSTREO, C. ; CIATTAGLIA, S. ; CISMONDI, F. ; CORATO, V. ; DAY, C. ; DIEGELE, E. ; FRANKE, T. ; GAIO, E. ; GLISS, C. ; HAERTL, T. ; IBARRA, A. ; HOLDEN, J. ; KEECH, G. ; KEMBLETON, R. ; LOVING, A. ; MAVIGLIA, F. ; MORRIS, J. ; MESZAROS, B. ; MOSCATO, I. ; PINTSUK, G. ; SICCINIO, M. ; TAYLOR, N. ; TRAN, M.Q. ; VORPAHL, C. ; WALDEN, H. ; YOU, J.H.: Overview of the DEMO staged design approach in Europe. In: *Nuclear Fusion* 59 (2019), apr, 6, 066013. – URL https://dx.doi.org/10.1088/1741-4326/ab1178

[Federici et al. 2018]   FEDERICI, G. ; BACHMANN, C. ; BARUCCA, L. ; BIEL, W. ; BOCCACCINI, L. ; BROWN, R. ; BUSTREO, C. ; CIATTAGLIA, S. ; CISMONDI, F. ; COLEMAN, M. ; CORATO, V. ; DAY, C. ; DIEGELE, E. ; FISCHER, U. ; FRANKE, T. ; GLISS, C. ; IBARRA, A. ; KEMBLETON, R. ; LOVING, A. ; MAVIGLIA, F. ; MESZAROS, B. ; PINTSUK, G. ; TAYLOR, N. ; TRAN, M.Q. ; VORPAHL, C. ; WENNINGER, R. ; YOU, J.H.: DEMO design activity in Europe: Progress and updates. In: *Fusion Engineering and Design* 136 (2018), 729–741. – URL https://www.sciencedirect.com/science/article/pii/S0920379618302898. – Special Issue: Proceedings of the 13th International Symposium on Fusion Nuclear Technology (ISFNT-13). – ISSN 0920-3796

[Felici 2011]   FELICI, F: *PhD thesis no. 5203 Real-time control of tokamak plasmas: from control of physics to physics-based control.* École Polytechnique Fédérale de Lausanne (EPFL), CH-1015 Lausanne, Switzerland, 2011

[Felici et al. 2021]   FELICI, F ; BLANKEN, T ; BOSMAN, T ; CARPANESE, F ; FISCHER, R ; GALPERTI, C ; GIANNONE, L ; KONG, M ; KUDLACEK, O ; MARASCHEK, M et al.: Integrated plasma state reconstruction, off-normal event handling and control, with application to TCV and ASDEX Upgrade. In: *IAEA Fusion Energy Conf.(Virtual Conference)*, 2021, p–EX

[Felici et al. 2016]   FELICI, F ; BLANKEN, T ; MALJAARS, E ; VAN DEN BRAND, H ; CITRIN, J ; HOGEWEIJ, D ; SCHEFFER, M ; DE BAAR, M. R. ; STEINBUCH et al.: Real-time model-based plasma state estimation, monitoring and integrated control in TCV, ASDEX-Upgrade and ITER. In: *26th IAEA Fusion Energy Conference, Kyoto, Japan*, 2016

[Felici et al. 2018]   FELICI, F ; CITRIN, J ; TEPLUKHINA, A A. ; REDONDO, J ; BOURDELLE, C ; IMBEAUX, F ; SAUTER, O: Real-time-capable prediction of temperature and density profiles in a tokamak using RAPTOR and a first-principle-based transport model. In: *Nuclear Fusion* 58 (2018), 9, 096006. – URL https://doi.org/10.1088/1741-4326/aac8f0

[Felici and Sauter 2012]   FELICI, F ; SAUTER, O: Non-linear model-based optimization of actuator trajectories for tokamak plasma profile control. In: *Plasma Physics and Controlled Fusion* 54 (2012), 2, 025002. – URL https://doi.org/10.1088/0741-3335/54/2/025002

242

[Felici et al. 2011]  FELICI, F ; SAUTER, O ; CODA, S ; DUVAL, B P. ; GOODMAN, T.P. ; MORET, J-M ; PALEY, J I.: Real-time physics-model-based simulation of the current density profile in tokamak plasmas. In: *Nuclear Fusion* 51 (2011), 8, 083052. – URL https://doi.org/10.1088/0029-5515/51/8/083052

[Felici et al. 2014]  FELICI, Federico ; BAAR, Marco de ; STEINBUCH, Maarten: A dynamic state observer for real-time reconstruction of the tokamak plasma profile state and disturbances. In: *2014 American Control Conference*, 2014, 4816–4823

[Felici and Oomen 2015]  FELICI, Federico ; OOMEN, Tom: Enhancing current density profile control in tokamak experiments using iterative learning control. In: *2015 54th IEEE Conference on Decision and Control (CDC)*, 2015, 5370–5377

[Ferron et al. 2015]  FERRON, J.R. ; HOLCOMB, C.T. ; LUCE, T.C. ; PARK, J.M. ; KOLEMEN, E. ; HAYE, R.J. L. ; SOLOMON, W.M. ; TURCO, F.: High internal inductance for steady-state operation in ITER and a reactor. In: *Nuclear Fusion* 55 (2015), jun, 7, 073030. – URL https://dx.doi.org/10.1088/0029-5515/55/7/073030

[Fietz et al. 2013]  FIETZ, S. ; FABLE, E. ; HOBIRK, J. ; FISCHER, R. ; FUCHS, C. ; PEREVERZEV, G. ; RYTER, F. et al.: Investigation of transport models in ASDEX Upgrade current ramps. In: *Nuclear Fusion* 53 (2013), apr, 5, 053004. – URL https://dx.doi.org/10.1088/0029-5515/53/5/053004

[File et al. 1971]  FILE, J. ; MILLS, R. G. ; SHEFFIELD, G. V.: Large Superconducting Magnet Designs for Fusion Reactors. In: *IEEE Transactions on Nuclear Science* 18 (1971), 4, 277–282

[Fisch and Boozer 1980]  FISCH, N. J. ; BOOZER, A. H.: Creating an Asymmetric Plasma Resistivity with Waves. In: *Phys. Rev. Lett.* 45 (1980), Sep, 720–722. – URL https://link.aps.org/doi/10.1103/PhysRevLett.45.720

[Fischer et al. 2016]  FISCHER, R. ; BOCK, A. ; DUNNE, M. ; FUCHS, J. C. ; GIANNONE, L. ; LACKNER, K. ; MCCARTHY, P. J. ; POLI, E. ; PREUSS, R. ; RAMPP, M. ; SCHUBERT, M. ; STOBER, J. ; SUTTROP, W. ; TARDINI, G. ; WEILAND, M. et al.: Coupling of the Flux Diffusion Equation with the Equilibrium Reconstruction at ASDEX Upgrade. In: *Fusion Science and Technology* 69 (2016), 2, 526–536. – URL https://doi.org/10.13182/FST15-185

[Fischer et al. 2010]  FISCHER, R. ; FUCHS, C. J. ; KURZAN, B. ; SUTTROP, W. ; WOLFRUM, E. et al.: Integrated Data Analysis of Profile Diagnostics at ASDEX Upgrade. In: *Fusion Science and Technology* 58 (2010), 2, 675–684. – URL https://doi.org/10.13182/FST10-110

[Fischer et al. 2020]  FISCHER, R. ; GIANNONE, L. ; ILLERHAUS, J. ; MCCARTHY, P. J. ; MC-DERMOTT, R. M. et al.: Estimation and Uncertainties of Profiles and Equilibria for Fusion Modeling Codes. In: *Fusion Science and Technology* 76 (2020), 8, 879–893. – URL https://doi.org/10.1080/15361055.2020.1820794

# Bibliography

[Fleschner 2022]    FLESCHNER, F: *H-mode: This discovery made ITER possible.* Press release Max Planck Institute for Plasma Physics, 2022. – URL https://www.ipp.mpg.de/5280411/ 05_22

[Freidberg 2007]    FREIDBERG, J: *Plasma Physics and Fusion Energy.* Cambridge University Press, 2007

[Galeev 1970]    GALEEV, A A.: In: *Sov. Phys. JETP* 71 (1970),  32, 752

[Galeev and Sagdeev 1968]    GALEEV, A A. ; SAGDEEV, R Z.:  Transport phenomena in a collisionless plasma in a toroidal magnetic system. In: *Sov. Phys. JETP* 26 (1968),  1,  233–240

[Garbet et al. 2004]    GARBET, X ; MANTICA, P ; RYTER, F ; CORDEY, G ; IMBEAUX, F ; SOZZI, C ; MANINI, A ; ASP, E ; PARAIL, V ; WOLF, R ; JET EFDA CONTRIBUTORS the: Profile stiffness and global confinement. In: *Plasma Physics and Controlled Fusion* 46 (2004), jul,  9,  1351. – URL https://dx.doi.org/10.1088/0741-3335/46/9/002

[Garcia et al. 2015]    GARCIA, J. ; CHALLIS, C. ; CITRIN, J. ; DOERK, H. ; GIRUZZI, G. ; GOERLER, T. ; JENKO, F. ; MAGET, P. ; CONTRIBUTORS, JET: Key impact of finite-beta and fast ions in core and edge tokamak regions for the transition to advanced scenarios. In: *Nuclear Fusion* 55 (2015), apr,  5,  053007. – URL https://dx.doi.org/10.1088/0029-5515/55/5/053007

[Garcia et al. 2018]    GARCIA, J ; GOERLER, T ; JENKO, F: Isotope and fast ions turbulence suppression effects: Consequences for high-$\beta$ ITER plasmas. In: *Physics of Plasmas* 25 (2018),  5,  055902. – URL https://doi.org/10.1063/1.5016331

[Geelen et al. 2015]    GEELEN, P ; FELICI, F ; MERLE, A ; SAUTER, O: Parameter estimation for a nonlinear control-oriented tokamak profile evolution model. 57 (2015),  12,  125008. – URL https://doi.org/10.1088/0741-3335/57/12/125008

[Giacomin et al. 2022]    GIACOMIN, M. ; PAU, A. ; RICCI, P. ; SAUTER, O. ; EICH, T. et al.: First-Principles Density Limit Scaling in Tokamaks Based on Edge Turbulent Transport and Implications for ITER. In: *Phys. Rev. Lett.* 128 (2022), May,  185003. – URL https: //link.aps.org/doi/10.1103/PhysRevLett.128.185003

[Giannone et al. 2013]    GIANNONE, L. ; REICH, M. ; MARASCHEK, M. ; POLI, E. ; RAPSON, C. ; BARRERA, L. ; MCDERMOTT, R. ; MLYNEK, A. ; RUAN, Q. ; TREUTTERER, W. ; WENZEL, L. ; BOCK, A. ; CONWAY, G. ; FISCHER, R. ; FUCHS, J.C. ; LACKNER, K. ; MCCARTHY, P.J. ; PREUSS, R. ; RAMPP, M. ; SCHUHBECK, K.H. ; STOBER, J. ; ZOHM, H.: A data acquisition system for real-time magnetic equilibrium reconstruction on ASDEX Upgrade and its application to NTM stabilization experiments. In: *Fusion Engineering and Design* 88 (2013),  12,  3299–3311. – URL https://www.sciencedirect.com/science/article/pii/S0920379613006844. – ISSN 0920-3796

[Gibson and JET Team 1998]    GIBSON, A. ; JET TEAM: Deuterium Tritium plasmas in the Joint European Torus (JET): Behavior and implications. In: *Physics of Plasmas* 5 (1998),  5, 1839–1847. – URL https://doi.org/10.1063/1.872854

[Giruzzi et al. 2015]    GIRUZZI, G. ; ARTAUD, J.F. ; BARUZZO, M. ; BOLZONELLA, T. ; FABLE, E. ; GARZOTTI, L. ; IVANOVA-STANIK, I. ; KEMP, R. ; KING, D.B. ; SCHNEIDER, M. ; STANKIEWICZ, R. ; STEPNIEWSKI, W. ; VINCENZI, P. ; WARD, D. ; ZAGORSKI, R.: Modelling of pulsed and steady-state DEMO scenarios. In: *Nuclear Fusion* 55 (2015), jun, 7, 073002. – URL https://dx.doi.org/10.1088/0029-5515/55/7/073002

[Goldston 1984]    GOLDSTON, Robert J.: Energy confinement scaling in Tokamaks: some implications of recent experiments with Ohmic and strong auxiliary heating. In: *Plasma Physics and Controlled Fusion* 26 (1984), jan, 1A, 87. – URL https://dx.doi.org/10.1088/0741-3335/26/1A/308

[Goodman et al. 2005]    GOODMAN, T P. ; BEHN, R ; CAMENEN, Y ; CODA, S ; FABLE, E ; HENDERSON, M A. ; NIKKOLA, P ; ROSSEL, J ; SAUTER, O ; SCARABOSIO, A ; ZUCCA, C et al.: Safety factor profile requirements for electron ITB formation in TCV. In: *Plasma Physics and Controlled Fusion* 47 (2005), nov, 12B, B107. – URL https://dx.doi.org/10.1088/0741-3335/47/12B/S09

[Gormezano et al. 2007]    GORMEZANO, C. ; SIPS, A.C.C. ; LUCE, T.C. ; IDE, S. ; BECOULET, A. ; LITAUDON, X. ; ISAYAMA, A. ; HOBIRK, J. ; WADE, M.R. ; OIKAWA, T. ; PRATER, R. ; ZVONKOV, A. ; LLOYD, B. ; SUZUKI, T. ; BARBATO, E. ; BONOLI, P. ; PHILLIPS, C.K. ; VDOVIN, V. ; JOFFRIN, E. ; CASPER, T. ; FERRON, J. ; MAZON, D. ; MOREAU, D. ; BUNDY, R. ; KESSEL, C. ; FUKUYAMA, A. ; HAYASHI, N. ; IMBEAUX, F. ; MURAKAMI, M. ; POLEVOI, A.R. ; ST JOHN, H.E.: Chapter 6: Steady state operation. In: *Nuclear Fusion* 47 (2007), jun, 6, S285. – URL https://dx.doi.org/10.1088/0029-5515/47/6/S06

[Grad and Rubin 1958]    GRAD, H ; RUBIN, H: Hydromagnetic equilibria and force-free fields. In: *Proceedings of the Second United Nations Conference on the Peaceful Uses of Atomic Energy (United Nations, Geneva, 1958)* 31 (1958), 190

[Greenwald et al. 1988]    GREENWALD, M ; TERRY, J L. ; WOLFE, S M. ; EJIMA, S ; BELL, M G. ; KAYE, S M. ; NEILSON, G H.: A new look at density limits in tokamaks. In: *Nuclear Fusion* 28 (1988), 12, 2199–2207. – URL https://doi.org/10.1088/0029-5515/28/12/009

[Greenwald 2002]    GREENWALD, Martin: Density limits in toroidal plasmas. In: *Plasma Physics and Controlled Fusion* 44 (2002), 8, R27–R53. – URL https://doi.org/10.1088/0741-3335/44/8/201

[Gruber et al. 1999]    GRUBER, O. ; WOLF, R. C. ; DUX, R. ; FUCHS, C. ; GÜNTER, S. ; KALLENBACH, A. ; LACKNER, K. ; MARASCHEK, M. ; MCCARTHY, P. J. ; MEISTER, H. ; PEREVERZEV, G. ; RYTER, F. ; SCHWEINZER, J. ; SEIDEL, U. ; SESNIC, S. ; STÄBLER, A. ; STOBER, J. et al.: Stationary *H*-Mode Discharges with Internal Transport Barrier on ASDEX Upgrade. In: *Phys. Rev. Lett.* 83 (1999), Aug, 1787–1790. – URL https://link.aps.org/doi/10.1103/PhysRevLett.83.1787

[Gude et al. 1999]    GUDE, A ; GÜNTER, S ; SESNIC, S: Seed island of neoclassical tearing modes at ASDEX Upgrade. In: *Nuclear Fusion* 39 (1999), 1, 127–131. – URL https://doi.org/10.1088/0029-5515/39/1/308

[Han et al. 2022]    HAN, H ; PARK, SJ ; SUNG, C ; KANG, J ; LEE, YH ; CHUNG, J ; HAHM, TS ; KIM, B ; PARK, J-K ; BAK, JG et al.: A sustained high-temperature fusion plasma regime facilitated by fast ions. In: *Nature* 609 (2022), 7926, 269–275. – URL https://doi.org/10.1038/s41586-022-05008-1. ISBN 1476-4687

[Harrer et al. 2022]    HARRER, G. F. ; FAITSCH, M. ; RADOVANOVIC, L. ; WOLFRUM, E. ; ALBERT, C. ; CATHEY, A. ; CAVEDON, M. ; DUNNE, M. ; EICH, T. ; FISCHER, R. ; GRIENER, M. ; HOELZL, M. ; LABIT, B. ; MEYER, H. ; AUMAYR, F. et al.: Quasicontinuous Exhaust Scenario for a Fusion Reactor: The Renaissance of Small Edge Localized Modes. In: *Phys. Rev. Lett.* 129 (2022), Oct, 165001. – URL https://link.aps.org/doi/10.1103/PhysRevLett.129.165001

[Hawryluk and TFTR Team 1998]    HAWRYLUK, R. J. ; TFTR TEAM: Fusion plasma experiments on TFTR: A 20 year retrospective. In: *Physics of Plasmas* 5 (1998), 5, 1577–1589. – URL https://doi.org/10.1063/1.872825

[Hayashi et al. 2017]    HAYASHI, N ; GARCIA, J ; HONDA, M ; NARITA, E ; IDE, S ; GIRUZZI, G ; SAKAMOTO, Y: Transport modelling of JT-60U and JET plasmas with internal transport barriers towards prediction of JT-60SA high-beta steady-state scenario. In: *Nuclear Fusion* 57 (2017), oct, 12, 126037. – URL https://doi.org/10.1088/1741-4326/aa88de

[Hein et al. 2010]    HEIN, T ; ANGIONI, C ; FABLE, E ; CANDY, J: Gyrokinetic study of the role of $\beta$ on electron particle transport in tokamaks. In: *Physics of Plasmas* 17 (2010), 10, 102309. – URL https://doi.org/10.1063/1.3503622

[Hender et al. 2007]    HENDER, T.C. ; WESLEY, J.C ; BIALEK, J. ; BONDESON, A. ; BOOZER, A.H. ; BUTTERY, R.J. ; GAROFALO, A. ; GOODMAN, T.P ; GRANETZ, R.S. ; GRIBOV, Y. ; GRUBER, O. ; GRYAZNEVICH, M. ; GIRUZZI, G. ; GUENTER, S. ; HAYASHI, N. ; HELANDER, P. ; HEGNA, C.C. ; HOWELL, D.F. ; HUMPHREYS, D.A. ; HUYSMANS, G.T.A. ; HYATT, A.W. ; ISAYAMA, A. ; JARDIN, S.C. ; KAWANO, Y. ; KELLMAN, A. ; KESSEL, C. ; KOSLOWSKI, H.R. ; HAYE, R.J. L. ; LAZZARO, E. ; LIU, Y.Q. ; LUKASH, V. ; MANICKAM, J. ; MEDVEDEV, S. ; MERTENS, V. ; MIRNOV, S.V. ; NAKAMURA, Y. ; NAVRATIL, G. ; OKABAYASHI, M. ; OZEKI, T. ; PACCAGNELLA, R. ; PAUTASSO, G. ; PORCELLI, F. ; PUSTOVITOV, V.D. ; RICCARDO, V. ; SATO, M. ; SAUTER, O. ; SCHAFFER, M.J. ; SHIMADA, M. ; SONATO, P. ; STRAIT, E.J. ; SUGIHARA, M. ; TAKECHI, M. ; TURNBULL, A.D. ; WESTERHOF, E. ; WHYTE, D.G. ; YOSHINO, R. ; ZOHM, H. ; ITPA MHD, DISRUPTION AND MAGNETIC CONTROL TOPICAL GROUP the: Chapter 3: MHD stability, operational limits and disruptions. In: *Nuclear Fusion* 47 (2007), jun, 6, S128. – URL https://dx.doi.org/10.1088/0029-5515/47/6/S03

[Heumann et al. 2015]    HEUMANN, Holger ; BLUM, Jacques ; BOULBE, Cedric ; FAUGERAS, Blaise ; SELIG, Gael ; ANÉ, J-M ; BRÉMOND, S ; GRANDGIRARD, V ; HERTOUT, P ; NARDON, E: Quasi-static free-boundary equilibrium of toroidal plasma with CEDRES++: Computational methods and applications. In: *Journal of Plasma Physics* 81 (2015), 3

[Hinton and Oberman 1969]    HINTON, F.L. ; OBERMAN, C.: Electrical conductivity of plasma in a spatially inhomogeneous magnetic field. In: *Nuclear Fusion* 9 (1969), dec, 4, 319. – URL https://dx.doi.org/10.1088/0029-5515/9/4/005

[Ho et al. 2021a]    HO, A. ; CITRIN, J. ; BOURDELLE, C. ; CAMENEN, Y. ; CASSON, F. J. ; PLASSCHE, K. L. van de ; WEISEN, H.: Neural network surrogate of QuaLiKiz using JET experimental data to populate training space. In: *Physics of Plasmas* 28 (2021), 3, 032305. – URL https://doi.org/10.1063/5.0038290

[Ho et al. 2021b]    HO, Aaron ; CITRIN, Jonathan ; BOURDELLE, Clarisse ; CASSON, Francis ; CHALLIS, Clive ; VAN DE PLASSCHE, Karel et al.: Predictive applications of the QuaLiKiz neural network within integrated modelling for JET scenarios. In: *APS Division of Plasma Physics Meeting Abstracts* Bd. 2021, 2021, NI02–006

[Hobirk et al. 2012]    HOBIRK, J ; IMBEAUX, F ; CRISANTI, F ; BURATTI, P ; CHALLIS, C D. ; JOFFRIN, E et al.: Improved confinement in JET hybrid discharges. In: *Plasma Physics and Controlled Fusion* 54 (2012), jul, 9, 095001. – URL https://dx.doi.org/10.1088/0741-3335/54/9/095001

[Hogeweij et al. 2012]    HOGEWEIJ, G M D. ; ARTAUD, J-F ; CASPER, T A. ; CITRIN, J ; IMBEAUX, F ; KOECHL, F ; LITAUDON, X ; VOITSEKHOVITCH, I: Optimizing the current ramp-up phase for the hybrid ITER scenario. In: *Nuclear Fusion* 53 (2012), 1, 013008. – URL https://doi.org/10.1088/0029-5515/53/1/013008

[Honda and Narita 2019]    HONDA, M ; NARITA, E: Machine-learning assisted steady-state profile predictions using global optimization techniques. In: *Physics of Plasmas* 26 (2019), 10, 102307. – URL https://doi.org/10.1063/1.5117846

[Horn 2020]    HORN, P: *Inclusion of physics constraints in neural network surrogate models for fusion simulation.* Master Thesis, Technische Universiteit Eindhoven, 2020

[Horton 1999]    HORTON, W.: Drift waves and transport. In: *Rev. Mod. Phys.* 71 (1999), Apr, 735–778. – URL https://link.aps.org/doi/10.1103/RevModPhys.71.735

[Humphreys et al. 2015]    HUMPHREYS, D ; AMBROSINO, G ; DE VRIES, P ; FELICI, F ; KIM, S H. ; JACKSON, G ; KALLENBACH, A ; KOLEMEN, E ; LISTER, J ; MOREAU, D ; PIRONTI, A ; RAUPP, G ; SAUTER, O ; SCHUSTER, E ; SNIPES, J ; TREUTTERER, W ; WALKER, M ; WELANDER, A ; WINTER, A ; ZABEO, L: Novel aspects of plasma control in ITER. In: *Physics of Plasmas* 22 (2015), 2, 021806. – URL https://doi.org/10.1063/1.4907901

[IEA 2019]    IEA: *Total primary energy supply by fuel, 1971 and 2019.* International Enegy Agency, Paris, 2019. – URL https://www.iea.org/data-and-statistics/charts/total-primary-energy-supply-by-fuel-1971-and-2019

[Imbeaux et al. 2015]    IMBEAUX, F. ; PINCHES, S.D. ; LISTER, J.B. ; BURAVAND, Y. ; CASPER, T. ; DUVAL, B. ; GUILLERMINET, B. ; HOSOKAWA, M. ; HOULBERG, W. ; HUYNH, P. ; KIM, S.H. ; MANDUCHI, G. ; OWSIAK, M. ; PALAK, B. ; PLOCIENNIK, M. ; ROUAULT, G. ; SAUTER, O. ; STRAND, P.: Design and first applications of the ITER integrated modelling and analysis suite. In: *Nuclear Fusion* 55 (2015), oct, 12, 123006. – URL https://dx.doi.org/10.1088/0029-5515/55/12/123006

# Bibliography

[ITER Organization 2018]    ITER Organization: *ITER Research Plan within the Staged Approach (Level III – Provisional Version)*. ITER technical report ITR-18-003, 2018

[ITER Physics Expert Group on Confinement and Transport et al. 1999]    ITER Physics Expert Group on Confinement and Transport ; ITER Physics Expert Group on Confinement Modelling and Database ; ITER Physics Basis Editors:  Chapter 2: Plasma confinement and transport. In: *Nuclear Fusion* 39 (1999),  12,  2175–2249. – URL https://doi.org/10.1088/0029-5515/39/12/302

[ITER Physics Expert Group on Confinement and Transport and ITER Physics Expert Group on Confinement Modelling and Database and ITER Physics Basis Editors 1999]    ITER Physics Expert Group on Confinement and Transport and ITER Physics Expert Group on Confinement Modelling and Database and ITER Physics Basis Editors: Chapter 2: Plasma confinement and transport. In: *Nuclear Fusion* 39 (1999), dec,  12,  2175. – URL https://dx.doi.org/10.1088/0029-5515/39/12/302

[ITER Physics Expert Group on Disruptions, Plasma Control and MHD and ITER Physics Basis Editors 1999]    ITER Physics Expert Group on Disruptions, Plasma Control and MHD and ITER Physics Basis Editors: Chapter 3: MHD stability, operational limits and disruptions. In: *Nuclear Fusion* 39 (1999), dec,  12,  2251. – URL https://dx.doi.org/10.1088/0029-5515/39/12/303

[Janky et al. 2021]    Janky, F. ; Fable, E. ; Englberger, M. ; Treutterer, W.: Validation of the Fenix ASDEX Upgrade flight simulator. In: *Fusion Engineering and Design* 163 (2021), 112126. – URL https://www.sciencedirect.com/science/article/pii/S0920379620306748. – ISSN 0920-3796

[Jardin et al. 2015]    Jardin, S. C. ; Ferraro, N. ; Krebs, I.: Self-Organized Stationary States of Tokamaks. In: *Phys. Rev. Lett.* 115 (2015), Nov,  215001. – URL https://link.aps.org/doi/10.1103/PhysRevLett.115.215001

[Jian et al. 2019]    Jian, X ; Chan, V S. ; Chen, J ; Bock, A ; Zohm, H ; Fable, E ; Reisner, M ; Guo, W ; Zhuang, G:  Key effects on the confinement improvement of the ASDEX Upgrade hybrid scenario. In: *Nuclear Fusion* 59 (2019), sep,  10,  106038. – URL https://doi.org/10.1088/1741-4326/ab3b44

[Joffrin et al. 2005]    Joffrin, E. ; Sips, A.C.C. et al.: The hybrid scenario in JET: towards its validation for ITER. In: *Nuclear Fusion* 45 (2005), jun,  7,  626. – URL https://dx.doi.org/10.1088/0029-5515/45/7/010

[Kadomtsev and Pogutse 1963]    Kadomtsev, B. B. ; Pogutse, O. P.: In: *Reviews of Plasma Physics ed. by M. A. Leontovich* 5 (1963), 249

[Kadomtsev and Pogutse 1971]    Kadomtsev, B.B. ; Pogutse, O.P.:  Trapped particles in toroidal magnetic systems. In: *Nuclear Fusion* 11 (1971), jan,  1,  67. – URL https://dx.doi.org/10.1088/0029-5515/11/1/010

[Kadomtsev and Shafranov 1971]   KADOMTSEV, BB ; SHAFRANOV, VD: A Stationary Tokamak. In: *Plasma Physics and Controlled Nuclear Fusion Research 1971. Vol. II. Proceedings of the Fourth International Conference on Plasma Physics and Controlled Nuclear Fusion Research,* 1971

[Kappatou et al. 2022]   KAPPATOU, Athina ; CHALLIS, Clive ; HOBIRK, Joerg ; LERCHE, Ernesto ; KING, Damian ; KEELING, David ; ANGIONI, Clemente ; AURIEMMA, Fulvio ; BELONOHY, Eva ; CASSON, Francis et al.: Sustained high fusion power production with the hybrid scenario in the recent JET DT campaign. In: *Bulletin of the American Physical Society* (2022)

[Kerekes et al. 2023]   KEREKES, Andelka ; BREUNING, Larissa ; VON MUELLER, Alexander ; GAWLICK, Julia ; WARMER, Felix ; FIETZ, Sina ; KEMBLETON, Richard ; CIATTAGLIA, Sergio ; HERING, Wolfgang ; ZOHM, Hartmut ; HAMACHER, Thomas: Operational characterization of tokamak and stellarator type fusion power plants from an energy system perspective. In: *Fusion Engineering and Design* 190 (2023), 113496. – URL https://www.sciencedirect.com/science/article/pii/S0920379623000807. – ISSN 0920-3796

[Kikuchi 1990]   KIKUCHI, M.: Steady state tokamak reactor based on the bootstrap current. In: *Nuclear Fusion* 30 (1990), feb, 2, 265. – URL https://dx.doi.org/10.1088/0029-5515/30/2/006

[Kikuchi et al. 2019]   KIKUCHI, M. ; TAKIZUKA, T. ; MEDVEDEV, S. ; ANDO, T. ; CHEN, D. ; LI, J.X. ; AUSTIN, M. ; SAUTER, O. ; VILLARD, L. ; MERLE, A. ; FONTANA, M. ; KISHIMOTO, Y. ; IMADERA, K.: L-mode-edge negative triangularity tokamak reactor. In: *Nuclear Fusion* 59 (2019), apr, 5, 056017. – URL https://dx.doi.org/10.1088/1741-4326/ab076d

[Kim et al. 2014]   KIM, D. ; GOODMAN, T. P. ; SAUTER, O.: Real-time sawtooth control and neoclassical tearing mode preemption in ITER. In: *Physics of Plasmas* 21 (2014), 6, 061503. – URL https://doi.org/10.1063/1.4884349

[Kim et al. 2016]   KIM, D ; MERLE, A ; SAUTER, O ; GOODMAN, T P: Simple predictive electron transport models applied to sawtoothing plasmas. In: *Plasma Physics and Controlled Fusion* 58 (2016), 5, 055002. – URL https://doi.org/10.1088/0741-3335/58/5/055002

[Kim et al. 2021]   KIM, S H ; POLEVOI, A R ; LOARTE, A ; MEDVEDEV, S Y. ; HUIJSMANS, G: A study of the heating and current drive options and confinement requirements to access steady-state plasmas at Q~5 in ITER and associated operational scenario development. In: *Nuclear Fusion* (2021), apr. – URL https://doi.org/10.1088/1741-4326/abf43e

[Kim and Lister 2012]   KIM, S.H. ; LISTER, J.B.: A potentially robust plasma profile control approach for ITER using real-time estimation of linearized profile response models. In: *Nuclear Fusion* 52 (2012), jul, 7, 074002. – URL https://dx.doi.org/10.1088/0029-5515/52/7/074002

[Kinsey et al. 2007]   KINSEY, J. E. ; WALTZ, R. E. ; CANDY, J.: The effect of plasma shaping on turbulent transport and ExB shear quenching in nonlinear gyrokinetic simulations. In: *Physics of Plasmas* 14 (2007), 10, 102306. – URL https://doi.org/10.1063/1.2786857

# Bibliography

[Klinger et al. 2019]    KLINGER, T. et al.: Overview of first Wendelstein 7-X high-performance operation. In: *Nuclear Fusion* 59 (2019), jun, 11, 112004. – URL https://dx.doi.org/10.1088/1741-4326/ab03a7

[Koechl et al. 2018]    KOECHL, F ; PINCHES, S D. ; CASSON, F J. ; CITRIN, J ; CORRIGAN, G ; DUBROV, M ; GRIBOV, Y ; HARTING, D ; KAVIN, A A. ; KHAYRUTDINOV, R R. ; KIM, S-H ; KNIGHT, P J. ; KONOVALOV, S V. ; LOARTE, A ; LUKASH, V E. ; MARIN, M ; MEDVEDEV, S ; PARAIL, V ; POLEVOI, A R. ; ROMANELLI, M: Optimising the ITER 15 MA DT baseline scenario by exploiting a self-consistent free-boundary core-edge-SOL workflow in IMAS. In: *2018 IAEA Fusion Energy Conf. (Gandhinagar, India, 22–27 October 2018)* (2018)

[Kong et al. 2019a]    KONG, M ; BLANKEN, T C. ; FELICI, F ; GALPERTI, C ; MALJAARS, E ; SAUTER, O ; VU, T ; CARPANESE, F ; MERLE, A ; MORET, J-M ; PESAMOSCA, F ; POLI, E ; REICH, M ; TEPLUKHINA, A A. et al.: Control of neoclassical tearing modes and integrated multi-actuator plasma control on TCV. In: *Nuclear Fusion* 59 (2019), 7, 076035. – URL https://doi.org/10.1088/1741-4326/ab1e1e

[Kong et al. 2022]    KONG, M ; FELICI, F ; SAUTER, O ; GALPERTI, C ; VU, T ; HAM, C J. ; HENDER, T C. ; MARASCHEK, M ; REICH, M et al.: Physics-based control of neoclassical tearing modes on TCV. In: *Plasma Physics and Controlled Fusion* 64 (2022), feb, 4, 044008. – URL https://dx.doi.org/10.1088/1361-6587/ac48be

[Kong et al. 2019b]    KONG, M. ; SAUTER, O. ; FELICI, F. ; HOGEWEIJ, G.M.D. ; MERLE, A. ; NOWAK, S. et al.: On the triggerless onset of 2/1 neoclassical tearing modes in TCV. In: *Nuclear Fusion* 60 (2019), dec, 2, 026002. – URL https://dx.doi.org/10.1088/1741-4326/ab56c5

[Krebs et al. 2017]    KREBS, I. ; JARDIN, S. C. ; GÆNTER, S. ; LACKNER, K. ; HOELZL, M. ; STRUMBERGER, E. ; FERRARO, N.: Magnetic flux pumping in 3D nonlinear magnetohydrodynamic simulations. In: *Physics of Plasmas* 24 (2017), 10, 102511. – URL https://doi.org/10.1063/1.4990704

[Kruskal et al. 1954]    KRUSKAL, Martin D. ; SCHWARZSCHILD, Martin ; CHANDRASEKHAR, Subrahmanyan: Some instabilities of a completely ionized plasma. In: *Proceedings of the Royal Society of London. Series A. Mathematical and Physical Sciences* 223 (1954), 1154, 348–360. – URL https://royalsocietypublishing.org/doi/abs/10.1098/rspa.1954.0120

[Kudlacek et al. 2021a]    KUDLACEK, O. ; BOSMAN, T. ; FELICI, F. ; GIANNONE, L. ; VAN MULDERS, S. ; SAUTER, O. ; SIEGLIN, B. ; TREUTTERER, W. ; VU, N.M.T. ; WEILAND, M. ; ANGIONI, C. ; BILATO, R. ; BONANOMI, N. ; GOMEZ-ORTIZ, I. ; GRÄTER, A. ; FISCHER, R. ; KONG, M. ; MACEINA, T. ; MARASCHEK, M. ; REICH, M. ; ZEHETBAUER, T.: Developments on actuator management, plasma state reconstruction, and control on ASDEX Upgrade. In: *Fusion Engineering and Design* 171 (2021), 112563. – URL https://www.sciencedirect.com/science/article/pii/S0920379621003392. – ISSN 0920-3796

[Kudlacek et al. 2021b]    KUDLACEK, O ; VAN MULDERS, S ; FELICI, F ; SAUTER, O ; FISCHER, R ; BONANOMI, N ; ANGIONI, C ; GRÄTER, A ; TREUTTERER, W ; ZEHETBAUER, T et al.: Fast

optimization of the central electron and ion temperature on ASDEX Upgrade based on Iterative Learning Control. In: *13th Technical Meeting on Plasma Control Systems, Data Management and Remote Experiments in Fusion Research*, 2021

[Kumar et al. 2020]    KUMAR, N ; CAMENEN, Y ; BENKADDA, S ; BOURDELLE, C ; LOARTE, A ; POLEVOI, A R. ; WIDMER, F: Turbulent transport driven by kinetic ballooning modes in the inner core of JET hybrid H-modes. In: *Nuclear Fusion* 61 (2020), dec, 3, 036005. – URL https://doi.org/10.1088/1741-4326/abd09c

[La Haye et al. 1997]    LA HAYE, R.J. ; LAO, L.L. ; STRAIT, E.J. ; TAYLOR, T.S.: High beta tokamak operation in DIII-D limited at low density/collisionality by resistive tearing modes. In: *Nuclear Fusion* 37 (1997), mar, 3, 397. – URL https://dx.doi.org/10.1088/0029-5515/37/3/I08

[La Haye et al. 2000]    LA HAYE, R.J. ; RICE, B.W. ; STRAIT, E.J.: Increasing the beta limit due to neoclassical tearing modes by raising the axial safety factor $q(0) > 1$. In: *Nuclear Fusion* 40 (2000), jan, 1, 53. – URL https://dx.doi.org/10.1088/0029-5515/40/1/304

[Lang et al. 2012]    LANG, P T. ; SUTTROP, W ; BELONOHY, E ; BERNERT, M ; DERMOTT, R M M. ; FISCHER, R ; HOBIRK, J ; KARDAUN, O J W F. ; KOCSIS, G ; KURZAN, B ; MARASCHEK, M ; MARNE, P de ; MLYNEK, A ; SCHNEIDER, P A. ; SCHWEINZER, J ; STOBER, J ; SZEPESI, T ; THOMSEN, K ; TREUTTERER, W ; WOLFRUM, E: High-density H-mode operation by pellet injection and ELM mitigation with the new active in-vessel saddle coils in ASDEX Upgrade. In: *Nuclear Fusion* 52 (2012), 2, 023017. – URL https://doi.org/10.1088/0029-5515/52/2/023017

[Lawson 1957]    LAWSON, J. D.: Some Criteria for a Power Producing Thermonuclear Reactor. In: *Proc. Phys. Soc. Sect. B* 70 (1957), 6–10

[Lazarus et al. 1990]    LAZARUS, E.A. ; LISTER, J.B. ; NEILSON, G.H.: Control of the vertical instability in tokamaks. In: *Nuclear Fusion* 30 (1990), jan, 1, 111. – URL https://dx.doi.org/10.1088/0029-5515/30/1/010

[Lin-Liu et al. 2003]    LIN-LIU, Y R. ; CHAN, V S. ; PRATER, R: Electron cyclotron current drive efficiency in general tokamak geometry. In: *Physics of Plasmas* 10 (2003), 10, 4064–4071. – URL https://doi.org/10.1063/1.1610472

[Lortz and Nuehrenberg 1978]    LORTZ, D. ; NUEHRENBERG, J.: Ballooning stability boundaries for the large-aspect-ratio tokamak. In: *Physics Letters A* 68 (1978), 1, 49–50. – URL https://www.sciencedirect.com/science/article/pii/0375960178907533. – ISSN 0375-9601

[Luce and Turco 2017]    LUCE, T ; TURCO, F: The new stable ITER Baseline Scenario with zero torque. In: *59th APS-DPP meeting (Milwaukee, October 2017)*, 2017

[Luce et al. 2001]    LUCE, T.C. ; WADE, M.R. ; POLITZER, P.A. et al.: Long pulse high performance discharges in the DIII-D tokamak. In: *Nuclear Fusion* 41 (2001), nov, 11, 1585. – URL https://dx.doi.org/10.1088/0029-5515/41/11/308

[Luda et al. 2021]   LUDA, T. ; ANGIONI, C. ; DUNNE, M.G. ; FABLE, E. ; KALLENBACH, A. ; BONANOMI, N. ; LUNT, T. ; SCHNEIDER, P.A. ; SICCINIO, M. ; TARDINI, G. et al.: Validation of a full-plasma integrated modeling approach on ASDEX Upgrade. In: *Nuclear Fusion* 61 (2021), nov, 12, 126048. – URL https://dx.doi.org/10.1088/1741-4326/ac3293

[Luda et al. 2020]   LUDA, T. ; ANGIONI, C. ; DUNNE, M.G. ; FABLE, E. ; KALLENBACH, A. ; BONANOMI, N. ; SCHNEIDER, P.A. ; SICCINIO, M. ; TARDINI, G. et al.: Integrated modeling of ASDEX Upgrade plasmas combining core, pedestal and scrape-off layer physics. In: *Nuclear Fusion* 60 (2020), feb, 3, 036023. – URL https://dx.doi.org/10.1088/1741-4326/ab6c77

[Luda et al. 2023]   LUDA, Teobaldo ; ANGIONI, Clemente ; DUNNE, Michael G. ; FABLE, Emiliano ; KALLENBACH, Arne ; BONANOMI, Nicola ; SCHNEIDER, Philip A. ; SICCINIO, Mattia ; TARDINI, Giovanni ; RODRIGUEZ-FERNANDEZ, Pablo ; HUGHES, Jerry W. ; HOWARD, Nathan T. ; FRASSINETTI, Lorenzo ; SAARELMA, Samuli: Validation of IMEP on Alcator C-Mod and JET-ILW ELMy H-mode plasmas. In: *Plasma Physics and Controlled Fusion* (2023). – URL http://iopscience.iop.org/article/10.1088/1361-6587/acb011

[Lütjens et al. 1996]   LÜTJENS, H ; BONDESON, A ; SAUTER, O: The CHEASE code for toroidal MHD equilibria. In: *Computer Physics Communications* 97 (1996), 3, 219–260. – URL https://doi.org/10.1016/0010-4655(96)00046-X. – ISSN 0010-4655

[Lux et al. 2016]   LUX, H ; KEMP, R ; FABLE, E ; WENNINGER, R: Radiation and confinement in 0D fusion systems codes. In: *Plasma Physics and Controlled Fusion* 58 (2016), may, 7, 075001. – URL https://dx.doi.org/10.1088/0741-3335/58/7/075001

[Maget et al. 2022]   MAGET, P ; MANAS, P ; ARTAUD, J-F ; BOURDELLE, C ; BUCALOSSI, J ; BUFFERAND, H ; CIRAOLO, G ; DESGRANGES, C ; DEVYNCK, P ; DUMONT, R ; FEDORCZAK, N ; FELICI, F ; GONICHE, M ; GUILLEMAUT, C ; GUIRLET, R ; GUNN, J P. ; LOARER, T ; MORALES, J ; SAUTER, O ; VAN MULDERS, S ; VÉZINET, D: Healing plasma current ramp-up by nitrogen seeding in the full tungsten environment of WEST. 64 (2022), 4, 045016. – URL https://doi.org/10.1088/1361-6587/ac4b93

[Maljaars et al. 2015]   MALJAARS, E. ; FELICI, F. ; BAAR, M.R. de ; DONGEN, J. van ; HOGEWEIJ, G.M.D. ; GEELEN, P.J.M. ; STEINBUCH, M.: Control of the tokamak safety factor profile with time-varying constraints using MPC. In: *Nuclear Fusion* 55 (2015), jan, 2, 023001. – URL https://dx.doi.org/10.1088/0029-5515/55/2/023001

[Maljaars et al. 2017]   MALJAARS, E. ; FELICI, F. ; BLANKEN, T.C. ; GALPERTI, C. ; SAUTER, O. ; BAAR, M.R. de ; CARPANESE, F. ; GOODMAN, T.P. ; KIM, D. ; KIM, S.H. ; KONG, M. ; MAVKOV, B. ; MERLE, A. ; MORET, J.M. ; NOUAILLETAS, R. ; SCHEFFER, M. ; TEPLUKHINA, A.A. ; VU, N.M.T. et al.: Profile control simulations and experiments on TCV: a controller test environment and results using a model-based predictive controller. In: *Nuclear Fusion* 57 (2017), oct, 12, 126063. – URL https://dx.doi.org/10.1088/1741-4326/aa8c48

[Manickam et al. 1994]   MANICKAM, J. ; CHANCE, M. S. ; JARDIN, S. C. ; KESSEL, C. ; MONTICELLO, D. ; POMPHREY, N. ; REIMAN, A. ; WANG, C. ; ZAKHAROV, L. E.: The prospects for

magnetohydrodynamic stability in advanced tokamak regimes. In: *Physics of Plasmas* 1 (1994), 5, 1601–1605. – URL https://doi.org/10.1063/1.870660

[Mantica et al. 2019]   MANTICA, P ; ANGIONI, C ; BONANOMI, N ; CITRIN, J ; GRIERSON, B A. ; KOECHL, F ; MARIANI, A ; STAEBLER, G M.: Progress and challenges in understanding core transport in tokamaks in support to ITER operations. In: *Plasma Physics and Controlled Fusion* 62 (2019), 1, 014021. – URL https://doi.org/10.1088/1361-6587/ab5ae1

[Marinoni et al. 2021]   MARINONI, Alessandro ; SAUTER, O. ; CODA, S.: A brief history of negative triangularity tokamak plasmas. In: *Reviews of Modern Plasma Physics* 5 (2021), 10, 6

[Martin and Takizuka 2008]   MARTIN, Y R. ; TAKIZUKA, T: Power requirement for accessing the H-mode in ITER. In: *Journal of Physics: Conference Series* 123 (2008), 012033. – URL https://doi.org/10.1088/1742-6596/123/1/012033

[Martynov 2005]   MARTYNOV, A: *PhD thesis no. 3218 Ideal MHD stability of tokamak plasmas with moderate and low aspect ratio*. École Polytechnique Fédérale de Lausanne (EPFL), CH-1015 Lausanne, Switzerland, 2005

[Mattei et al. 2016]   MATTEI, M ; ALBANESE, R ; AMBROSINO, R: *Final Report on Deliverable PMI-5.2.1-T010-D001 Scenario Modelling*. Eurofusion, 2016

[Maviglia et al. 2021]   MAVIGLIA, F. ; SICCINIO, M. ; BACHMANN, C. ; BIEL, W. ; CAVEDON, M. ; FABLE, E. ; FEDERICI, G. ; FIRDAOUSS, M. ; GERARDIN, J. ; HAUER, V. ; IVANOVA-STANIK, I. ; JANKY, F. ; KEMBLETON, R. ; MILITELLO, F. ; SUBBA, F. ; VAROUTIS, S. ; VORPAHL, C.: Impact of plasma-wall interaction and exhaust on the EU-DEMO design. In: *Nuclear Materials and Energy* 26 (2021), 100897. – URL https://www.sciencedirect.com/science/article/pii/S2352179120301587. – ISSN 2352-1791

[Mazzi et al. 2022]   MAZZI, S. ; GARCIA, J. ; ZARZOSO, D. ; KAZAKOV, Ye. O. ; ONGENA, J. ; DREVAL, M. ; NOCENTE, M. ; ŠTANCAR, Ž. ; SZEPESI, G. ; ERIKSSON, J. ; SAHLBERG, A. ; BENKADDA, S. et al.: Enhanced performance in fusion plasmas through turbulence suppression by megaelectronvolt ions. In: *Nature Physics* 18 (2022), 7, 776–782. – URL https://doi.org/10.1038/s41567-022-01626-8. ISBN 1745-2481

[Mazzucato 1976]   MAZZUCATO, E.: Small-Scale Density Fluctuations in the Adiabatic Toroidal Compressor. In: *Phys. Rev. Lett.* 36 (1976), Apr, 792–794. – URL https://link.aps.org/doi/10.1103/PhysRevLett.36.792

[McClenaghan et al. 2020]   MCCLENAGHAN, J ; GAROFALO, A M. ; LAO, L L. ; WEISBERG, D B. ; MENEGHINI, O ; SMITH, S P. ; LYONS, B C. ; STAEBLER, G M. ; DING, S Y. ; HUANG, J ; GONG, X ; QIAN, J ; REN, Q ; HOLCOMB, C T.: Transport at high $\beta_p$ and development of candidate steady state scenarios for ITER. In: *Nuclear Fusion* 60 (2020), mar, 4, 046025. – URL https://doi.org/10.1088/1741-4326/ab74a0

# Bibliography

[Meneghini et al. 2017]   MENEGHINI, O ; SMITH, S P. ; SNYDER, P B. ; STAEBLER, G M. ; CANDY, J ; BELLI, E ; LAO, L ; KOSTUK, M ; LUCE, T ; LUDA, T ; PARK, J M. ; POLI, F: Self-consistent core-pedestal transport simulations with neural network accelerated models. In: *Nuclear Fusion* 57 (2017), 8, 086034. – URL https://doi.org/10.1088/1741-4326/aa7776

[Meneghini et al. 2015]   MENEGHINI, O. ; SMITH, S.P. ; LAO, L.L. ; IZACARD, O. ; REN, Q. ; PARK, J.M. ; CANDY, J. ; WANG, Z. ; LUNA, C.J. ; IZZO, V.A. ; GRIERSON, B.A. ; SNYDER, P.B. ; HOLLAND, C. ; PENNA, J. ; LU, G. ; RAUM, P. ; MCCUBBIN, A. ; ORLOV, D.M. ; BELLI, E.A. ; FERRARO, N.M. ; PRATER, R. ; OSBORNE, T.H. ; TURNBULL, A.D. ; STAEBLER, G.M. et al.: Integrated modeling applications for tokamak experiments with OMFIT. In: *Nuclear Fusion* 55 (2015), jul, 8, 083008. – URL https://dx.doi.org/10.1088/0029-5515/55/8/083008

[Meneghini et al. 2016]   MENEGHINI, O. ; SNYDER, P. B. ; SMITH, S. P. ; CANDY, J. ; STAEBLER, G. M. ; BELLI, E. A. ; LAO, L. L. ; PARK, J. M. ; GREEN, D. L. ; ELWASIF, W. ; GRIERSON, B. A. ; HOLLAND, C.: Integrated fusion simulation with self-consistent core-pedestal coupling. In: *Physics of Plasmas* 23 (2016), 4, 042507. – URL https://doi.org/10.1063/1.4947204

[Mercier 1979]   MERCIER, C.: Summary on closed plasma systems. In: *Plasma Physics and Controlled Nuclear Fusion Research (Proc. 7th Int. Conf. Innsbruck, 1978)* 1 (1979), 701

[Mitchell et al. 2022]   MITCHELL, J ; PARROTT, A ; CASSON, F J. ; ERIKSSON, F E. ; KOECHL, F ; LENNHOLM, M ; MEYER, H ; BARDSLEY, O ; ALEIFERIS, S: Trajectory optimisation achieves non-inductive ramp-up for STEP. In: *32nd Symposium on Fusion Technology, 18th–23rd September 2022, Dubrovnik, Croatia*, 2022

[Moreau et al. 2013]   MOREAU, D. ; WALKER, M.L. ; FERRON, J.R. ; LIU, F. ; SCHUSTER, E. ; BARTON, J.E. ; BOYER, M.D. ; BURRELL, K.H. ; FLANAGAN, S.M. ; GOHIL, P. ; GROEBNER, R.J. ; HOLCOMB, C.T. ; HUMPHREYS, D.A. ; HYATT, A.W. ; JOHNSON, R.D. ; HAYE, R.J. L. ; LOHR, J. ; LUCE, T.C. ; PARK, J.M. ; PENAFLOR, B.G. ; SHI, W. ; TURCO, F. ; WEHNER, W. ; MEMBERS the ITPA-IOS group ; EXPERTS: Integrated magnetic and kinetic control of advanced tokamak plasmas on DIII-D based on data-driven models. In: *Nuclear Fusion* 53 (2013), may, 6, 063020. – URL https://dx.doi.org/10.1088/0029-5515/53/6/063020

[Moret et al. 2015]   MORET, J.-M. ; DUVAL, B.P. ; LE, H.B. ; CODA, S. ; FELICI, F. ; REIMERDES, H.: Tokamak equilibrium reconstruction code LIUQE and its real time implementation. In: *Fusion Engineering and Design* 91 (2015), 1–15. – URL https://www.sciencedirect.com/science/article/pii/S0920379614005973. – ISSN 0920-3796

[Moret et al. 1997]   MORET, J.-M. ; FRANKE, S. ; WEISEN, H. ; ANTON, M. ; BEHN, R. ; DUVAL, B. P. ; HOFMANN, F. ; JOYE, B. ; MARTIN, Y. ; NIESWAND, C. ; PIETRZYK, Z. A. ; TOLEDO, W. van: Influence of Plasma Shape on Transport in the TCV Tokamak. In: *Phys. Rev. Lett.* 79 (1997), Sep, 2057–2060. – URL https://link.aps.org/doi/10.1103/PhysRevLett.79.2057

[Murakami 1983]   MURAKAMI, M.: In: *Proc. 9th Int. Conf. Plasma Physics and Controlled Nuclear Fusion Research 1982 (Baltimore, MD, 1982)* 1 (1983), 61

[Neu et al. 2002]    NEU, R ; DUX, R ; GEIER, A ; KALLENBACH, A ; PUGNO, R ; ROHDE, V et al.: Impurity behaviour in the ASDEX Upgrade divertor tokamak with large area tungsten walls. In: *Plasma Physics and Controlled Fusion* 44 (2002), may, 6, 811. – URL https://dx.doi.org/10.1088/0741-3335/44/6/313

[Neyatani and the JT-60 Team 1996]    NEYATANI, Y ; THE JT-60 TEAM: Improved confinement with plasma profile and shape controls in JT-60U. In: *Plasma Physics and Controlled Fusion* 38 (1996), dec, 12A, A181. – URL https://dx.doi.org/10.1088/0741-3335/38/12A/014

[Nicholas et al. 2021]    NICHOLAS, T.E.G. ; DAVIS, T.P. ; FEDERICI, F. ; LELAND, J. ; PATEL, B.S. ; VINCENT, C. ; WARD, S.H.: Re-examining the role of nuclear fusion in a renewables-based energy mix. In: *Energy Policy* 149 (2021), 112043. – URL https://www.sciencedirect.com/science/article/pii/S0301421520307540. – ISSN 0301-4215

[Nocedal and Wright 2006]    NOCEDAL, J ; WRIGHT, S J.: *Numerical Optimization.* Second. Springer, 2006

[Ostuni et al. 2022]    OSTUNI, V. ; MORALES, J. ; ARTAUD, J.-F. ; BOURDELLE, C. ; MANAS, P. ; FEDORCZAK, N. ; DUMONT, R. ; GONICHE, M. ; MAGET, P. ; PEYSSON, Y. et al.: Core radiative collapse characterisation and integrated modelling in WEST plasmas. In: *Nuclear Fusion* 62 (2022), sep, 10, 106034. – URL https://dx.doi.org/10.1088/1741-4326/ac8cd6

[Pajares et al. 2019]    PAJARES, A. ; WEHNER, W.P. ; SCHUSTER, E. ; EIDIETIS, N. ; WELANDER, A. ; LA HAYE, R. ; FERRON, J. ; BARR, J. ; WALKER, M. ; HUMPHREYS, D. ; HYATT, A.: Integrated current profile, normalized beta and NTM control in DIII-D. In: *Fusion Engineering and Design* 146 (2019), 559–562. – URL https://www.sciencedirect.com/science/article/pii/S0920379619300298. – SI:SOFT-30. – ISSN 0920-3796

[Park et al. 2017]    PARK, J M. ; MURAKAMI, M. ; ST. JOHN, H E. ; LAO, L L. ; CHU, M S. ; PRATER, R.: An efficient transport solver for tokamak plasmas. In: *Computer Physics Communications* 214 (2017), 1 – 5. – URL http://www.sciencedirect.com/science/article/pii/S0010465516303976. – ISSN 0010-4655

[Peacock et al. 1969]    PEACOCK, N. J. ; ROBINSON, D. C. ; FORREST, M. J. ; WILCOCK, P. D. ; SANNIKOV, V. V.: Measurement of the Electron Temperature by Thomson Scattering in Tokamak T3. In: *Nature* 224 (1969), 5218, 488–490. – URL https://doi.org/10.1038/224488a0. ISBN 1476-4687

[Pereverzev and Corrigan 2008]    PEREVERZEV, G V. ; CORRIGAN, G: Stable numeric scheme for diffusion equation with a stiff transport. In: *Computer Physics Communications* 179 (2008), 8, 579–585. – URL https://www.sciencedirect.com/science/article/pii/S001046550800218X

[Pereverzev and Yushmanov 2002]    PEREVERZEV, Gregorij V. ; YUSHMANOV, PN: ASTRA. Automated system for transport analysis in a tokamak. (2002)

[Petty et al. 2009]    PETTY, C. C. ; AUSTIN, M. E. ; HOLCOMB, C. T. ; JAYAKUMAR, R. J. ; LA HAYE, R. J. ; LUCE, T. C. ; MAKOWSKI, M. A. ; POLITZER, P. A. ; WADE, M. R.: Magnetic-Flux Pumping

in High-Performance, Stationary Plasmas with Tearing Modes. In: *Phys. Rev. Lett.* 102 (2009), Jan, 045005. – URL https://link.aps.org/doi/10.1103/PhysRevLett.102.045005

[Petty et al. 2015]    PETTY, C.C. ; KINSEY, J.E. ; HOLCOMB, C.T. ; DEBOO, J.C. ; DOYLE, E.J. ; FERRON, J.R. ; GAROFALO, A.M. ; HYATT, A.W. ; JACKSON, G.L. ; LUCE, T.C. ; MURAKAMI, M. ; POLITZER, P.A. ; REIMERDES, H.:  High-beta, steady-state hybrid scenario on DIII-D.  In: *Nuclear Fusion* 56 (2015), dec, 1, 016016. – URL https://dx.doi.org/10.1088/0029-5515/56/1/016016

[Piron et al. 2021]    PIRON, C. ; FELICI, F. ; FAUGERAS, B. ; FERRON, N. ; MANDUCHI, G. ; MARCONATO, N. ; MEEKES, C. ; PIRON, L. ; STANCAR, Z. ; VALCARCEL, D. ; VOLTOLINA, D. ; WEILAND, M.: Development of the RAPTOR suite of codes towards real-time reconstruction of JET discharges.  In: *Fusion Engineering and Design* 169 (2021), 112431. – URL https://www.sciencedirect.com/science/article/pii/S0920379621002076. – ISSN 0920-3796

[Piron et al. 2015]    PIRON, C. ; FELICI, F. ; KIM, D. ; RAPSON, C.J. ; REICH, M. ; SAUTER, O. ; GOODMAN, T. ; TREUTTERER, W. ; BRAND, H. Van den ; CHAPMAN, I. ; FINOTTI, C. ; MANDUCCHI, G. ; MARCHIORI, G. ; MARELLI, L. ; KUDLACEK, O. ; PIOVESAN, P. ; TALIERCIO, C.: Real-time simulation of internal profiles in the presence of sawteeth using the RAPTOR code and applications to ASDEX Upgrade and RFX-mod.  In: *Europhysics Conference Abstracts* 39E (2015), P1.145. – URL http://ocs.ciemat.es/EPS2015PAP/pdf/P1.145.pdf. – Proceedings of 42nd EPS Conf. on Plasma Phys. Control. Fusion, (Lisbon, Portugal)

[Polevoi et al. 2020]    POLEVOI, A R. ; IVANOV, A A. ; MEDVEDEV, S Y. ; HUIJSMANS, G T A. ; KIM, S H. ; LOARTE, A ; FABLE, E ; KUYANOV, A Y.: Reassessment of steady-state operation in ITER with NBI and EC heating and current drive.  In: *Nuclear Fusion* 60 (2020), 9, 096024. – URL https://doi.org/10.1088/1741-4326/aba335

[Polevoi et al. 2015]    POLEVOI, A R. ; LOARTE, A ; HAYASHI, N ; KIM, H S. ; KIM, S H. ; KOECHL, F ; KUKUSHKIN, A S. ; LEONOV, V M. ; MEDVEDEV, S Y. ; MURAKAMI, M ; NA, Y S. ; PANKIN, A Y. ; PARK, J M. ; SNYDER, P B. ; SNIPES, J A. ; ZHOGOLEV, V E.: Assessment of operational space for long-pulse scenarios in ITER.  In: *Nuclear Fusion* 55 (2015), 6, 063019. – URL https://doi.org/10.1088/0029-5515/55/6/063019

[Poli et al. 2001]    POLI, E. ; PEETERS, A.G. ; PEREVERZEV, G.V.:  TORBEAM, a beam tracing code for electron-cyclotron waves in tokamak plasmas. In: *Computer Physics Communications* 136 (2001), 1, 90–104. – URL https://www.sciencedirect.com/science/article/pii/S0010465501001461. – ISSN 0010-4655

[Poli 2018]    POLI, Francesca M.:  Integrated Tokamak modeling: When physics informs engineering and research planning. In: *Physics of Plasmas* 25 (2018), 5, 055602. – URL https://doi.org/10.1063/1.5021489

[Porcelli et al. 1996]    PORCELLI, F ; BOUCHER, D ; ROSENBLUTH, M N.: Model for the sawtooth period and amplitude. In: *Plasma Physics and Controlled Fusion* 38 (1996), dec, 12, 2163. – URL https://dx.doi.org/10.1088/0741-3335/38/12/010

[Pucella et al. 2021]    PUCELLA, G. ; BURATTI, P. ; GIOVANNOZZI, E. ; ALESSI, E. ; AURIEMMA, F. ; BRUNETTI, D. ; FERREIRA, D.R. ; BARUZZO, M. ; FRIGIONE, D. ; GARZOTTI, L. ; JOFFRIN, E. ; LERCHE, E. ; LOMAS, P.J. ; NOWAK, S. ; PIRON, L. ; RIMINI, F. ; SOZZI, C. ; EESTER, D. V. ; CONTRIBUTORS, JET:  Onset of tearing modes in plasma termination on JET: the role of temperature hollowing and edge cooling.  In: *Nuclear Fusion* 61 (2021), mar,  4,  046020. – URL https://dx.doi.org/10.1088/1741-4326/abe3c7

[Puetterich et al. 2019]    PUETTERICH, T. ; FABLE, E. ; DUX, R. ; O'MULLANE, M. ; NEU, R. ; SICCINIO, M.: Determination of the tolerable impurity concentrations in a fusion reactor using a consistent set of cooling factors.  In: *Nuclear Fusion* 59 (2019), mar,  5,  056013. – URL https://dx.doi.org/10.1088/1741-4326/ab0384

[Ravensbergen et al. 2017]    RAVENSBERGEN, T. ; VRIES, P.C. de ; FELICI, F. ; BLANKEN, T.C. ; NOUAILLETAS, R. ; ZABEO, L.:  Density control in ITER: an iterative learning control and robust control approach.  In: *Nuclear Fusion*  58 (2017), dec,  1,  016048. –  URL https://dx.doi.org/10.1088/1741-4326/aa95ce

[Ravensbergen et al. 2023]    RAVENSBERGEN, Timo ; ZABEO, Luca ; DE VRIES, Peter ; PANGIONE, L. ; TREUTTERER, Wolfgang ; DE TOMMASI, Gianmaria ; LEE, Woong ryol ; TAK, Taehyun ; ZAGAR, Anze:  Strategy towards model-based design and testing of the ITER Plasma Control System.  In: *Fusion Engineering and Design*  188 (2023),  113440. –  URL https://www.sciencedirect.com/science/article/pii/S0920379623000248. – ISSN 0920-3796

[Redl et al. 2021]    REDL, A. ; ANGIONI, C. ; BELLI, E. ; SAUTER, O.:  A new set of analytical formulae for the computation of the bootstrap current and the neoclassical conductivity in tokamaks.  In: *Physics of Plasmas* 28 (2021),  2,  022502. – URL https://doi.org/10.1063/5.0012664

[Reimerdes et al. 2002]    REIMERDES, H. ; SAUTER, O. ; GOODMAN, T. ; POCHELON, A.:  From Current-Driven to Neoclassically Driven Tearing Modes. In: *Phys. Rev. Lett.* 88 (2002), Feb, 105005. – URL https://link.aps.org/doi/10.1103/PhysRevLett.88.105005

[Reisner et al. 2020]    REISNER, M. ; FABLE, E. ; STOBER, J. ; BOCK, A. ; NAVARRO, A. B. ; SIENA, A. D. ; FISCHER, R. ; BOBKOV, V. ; MCDERMOTT, R. et al.: Increased core ion temperatures in high-beta advanced scenarios in ASDEX upgrade. In: *Nuclear Fusion* 60 (2020), jul,  8, 082005. – URL https://dx.doi.org/10.1088/1741-4326/ab8b32

[Rodriguez-Fernandez et al. 2022a]    RODRIGUEZ-FERNANDEZ, P. ; CREELY, A.J. ; GREENWALD, M.J. ; BRUNNER, D. ; BALLINGER, S.B. ; CHROBAK, C.P. ; GARNIER, D.T. ; GRANETZ, R. ; HARTWIG, Z.S. ; HOWARD, N.T. ; HUGHES, J.W. ; IRBY, J.H. ; IZZO, V.A. ; KUANG, A.Q. ; LIN, Y. ; MARMAR, E.S. ; MUMGAARD, R.T. ; REA, C. ; REINKE, M.L. ; RICCARDO, V. ; RICE, J.E. ; SCOTT, S.D. ; SORBOM, B.N. ; STILLERMAN, J.A. ; SWEENEY, R. ; TINGUELY, R.A. ; WHYTE, D.G. ; WRIGHT, J.C. ; YURYEV, D.V.: Overview of the SPARC physics basis towards the exploration of burning-plasma regimes in high-field, compact tokamaks. In: *Nuclear Fusion* 62 (2022), mar,  4,  042003. – URL https://dx.doi.org/10.1088/1741-4326/ac1654

## Bibliography

[Rodriguez-Fernandez et al. 2020]  RODRIGUEZ-FERNANDEZ, P ; HOWARD, N T. ; GREENWALD, M J. ; CREELY, A J. ; HUGHES, J W. ; WRIGHT, J C. ; HOLLAND, C ; LIN, Y ; SCIORTINO, F: Predictions of core plasma performance for the SPARC tokamak. In: *Journal of Plasma Physics* 86 (2020), 5, 865860503

[Rodriguez-Fernandez et al. 2022b]  RODRIGUEZ-FERNANDEZ, P. ; HOWARD, N.T. ; CANDY, J.: Nonlinear gyrokinetic predictions of SPARC burning plasma profiles enabled by surrogate modeling. In: *Nuclear Fusion* 62 (2022), may, 7, 076036. – URL https://dx.doi.org/10.1088/1741-4326/ac64b2

[Rogelj et al. 2016]  ROGELJ, Joeri ; ELZEN, Michel den ; HÖHNE, Niklas ; FRANSEN, Taryn ; FEKETE, Hanna ; WINKLER, Harald ; SCHAEFFER, Roberto ; SHA, Fu ; RIAHI, Keywan ; MEINSHAUSEN, Malte: Paris Agreement climate proposals need a boost to keep warming well below 2 °C. In: *Nature* 534 (2016), 7609, 631–639. – URL https://doi.org/10.1038/nature18307. ISBN 1476-4687

[Romanelli et al. 2014]  ROMANELLI, Michele ; CORRIGAN, Gerard ; PARAIL, Vassili ; WIESEN, Sven ; AMBROSINO, Roberto ; BELO, Paula Da Silva A. ; GARZOTTI, Luca ; HARTING, Derek ; KÖCHL, Florian ; KOSKELA, Tuomas et al.: JINTRAC: A System of Codes for Integrated Simulation of Tokamak Scenarios. In: *Plasma and Fusion Research* 9 (2014), 3403023–3403023

[Romero and JET-EFDA Contributors 2010]  ROMERO, J.A. ; JET-EFDA CONTRIBUTORS: Plasma internal inductance dynamics in a tokamak. In: *Nuclear Fusion* 50 (2010), sep, 11, 115002. – URL https://dx.doi.org/10.1088/0029-5515/50/11/115002

[Ryter et al. 2001]  RYTER, F. ; LEUTERER, F. ; PEREVERZEV, G. ; FAHRBACH, H.-U. ; STOBER, J. ; SUTTROP, W. ; TEAM, ASDEX U.: Experimental Evidence for Gradient Length-Driven Electron Transport in Tokamaks. In: *Phys. Rev. Lett.* 86 (2001), Mar, 2325–2328. – URL https://link.aps.org/doi/10.1103/PhysRevLett.86.2325

[Saarelma et al. 2017]  SAARELMA, S ; CHALLIS, C D. ; GARZOTTI, L ; FRASSINETTI, L ; MAGGI, C F. ; ROMANELLI, M ; STOKES, C et al.: Integrated modelling of H-mode pedestal and confinement in JET-ILW. In: *Plasma Physics and Controlled Fusion* 60 (2017), nov, 1, 014042. – URL https://dx.doi.org/10.1088/1361-6587/aa8d45

[Sabbagh et al. 2006]  SABBAGH, S. A. ; BELL, R. E. ; MENARD, J. E. ; GATES, D. A. ; SONTAG, A. C. ; BIALEK, J. M. ; LEBLANC, B. P. ; LEVINTON, F. M. ; TRITZ, K. ; YUH, H.: Active Stabilization of the Resistive-Wall Mode in High-Beta, Low-Rotation Plasmas. In: *Phys. Rev. Lett.* 97 (2006), Jul, 045004. – URL https://link.aps.org/doi/10.1103/PhysRevLett.97.045004

[Saibene et al. 1999]  SAIBENE, G. ; HORTON, L.D. ; SARTORI, R. ; BALET, B. ; CLEMENT, S. ; CONWAY, G.D. ; CORDEY, J.G. ; ESCH, H.P.L. D. ; INGESSON, L.C. ; LINGERTAT, J. ; MONK, R.D. ; PARAIL, V.V. ; SMITH, R.J. ; TARONI, A. ; THOMSEN, K. ; HELLERMANN, M.G. von: The influence of isotope mass, edge magnetic shear and input power on high density ELMy H

modes in JET. In: *Nuclear Fusion* 39 (1999), sep, 9, 1133. – URL https://dx.doi.org/10.1088/0029-5515/39/9/307

[Sauter 2016]   SAUTER, O.: Geometric formulas for system codes including the effect of negative triangularity. In: *Fusion Engineering and Design* 112 (2016), 633–645. – URL https://www.sciencedirect.com/science/article/pii/S0920379616303234. – ISSN 0920-3796

[Sauter et al. 1998]   SAUTER, O. ; ANGIONI, C. ; BOUCHER, D. ; FURNO, I. ; POCHELON, A. ; PORCELLI, F.: Sawtooth period simulations of TCV discharges. In: *Proc. Joint Varenna-Lausanne Int. Workshop on Theory of Fusion Plasmas, Varenna, Italy, August, 1999*, 1998, 403 – 408

[Sauter et al. 2001]   SAUTER, O ; ANGIONI, C ; CODA, S ; GOMEZ, P ; GOODMAN, T P. ; HENDERSON, M A. ; HOFMANN, F ; HOGGE, J-P ; MORET, J-M ; NIKKOLA, P ; PIETRZYK, Z A. ; WEISEN, H et al.: Steady-state fully noninductive operation with electron cyclotron current drive and current profile control in the tokamak à configuration variable (TCV). In: *Physics of Plasmas* 8 (2001), 5, 2199–2207. – URL https://doi.org/10.1063/1.1355317

[Sauter et al. 1999]   SAUTER, O ; ANGIONI, C ; LIN-LIU, Y R.: Neoclassical conductivity and bootstrap current formulas for general axisymmetric equilibria and arbitrary collisionality regime. In: *Physics of Plasmas* 6 (1999), 7, 2834–2839. – URL https://doi.org/10.1063/1.873240

[Sauter et al. 2002a]   SAUTER, O ; ANGIONI, C ; LIN-LIU, Y R.: Erratum: "Neoclassical conductivity and bootstrap current formulas for general axisymmetric equilibria and arbitrary collisionality regime" [Phys. Plasmas 6, 2834 (1999)]. In: *Physics of Plasmas* 9 (2002), 12, 5140–5140. – URL https://doi.org/10.1063/1.1517052

[Sauter et al. 2014]   SAUTER, O. ; BRUNNER, S. ; KIM, D. ; MERLO, G. ; BEHN, R. ; CAMENEN, Y. ; CODA, S. ; DUVAL, B. P. ; FEDERSPIEL, L. ; GOODMAN, T. P. ; KARPUSHOV, A. ; MERLE, A. et al.: On the non-stiffness of edge transport in L-mode tokamak plasmas. In: *Physics of Plasmas* 21 (2014), 5, 055906. – URL https://doi.org/10.1063/1.4876612

[Sauter et al. 2002b]   SAUTER, O ; BUTTERY, R J. ; FELTON, R ; HENDER, T C. ; HOWELL, D F. et al.: Marginal $\beta$-limit for neoclassical tearing modes in JET H-mode discharges. In: *Plasma Physics and Controlled Fusion* 44 (2002), aug, 9, 1999. – URL https://dx.doi.org/10.1088/0741-3335/44/9/315

[Sauter et al. 2000]   SAUTER, O ; HENDERSON, M A. ; HOFMANN, F ; GOODMAN, T et al.: Steady-State Fully Noninductive Current Driven by Electron Cyclotron Waves in a Magnetically Confined Plasma. In: *Physical Review Letters* 84 (2000), 3322–3325. – URL https://link.aps.org/doi/10.1103/PhysRevLett.84.3322

[Sauter et al. 2010]   SAUTER, O ; HENDERSON, M A. ; RAMPONI, G ; ZOHM, H ; ZUCCA, C: On the requirements to control neoclassical tearing modes in burning plasmas. In: *Plasma Physics and Controlled Fusion* 52 (2010), jan, 2, 025002. – URL https://dx.doi.org/10.1088/0741-3335/52/2/025002

# Bibliography

[Sauter et al. 1997]   SAUTER, O. ; LA HAYE, R. J. ; CHANG, Z. ; GATES, D. A. ; KAMADA, Y. ; ZOHM, H. et al.: Beta limits in long-pulse tokamak discharges. In: *Physics of Plasmas* 4 (1997), 5, 1654–1664. – URL https://doi.org/10.1063/1.872270

[Sauter and Medvedev 2013]   SAUTER, O. ; MEDVEDEV, S.Yu.: Tokamak coordinate conventions: COCOS. In: *Computer Physics Communications* 184 (2013), 2, 293–302. – URL https://www.sciencedirect.com/science/article/pii/S0010465512002962. – ISSN 0010-4655

[Sauter et al. 2021]   SAUTER, O ; VALLAR, M ; LABIT, B ; KARPUSHOV, A ; BAGNATO, F ; CODA, S ; MERLE, A ; PÜTTERICH, T ; BOBKOV, V ; DUNNE, MG et al.: ITER baseline scenario investigations on TCV and comparison with AUG. In: *28th IAEA Fusion Energy Conf.*, 2021

[Sauter et al. 2002c]   SAUTER, O. ; WESTERHOF, E. ; MAYORAL, M. L. ; ALPER, B. ; BELO, P. A. ; BUTTERY, R. J. ; GONDHALEKAR, A. ; HELLSTEN, T. ; HENDER, T. C. ; HOWELL, D. F. ; JOHNSON, T. ; LAMALLE, P. ; MANTSINEN, M. J. ; MILANI, F. ; NAVE, M. F. F. ; NGUYEN, F. ; PECQUET, A. L. ; PINCHES, S. D. ; PODDA, S. ; RAPP, J.: Control of Neoclassical Tearing Modes by Sawtooth Control. In: *Phys. Rev. Lett.* 88 (2002), Feb, 105001. – URL https://link.aps.org/doi/10.1103/PhysRevLett.88.105001

[Sauter et al. 2011]   SAUTER, P. ; PÜTTERICH, T. ; RYTER, F. ; VIEZZER, E. ; WOLFRUM, E. ; CONWAY, G.D. ; FISCHER, R. ; KURZAN, B. ; MCDERMOTT, R.M. ; RATHGEBER, S.K. et al.: L- to H-mode transitions at low density in ASDEX Upgrade. In: *Nuclear Fusion* 52 (2011), dec, 1, 012001. – URL https://dx.doi.org/10.1088/0029-5515/52/1/012001

[Scarabosio et al. 2009]   SCARABOSIO, A. ; HAAS, G. ; MÜLLER, H.W. ; PUGNO, R. ; WISCHMEIER, M.: Measurements of neutral gas fluxes under different plasma and divertor regimes in ASDEX Upgrade. In: *Journal of Nuclear Materials* 390-391 (2009), 494–497. – URL https://www.sciencedirect.com/science/article/pii/S0022311509001652. – Proceedings of the 18th International Conference on Plasma-Surface Interactions in Controlled Fusion Device. – ISSN 0022-3115

[Schneider et al. 2000]   SCHNEIDER, W ; MCCARTHY, PJ ; LACKNER, K ; GRUBER, O ; BEHLER, K ; MARTIN, P ; MERKEL, R: ASDEX upgrade MHD equilibria reconstruction on distributed workstations. In: *Fusion Engineering and Design* 48 (2000), 1, 127–134. – URL https://www.sciencedirect.com/science/article/pii/S0920379600001095. – ISSN 0920-3796

[Schramm et al. 2022]   SCHRAMM, R ; BOCK, A ; VAN MULDERS, S ; STOBER, J ; FABLE, E ; SAUTER, O ; ZOHM, H et al.: Model based formation of Advanced Tokamak discharges. In: *IAEA Technical Meeting on Long Pulse Operation*, 2022

[Shafranov 1957]   SHAFRANOV, V D.: On magnetohydrodynamical equilibrium configurations. In: *Journal of Experimental and Theoretical Physics* 33 (1957), 710

[Shimada et al. 2007]   SHIMADA, M ; CAMPBELL, D J. ; MUKHOVATOV, V ; FUJIWARA, M ; KIRNEVA, N ; LACKNER, K ; NAGAMI, M ; PUSTOVITOV, V D. ; UCKAN, N ; WESLEY, J ; ASAKURA, N ; COSTLEY, A E. ; DONNÉ, A J H. ; DOYLE, E J. ; FASOLI, A ; GORMEZANO, C ; GRIBOV, Y ;

GRUBER, O ; HENDER, T C. ; HOULBERG, W ; IDE, S ; KAMADA, Y ; LEONARD, A ; LIPSCHULTZ, B ; LOARTE, A ; MIYAMOTO, K ; MUKHOVATOV, V ; OSBORNE, T H. ; POLEVOI, A ; SIPS, A C C.: Chapter 1: Overview and summary. In: *Nuclear Fusion* 47 (2007), 6, S1–S17. – URL https://doi.org/10.1088/0029-5515/47/6/S01

[Siccinio et al. 2018]    SICCINIO, M. et al.:  Development of a plasma scenario for the EU-DEMO: current activities and perspectives.  (2018). – Proceedings of the 2018 IAEA Fusion Energy Conf. (Gandhinagar, India, 22–27 October 2018)

[Siccinio et al. 2020]    SICCINIO, M. ; BIEL, W. ; CAVEDON, M. ; FABLE, E. ; FEDERICI, G. ; JANKY, F. ; LUX, H. ; MAVIGLIA, F. ; MORRIS, J. ; PALERMO, F. ; SAUTER, O. ; SUBBA, F. ; ZOHM, H.: DEMO physics challenges beyond ITER. In: *Fusion Engineering and Design* 156 (2020), 111603. – URL https://www.sciencedirect.com/science/article/pii/S0920379620301514. – ISSN 0920-3796

[Siccinio et al. 2019]    SICCINIO, M. ; FEDERICI, G. ; KEMBLETON, R. ; LUX, H. ; MAVIGLIA, F. ; MORRIS, J.:  Figure of merit for divertor protection in the preliminary design of the EU-DEMO reactor. In: *Nuclear Fusion* 59 (2019), aug, 10, 106026. – URL https://dx.doi.org/10.1088/1741-4326/ab3153

[Silvagni et al. 2023]    SILVAGNI, D. ; DUNNE, M. ; LUDA, T. ; BOCK, A. ; BURCKHART, A. ; FISCHER, R. ; GRIENER, M ; MCDERMOTT, R ; PLANK, U ; PÜTTERICH, T ; REISNER, M ; STOBER, J ; AL, B ; TARDINI, G ; ZOHM, H et al.: The impact of divertor neutral pressure on confinement degradation of Advanced Tokamak Scenarios at ASDEX Upgrade. In: *subm. Nuclear Fusion* (2023)

[Soeldner and The JET Team 1997]    SOELDNER ; THE JET TEAM: Shear optimization experiments with current profile control on JET. In: *Plasma Physics and Controlled Fusion* 39 (1997), dec, 12B, B353. – URL https://dx.doi.org/10.1088/0741-3335/39/12B/027

[Spitzer 1962]    SPITZER, L: *Physics of Fully Ionized Gases*. Second. Interscience Publishers ING, New York, 1962

[Stix 1972]    STIX, T H.: Heating of toroidal plasmas by neutral injection. In: *Plasma Physics* 14 (1972), apr, 4, 367. – URL https://dx.doi.org/10.1088/0032-1028/14/4/002

[Stober et al. 2000]    STOBER, J ; GRUBER, O ; KALLENBACH, A ; MERTENS, V ; RYTER, F ; STAEBLER, A ; SUTTROP, W ; TREUTTERER, W et al.: Effects of triangularity on confinement, density limit and profile stiffness of H-modes on ASDEX upgrade. In: *Plasma Physics and Controlled Fusion* 42 (2000), may, 5A, A211. – URL https://dx.doi.org/10.1088/0741-3335/42/5A/324

[Stober et al. 2020]    STOBER, J ; REISNER, M ; ANGIONI, C ; NAVARRO, A B. ; BOBKOV, V ; BOCK, A ; DENISOV, G ; FABLE, E ; FISCHER, R ; GANTENBEIN, G ; GIL, L ; GOERLER, T ; IGOCHINE, V ; KASPAREK, W ; LEUTERER, F ; LITVAK, A ; MCDERMOTT, R ; MEIER, A ; MONACO, F ; MUENICH, M ; NICHIPORENKO, V ; PLAUM, B ; PLANK, U ; POLI, E ; POPOV, L ; PUETTERICH,

Th ; Scherer, Th ; Schubert, M ; Suttrop, W ; Tai, E ; Thumm, M ; Wagner, D ; Zohm, H:
Exploring fusion-reactor physics with high-power electron cyclotron resonance heating on
ASDEX Upgrade. In: *Plasma Physics and Controlled Fusion* 62 (2020), 2, 024012. – URL
https://doi.org/10.1088/1361-6587/ab512b

[Stober et al. 2007]    Stober, J. ; Sips, A.C.C. ; Angioni, C. ; Forest, C.B. ; Gruber, O. ;
Hobirk, J. ; Horton, L.D. ; Maggi, C.F. ; Maraschek, M. ; Martin, P. ; Carthy, P.J. M. ;
Mertens, V. ; Na, Y.-S. ; Reich, M. ; Staebler, A. ; Tardini, G. ; Zohm, H. et al.: The role of
the current profile in the improved H-mode scenario in ASDEX Upgrade. In: *Nuclear Fusion*
47 (2007), jul, 8, 728. – URL https://dx.doi.org/10.1088/0029-5515/47/8/002

[Stober et al. 2015]    Stober, J ; Sommer, F ; Angioni, C ; Bock, A ; Fable, E ; Leuterer, F ;
Monaco, F ; Müller, S ; Münich, M ; Petzold, B ; Poli, E ; Schubert, M ; Schütz, H ;
Wagner, D ; Zohm, H ; Kasparek, W ; Plaum, B ; Meier, A ; Scherer, Th ; Strauss, D ;
Jelonnek, J ; Thumm, M ; Litvak, A ; Denisov, G G. ; Chirkov, A V. ; Tai, E M. ; Popov, L G. ;
Nichiporenko, V O. ; Myasnikov, V E. ; Soluyanova, E A. ; Malygin, V: High power ECRH
and ECCD in moderately collisional ASDEX Upgrade H- modes and status of EC system
upgrade. In: *EPJ Web of Conferences* 87 (2015), 02004

[Strait 1994]    Strait, E. J.: Stability of high beta tokamak plasmas*. In: *Physics of Plasmas* 1
(1994), 5, 1415–1431. – URL https://doi.org/10.1063/1.870691

[Sykes et al. 2017]    Sykes, A. ; Costley, A.E. ; Windsor, C.G. ; Asunta, O. ; Brittles, G. ;
Buxton, P. ; Chuyanov, V. ; Connor, J.W. ; Gryaznevich, M.P. ; Huang, B. ; Hugill, J. ;
Kukushkin, A. ; Kingham, D. ; Langtry, A.V. ; McNamara, S. ; Morgan, J.G. ; Noonan,
P. ; Ross, J.S.H. ; Shevchenko, V. ; Slade, R. ; Smith, G.: Compact fusion energy based
on the spherical tokamak. In: *Nuclear Fusion* 58 (2017), nov, 1, 016039. – URL https:
//dx.doi.org/10.1088/1741-4326/aa8c8d

[Sykes and Wesson 1980]    Sykes, A. ; Wesson, J. A.: Major Disruptions in Tokamaks. In: *Phys.
Rev. Lett.* 44 (1980), May, 1215–1218. – URL https://link.aps.org/doi/10.1103/PhysRevLett.
44.1215

[Taylor et al. 1994]    Taylor, T S. ; John, H S. ; Turnbull, A D. ; Lin-Liu, V R. ; Burrell, K H. ;
Chan, V ; Chu, M S. ; Ferron, J R. ; Lao, L L. ; Haye, R J L. ; Lazarus, E A. ; Miller, R L. ;
Politzer, P A. ; Schissel, D P. ; Strait, E J.: Optimized profiles for improved confinement
and stability in the DIII-D tokamak. In: *Plasma Physics and Controlled Fusion* 36 (1994),
dec, 12B, B229. – URL https://dx.doi.org/10.1088/0741-3335/36/12B/019

[Teplukhina et al. 2017]    Teplukhina, A A. ; Sauter, O ; Felici, F ; Merle, A ; Kim, D:
Simulation of profile evolution from ramp-up to ramp-down and optimization of tokamak
plasma termination with the RAPTOR code. In: *Plasma Physics and Controlled Fusion* 59
(2017), 12, 124004. – URL https://doi.org/10.1088/1361-6587/aa857e

[Teplukhina 2018]    Teplukhina, Anna: *PhD thesis no. 8478 Realistic multi-machine tokamak
profile simulations and numerical ramp-down optimization using the RAPTOR code.* École

Polytechnique Fédérale de Lausanne (EPFL), CH-1015 Lausanne, Switzerland, 2018. – URL http://infoscience.epfl.ch/record/254942

[The DIFFER Team 2017]    THE DIFFER TEAM: *DIFFER Strategic Plan 2017-2022. Tech. rep.* Institute for Fundamental Energy Research, Eindhoven, 2017. – URL https://www.differ.nl/strategic-plan

[Troyon 1984]    TROYON, F.: MHD-Limits to Plasma Confinement. In: *Plasma Phys. Control. Fusion* 26 (1984), 209–215

[Troyon et al. 1988]    TROYON, F ; ROY, A ; COOPER, W A. ; YASSEEN, F ; TURNBULL, A: Beta limit in tokamaks. Experimental and computational status. In: *Plasma Physics and Controlled Fusion* 30 (1988), oct, 11, 1597. – URL https://dx.doi.org/10.1088/0741-3335/30/11/019

[Turco et al. 2018]    TURCO, F. ; LUCE, T.C. ; SOLOMON, W. ; JACKSON, G. ; NAVRATIL, G.A. ; HANSON, J.M.:   The causes of the disruptive tearing instabilities of the ITER Baseline Scenario in DIII-D. In: *Nuclear Fusion* 58 (2018), sep, 10, 106043. – URL https://dx.doi.org/10.1088/1741-4326/aadbb5

[Turnbull et al. 1988]    TURNBULL, A.D. ; ROY, A. ; SAUTER, O. ; TROYON, F.S.:   Current and beta limitations for the TCV tokamak. In: *Nuclear Fusion* 28 (1988), aug, 8, 1379. – URL https://dx.doi.org/10.1088/0029-5515/28/8/006

[Turnbull et al. 1989]    TURNBULL, A.D. ; YASSEEN, F. ; ROY, A. ; SAUTER, O. ; COOPER, W.A. ; NICLI, S. ; TROYON, F.: Low-n ideal MHD stability of tokamaks: Current and beta limits. In: *Nuclear Fusion* 29 (1989), apr, 4, 629. – URL https://dx.doi.org/10.1088/0029-5515/29/4/008

[van de Plassche et al. 2020]    VAN DE PLASSCHE, K L. ; CITRIN, J ; BOURDELLE, C ; CAMENEN, Y ; CASSON, F J. ; DAGNELIE, V I. ; FELICI, F ; HO, A ; VAN MULDERS, S: Fast modeling of turbulent transport in fusion plasmas using neural networks. In: *Physics of Plasmas* 27 (2020), 2, 022310. – URL https://doi.org/10.1063/1.5134126

[van Dongen et al. 2014]    VAN DONGEN, J ; FELICI, F ; HOGEWEIJ, G M D. ; GEELEN, P ; MALJAARS, E: Numerical optimization of actuator trajectories for ITER hybrid scenario profile evolution. In: *Plasma Physics and Controlled Fusion* 56 (2014), 12, 125008. – URL https://doi.org/10.1088/0741-3335/56/12/125008

[Van Mulders et al. 2021a]    VAN MULDERS, S ; FELICI, F ; SAUTER, O ; CITRIN, J ; HO, A ; MARIN, M ; VAN DE PLASSCHE, K L.:   A novel tool for rapid optimization of stationary tokamak plasmas using RAPTOR-QLKNN applied to the ITER hybrid scenario. In: *47th EPS Conference on Plasma Physics (EPS 2021)*, 2021, p5–1053

[Van Mulders et al. 2021b]    VAN MULDERS, S. ; FELICI, F. ; SAUTER, O. ; CITRIN, J. ; HO, A. ; MARIN, M. ; VAN DE PLASSCHE, K.L.: Rapid optimization of stationary tokamak plasmas in RAPTOR: demonstration for the ITER hybrid scenario with neural network surrogate

transport model QLKNN. In: *Nuclear Fusion* 61 (2021), 8, 086019. – URL https://doi.org/10.1088/1741-4326/ac0d12

[Verdoolaege et al. 2021] VERDOOLAEGE, G ; KAYE, S M. ; ANGIONI, C ; KARDAUN, O ; MASLOV, M ; ROMANELLI, M ; RYTER, F ; THOMSEN, K: The updated ITPA global H-mode confinement database: description and analysis. In: *Nuclear Fusion* (2021). – URL http://iopscience.iop.org/article/10.1088/1741-4326/abdb91

[Viezzer 2018] VIEZZER, E.: Access and sustainment of naturally ELM-free and small-ELM regimes. In: *Nuclear Fusion* 58 (2018), sep, 11, 115002. – URL https://dx.doi.org/10.1088/1741-4326/aac222

[Vu et al. 2019] VU, N.M. T. ; BLANKEN, T.C. ; FELICI, F. ; GALPERTI, C. ; KONG, M. ; MALJAARS, E. ; SAUTER, O.: Tokamak-agnostic actuator management for multi-task integrated control with application to TCV and ITER. In: *Fusion Engineering and Design* 147 (2019), 111260. – URL https://www.sciencedirect.com/science/article/pii/S0920379619307380. – ISSN 0920-3796

[Vu et al. 2021] VU, Trang ; FELICI, Federico ; GALPERTI, Cristian ; MARASCHEK, Marc ; PAU, Alessandro ; RISPOLI, Natale ; SAUTER, Olivier ; SIEGLIN, Bernhard: *Integrated Real-Time Supervisory Management for Off-Normal-Event Handling and Feedback Control of Tokamak Plasmas.* 2021

[Wagner et al. 1982] WAGNER, F. ; BECKER, G. ; BEHRINGER, K. ; CAMPBELL, D. ; EBERHAGEN, A. ; ENGELHARDT, W. ; FUSSMANN, G. ; GEHRE, O. ; GERNHARDT, J. ; GIERKE, G. v. ; HAAS, G. ; HUANG, M. ; KARGER, F. ; KEILHACKER, M. ; KLÜBER, O. ; KORNHERR, M. ; LACKNER, K. ; LISITANO, G. ; LISTER, G. G. ; MAYER, H. M. ; MEISEL, D. ; MÜLLER, E. R. ; MURMANN, H. ; NIEDERMEYER, H. ; POSCHENRIEDER, W. ; RAPP, H. ; RÖHR, H. ; SCHNEIDER, F. ; SILLER, G. ; SPETH, E. ; STÄBLER, A. ; STEUER, K. H. ; VENUS, G. ; VOLLMER, O. ; YÜ, Z.: Regime of Improved Confinement and High Beta in Neutral-Beam-Heated Divertor Discharges of the ASDEX Tokamak. In: *Phys. Rev. Lett.* 49 (1982), Nov, 1408–1412. – URL https://link.aps.org/doi/10.1103/PhysRevLett.49.1408

[Wagner et al. 2010] WAGNER, F ; BECOULET, A ; BUDNY, R ; ERCKMANN, V ; FARINA, D ; GIRUZZI, G ; KAMADA, Y ; KAYE, A ; KOECHL, F ; LACKNER, K ; MARUSHCHENKO, N ; MURAKAMI, M ; OIKAWA, T ; PARAIL, V ; PARK, J M. ; RAMPONI, G ; SAUTER, O ; STORK, D ; THOMAS, P R. ; TRAN, Q M. ; WARD, D ; ZOHM, H ; ZUCCA, C: On the heating mix of ITER. In: *Plasma Physics and Controlled Fusion* 52 (2010), 12, 124044. – URL https://doi.org/10.1088/0741-3335/52/12/124044

[Wang et al. 2017] WANG, Hexiang ; SCHUSTER, Eugenio ; RAFIQ, Tariq ; KRITZ, Arnold ; DING, Siye: Model-based optimal scenario planning in EAST. In: *Fusion Engineering and Design* 123 (2017), 569–573. – URL https://www.sciencedirect.com/science/article/pii/S0920379617303630. – Proceedings of the 29th Symposium on Fusion Technology (SOFT-29) Prague, Czech Republic, September 5-9, 2016. – ISSN 0920-3796

[Wang et al. 2021]   WANG, L. ; WANG, H. Q. ; DING, S. ; GAROFALO, A. M. ; GONG, X. Z. ; ELDON, D. ; GUO, H. Y. ; LEONARD, A. W. ; HYATT, A. W. ; QIAN, J. P. ; WEISBERG, D. B. ; MCCLENAGHAN, J. ; FENSTERMACHER, M. E. ; LASNIER, C. J. ; WATKINS, J. G. ; SHAFER, M. W. ; XU, G. S. ; HUANG, J. ; REN, Q. L. ; BUTTERY, R. J. ; HUMPHREYS, D. A. ; THOMAS, D. M. ; ZHANG, B. ; LIU, J. B.: Integration of full divertor detachment with improved core confinement for tokamak fusion plasmas. In: *Nature Communications* 12 (2021), 1, 1365. – URL https://doi.org/10.1038/s41467-021-21645-y. ISBN 2041-1723

[Warmer et al. 2016]   WARMER, F ; BEIDLER, C D. ; DINKLAGE, A ; WOLF, R ; TEAM, The W7-X: From W7-X to a HELIAS fusion power plant: motivation and options for an intermediate-step burning-plasma stellarator. In: *Plasma Physics and Controlled Fusion* 58 (2016), jun, 7, 074006. – URL https://dx.doi.org/10.1088/0741-3335/58/7/074006

[Wehner et al. 2017]   WEHNER, William ; BARTON, Justin ; LAURET, Menno ; SCHUSTER, Eugenio ; FERRON, John R. ; HOLCOMB, Chris ; LUCE, Tim C. ; HUMPHREYS, David A. ; WALKER, Michael L. ; PENAFLOR, Ben G. ; JOHNSON, Robert D.: Optimal current profile control for enhanced repeatability of L-mode and H-mode discharges in DIII-D. In: *Fusion Engineering and Design* 123 (2017), 513–517. – URL https://www.sciencedirect.com/science/article/pii/S0920379617302259. – Proceedings of the 29th Symposium on Fusion Technology (SOFT-29) Prague, Czech Republic, September 5-9, 2016. – ISSN 0920-3796

[Wehner et al. 2019]   WEHNER, W.P. ; SCHUSTER, E. ; BOYER, M.D. ; POLI, F.M.: TRANSP-based optimization towards tokamak scenario development. In: *Fusion Engineering and Design* 146 (2019), 547–550. – URL https://www.sciencedirect.com/science/article/pii/S0920379619300274. – SI:SOFT-30. – ISSN 0920-3796

[Weiland et al. 2018]   WEILAND, M ; BILATO, R ; DUX, R ; GEIGER, B ; LEBSCHY, A ; FELICI, F ; FISCHER, R ; RITTICH, D ; VAN ZEELAND, M: RABBIT: Real-time simulation of the NBI fast-ion distribution. In: *Nuclear Fusion* 58 (2018), 8, 082032. – URL https://doi.org/10.1088/1741-4326/aabf0f

[Weiland et al. 2023]   WEILAND, Markus ; BILATO, Roberto ; SIEGLIN, Bernhard ; FELICI, Federico ; GIANNONE, Louis ; KUDLACEK, Ondrej ; RAMPP, Markus ; SCHEFFER, Mark ; TREUTTERER, W ; ZEHETBAUER, Thomas: Real-time implementation of the high-fidelity NBI code RABBIT into the Discharge Control System of ASDEX Upgrade. In: *Nuclear Fusion* (2023). – URL http://iopscience.iop.org/article/10.1088/1741-4326/acc31c

[Weisen et al. 2005]   WEISEN, H ; ZABOLOTSKY, A ; ANGIONI, C ; FURNO, I ; GARBET, X ; GIROUD, C ; LEGGATE, H ; MANTICA, P ; MAZON, D ; WEILAND, J ; ZABEO, L ; ZASTROW, K.-D: Collisionality and shear dependences of density peaking in JET and extrapolation to ITER. In: *Nuclear Fusion* 45 (2005), 2, L1–L4. – URL https://doi.org/10.1088/0029-5515/45/2/L01

[Wesson 2004]   WESSON, J: *Tokamaks*. Third. Oxford Science Publications, 2004

# Bibliography

[Wesson et al. 1989]   WESSON, J.A. ; GILL, R.D. ; HUGON, M. ; SCHUELLER, F.C. ; SNIPES, J.A. ; WARD, D.J. et al.: Disruptions in JET. In: *Nuclear Fusion* 29 (1989), apr, 4, 641. – URL https://dx.doi.org/10.1088/0029-5515/29/4/009

[Wilson et al. 2020]   WILSON, Howard ; CHAPMAN, Ian ; DENTON, Tris ; MORRIS, William ; PATEL, Bhavin ; VOSS, Garry ; WALDON, Chris et al.: STEP on the pathway to fusion commercialization. In: *Commercialising Fusion Energy*. IOP Publishing, 2020 (2053-2563), 8–1 to 8–18. – URL https://dx.doi.org/10.1088/978-0-7503-2719-0ch8. – ISBN 978-0-7503-2719-0

[Witrant et al. 2007]   WITRANT, E ; JOFFRIN, E ; BRÉMOND, S ; GIRUZZI, G ; MAZON, D ; BARANA, O ; MOREAU, P: A control-oriented model of the current profile in tokamak plasma. In: *Plasma Physics and Controlled Fusion* 49 (2007), 7, 1075. – URL https://doi.org/10.1088/0741-3335/49/7/009

[Zagorski et al. 2013]   ZAGORSKI, R. ; IVANOVA-STANIK, R.I. ; STANKIEWICZ, R.: Simulations with the COREDIV code of DEMO discharges. In: *Nuclear Fusion* 53 (2013), jun, 7, 073030. – URL https://dx.doi.org/10.1088/0029-5515/53/7/073030

[Zohm et al. 2013]   ZOHM, H. ; ANGIONI, C. ; FABLE, E. ; FEDERICI, G. ; GANTENBEIN, G. ; HARTMANN, T. ; LACKNER, K. ; POLI, E. ; PORTE, L. ; SAUTER, O. ; TARDINI, G. ; WARD, D. ; WISCHMEIER, M.: On the physics guidelines for a tokamak DEMO. In: *Nuclear Fusion* 53 (2013), jun, 7, 073019. – URL https://dx.doi.org/10.1088/0029-5515/53/7/073019

[Zucca et al. 2008]   ZUCCA, C ; SAUTER, O ; ASP, E ; CODA, S ; FABLE, E ; GOODMAN, T P. ; HENDERSON, M A.: Current density evolution in electron internal transport barrier discharges in TCV. In: *Plasma Physics and Controlled Fusion* 51 (2008), dec, 1, 015002. – URL https://dx.doi.org/10.1088/0741-3335/51/1/015002

[Zylstra et al. 2022]   ZYLSTRA, A. B. ; HURRICANE, O. A. ; CALLAHAN, D. A. ; KRITCHER, A. L. ; RALPH, J. E. ; ROBEY, H. F. ; ROSS, J. S. ; YOUNG, C. V. et al.: Burning plasma achieved in inertial fusion. In: *Nature* 601 (2022), 7894, 542–548. – URL https://doi.org/10.1038/s41586-021-04281-w

# Simon Van Mulders

simon.vanmulders@hotmail.com | +41 789506866 | linkedIn/simon-van-mulders-895bb915a
Ch. de la Venoge 2 | 1025 Saint Sulpice (Switzerland)
Belgium | 01.05.1995

## WORK EXPERIENCE

**ITER Organization**                                       St-Paul-Lez-Durance, France | May 2023 – Apr 2025
Post-Doctoral Scientific Researcher
Equilibrium reconstruction and plasma state estimation for ITER using a suite of synthetic diagnostics and high-fidelity plasma simulations

**Swiss Plasma Center** | **EPFL**                          Lausanne, Switzerland | Oct 2018 – Apr 2023
Doctoral researcher
Tokamak plasma physics modeling, control and optimization

- Code development and maintenance of real-time capable tokamak plasma transport simulator (RAPTOR) in MATLAB, including integration of reduced physics models and the employment of efficient numerical schemes
- Experimental validation of reduced physics models
- Tokamak profile control and numerical optimization of ramp-up, flat-top and ramp-down phases
- Participation in international tokamak experiments at TCV (Lausanne, Switzerland) and AUG (Garching, Germany)

Supervisors: Dr O. Sauter and Dr F. Felici

## EDUCATION

**Ph.D. in Plasma Physics**                                 Lausanne, Switzerland | Oct 2018 - Apr 2023
Ecole Polytechnique Fédérale de Lausanne (EPFL)
Courses on control and operation of tokamaks, magnetic confinement, plasma instabilities and plasma diagnostics

**M.Sc. in Energy Engineering**                             Leuven, Belgium | Sept 2016 - Jun 2018
KU Leuven
*Magna Cum Laude*
Selected courses: numerical methods, thermal systems, turbomachinery, mechanical drive systems, power electronics, electrical drives, power systems, nuclear energy, control theory
Specialisation: thermo-mechanical energy | Master thesis: Design and performance analysis of a cooling tower for a low-temperature geothermal power plant – Supervisor: Dr W. D'Haeseleer

**Erasmus Exchange Semester**                               Lausanne, Switzerland | Sept 2017 - Feb 2018
Ecole Polytechnique Fédérale de Lausanne (EPFL)
Courses: energy storage, aerodynamics, turbulence, plasma physics, two-phase flows and heat transfer

**B.Sc. in Mechanical and Electrical Engineering**          Leuven, Belgium | Sept 2013 - Jun 2016
KU Leuven
*Cum Laude*

## AWARDS

**Exceptional Poster Award**                                San Diego, USA | July 2022
11th ITER International School, ITER Plasma Scenarios and Control

## SKILLS AND INTERESTS

**Programming:** MATLAB, Python, Git, Latex
**Languages:** Dutch (native), English (fluent), French (working), German, Italian (basic)
**Personal interests:** Long-distance running, hiking, cycling, skiing, history and literature

# PUBLICATION LIST

<u>First author</u>
Van Mulders, S. et al. (2023) to be submitted to **Plasma Phys. Control. Fusion**
*"Ramp-down optimization with the RAPTOR code, from ASDEX Upgrade to DEMO."*

Van Mulders, S. et al. (2023) to be submitted to **Nuclear Fusion**
*"Inter-discharge optimization for fast, reliable access to ASDEX Upgrade AT scenario."*

Van Mulders, S. et al. (2021) **Nuclear Fusion** 61 8, p. 086019
*"Rapid optimization of stationary tokamak plasmas in RAPTOR: demonstration for the ITER hybrid scenario with neural network surrogate transport model QLKNN."*

<u>Co-author</u>
Siccinio, M. et al. (2022) **Fusion Engineering and Design** 179, p. 113123
*"Impact of the plasma operation on the technical requirements in EU-DEMO."*

Maget, P. et al. (2022) **Plasma Phys. Control. Fusion** 64 4, p. 045016
*"Healing plasma current ramp-up by Nitrogen seeding in the full Tungsten environment of WEST."*

Kudlacek, O. et al. (2021) **Fusion Engineering and Design** 171, p. 112563
*"Developments on actuator management, plasma state reconstruction, and control on ASDEX-Upgrade."*

van de Plassche, K. L. et al. (2020) **Physics of Plasmas** 27 2, p. 022310
*"Fast modeling of turbulent transport in fusion plasmas using neural networks."*

# CONFERENCE PARTICIPATION

**2022 Theory of Fusion Plasmas, Varenna – Lausanne International Workshop, Varenna, Italy, September 12 - 16**
Invited oral presentation: *"Full-discharge simulation and optimization with the RAPTOR code, from AUG to ITER and DEMO."*

**2022 11th ITER International School, ITER Plasma Scenarios and Control, San Diego, USA, July 25 – 29**
Poster: *"Full-discharge simulation and optimization with the RAPTOR code, from AUG to ITER and DEMO."*

**2021 ASDEX Upgrade Programm Seminar, Schloss Ringberg, Kreuth, Germany, October 25-29**
Oral presentation: *"Optimizing the evolution of AT scenarios."*

**2021 47th Annual EPS Plasma Conference, Sitges, Spain (remote), June 21-25**
Poster: *"A novel tool for rapid optimization of stationary tokamak plasmas using RAPTOR-QLKNN applied to the ITER hybrid scenario."*

**2021 26th Integrated Operation Scenarios Topical Group Meeting, remote, May 17-21**
Oral presentation: *"Rapid optimization of stationary tokamak plasmas in RAPTOR."*

**2021 26th Transport and Confinement Topical Group Meeting, remote, March 22-25**
Oral presentation: *"Application of QLKNN10D for optimization of the ITER Hybrid Scenario."*

**2020 Theory of Fusion Plasmas, Varenna – Lausanne International Workshop, Lausanne, Switzerland, October 12 - 16**
Poster: *"Optimized DEMO ramp-down trajectories for safe and fast plasma termination."*

**2019 Annual Meeting of the Swiss and Austrian Physical Society, Zürich, Switzerland, August 27 - 30**
Oral presentation: *"Non-linear model-based optimization of stationary tokamak plasma profiles using RAPTOR."*